



MONASH University

---

**Selective Laser Melting of Ti6Al4V**

**Lattice Structures for Bone Implants**

---

Ezgi Onal

Master of Engineering Science and Bachelor of Science in  
Materials Science and Engineering

Supervisors:

Dr. Andrey Molotnikov

Dr. Jess Frith

Dr. Bernard Chen

Prof. Xinhua Wu

*A thesis submitted for the degree of Doctor of Philosophy at*

*Monash University in 2019*

Department of Materials Science and Engineering  
Monash University  
Clayton Campus, Victoria, Australia

## COPYRIGHT NOTICE

© Ezgi Onal (2019). Except as provided in the Copyright Act 1968, this thesis may not be reproduced in any form without the written permission of the author.

I certify that I have made all reasonable efforts to secure copyright permissions for third-party content included in this thesis and have not knowingly added copyright content to my work without the owner's permission.

### ABSTRACT

The use of lattice structures in the design of the orthopaedic implants is gaining popularity and underpins the development of next-generation customised implants. Lattice structures offer tailorable mechanical properties, space for bone in-growth and porous network for nutrient-waste exchange between the surrounding tissues. The advances in additive manufacturing have enabled the process-ability of the complex and intricate lattice structures. This is reflected in the increasing number of literature focussing on the performance and properties of the lattice structures. Most of the reported studies for bone tissue engineering utilise selective laser melting of Ti6Al4V alloy due to favourable mechanical properties, corrosion resistance and biocompatibility of Ti6Al4V alloy and the wide adoption of SLM machines. In this thesis we investigated new designs and processability methods of the Ti6Al4V lattice structures manufactured by selective laser melting technology. Specifically, functionally gradient porous designs and hollow-beam lattice are proposed to improve mechanical and biological properties of lattice scaffolds simultaneously. Furthermore, use of single point exposure strategy is explored as an attractive method for fabrication of lattice structures.

Commercial SLM machines were used to fabricate the scaffolds with Ti6Al4V powder. The scaffolds were characterised by scanning and transmission electron microscopes, the mechanical properties were assessed by static compression testing and *in-vitro* performance was studied by using osteoblast cells.

## ABSTRACT

---

Our study on functionally gradient designs combined results of mechanical and *in-vitro* biological studies. We show that implant designs can be improved by incorporating porous structures with gradually and continuously changing struts. Functionally gradient scaffolds with large pores (~1100  $\mu\text{m}$ ) in the outer surface allow cell attachment and migration; while the small pores (~900  $\mu\text{m}$ ) in the centre provide adequate mechanical stability to the implant are proposed. Our second study explored the hollow-tube lattice structure design which offers an ample space and channels to be loaded with therapeutic agents for controlled targeted drug-release. Hollow-beam lattice structures are found to possess higher stiffness and strength values (30-60% higher) than the solid-beam lattice structures counterparts at the same relative density. Furthermore, the cell colonisation throughout the hollow-beam scaffolds was more uniform, indicating better cell migration in these scaffolds. Our results demonstrated that hollow-beam lattices offer improved mechanical and biological properties and have the potential to be used for functionalised next-generation implants. Our last study focused on the processability of lattice structures investigated a largely unexplored alternative method of single point exposure scanning strategy. It offers a number of advantages over the contour-hatching scanning strategy. For example, the long file preparation times and high computational cost of complex STL files could be avoided in addition to having a direct control on the dimensions of the structures at each layer. This study revealed a saturation point for the maximum achievable strut size (520  $\mu\text{m}$  at 0.5 J of energy input). In addition, novel features were observed in double melted areas, which represents the strut junctions, with more homogeneous  $\alpha$ -lath sizes (200-300 nm) than the ones observed in the single melted areas (10 nm-1  $\mu\text{m}$ ).

Overall, this PhD thesis presents the results of our major three areas of study on the lattice structures; functionally gradient structures, hollow-beam lattices, and single point exposure



## ABSTRACT

---

scanning strategy. The interconnection between these studies lie in the goal of improving the design and processability of lattice structures for orthopaedic implant use. Major conclusions include suggestions for optimum pore size and distribution in functionally gradient structures and channel size for the hollow-beam lattices as well as for the processability window for the single point exposure method.

## GENERAL DECLARATION

---

### GENERAL DECLARATION

Declaration for thesis based or partially based on conjointly published or unpublished work.

In accordance with Monash University Graduate Research Thesis Examination Procedures section 1.9, the following declarations are made:

I hereby declare that this thesis contains no material which has been accepted for the award of any other degree or diploma at any university or equivalent institution and that, to the best of my knowledge and belief, this thesis contains no material previously published or written by another person, except where due reference is made in the text of the thesis.

This thesis includes 2 original papers published in peer reviewed journals. The core theme of the thesis is the selective laser melting of the Ti6Al4V architected structures for the use of bone implants. The ideas, development and writing up of all the papers in the thesis were the principal responsibility of myself, the student, working within the Materials Science and Engineering Department under the supervision of Dr. Andrey Molotnikov.

The inclusion of co-authors reflects the fact that the work came from active collaboration between researchers and acknowledges input into team-based research.

In the case of Chapter 4 and 5, my contribution to the work involved the following:

Thesis Chapter	Publication Title	Status	Nature and % of student contribution	Co-author name(s) Nature and % of Co-author's contribution	Co-author(s), Monash student Y/N
Chapter 4	Mechanical Properties and In Vitro Behavior of	Accepted	85% Concept and collecting data and	1. Jessica E. Frith, Editing manuscript and assisted in research planning (Supervisor)	No

## GENERAL DECLARATION

	Additively Manufactured and Functionally Graded Ti6Al4V Porous Scaffolds		writing first draft	2. Marten Jurg, Design of lattice structures, 15% 3. Xinhua Wu, Editing manuscript (Supervisor) 4. Andrey Molotnikov, Editing manuscript and assisted in research planning (Supervisor)	Yes  No  No
Chapter 5	Novel microstructural features of selective laser melted lattice structures fabricated with single point exposure scanning	Accepted	75% Concept and collecting data and writing first draft	1. Alexander E. Medvedev, acquired TEM and EBSD images and contributed to discussion, 20% 2. Sander M.A. Leeftang, Fabrication of the samples, 5% 3. Andrey Molotnikov, Editing manuscript and assisted in research planning (Supervisor) 4. Amir A. Zadpoor, Editing manuscript and assisted in research planning (Supervisor)	No  No  No  No

I have renumbered sections of submitted or published papers in order to generate a consistent presentation within the thesis.

**Student signature:**

Date: 29/11/2019

The undersigned hereby certify that the above declaration correctly reflects the nature and extent of the student's and co-authors' contributions to this work. In instances where I am not the responsible author I have consulted with the responsible author to agree on the respective contributions of the authors.

**Main Supervisor signature:**

Date: 29/11/2019

## PUBLICATIONS, PRESENTATIONS AND AWARDS DURING ENROLMENT

### **Publications:**

1. **E.Onal**, J.E. Frith, M. Jurg, X. Wu, A. Molotnikov, Mechanical Properties and *In Vitro* Behavior of Additively Manufactured and Functionally Graded Ti6Al4V Porous Scaffolds, *Metals* **2018**, 8, 200. (Chapter 4 of the thesis)
2. **E.Onal**, A.E. Medvedev, S.M.A. Leeftang, A. Molotnikov, A.A. Zadpoor, Novel microstructural features of selective laser melted lattice structures fabricated with single point exposure scanning, *Additive Manufacturing* 29 (**2019**) 100785. (Chapter 5 of the thesis)

### **Presentations:**

1. Materials Research Society (MRS) Fall Conference, Nov 2018, Boston, MA, USA. Presentation on “Selective Laser Melting of Ti6Al4V Lattice Structures with Hollow Struts: Processability & Mechanical Behaviour”.
2. Asia-Pacific International Conference on Additive Manufacturing (APICAM), Dec 2017, Melbourne, VIC, Australia. Presentation on “Additively Manufactured Functionally Graded Ti6Al4V Porous Scaffolds: Design, Mechanical Behaviour and *In Vitro* Response”.
3. Annual Australasian Society for Biomaterials and Tissue Engineering (ASBTE), Apr 2017, Canberra, ACT, Australia. Poster on “*In Vitro* and Mechanical Response of Gradient Porosity Ti6Al4V Scaffolds for Orthopaedic Implants”.
4. Combined Australian Materials Societies (CAMS), Dec 2016, Melbourne, VIC, Australia. Presentation on “Cellular Response of Porous Ti6Al4V Bone Scaffolds Fabricated by Selective Laser Melting”.

5. Australian Biomedical Engineering Conference (ABEC), Oct 2016, Brisbane, QLD, Australia. Presentation on “Cellular Response of Porous Ti-6Al-4V Bone Scaffolds fabricated by Selective Laser Melting”.

**Awards:**

1. **Monash Institute of Medical Engineering Travel Grant** (\$2,500 AUD) in 2017. Competitive travel grant award to visit the Design School of Loughborough University in the UK. This visit’s aim was to collaborate with design engineers and researchers to develop topologically-optimised orthopaedic implants.
2. **MTPConnect – Accelerating Australia SPARK Global Meeting** (\$3,000 AUD) in 2017. Competitive funding to attend Stanford SPARK Biomedical Innovation & Entrepreneurship Workshop, held in University of Tokyo, Japan. The two-week intense workshop was based on the application of translational research and commercialisation of medical products.
3. **Monash University Graduate Research Travel Grant** (\$3,000 AUD) in 2017. This grant was used to visit the Technical University of Delft in the Netherlands to collaborate with Prof. Amir Zadpoor from the Department of Biomechanical Engineering for three months in 2017.

**Scholarships:**

1. **Australian Postgraduate Award Scholarship** (8<sup>th</sup> Feb 2016 to 7<sup>th</sup> May 2019) - \$85,436 AUD
2. **Monash Departmental Scholarship** (8<sup>th</sup> Mar 2016 to 8<sup>th</sup> Mar 2019) - \$9,000 AUD

## Ph.D. COURSEWORK

As part of the Ph.D. program at Monash University, the Faculty of Engineering requires the Ph.D. candidates to enrol and pass two coursework, based on their interest and project. For this purpose, the ‘Mechanical Systems Design’ unit was taken in 2016 to learn more about systems engineering and get practical experience on design and simulation software. In 2018, the ‘Translation and Commercialisation of Medical Technologies’ unit was taken to complement my learning from the Stanford SPARK program in translational research and commercialisation of medical devices. The details of these courses are explained further.

### 1. MECHANICAL SYSTEMS DESIGN (MEC6883)

This unit emphasised on the engineering design with a focus on designing a system rather than the individual components of a system. In this way the unit integrated mechanical design with material selection, manufacture, and control systems, and the needs of in-service monitoring to optimize system performance.

Quality management systems, Lean techniques and Life-cycle assessment was applied to the proposed product or service to understand system variability, maximize and maintain value-creation and assess environmental impacts. As part of the unit, the design project included design of ‘human-powered transport’ system. This design project had a strong practical focus with extensive use of computer aided design and analysis software.

### 2. TRANSLATION AND COMMERCIALISATION OF MEDICAL TECHNOLOGIES (ENG 6007)

This unit provided an overview of the various aspects of translation and commercialisation of medical technologies in order to provide specific training that is highly relevant to the medical technology industry. The topics covered in the unit included policy and the International and national regulatory environment, medical device reimbursement, bioethics, intellectual property, product development and manufacturing, and health economics. The topics was taught in part by practitioners and other guest speakers who are highly skilled in their fields.

### ACKNOWLEDGEMENTS

I would like to express my sincere gratitude to my main supervisor, Dr. Andrey Molotnikov, for his guidance and help through my research project, as well as his great contribution to my professional development. I would like to thank my co-supervisors, Dr. Jess Frith, Dr. Bernard Chen and Prof. Xinhua Wu for sharing their knowledge and providing me continuous help over the course of my project.

I would like to acknowledge the Australian Postgraduate Awards (APA) for the financial support and the funding support from the ARC Research Hub for Transforming Australia's Manufacturing Industry through High Value Additive Manufacturing (IH130100008).

I would also like to thank Prof. Laurence Meagher, Dr. Dacian Tomus, A/Prof. Aijun Huang for their valuable suggestions during my Ph.D. milestones.

I would like to express my appreciation to Prof. Kiyonori Suzuki, Prof. Nick Birbilis, A/Prof. Philip Nakashima, Mr. James Griffith, Dr. Jisheng Ma for their continuous support and the opportunities they have provided to me. Also thanks to the staff and colleagues in the Department of Materials Science and Engineering, including Edna, Kris, Michelle, Graham, Daniel for their kind help and support.

I would like to acknowledge Monash Centre for Additive Manufacturing (MCAM), Woodside Innovation Lab and Monash Centre for Electron Microscope (MCEM) for the use of their facilities. Special thanks to Monash Institute of Medical Engineering (MIME) for the travel grants they provided for my project.

My appreciation extends to my colleagues and friends at Monash University, including Erin, Georgia, Kira, Marten, Lee, Gee, Gabi, Kai, Fred, Lachie and others for the nice and friendly work environment.

Finally, I would like to thank my parents and sisters for all the love, support and encouragement and special thanks to my lovely husband who has been the biggest supporter during my Ph.D. and has been always by my side when I needed.

For all my friends in Australia and overseas, thank you all for your friendship and support. I am sorry that I am not able to mention all people who contributed to this work. I would like to thank all of you.

## TABLE OF CONTENTS

---

### TABLE OF CONTENTS

COPYRIGHT NOTICE.....	1
ABSTRACT.....	2
GENERAL DECLARATION .....	5
PUBLICATIONS, PRESENTATIONS AND AWARDS DURING ENROLMENT .....	7
Ph.D. COURSEWORK .....	9
ACKNOWLEDGEMENTS.....	10
LIST OF FIGURES .....	15
LIST OF TABLES.....	22
LIST OF SYMBOLS AND ABBREVIATIONS .....	23
Symbols.....	23
Abbreviations.....	24
CHAPTER 1. INTRODUCTION .....	28
1.1. General Overview and Motivation.....	29
CHAPTER 2. LITERATURE REVIEW .....	34
2.1. Introduction.....	36
2.1.1. Lattice structures.....	38
2.1.3. Manufacturing of Lattice Structures .....	40
2.2. Introduction of Additive Manufacturing (AM).....	42
2.2.1. Direct Metal Deposition (DMD).....	43
2.2.2. Electron beam melting (EBM).....	44
2.3 Selective Laser Melting (SLM) .....	46
2.3.1. Process Description.....	46
2.3.2. Process Variables.....	48

---



## TABLE OF CONTENTS

---

2.3.3. Process Limitations .....	55
2.4. Selective Laser Melted Ti6Al4V Lattice Structures .....	58
2.4.2. Morphological properties of SLM Ti6Al4V .....	59
2.4.3. Mechanical Response of SLM Ti6Al4V lattices .....	65
2.4.4. Biological Response of SLM Ti6Al4V lattices .....	79
2.5. Case Studies .....	85
2.6 Gaps in literature .....	88
2.7. Conclusion of Literature Review .....	90
Chapter 3. Materials and Methods .....	91
3.1. Selective Laser Melting and Process Parameters.....	92
3.1.1. Concept Laser MLab Cusing Machine .....	92
3.1.2. Realizer SLM 125 Machine .....	93
3.2. Design of Scaffolds.....	94
3.2.1. Functionally Gradient Structures .....	94
3.2.2. Hollow-beam Lattice Structures .....	94
3.2.3. Single Struts for Single Point Exposure Study .....	95
3.3. Morphology Characterization .....	96
3.3.1. Dimensional Analysis .....	96
3.3.2. Micro-Computed Tomography .....	97
3.3.3. Density Measurements.....	97
3.3.4. Microstructure Analysis.....	99
3.3.4. Texture Studies .....	99
3.4. Mechanical Testing .....	99
3.4.1. Compression Test.....	99
3.4.2. Hardness Test.....	100

---

## TABLE OF CONTENTS

---

3.5. <i>In-Vitro</i> Assessments .....	100
Chapter 4. Functionally Gradient Porous Structure .....	102
4.1. Introduction.....	103
4.2. Preliminary Study .....	104
4.3. Research Paper.....	111
4.4. Supplementary Data.....	134
4.5. Conclusion of the Chapter .....	140
Chapter 5. Single Point Exposure Scanning Strategy for SLM .....	142
5.1. Introduction.....	143
5.3. Research Paper.....	145
5.4. Supplementary Data.....	160
5.4.1. Supplementary Data to the Published Paper.....	160
5.4.2. Additional Supplementary Data.....	163
5.4. Conclusion of the Chapter .....	170
Chapter 6. Hollow-tube Lattice Structures .....	172
6.1. Introduction.....	173
6.2. Methods and Materials.....	177
6.2.3. Study Design.....	177
6.2.3. Morphological properties.....	180
6.2.4. Mechanical Properties and Deformation Response .....	181
6.2.5. <i>In-Vitro</i> Study .....	181
6.3. Results.....	182
6.3.1. Morphological Properties.....	182
6.3.2. Mechanical Properties.....	187
6.3.3. <i>In-vitro</i> Response .....	191

---

## TABLE OF CONTENTS

---

6.6. Discussion .....	193
6.8. Conclusion of the Chapter .....	196
Chapter 7. Conclusions and Future Work.....	197
7.2. Conclusions.....	198
7.2. Future Work .....	201
REFERENCES .....	203

## LIST OF FIGURES

---

### LIST OF FIGURES

Figure 1. 1. Illustration demonstrating the interdisciplinary nature of the study.....	30
Figure 1. 2. Summary of the main objective of the thesis and thesis chapters satisfying the objective by two main approaches: Design and Process. ....	31
Figure 2. 1 Ashby chart of density-modulus, with the contours of the specific modulus $E/\rho$ [9] .....	37
Figure 2. 2 CAD-based unit cells library [19] .....	39
Figure 2. 3 TPMS-based unit cell library, a) P surface, b) G surface, c) D surface, d) I-WP surface [20] .....	39
Figure 2. 4 Examples of topology optimized unit cells [21].....	40
Figure 2. 5 Schematic illustration of water-jet cutting of Ti6Al4V plate (left) and assembling of the unit cells by press-fitting (right) to fabricate a lattice scaffold [23]. ....	41
Figure 2. 6 Schematic illustration of deformation forming process. Tetrahedral core is made by bending the nodes of the hexagonal perforated metallic sheet [24]. ....	41
Figure 2. 7 Direct Metal Deposition process, (a) schematic view [36], (b) process in action [37]. ....	44
Figure 2. 8 Schematic (a) SLM machine parts, and (b) processing parameters [48]. ....	47
Figure 2. 9 SEM images showing characteristic morphologies of stainless steel powder: (a) gas atomization (b) water atomization [53] .....	48
Figure 2. 10 Melting of powder layer with 38% (left) and 45% (right) packing density [56] ..	49
Figure 2. 11 Influence of hatch spacing. Left images belong to the sample that was scanned with a hatch spacing of 50 $\mu\text{m}$ : (a) top view; (b) side view; (c) front view; and (d) the scanning strategy and parameters applied. Right images belong to the sample that was scanned with a hatch spacing of 100 $\mu\text{m}$ : (e) top view; (f) side view; (g) front view; and (h) the scanning strategy and parameters applied [60]. ....	52
Figure 2. 12 Density of selective laser melting Ti6Al4V samples with different scanning speeds and hatch spacings (Laser power = 400 W, Layer thickness = 200 $\mu\text{m}$ ) [71]. ....	53
Figure 2. 13 Illustration of (a) uni-directional, (b) bi-directional, (c) island scanning, for	

## LIST OF FIGURES

contour-hatching scanning strategy [73].....	54
Figure 2. 14 Illustration of contour-hatching and single point exposure scanning strategy, showing the laser path to achieve desired circular shape [76].....	55
Figure 2. 15 (a) SEM image of a strut, T and B refer to top and bottom surfaces, respectively. (b) The comparison of surface roughness between as-produced top and bottom surface. (Pa: the average roughness, Pz: absolute difference between 10 highest peaks and deepest valleys) [82]. ....	56
Figure 2. 16 Lattice Ti6Al4V bone implants are gaining interest from (a) industry (Image source: Arcam) and (b) academia (Image source: RMIT University) .....	59
Figure 2. 17 SLM porous Ti6Al4V scaffold with designed pore diameter of 1000 $\mu\text{m}$ (indicated as black circle) and the actual measurement of the pore diameters. The designed pore dimensions were reduced to approx. 700 $\mu\text{m}$ , indicating a defined processing overhang of approx. 150 $\mu\text{m}$ [87] .....	60
Figure 2. 18 (a-c) 3D rendering of the micro-Ct volumes of diamond lattice cells with different strut thicknesses, (d-f) the segmented pores for lattices [93].....	61
Figure 2. 19 (a) Ternary phase diagram of Ti6Al4V [102], (b) Schematic graph to show the relationship between phase selection and cooling rate during solidification (from 1050°C) [103], Optical microscope images of (c) equiaxed, (d) bi-modal, (e) lamellar [104], (f) acicular [105] Ti6Al4V microstructure morphologies.....	63
Figure 2. 20 (a) Optical microscope image of SLM Ti6Al4V, (b) EBSD $\alpha'$ orientation map (the black arrow indicates the building direction), (c) orientation map of the reconstructed $\beta$ phase [101] .....	64
Figure 2. 21 Globular ‘Reference’ (a) and lamellar SLM (b) structures of TiAl6V4 alloy and the effect of thermomechanical treatment on the microstructure of the SLM samples (c–e) [92].....	65
Figure 2. 22 Pin-jointed frameworks collapse when loaded (a) by struts rotating around the joints (if joints are welded together, the struts <i>bend</i> ), and (b) by stretching of the struts ( <i>stretch-dominated</i> ) [113]. ....	67
Figure 2. 23 (a) Relative strength vs Relative density on logarithmic scale for cellular structures, <i>bending dominated</i> structures follow the trajectory of slope 1.5, whereas the <i>stretch dominated</i> structures along the trajectory of slope 1. (b) Relative modulus vs	

## LIST OF FIGURES

---

Relative density on logarithmic scale, <i>bending dominated</i> line structures follow the slope of 1, and the <i>stretch dominated</i> structures follow the slope of 2 [112].	69
Figure 2.24 Illustrated stress-strain curves demonstrating the deformation characteristics of stretch and bending dominated structures [124].	70
Figure 2. 25 Micro and nano scale ultralight lattice structures, (a) Octet-truss unit cells [125], and (b) Tetrakaidecahedron unit cell [125]. (c) Hierarchical hollow microstructure, combined of tetrahedron and octahedron [129].	71
Figure 2. 26 Failure modes of FBCCZ (representing diagonal shear band collapse), and FBCCXYZ (representing horizontal layer collapse) [133].	72
Figure 2. 27 Local distribution of maximum (a, d) and minimum (b, e) principal strains in single struts of the heat treated bcc (bending-dominated) and f2ccz (stretch-dominated) structure, respectively. The images were obtained at a macroscopic strain of $-1.5\%$ (compressive force). The directions of the local maximum principal strains are plotted as yellow lines in the enlargements (c, f) corresponding to the areas marked by the red squares in (a) and (d), respectively [140].	74
Figure 2. 28 The topology-property relationships predicted by analytical models for a variety of beam-based lattice structures. The elastic modulus (a) and yield strength (b) vs Relative density.	75
Figure 2. 29 SEM images of fracture surface after fatigue tests: (a) Samples mostly fracture close to the nodes. (b) A crack, which initiated and propagated close to a node for tension-compression fatigue. (c) The fracture surface in tension-tension fatigue showed signs of both fatigue crack propagation (upper right) and ductile overload fracture (lower left). (d) The fracture surface after compression-compression fatigue failure [162].	77
Figure 2. 30 The cyclic loading curve exhibits three different stages during compression–compression fatigue testing of porous titanium samples [163].	78
Figure 2. 31 In-vitro Biological Response Top: New tissue formation in 3D matrix channels. Actin fibres are stained with phalloidin-FITC and visualized under confocal laser scanning microscope. Tissue formation is shown in the channels of (i) triangular, (ii) square, (iii) hexagonal and (iv) round shape after culturing MC3T3-E1 cells after 21 days. Bottom: Numerical simulation of tissue formation <i>in-vitro</i> [188].	82
Figure 2. 32 a) reconstructed 3-D scapular tumor model. b) The virtual 3-D model of scapular	

---

## LIST OF FIGURES

---

prosthesis. c) The size of excised tumor and prosthesis was well matched. d) X-ray showed a proper shoulder articulation at 21 months postoperatively [199] .....	87
Figure 2. 33 (a) Custom designed tibia prosthesis, manufactured by EBM, (b) Successful implantation of the prosthesis, the ligaments were preserved and sutured to the proximal tibia space through porous structure [202].....	88
Figure 3. 1 SLM machines used: Concept Laser Mlab Cusing and Realizer SLM 125 .....	93
Figure 3. 2 Apparatus used for density measurements: (a) digital densitometry, (b) gas pycnometry. ....	98
Figure 4. 1 a) Madagascar lace leaf [205], b) lattice structure cocoon [207], c) bone structure [208].....	103
Figure 4. 2 Selected unit cell topologies to manufacture and mechanically test as a preliminary study. The compression test was performed with an Instron 5982 mechanical testing machine with a load capacity of 100 kN and compression rate of 0.06 mm/s. Elastic modulus for each sample was calculated from the initial linear-elastic region and are given in below table. ....	105
Figure 4. 3 Dodecahedron, octahedron and solid plates manufactured for preliminary <i>in-vitro</i> testing.....	107
Figure 4. 4 Cell viability measured by MTS assay for the eight treatments. P refers to porous specimens, S refers to solid specimens and CM is control medium. Values presented are mean average $\pm$ SD (n=3). Horizontal bars (*) and (**) denote the statistically difference when compared using One-Way ANOVA with Tukey-Kramer post-hoc analysis (at $p<0.05$ ). ....	108
Figure 4. 5 Low and high magnification fluorescence micrographs representing cell attachment of MG63 after 24 h incubation when cells were seeded by Method A and Method B on solid and porous plates and coverslips.....	109
Figure 4. 6 Fluorescent micrographs showing cell attachment on the octahedron and dodecahedron plates.....	110
Figure 4. 7 Compressive mechanical properties of uniform and gradient BCC structures. Data	

---

## LIST OF FIGURES

---

were presented as mean $\pm$ SD (n=5). (**** p<0.0001 when compared using ANOVA Tukey-Kramer Post-Hoc) (Supplementary Figure 1). .....	134
Figure 4. 8 SEM images of U0.4 scaffold incubated with MC3T3-E1 cells for 7 days. Images from top to bottom refers to respectively the top, middle and bottom surface of the scaffold along the vertical plane. Sells were seeded from the top surface. Cells were observed in all surfaces (Supplementary Figure 2). .....	135
Figure 4. 9 SEM images of U0.6 scaffold incubated with MC3T3-E1 cells for 7 days. Images from top to bottom refers to respectively the top, middle and bottom surface of the scaffold along the vertical plane. Sells were seeded from the top surface. The number of cells decreased towards to the bottom surface. Highlights were used to point out cells when they are not visible (Supplementary Figure 3). .....	136
Figure 4. 10 SEM images of U0.8 scaffold incubated with MC3T3-E1 cells for 7 days. Images from top to bottom refers to respectively the top, middle and bottom surface of the scaffold along the vertical plane. Sells were seeded from the top surface. The cell distribution was non-uniform in all surfaces and there were less number of observed cells throughout the scaffold (Supplementary Figure 4). .....	137
Figure 4. 11 SEM images of Dense-In scaffold incubated with MC3T3-E1 cells for 7 days. Images from top to bottom refers to respectively the top, middle and bottom surface of the scaffold along the vertical plane. Sells were seeded from the top surface. Cells were observed in all surfaces, but the distribution of cells was non-uniform on the bottom surface (Supplementary Figure 5). .....	138
Figure 4. 12 SEM images of Dense-Out scaffolds incubated with MC3T3-E1 cells for 7 days. Images from top to bottom refers to respectively the top, middle and bottom surface of the scaffold along the vertical plane. Sells were seeded from the top surface. There were no visible cells in the scanned regions (Supplementary Figure 6). .....	139
Figure 5. 1 A lattice cubic specimen with BCC unit cells was fabricated to demonstrate the capability of the single point exposure strategy to make angled struts and complex lattices (Figure S1). .....	160
Figure 5. 2 The 3D models of the struts reconstructed using the micro-CT images. The red colored parts are the internal pores and the grey parts are the specimens (Figure S2). ..	162

---



## LIST OF FIGURES

---

Figure 5. 3 Surface profile of the single struts fabricated at the laser power of (a) 128 W and (b) 144 W, and neighbouring struts at the process parameters of (c) 128 W-750 $\mu$ s and (d) 96W-1150 $\mu$ s. Here A2 and B2 refers to double-melted struts.....	164
Figure 5. 4 Surface height profiles of neighbouring struts fabricated at 128W-750 $\mu$ s and 96W-1150 $\mu$ s. The profiles were obtained by the Mitutoyo Surftest equipment. A2 and B2 refer to double-melted struts. ....	165
Figure 5. 5 The surface of the neighbouring struts and double-melted struts (A2 and B2), fabricated at 96W-1150 $\mu$ s, observed under the SEM. ....	166
Figure 5. 6 (a) SEM image of internal pore in the double-melted strut, (b-d) EDX elemental mapping, (e) EDX line analysis of the same area. ....	168
Figure 5. 7 Ultra-High-Resolution mode under the SEM, images of unpolished (a) single strut and (b) bulk Ti6Al4V cube. ....	169
Figure 6. 1 Hollow lattice structures in (a) biology [224], (b) architecture [222] ,and (c) micro/nano size [225]. ....	173
Figure 6. 2 CAD illustrations of (a) solid unit cells and unit cells with hollow-tube thickness of (b) 0.6 mm and (c) 0.3 mm for the BCC, zBCC and 2zBCC topologies. (d) Cubic scaffolds made of 4x4x4 unit cells with scaffold edge length of 15mm. ....	179
Figure 6. 3 (a) As-fabricated cubis scaffolds imaged by digital camera, (b) micro-CT images of 2zBCC with voxel size of 22.8 $\mu$ m from different locations, (c) constructed into a 3D model, (d) and sliced in the half. (e) Micro-CT image of 2zBCC with voxel size of 5 $\mu$ m, showing internal porosity. ....	183
Figure 6. 4 SEM images of hollow (a) BCC, (b) zBCC, (c) 2zBCC scaffolds. Each coloured line represents different pores, introduced by the design. (d) Optical microscope image of hollow BCC scaffold, the white boxes show the martensitic $\alpha$ -laths. ....	186
Figure 6. 5 Stress-strain curves of (a) BCC, (b) zBCC and (c) 2zBCC hollow and solid lattices. (d) Relative density vs Relative Elastic Modulus of all the structures with fitted power law curves. ....	188
Figure 6. 6 Failure modes of BCC, zBCC and 2zBCC structures with hollow-tubes (0.3mm thickness) and solid-beams. Left images represent the initial state, middle and right images present the progressive failure. Arrows point the regions of deformation and	

---

## LIST OF FIGURES

---

failure (Scale bars = 15mm).....	190
Figure 6. 7 Cell proliferation measured by MTS assay after culturing 1 and 7 days on the solid and hollow lattice structures. Data were presented as mean $\pm$ SD (n=3). (** $p < 0.001$ and *** $p < 0.0001$ when compared using ANOVA Tukey-Kramer post-hoc test).	
.....	192
Figure 6. 8 Fluorescence micrographs representing merged Hoechst stained nucleus (blue) and actin cytoskeleton (red) of MC3T3-E1 preosteoblast cells on the solid and hollow-beam BCC and 2zBCC structures after culturing for 1 day and 7 days. Top represents the side where cells were seeded onto the samples.....	193

## LIST OF TABLES

---

### LIST OF TABLES

Table 2. 1 Industries and applications have token up SLM. ....	47
Table 2. 2 The chemical composition of Ti6Al4V [85].....	58
Table 2. 3 Mechanical properties of Ti6Al4V ELI outlined in the ASTM F136 Standard [85] .....	58
Table 2. 4 Unit cell geometries and their mechanical properties, reported in literature.....	73
Table 2. 5 Compressive properties of human cancellous bone [169] .....	79
Table 2. 6 Clinical case studies reported on custom-designed porous implants.....	86
Table 3. 1 Process Parameters used for Concept Laser Mlab Cusing with Ti6Al4V ELI powders .....	92
Table 3. 2 The laser power and exposure time values used to manufacture struts by single point exposure strategy. ....	96
Table 4. 1 Elastic modulus of the uniform scaffolds with different unit cell geometries and strut thicknesses. ....	105
Table 5. 1 Relative density calculation of the of the bulk material constituting the struts of the BCC cubic scaffold using Archimedes principle (Table S1).....	160
Table 5. 2 Porosity measurements calculated from the micro-CT images of the specimens. The values do not represent the real volume values as they are based on the 3D model. The ratio of the volumes should be taken into consideration (Table S2). ....	161
Table 6. 1 Hollow-beam lattice structure design parameters.....	178
Table 6. 2 The volume fraction and relative density of the specimens.....	184
Table 6. 3 The summary of the mechanical properties of hollow and solid beam structures measured by compression tests (Mean $\pm$ SD).....	188

---

## LIST OF SYMBOLS AND ABBREVIATIONS

### Symbols

Listed in the order of appearance in the thesis.

$R_a$	Roughness average
$R_{max}$	Maximum roughness depth
$P$	Laser power
$t$	Layer thickness
$v$	Scanning velocity
$E$	Volumetric energy density
$h$	Hatch spacing
$p^*$	Density of cellular structure
$p^o$ or $p_s$	Density of solid
$M$	Maxwell stability
$\sigma$	Stress
$\varepsilon$	Strain
$\sigma_y^*$	Yield strength of cellular structure

## LIST OF SYMBOLS AND ABBREVIATIONS

---

$\sigma_y^o$ or $\sigma_s$	Yield strength of solid
$E_y^*$	Elastic modulus of cellular structure
$E_y^o$ or $E_s$	Elastic modulus of solid
$V$	Volume
$W_a$	Weight in air
$W_e$	Weight in ethanol
$V_f$	Volume fraction
$V_t$	Volume total

## Abbreviations

Listed in the order of appearance in the thesis.

AM	Additive Manufacturing
SLM	Selective Laser Melting
BCC	Body Centred Cubic
DMD	Direct Metal Deposition
EBM	Electron Beam Melting
ELI	Extra Low Interstitials
CAD	Computer Aided Design

## LIST OF SYMBOLS AND ABBREVIATIONS

---

TPMS	Triply Periodic Minimal Surfaces
3d	3-dimensional
RD	Rapid Prototyping
RM	Rapid Manufacturing
DDM	Direct Digital Manufacturing
DED	Direct Energy Deposition
FDM	Fused Deposition Modelling
VED	Volumetric Energy Density
SEM	Scanning Electron Microscope
DoE	Design of Experiments
BIC	Bone to Implant Contact
CT	Computed Tomography
HF	Hydrofluoric acid
HIP	Hot Isostatic Pressing
RD	Relative Density
FCCz	Face centred cubic with vertical struts
FBCCz	Face and body centred cubic with vertical struts
FBCCxyz	Face and body centred cubic with horizontal and vertical struts
FEA	Finite Element Analysis
HAp	Hydroxylapatite

## LIST OF SYMBOLS AND ABBREVIATIONS

---

hPDC(s)	Human Periosteum Derived Cells
hMSC(s)	Human Mesenchymal Stem Cells
MRI	Magnetic Resonance Imaging
EDM	Electrical Discharge Machine
OPU	Oxide Polishing Solution
OM	Optical Microscope
OD	Optical Density
TEM	Transmission Electron Microscope
STEM	Scanning Transmission Electron Microscope
SAED	Selected Area Electron Diffraction
EBSD	Electron Backscatter Diffraction
SD	Standard Deviation
FIB	Focused Ion Beam
zBCC	BCC unit cell with extra trusses at the corner nodes
2zBCC	BCC unit cell with extra trusses at the corner and centre nodes
SPPW	Self-Propagating Photopolymer Waveguide

---

*“When modern humans builds large load-bearing structures, they use dense solids: steel, concrete, glass. When nature does the same, it generally uses cellular materials: wood, bone, coral. There must be good reasons for it”.*

-M.F. Ashby



# CHAPTER 1. INTRODUCTION

### 1.1. General Overview and Motivation

Additive manufacturing (AM) is revolutionizing the way we think of materials, products and manufacturing, and disrupting many industries, including healthcare. Additively manufactured customized prosthetics and implants are gaining popularity due to their superior function and performance, accessibility and cost. Because of its digital nature that includes digital design and manufacturing, as well as its disruptive influence on global manufacturing market, AM is considered as one of 4<sup>th</sup> Industrial Revolution technology and is the fastest growing manufacturing sector globally [1].

Orthopaedic implants are medical devices manufactured to replace or support a damaged bone or joint. Current orthopaedic implants are manufactured in different shapes and sizes to cater for everyone. However, this generally requires a representative from the manufacturing company to aid the clinician during the operation to find the right match. Next generation orthopaedic implants are ideally customised in their anatomic shape to fit into the defected bone area, which will eliminate the time that the clinician spends finding the right match during the surgery. In addition, these implants should mimic the structure and mechanical properties of the host bone. Each bone in our body is different based on the location, the stress applied on them, as well as our age, sex and physical condition.

Metallic materials including stainless steel, cobalt-chromium and titanium alloys are the primary choice for the orthopaedic implants due to their biocompatibility and mechanical properties [2]. Among them, Ti6Al4V is the most widely used as it is lightweight and highly corrosion resistant. However, it is not wise to use the same material for different bones, unless its properties are modified accordingly to the host bone. For example, the mechanical and physical requirements of an implant are different when it is designed for knee, for which loading conditions should be considered, or for a skull, for which loading conditions are not necessarily important but being lightweight is. Therefore, the implants should be customised based on the anatomic and mechanical requirements. The mechanical properties of biomaterials can be altered by changing their porosity [3]. Additive manufacturing is promising manufacturing technique to produce complex shapes with tailored porosity.

Porous or cellular solids offer tailorable mechanical properties, ample space and a porous network for cell attachment, migration and bone in-growth. In recent years, the interest towards porous bone scaffolds has risen amongst researchers. Some of the areas that research has focused on are mechanical and biological properties of different designs, design optimization, manufacturing and post-processing, and microstructure. However, there are still largely unexplored gaps on porous scaffolds in terms of their design and manufacturing in literature.

In this work, three research objectives were identified and investigated, which aim to contribute to the field of selective laser melting of porous Ti6Al4V structures to be used as bone scaffolds. The interdisciplinary nature of the project is summarised in Fig. 1.1. These objectives are:

- i. Understanding the interplay between mechanical and biological behaviour of functionally gradient structures and their optimization based on the assessment of both of these behaviours.
- ii. Studying the processability of lattices and exploring an alternative scanning strategy of SLM for lattice manufacturing that can beneficially provide control over dimension, computational cost and build time.
- iii. Exploring and establishing guidelines for the processing and mechanical response of novel lattice designs, such as hollow-tube lattices, which introduce channels and pores that provide space to incorporate drugs or bone morphogenetic proteins.

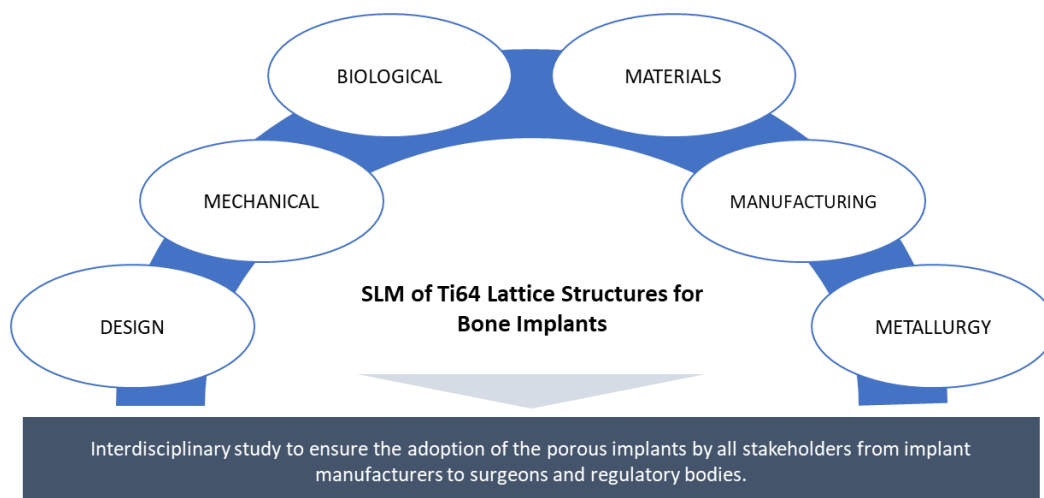


Figure 1. 1. Illustration demonstrating the interdisciplinary nature of the study.

## CHAPTER 1. INTRODUCTION

The sum of these objectives is to advance the functionality and performance of porous orthopaedic implants manufactured by selective laser melting technology. Figure 1. 2 illustrates the structure of the project and the summary of the work that has been done to meet the listed objectives.

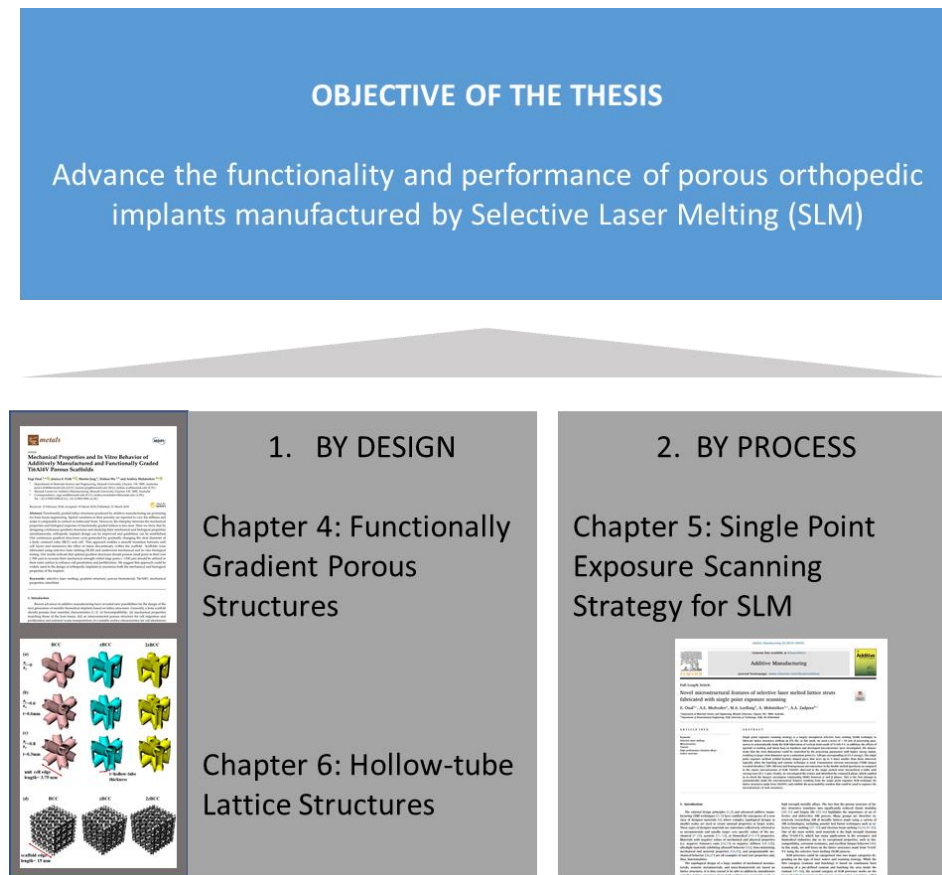


Figure 1. 2. Summary of the main objective of the thesis and thesis chapters satisfying the objective by two main approaches: Design and Process.

The thesis is subdivided into seven chapters and illustrated in below figure.

- The first chapter presents the general overview of additive manufacturing and provides a motivation for studying novel fabrication methods of orthopaedic implants.
- In Chapter 2, a literature review covering porous structures and their manufacturing is presented, followed by an introduction to additive manufacturing. The literature survey

specifically focuses on selective laser melting of Ti6Al4V and porous structures, as well as clinical case studies.

- In Chapter 3, materials and methods used for this project is outlined. SLM machines used for manufacturing samples are introduced and process parameters defined. Details of the sample designs are given. Experimental settings for characterization including sample morphology, microstructure, mechanical properties and *in-vitro* biological response are also presented in detail.
- Chapter 4 presents the study on the functionally gradient porous structures and includes the published paper in Metals journal. After identifying the need to investigate functionally gradient porous structures with gradually and continuously changing layers, two gradient and three uniform BCC scaffolds were designed and manufactured by Concept Laser MLab machine. We realised the need to study mechanical and biological response in-parallel since these two properties possess contrasting requirements. For this purpose, the mechanical properties and deformation behaviour were studied by compression testing and the *in-vitro* biological response was investigated by using mouse pre-osteoblast cells. This work aimed to establish guidelines for optimized gradient designs that can be used as bone scaffolds.
- Chapter 5 presents the study on single point exposure scanning strategy, which is a largely unexplored SLM scanning strategy. Single point exposure offers advantages for lattice structures such as decreased computational cost and build time, and better control on strut dimensions. Single struts were designed and manufactured with over 50 process parameters to identify the effect of parameters on morphology and microstructure. Further, lateral heat and double-melting effects were investigated by fabricating struts in certain arrangements. The morphology, microstructure, texture and hardness were assessed. This study aimed to explore an alternative SLM scanning strategy to improve the processability and properties of lattice scaffolds.
- Chapter 6 presents the study on the hollow-tube lattice structures. For this work, three unit cell topologies with solid-beam and hollow-tube struts were manufactured. The mechanical properties and deformation behaviour was assessed by compression testing.

In-vitro studies looked at the difference in cell proliferation between the solid-beam and hollow-beam lattice structures, as well as between the different topologies. It was shown that hollow-tube lattices exhibit superior mechanical properties and biological response compared to the solid-beam lattices of the same relative density. This study further assesses the properties of hollow-beam lattice structures, which has the potential to be functionalised by incorporating drug-delivery systems into their additional channels and tubes.

- Chapter 7 summarizes the main outcomes of the thesis and Ph.D. study. It also includes proposals for future work.

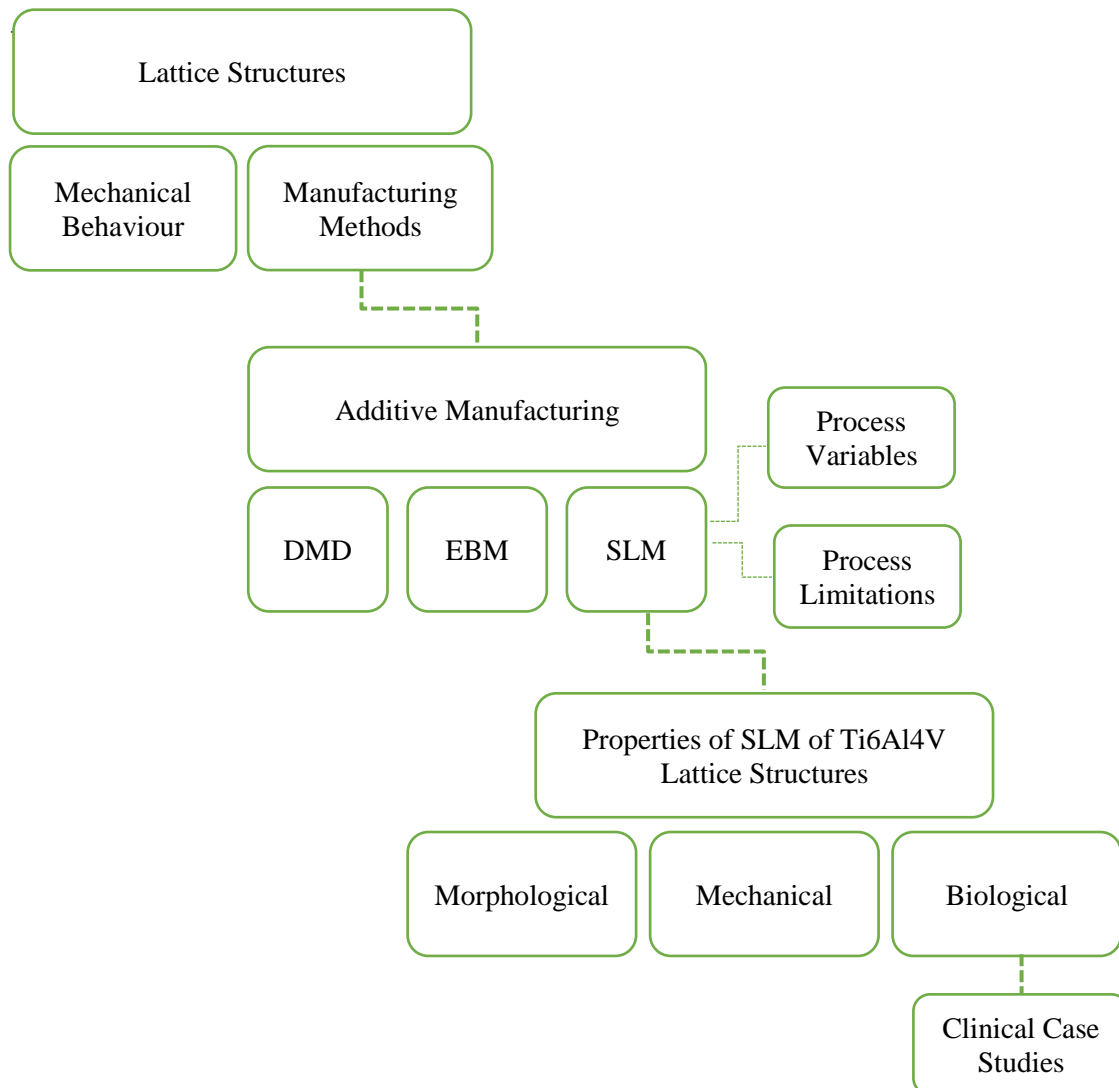
## CHAPTER 2. LITERATURE REVIEW

Bone is a dynamic and diverse tissue that continues to remodel throughout its life [4, 5]. There are more than 200 bones in the human skeletal system, and the morphological and mechanical properties of the each bone is different and influenced by the loading conditions [5]. Bone defects and failure happen due to trauma, infection, cancer and aging. There were approximately 5.3 million orthopaedic surgeries in 2012 in the USA alone [6] and the global orthopaedics market was valued at approximately at \$53 billion in 2017 [7]. Bone auto-grafting, which involves transplanting patient's bone from another location to treat bone defects, served as the gold standard for bone grafting due to their histocompatibility and non-immunogenicity [5]. However, bone auto-grafting poses high risk of infection, considerable pain and surgical limitations [8].

Bone tissue engineering aims to introduce new functional synthetic bone grafts or scaffolds to treat bone defects and induce bone regeneration. Engineered scaffolds have the potential to fully replace the conventionally used auto-grafted bone due to their limitless supply and advanced functional properties. An ideal engineered scaffold should mimic the physical and mechanical properties of the host bone. This can be achieved by introducing a porous network to scaffolds which can anatomically fit perfectly into the defected bone area. Preferably, the implant is customised to match both the outer shape and inner porous structure of the bone. These customised implants are considered as next-generation orthopaedic implants and they have gained broad attention from researchers and industry.

There are numerous reports in literature focusing on different aspects of the customised porous implants. This study aims to contribute to advancing the next-generation customised implants through lattice structure design and processing. Here, the literature review first introduces the lattice structures, their designs, mechanical properties and manufacturing methods. Then, metallic AM methods are evaluated and a rigorous review on selective laser melting of Ti6Al4V is performed, including a discussion of the SLM process parameters and limitations. Further, since this Ph.D. project is a multi-disciplinary project between engineering and medicine, specific literature review covering morphological, mechanical and biological properties of SLM Ti6Al4V lattice structures are given. Finally, clinical case studies and results from follow ups at 1-2 years' timeframe are presented. The framework of the literature review is given in the diagram below.





## 2.1. Introduction

Modern engineering applications require materials which are lighter, tougher, and stronger and can be obtained in a sustainable matter at a lower price than in the past. Most of the materials we use nowadays are not the materials found in nature but they are highly-engineered and tailored multi-functional materials. These materials are often synthesised using a combination of two or three constituents and are known as “*architected*” or “*hybrid*” materials. In some cases, the properties of the hybrid materials are attributed to a specific arrangement of these

constituents. [9]. Architected materials play an important role in materials engineering because they have the potential to fill the gap in Ashby plots.

Figure 2. 1 is an example of Ashby chart of density vs Young's modulus. A part of this chart is populated with known materials but it also shows gaps in the left upper and right bottom corners. These holes can be filled by new materials, of which either the composition, microstructure or architecture needs to be modified.

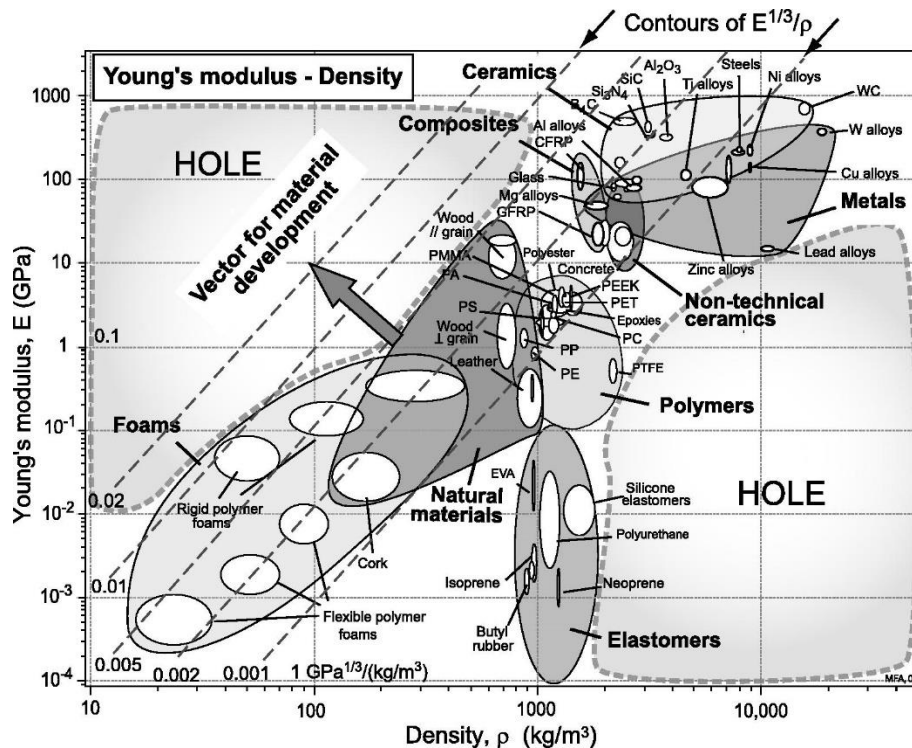


Figure 2. 1 Ashby chart of density-modulus, with the contours of the specific modulus  $E/\rho$  [9]

Some well-established architected materials include foams, sandwich structures, lattice structures, composites, etc. all of which have unique and interesting properties. As the scope of this thesis is particularly on lattice structures, a more detailed review on lattice structures will be presented.

The literature review covers the manufacturing of lattice structures, including additive manufacturing technologies. It is followed by a detailed description of a selective laser melting process and use of a titanium alloy, specifically Ti6Al4V ELI for manufacturing of the lattice

structures. Finally, the morphological properties, mechanical performance and biological response of SLM produced Ti6Al4V lattices is discussed and several case studies are presented.

### 2.1.1. Lattice structures

Lattice structures are a sub-category of cellular materials and can be defined as reticulated truss structures made of lattice elements (rods, beams or shells), generated by tessellating a unit cell in a space with no gaps between cells [10]. The topology of the unit cell is critical in controlling the performance of the lattice structures and can be classified into the following groups:

- CAD-based [11, 12],
- Implicit surfaces [13, 14],
- Topology optimized unit cells [15, 16].

The CAD-based designs are based on Platonic or Archimedean polyhedral solids such as simple cubic, rhombic-dodecahedra, diamond, and octet unit cells [16] (Figure 2. 2). Implicit-based unit cells, which can be referred to as triply periodic minimal surfaces (TPMS), have minimal surfaces without self-interactions and mean curvature of zero [17] (Figure 2. 3). Some of the famous TPMS examples are Schwartz's P-surface, Schwartz's diamond and gyroid unit cell. Topology optimized unit cells are gaining popularity in literature and are based on the numerical methods which optimize the geometry of the unit cell to satisfy objective functions [18] such as enhanced mechanical performance or minimum material usage (Figure 2. 4).

Lattice structures offer a degree of freedom in the design of a material. Unit cell geometry, unit cell size and distribution, truss thickness and porosity are some of the design elements that can be controlled. By changing the architecture of the lattice structures, properties of the material such as mechanical, biological and acoustic can be tailored to specific requirements. Due to a large degree of freedom in design, lattice structures have a great potential to fill the gaps in Ashby charts and to be utilized for advanced engineering applications.

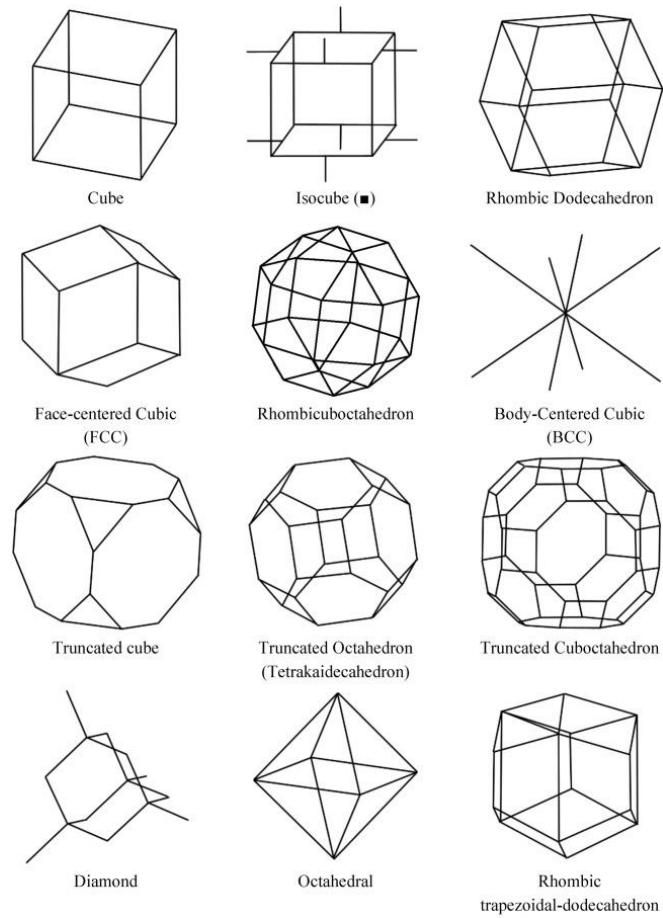


Figure 2. 2CAD-based unit cells library [19]

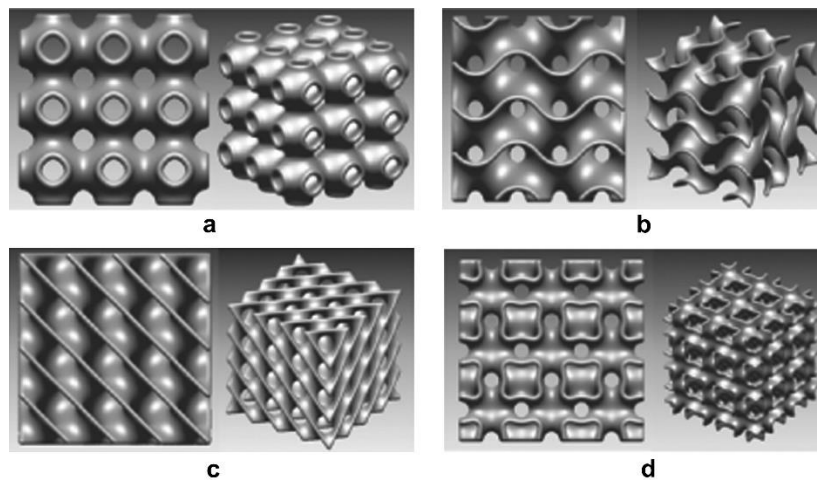


Figure 2. 3 TPMS-based unit cell library, a) P surface, b) G surface, c) D surface, d) I-WP surface [20]

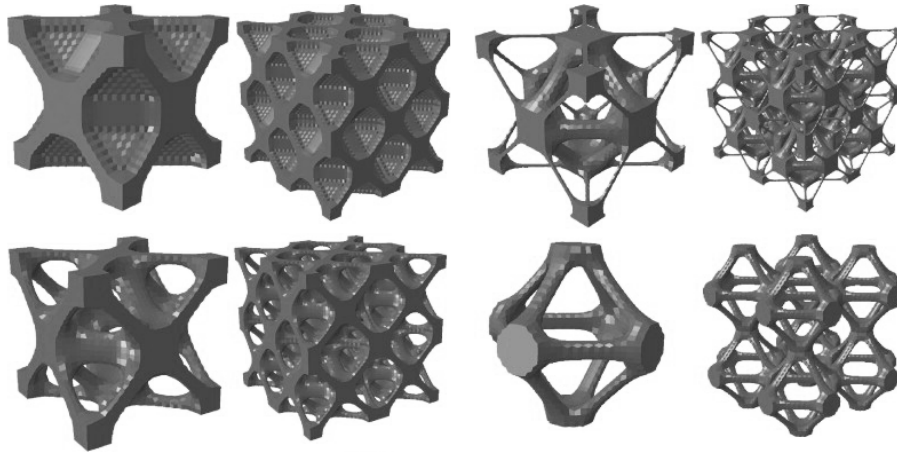


Figure 2. 4 Examples of topology optimized unit cells [21]

### 2.1.3. Manufacturing of Lattice Structures

Manufacturing of the lattice structures is a challenging task. The difficulty of manufacturing the lattices is due to their complex and intricate geometries and some of the challenges include being highly labour-intensive, costly and slow to manufacture. However, the advances in additive manufacturing provide new avenues for exploring and manufacturing many of the aforementioned lattice topologies. The most common manufacturing methods used before additive manufacturing included cutting, weaving, braising, deformation forming and casting [22]. These methods are summarized briefly to highlight their challenges.

- i. Water-jet cutting uses a high-pressure jet of water, or mixture of water and abrasives, to cut metallic or plastic sheets (Figure 2. 5). The major drawback of this method is that individual unit cells are first cut and then assembled into a final shape or product. The assembly occurs through press-fitting of the segments, which significantly increases the overall production time [22, 23].

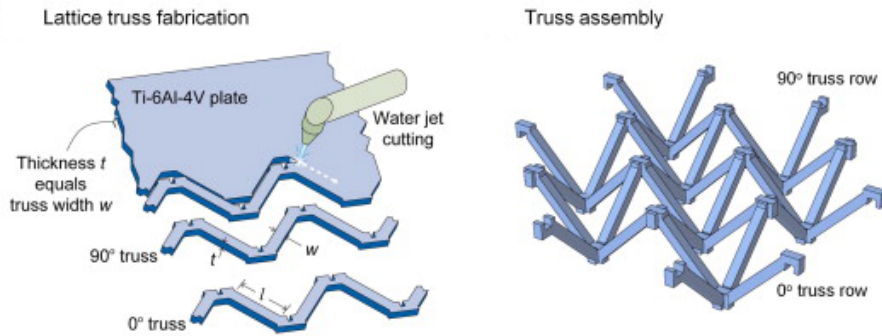


Figure 2. 5 Schematic illustration of water-jet cutting of Ti6Al4V plate (left) and assembling of the unit cells by press-fitting (right) to fabricate a lattice scaffold [23].

- ii. Weaving is a metallic textile technology that uses metallic flexible wires [24]. Braising, which is a metal-joining process by melting and flowing a filler material [25], needs to be used with weaving to stabilize the flexible wires.
- iii. Deformation forming utilizes press-forming of patterned and perforated sheets to bend the sheets at the nodes [24] (Figure 2. 6). The deformed sheets can be brought together to form sandwich panels or scaffolds.

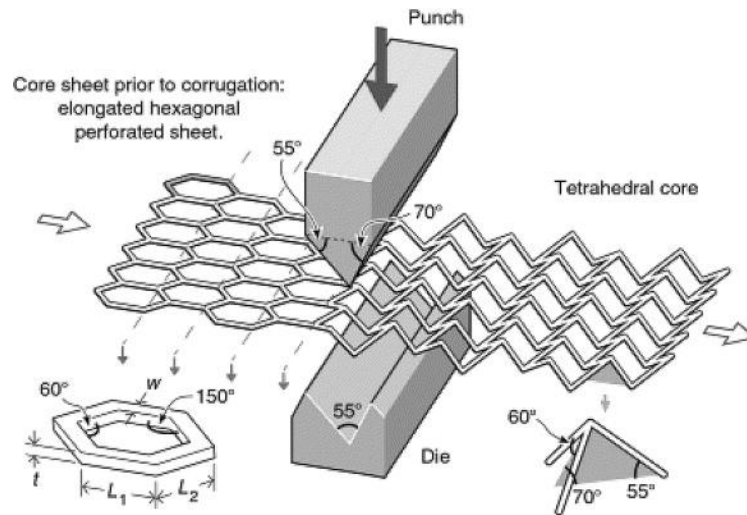


Figure 2. 6 Schematic illustration of deformation forming process. Tetrahedral core is made by bending the nodes of the hexagonal perforated metallic sheet [24].

- iv. Investment casting of a metallic liquid into a lattice-shaped ceramic mold is another method used to manufacture lattice scaffolds or sandwich panels. Molds are generally created by injection molding or rapid prototyping of a polymer frame, which is then coated by ceramic slurry and dried [26]. The polymer scaffold is generally removed by vaporization to create space for the metallic liquid. The casting process limits the minimum dimensions that can be achieved due to slow metallic flow around the thin nodes [26].

Additive manufacturing (AM) is defined in the ASTM F2792 standard as ‘the process of joining materials to make objects from 3D model data, usually layer upon layer, as opposed to subtractive manufacturing methodologies’ [27]. AM techniques are better suited to manufacturing lattice structures compared to the traditional methods. With additive manufacturing methods, a material can be placed where it is required as a result of the layer-by-layer fabrication approach. This provides the high precision required for the manufacturing of lattice structures and avoids the need for post-processing, such as braising, which is required for most of the traditional manufacturing methods. AM further saves enormous time and money compared to other methods [28]. AM technologies are specialized based on the material used, its solidification technique and the concept of the machine. The AM methods are explained in the next section.

## 2.2. Introduction of Additive Manufacturing (AM)

Additive manufacturing describes the fabrication approach that relies on building the product in a layer-by-layer fashion. Three basic components of AM are: a CAD software to design the product, the AM machine and the feedstock material.

AM is also referred to as 3D printing, rapid prototyping (RP), rapid manufacturing (RM) and direct digital manufacturing (DDM) in literature and media. AM includes various manufacturing processes such as material extrusion, directed energy deposition (DED), material jetting, binder jetting, vat polymerization and powder bed fusion. AM technologies



can produce parts using many different materials, ranging from metals and polymers to human tissue and food. Many industries can benefit from additive manufacturing and the main industries that have embraced AM and are driving the change are aerospace, automotive and healthcare [29].

The commercial history of AM began in 1987, when 3D System introduced a stereolithography (SL) machine, the SLA-1 [28]. In early 1990s, fused deposition modelling (FDM) was developed. It was followed by the invention of multicolour jet binding by MIT, powder-sintering methods, and powder-based fusion technologies in the 2000s [30]. AM is now the fastest growing sector of manufacturing globally [1]. The AM industry grew US\$1 billion to US\$5.165 billion in 2015 alone, representing a total compound annual growth rate of 25.9% [31]. Airbus, General Electric, Stryker, Audi, Siemens, BMW, Hewlett-Packard and Nike are some of the leading global companies that are using AM technologies extensively [32].

Despite the fact that there are different processes and names for each AM technology, the basic working principle of AM processes are similar. The CAD model is first sketched and converted into an industry standard STL file that can be read and sliced by an AM machine. The AM machine can use a sheet, filament, powder or liquid feedstock material to add successive layers upon each other until the part is build. AM technologies have specialised names based on the feedstock material and the concept of the machine. Among these technologies, metal AM technologies include direct metal deposition (DMD), electron beam melting (EBM) and selective laser melting (SLM). These methods will be discussed further due to their relevance for the proposed project.

### 2.2.1. Direct Metal Deposition (DMD)

DMD uses a feed nozzle to drive the powder where the laser is scanning to melt and consolidate the powder materials at that exact point (Figure 2. 7). DMD nozzle can have six degrees of freedom and multiple materials can be delivered at the same time, which makes DMD technology popular not only for building a part but also for coating and rebuilding/repairing



parts [33]. Global manufacturers of DMD machines include Trumpf (Germany) and Optomec (USA).

A motion control program, developed from the CAD model of the desired part, is used to control the motion of a laser focal spot [34]. Metal powders are injected into the laser focal zone and go through melting and solidification stages during the process. Successive layers are then stacked to fabricate the whole component based on the CAD model.

The challenges for DMD include surface roughness (approximately  $R_a$  of 10-20  $\mu\text{m}$  and  $R_{\text{max}}$  of 85-115  $\mu\text{m}$  [35]), dimensional inaccuracy compared to designed models, the need for post treatments to achieve required dimensions, and surface, residual stress and distortion of the deposited layers [34]. These challenges can be addressed by modifying the process parameters, such as laser power, scan speed and pattern, and optimizing the motion path and control code.

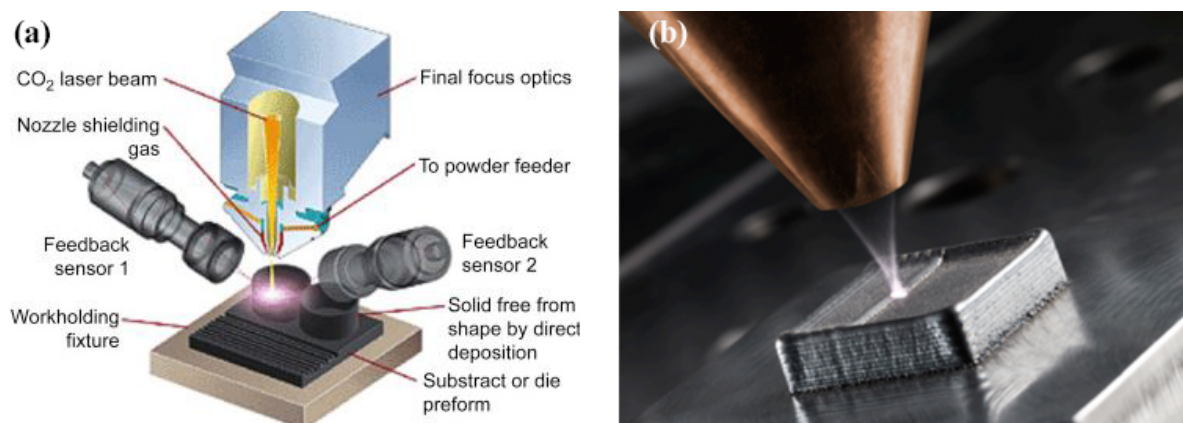


Figure 2. 7 Direct Metal Deposition process, (a) schematic view [36], (b) process in action [37].

### 2.2.2. Electron beam melting (EBM)

EBM is based on the principle of using electron beam for melting of the metallic powders. For EBM, a powder bed is selectively melted by the electron beam in successive layers to achieve a desired part. Due to high operating temperatures ( $>1000\text{ }^{\circ}\text{C}$ ), the process needs to be carried out in a closed chamber with an inert gas environment. Mean or average powder particle sizes

used for EBM can range from 10  $\mu\text{m}$  to 60  $\mu\text{m}$ ; with nominal sizes of  $\sim 40$   $\mu\text{m}$  [38]. Material systems used for EBM include stainless steel (17-4), tool steel (H13), Ni-based superalloys (625 and 718), Co-based superalloys (Stellite 21), low-expansion alloys (Invar), hardmetals (NiWC), intermetallic compounds, aluminum, copper, titanium, beryllium and niobium [39]

The key advantage of EBM is reduced residual stresses during processing of metallic powders due to slower cooling rates. The powder bed can be heated by scanning the electron beam several times across the build plate to maintain the temperature within the building volume, which will decrease the temperature gradients and therefore cooling rate [40]. However, EBM has also several disadvantages such as a poor surface quality, high cost of machine maintenance and raw material. The leading global EBM machine supplier is Arcam (GE Additive), which is also the founder of the technology.

EBM resembles selective laser melting since both are powder-bed based processes, and the difference comes from the source of energy; electron beam vs laser. Literature revealed a number of studies comparing EBM and SLM [38, 41-46]. These studies show that both processes have their own advantages and disadvantages. For example, due to high velocities of electron beam, the building time can be less for EBM than SLM; however, the parts might have higher surface roughness. Therefore, the user should consider and compare these two powder-bed based AM methods based on the needs of the desired part.

In summary, AM offers a selection of processing methods than can be applied for different materials and applications. The users should identify the best AM solution for their needs, considering the limitations and advantages of AM processes. The freedom and flexibility that AM technologies offer is affecting the global manufacturing scene. AM is shifting the centralised manufacturing system to distributed manufacturing that permits customisation of product and flexibility of fabrication technology [47]. This change in global manufacturing is among the emerging concepts, identified as part of Industry 4.0, by World Economic Forum. AM can be identified as a disruptive technology not only as a fabrication method but also in its impact on global market. In this work, SLM process was selected due to its popularity and ability to fabricate complex Ti6Al4V lattice structures and the next section will describe the process in more details and discuss critical operating parameters which can affect the manufacturing of the lattice structures.

## 2.3 Selective Laser Melting (SLM)

SLM is a technology that uses high power laser to selectively melt the metallic powders. Most commonly used materials for this technology are titanium and aluminium alloys, stainless steel, cobalt chrome and nickel alloys. Due to the high temperatures required to melt the metallic alloys, the process is carried out in a closed chamber with an inert gas such as Argon or Nitrogen to avoid undesirable chemical reactions like oxidation. SLM can be seen as a welding process, where the micron size powders are fused together at each layer to form a 3D model.

SLM technology was invented by Fraunhofer Institute ILT in Aachen, Germany [1]. SLM is now one of the fastest growing AM technologies globally. From 800 metallic AM machines sold globally in 2015, 720 (90% of the total) of them were SLM machines [31]. Global commercial SLM machine manufacturers are EOS (Germany), Concept Laser (USA/Germany), SLM Solutions (Germany), Renishaw (UK), Sisma (Italy).

Disadvantages of this technology include high material, machine and manufacturing costs, limited build dimensions, poor surface finish and the need for support structures. Key advantages include high resolution, ability to manufacture complex structures, high mechanical properties and high rates of material recycling.

### 2.3.1. Process Description

SLM is a powder-based AM process that uses high intensity laser to melt metallic powders selectively, based on a CAD model. The SLM machine reads the CAD model in slices and melts the desired spots at each layer. The building starts on a base plate, generally of the same alloy as the powder material. When the part is built after the successive selective melting of the layers, the residual powder is removed and the part is cut from the base plate. The SLM hardware system includes the laser system, building chamber, powder chamber, coater and gas circulating system (Figure 2. 8a)

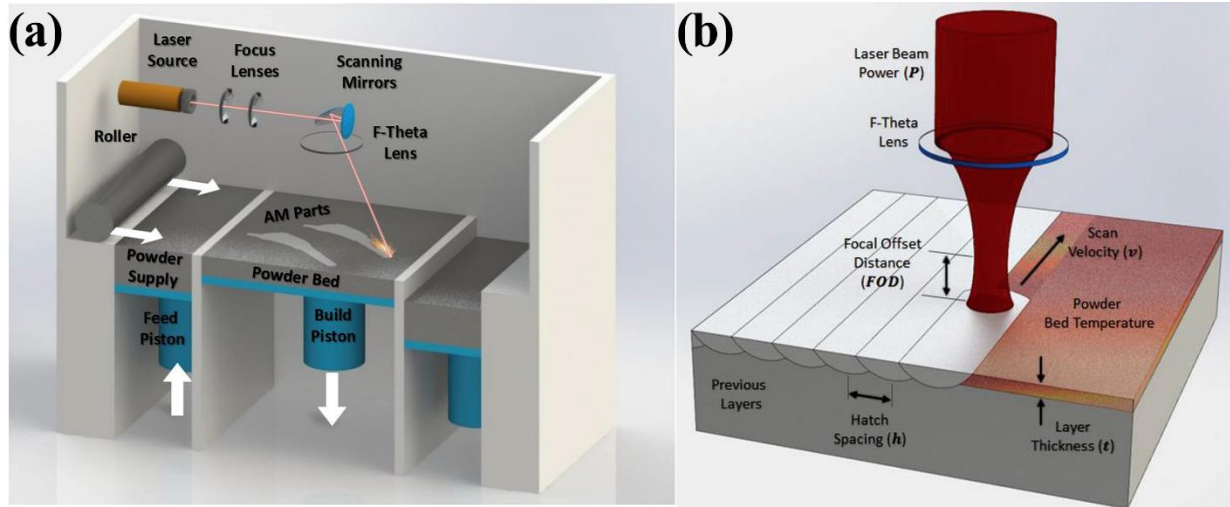


Figure 2. 8 Schematic (a) SLM machine parts, and (b) processing parameters [48].

Critical process parameters of the SLM process include laser power ( $P$ ), layer thickness ( $t$ ), scanning speed ( $v$ ) and strategy. These parameters need to be adjusted to make sure the neighbouring spots and the next layers are fused together (Figure 2. 8b). During the SLM process the powder melts and solidifies at a rapid rate of around  $10^4 - 10^6$  K/s [49]. Therefore, critical physical phenomena such as the absorptivity of the material to laser irradiation, thermal fluctuations, balling phenomena and energy density should be considered for each material and process [50]. Due to access to a wide range of materials and freedom in design, SLM is used in different industries, some of which are summarized in Table 2. 1:

Table 2. 1 Industries and applications have token up SLM.

Dental	dental prostheses, implants, bridges, crowns
Medical	medical implants, surgical tools, endoscopy
Aerospace	lightweight parts, combustion engines, heat exchanger
Automotive	car seats, custom designed panels, gearbox, wheels
Fashion	jewellery, clothing, watches
Machining/Mechanical parts	tools, mold making

### 2.3.2. Process Variables

Some processing parameters that are critical for the part are controlled by the user. Therefore, it is important to know of these parameters and their potential effect on the parts properties.

#### 2.3.2.1. Powder

The composition, size distribution, shape, optical and heat transfer properties, and microstructure are important parameters of the powder used for the SLM process. Powder characteristics have direct impact on the part quality, and therefore the user needs to consider these parameters when purchasing the powder. Ideal powder morphology for SLM can be described in broad terms as spherically shaped powder with a size range of 20-85  $\mu\text{m}$ , and high-packing and flow characteristics. Powder should also be free of internal porosity and impurities [51]. Technologies used for metallic powder production for SLM include high-frequency discharge of atomization, gas, water, plasma with a rotating electrode, and plasma in crossed flows [52].

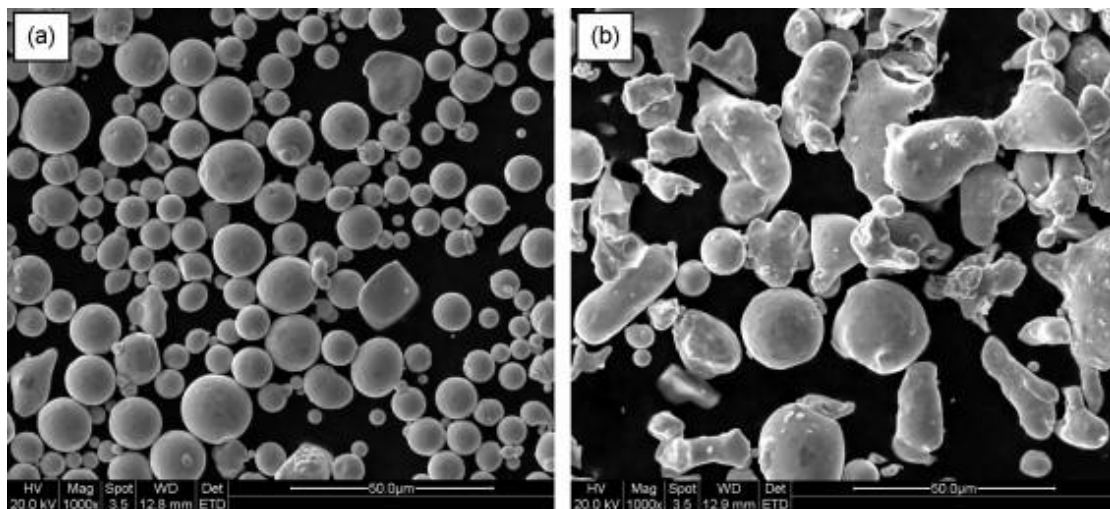


Figure 2. 9 SEM images showing characteristic morphologies of stainless steel powder: (a) gas atomization (b) water atomization [53]

Li et al. [53] compared the stainless steel powders, produced by gas atomization and water atomization, which had different shapes and packing densities (Figure 2. 9). They found that the parts built using spherical powder produced by gas atomization possessed a denser structure than the parts built on irregular shaped water atomized powders, due to high packing density, better wetting ability and lower oxygen content. Other studies demonstrated the benefits of using spherical powders on apparent density of SLM parts [54] and mass flow rate [55]. Effect of powder packing density on the melt pool stability was also simulated and it is found that by increasing the packing density from 38% to 45%, the balling effect can be eliminated by forming continuous melt pool (Figure 2. 10).

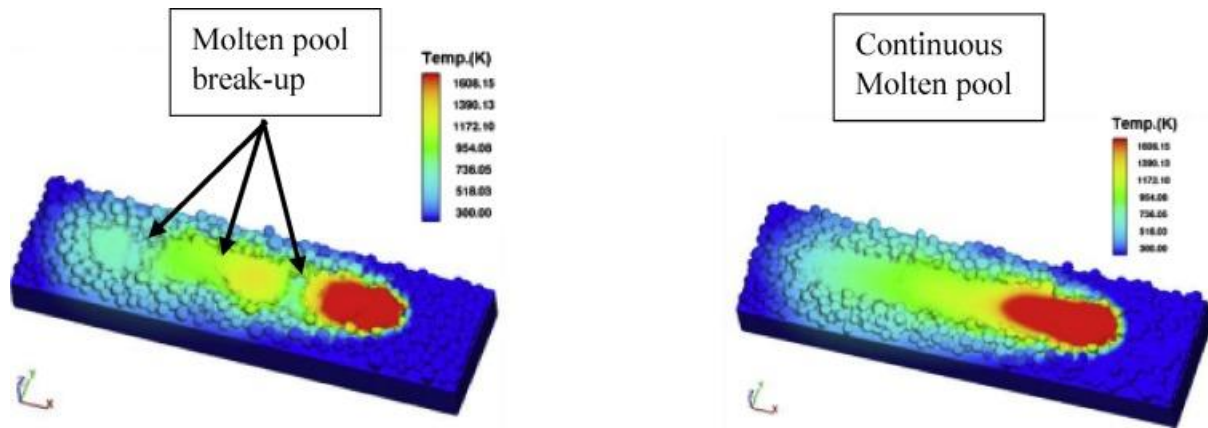


Figure 2. 10 Melting of powder layer with 38% (left) and 45% (right) packing density [56]

### 2.3.2.2. Energy Density

The SLM process can be controlled by varying laser power ( $P$ ), layer thickness ( $t$ ) and scanning speed ( $v$ ). These parameters are combined in an energy density equation, called volumetric energy density (VED), and can be used to evaluate the quality of the end-product for SLM [57-59]. VED is defined as the amount of energy delivered per unit volume of powder deposited in the bed and is expressed in Equation 2.1 [60]:

$$E = \frac{P_{laser}}{v_{scan} \cdot h_{space} \cdot t_{layer}} \quad 2.1$$



Here,  $P$  is the laser power (in  $\text{J s}^{-1}$ ),  $v$  is the scanning velocity (in  $\text{m s}^{-1}$ ),  $h$  is the hatch spacing (in m),  $t$  is the layer thickness (in m) and  $E$  is the volumetric energy density (in  $\text{J m}^{-3}$ ). VED values can be specifically used to identify a process window for each material system for a specific SLM machine to achieve the best melting conditions. The majority of these studies are focused on minimizing the residual porosity based on the energy density approach [61]. When defining the precise VED window for any material, the user should consider two sides:

- What is the minimum VED point that leads to insufficient bonding of the layers and therefore macroscopic pores?
- What is the maximum VED point that results in excessive energy and keyhole pore formation [62]?

VED equation shows the importance of SLM process parameters including laser power, scan velocity, hatch spacing and layer thickness, which are explained below in more details.

- i. Laser power must be carefully chosen in order to make sure it is enough power to melt the powder and fuse the consecutive layers with each other. It is also as important to define the maximum laser power to be used as the high laser energy can evaporate the material and lead to porosity and poor surface quality. Most of the commercial SLM machines are equipped with lasers ranging from 100W to 1KW laser power.
- ii. Scan velocities can range from 50-1100 mm/s [63, 64] and have a significant effect on the quality of the part and the productivity of the machine. For instance, Thijs et al. [60] showed that lower scanning velocity (50 mm/s and 100 mm/s) resulted in a better alignment of grains with building direction as well as coarser microstructure for Ti6Al4V as compared to the scanning velocity of 200 mm/s. Generally, lower scanning velocities result in higher energy densities and can cause keyhole pore formation. Scanning velocity should be chosen considering the material, the design, and the other process parameters given in the VED equation.
- iii. Hatch spacing influences the overlapping between two neighbouring scans in contour-hatching scanning strategy. Pore formation due to insufficient melting was observed to form when the hatch distance is larger than 70% of the laser beam diameter [65].

However, it is also known that small hatch distances ( $<50\text{ }\mu\text{m}$ ) can cause porosities due to excessive energy input [60, 66] (Figure 2. 11).

- iv. Layer thickness determines the amount of powder needed to be melt by the laser. Smaller layer thickness results in better melting of the powders and bonding of the layers, however smaller layer thickness also results in longer processing time. Therefore, the user needs to optimise the layer thickness based on the powder size distribution and desired part quality. Suggested layer thickness ranges between  $20\text{-}80\text{ }\mu\text{m}$  [67-69].

In summary, the VED equation should be considered carefully when designing experiments for SLM manufacturing. The laser power, scan speed, hatch and layer thickness should be identified considering their effect on overall energy density. For example, Figure 2. 12 shows the influence of scanning velocity and hatch distance on the densities of SLM Ti6Al4V. It can be seen that their combined effect is more influential than an individual contribution. It is common to use design of experiment (DoE) approaches, such as Taguchi, to understand and optimize the SLM process parameters for a given material system [70].



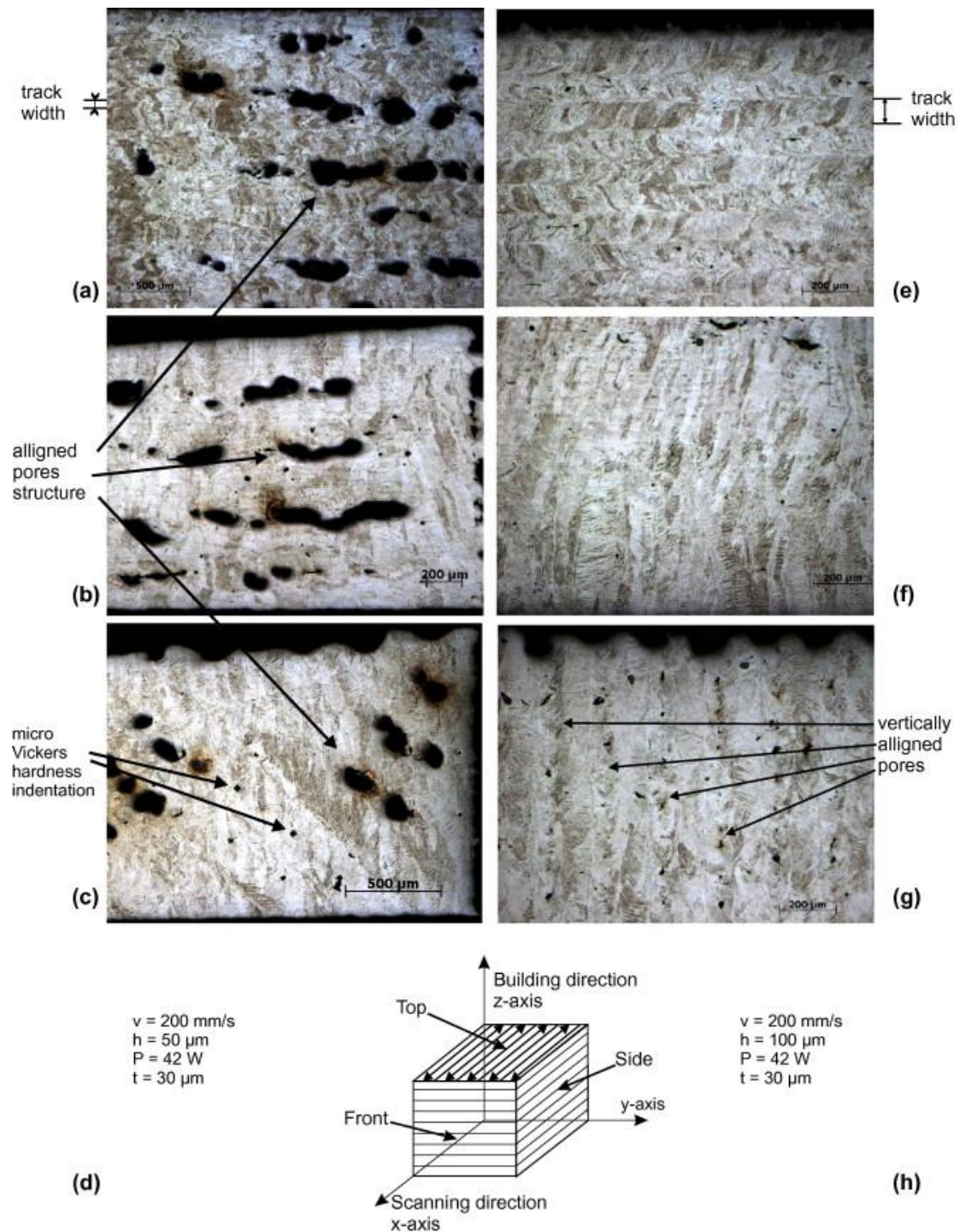


Figure 2. 11 Influence of hatch spacing. Left images belong to the sample that was scanned with a hatch spacing of 50  $\mu\text{m}$ : (a) top view; (b) side view; (c) front view; and (d) the scanning strategy and parameters applied. Right images belong to the sample that was scanned with a hatch spacing of 100  $\mu\text{m}$ : (e) top view; (f) side view; (g) front view; and (h) the scanning strategy and parameters applied [60].

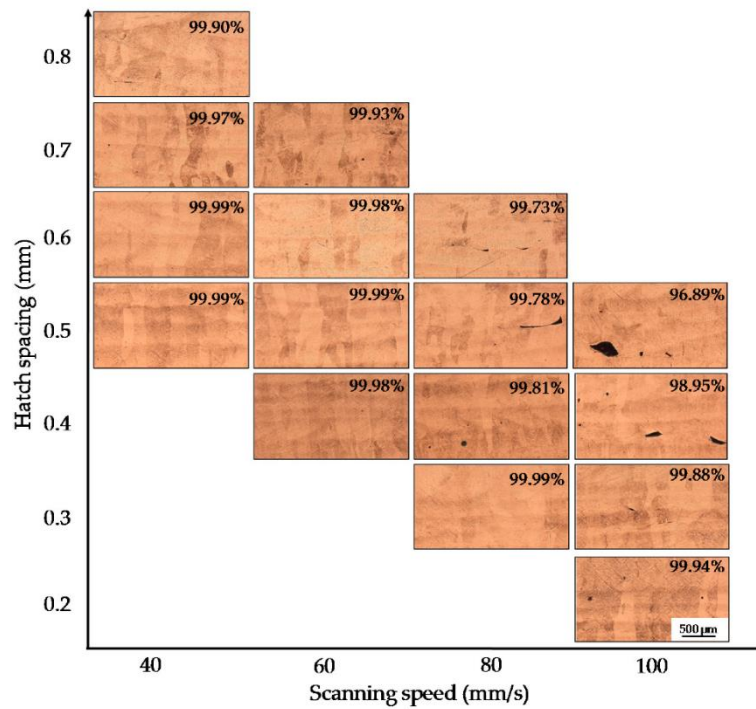


Figure 2. 12 Density of selective laser melting Ti6Al4V samples with different scanning speeds and hatch spacings (Laser power = 400 W, Layer thickness = 200  $\mu$ m) [71].

### 2.3.2.3. Scanning Strategy

The laser can follow different paths to solidify a material, as illustrated in Fig. 2.13. This is known as laser scanning strategy and can be grouped into contour-hatching scanning strategy or single-point-exposure scanning strategy. The contour-hatching is the most popular strategy and involves the laser scanning of the contour (outer line) and filling the inside region of the contour in a rastering manner. Hatching can be done in different paths, including uni-directional, bi-directional and island scanning (Figure 2. 13).

The single-point exposure strategy exposes the laser to a small region of the material (spot) for a short period of time before moving to the next location (Figure 2. 14). When moving between the spots, the laser turns off. The main advantage of the single-point exposure over the contour-hatching is that the user has direct control on the part dimensions at each layer [72]. This can be particularly beneficial for lattice structures as the dimensions of the struts are very critical in controlling the mechanical performance of the lattice structure. Another benefit of using

single point scanning strategy for lattice structures is cutting down the computational cost. Since there is no pre-defined strut thickness, scaffolds can be designed in single lines. This significantly reduces the file preparation and model slicing times.

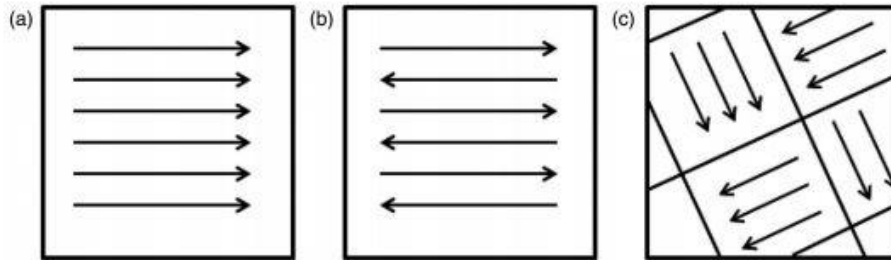


Figure 2. 13 Illustration of (a) uni-directional, (b) bi-directional, (c) island scanning, for contour-hatching scanning strategy [73].

A review of current literature revealed only a handful of studies on the single point exposure scanning strategy [74-77]. The main focus of these studies was establishing a relationship between the process parameters and the mechanical performance of the lattice structures. The results show that single point exposure scanning strategy is capable of fabricating dense struts and the mechanical properties of the lattice structures manufactured with this strategy is comparable to those manufactured by contour-hatching scanning strategy. Fundamental studies on the single point exposure scanning strategy is missing in literature, including studies on laser-powder interaction, and process parameter-microstructure and defect relationship. These concepts will be explained in-depth in Chapter 5 of this thesis.

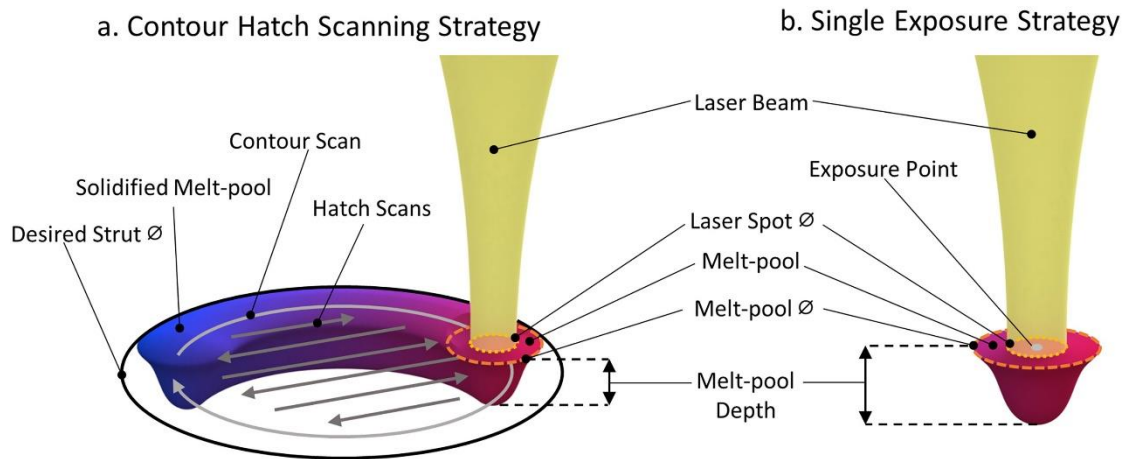


Figure 2. 14 Illustration of contour-hatching and single point exposure scanning strategy, showing the laser path to achieve desired circular shape [76].

In summary, process variables including powder properties, laser power, scanning velocity or exposure time, layer thickness and laser scanning strategy are critical in controlling the morphology, density and mechanical performance of SLM lattice structures. The user needs to carefully consider all these variables during the design stage of the lattices. The next section covers the process limitations that the user should also consider for SLM processing of lattice structures.

### 2.3.3. Process Limitations

While SLM process can produce intricate parts, it has also a number of limitations. For instance, high surface roughness values and porosity formation can be limiting factors for some applications. Although SLM is an advanced manufacturing method, these process limitations should be considered and optimized for each material and application [78].

#### 2.3.3.1. Surface Roughness

Surface properties of SLM fabricated porous Ti6Al4V lattices highly depend on the SLM equipment used for their fabrication and the process parameters such as layer thickness, laser power and scanning speed. SLM parts usually present an average surface roughness of 10-50

$\mu\text{m } R_a$  [79], whereas most of the machined parts have an average surface roughness of  $0.9 \mu\text{m } R_a$  [80]. High surface roughness values of the SLM parts is caused by the ‘stair step’ effect, which is the stepped approximation by layers and inclined surfaces in layer additive manufacturing processes [72]. Another contribution to surface roughness includes un-molten powders attaching to the melt pool during cooling. In addition to process parameters, the fabrication orientation, sloping angles and the surface (bottom vs. top) also affects the surface roughness. For instance, Figure 2. 15 shows that the bottom surface of a strut has almost double the surface roughness values compared to the top surface.

Although high surface roughness is problematic in terms of mechanical properties, especially fatigue, it can be beneficial for medical implants. A systematic review on the surface roughness and bone healing published by Shalabi et al. [81] concluded that bone-to-implant contact (BIC) enhances with increasing surface roughness. Post-processing surface treatments are also available to modify the surface roughness of SLM parts if needed. For lattice structures, available post-processing surface treatments include chemical etching or electropolishing due to the intricate and small features.

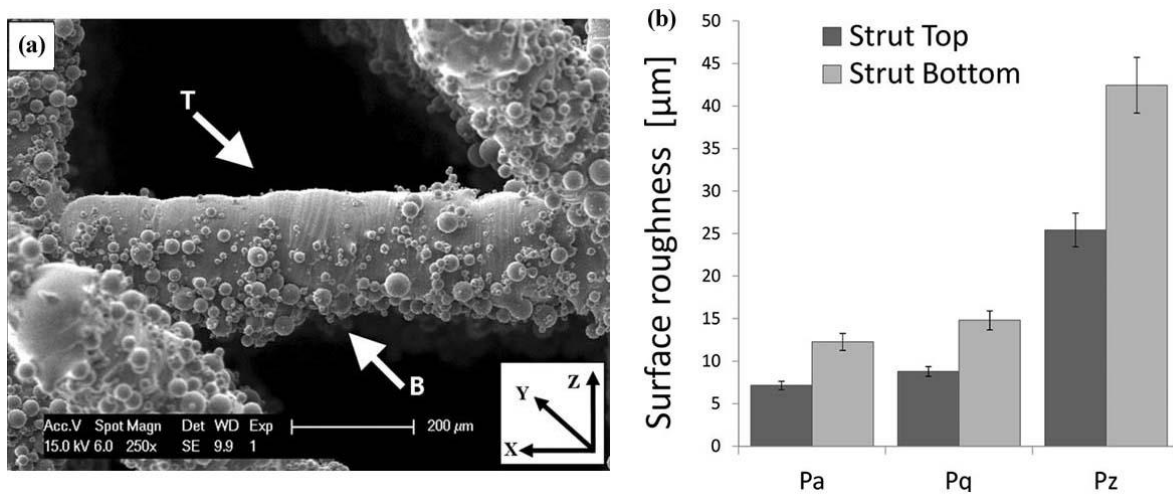


Figure 2. 15 (a) SEM image of a strut, T and B refer to top and bottom surfaces, respectively. (b) The comparison of surface roughness between as-produced top and bottom surface. (Pa: the average roughness, Pz: absolute difference between 10 highest peaks and deepest valleys) [82].



### 2.3.3.2. Porosity

Pore formation is another commonly observed process limitation in SLM, both for bulk materials and lattice structures. Similar to surface roughness, internal porosity formation can be controlled or optimized by the processing parameters. Major reasons causing internal porosity are insufficient melting, excessive energy causing a keyhole effect, presence of oxides and oxidation, and the scattering of the condensate particles [83].

Insufficient melting is an outcome of low laser energy densities per powder volume, and can be eliminated by choosing the right process parameters (see Chapter 2.3.2.2. for more details). Keyhole melting occurs when excessive energy causes a gas entrapment in the melt pool [84] and can be eliminated by optimising the process parameters. Keyhole pores are generally irregularly shaped, continuous and located in the middle of the melt-pools.

Pore formation due to oxidation is material dependant and can be eliminated by working in the right inert gas environment for a given material. The scattering of the condensed particles can also cause internal porosity and occurs when the laser power is enough to both melt and vaporise the material, disturbing the molten spot to scatter particles with vapour. If vaporisation is eliminated by working with the right process parameters, the porosity formation due to the particle scattering can be eliminated.

In conclusion, SLM is a popular and effective AM method for fabricating metallic lattice structures, and although there are a number of processing limitations, such as surface roughness and porosity, these can be eliminated or controlled by choosing the right process parameters. In the next chapter, the literature review focuses on the morphology, mechanical properties and biological response of SLM Ti6Al4V lattice structures.

## 2.4. Selective Laser Melted Ti6Al4V Lattice Structures

Ti6Al4V ELI is the most widely used implant material due to being biocompatible and lightweight with exceptional corrosion resistance. The chemical composition of Ti6Al4V ELI is given in Table 2. 2. The addition of the alloying element Al tends to stabilize the  $\alpha$ -phase, whereas V tends to stabilize the  $\beta$ -phase. The  $\alpha$ - $\beta$  phase offers a wide range of properties including good weldability, excellent strength and oxidation resistance ( Table 2. 3).

Table 2. 2 The chemical composition of Ti6Al4V [85]

<b>Aluminium (Al)</b>	5.5-6.5%	<b>Carbon (max)</b>	0.08%
<b>Vanadium (V)</b>	3.5-4.5%	<b>Nitrogen (max)</b>	0.05%
<b>Iron (max)</b>	0.25%	<b>Hydrogen</b>	0.012%
<b>Oxygen (max)</b>	0.13%	<b>Titanium</b>	Balance

Table 2. 3 Mechanical properties of Ti6Al4V ELI outlined in the ASTM F136 Standard [85]

<b>Property</b>	<b>Ti6Al4V</b>	<b>Property</b>	<b>Ti6Al4V</b>
<b>Tensile strength (MPa)</b>	860	<b>Density (g/cm<sup>3</sup>)</b>	4.43
<b>Yield strength (MPa)</b>	795	<b>Melting point (°C)</b>	1600-1660
<b>Elastic modulus (GPa)</b>	114	<b>Hardness, Vickers</b>	341
<b>Elongation (%)</b>	10	<b>Elastic Modulus (GPa)</b>	114

SLM Ti6Al4V lattice scaffolds are attaining a growing interest from researchers and global medical device manufacturers (Figure 2. 16) such as Stryker, Zimmer Biomet and Johnson & Johnson. Since SLM of metallic lattice bone scaffolds is a relatively new area, there are a lot of questions to explore including optimum lattice design and reliable process conditions that can be certified. The morphological, mechanical and biological behaviour of SLM Ti6Al4V

lattice structures are reviewed, which aid in establishing optimum lattice designs and process variables.

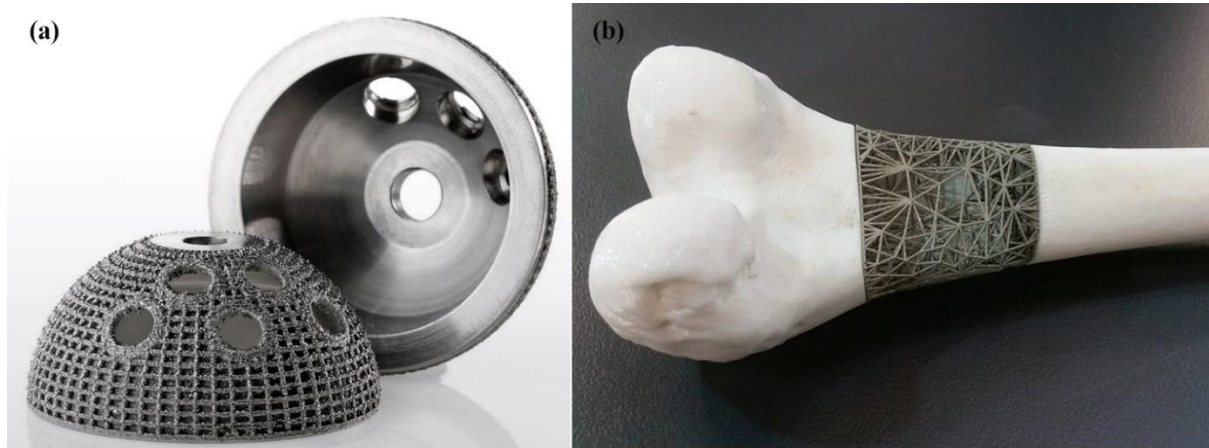


Figure 2. 16 Lattice Ti6Al4V bone implants are gaining interest from (a) industry (Image source: Arcam) and (b) academia (Image source: RMIT University)

### 2.4.2. Morphological properties of SLM Ti6Al4V

#### 2.4.2.1. Geometrical Controllability

Selective laser melting is capable of manufacturing complex lattice Ti6Al4V structures with controlled architecture, however dimensional differences occur between the designed and fabricated parts [86]. Morphological studies from the acquired micro-CT imaging of the fabricated lattices showed an increase in the strut thickness (in the range of 100-150  $\mu\text{m}$ 's) as compared to designed strut thicknesses [86, 87]. This increase in strut thickness causes a decrease in pore size, and therefore porosity, as compared to designed values.

The morphological difference between design and reality comes from the nature of processing and the lattice geometry. Firstly, un-molten particles attached to the melt-pool increases the thickness of the struts [74] (Figure 2. 17). Secondly, the struts angled in the building direction exhibit the staircase effect [88]. Finally, the melt pool size may be different than the designed and given process parameters (laser spot size, scanning strategy, etc) [60].



A number of research papers have shown that chemical etching and electro polishing is effective to remove the unmolten particles from the surface of the fabricated lattices, which will decrease the strut thickness and help to achieve designed dimensions. For example, Pyka et al. [82] applied a combination of chemical etching and electrochemical polishing using HF-based solutions. Chemical etching removed the unmolten powder from the struts and electropolishing decreased the surface roughness further by almost 50% homogeneously throughout the scaffold. Another study used chemical polishing of SLM porous structures in HF acids and HF/HNO<sub>3</sub> acid mixtures [89]. Although these studies show that surface roughness can be improved by chemical etching or polishing, the post-processed parts exhibited lower compressive strength and elastic modulus as a result of thinning the struts. The sacrifice in mechanical properties should be considered during the design stage if post-processing is planned.

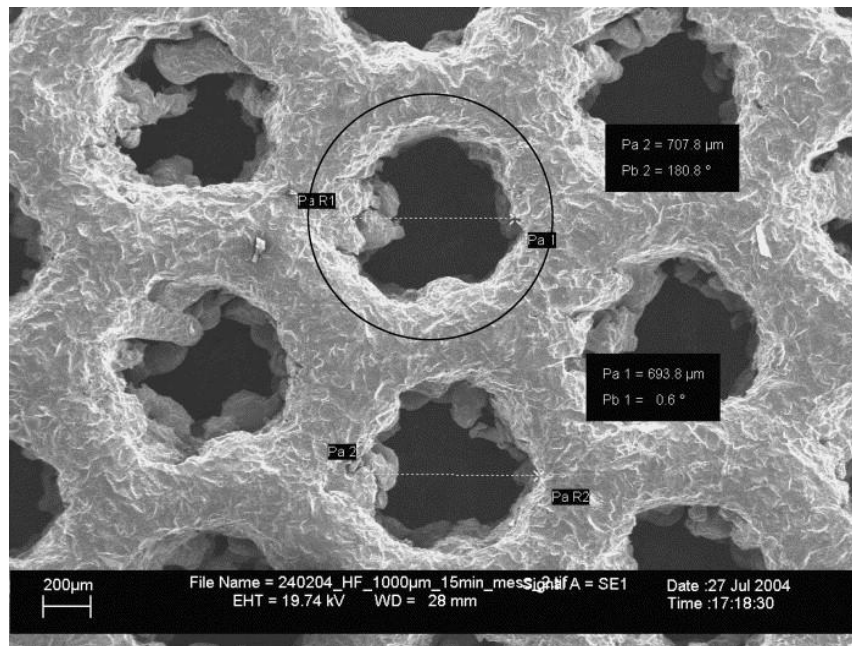


Figure 2. 17 SLM porous Ti6Al4V scaffold with designed pore diameter of 1000 μm (indicated as black circle) and the actual measurement of the pore diameters. The designed pore dimensions were reduced to approx. 700 μm, indicating a defined processing overhang of approx. 150 μm [87]

SLM process parameters can be optimized to achieve relative densities of above 98% in Ti6Al4V samples [60, 90, 91]. Micro-CT imaging technique is reported to be more accurate in

calculating the porosity compared to Archimedes method [90, 92]. Micro-CT studies performed on lattice Ti6Al4V lattices show the tendency of pores to form in the middle of the struts [93] (Figure 2. 18). Internal porosity can be controlled by optimized process parameters or post-processing methods.

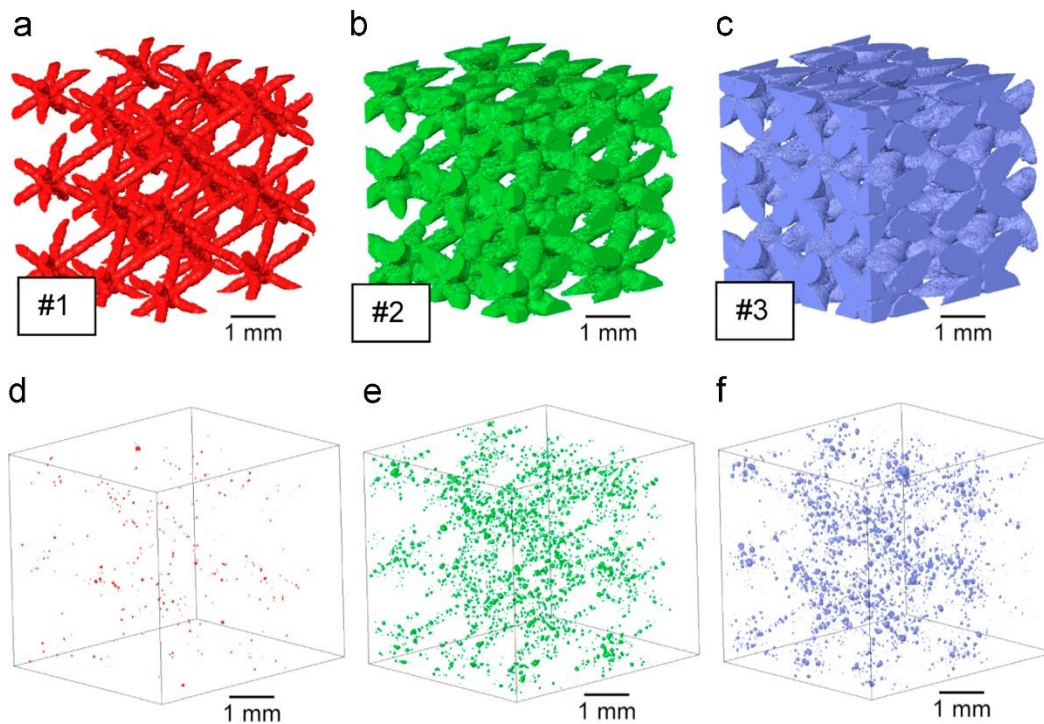


Figure 2. 18 (a-c) 3D rendering of the micro-Ct volumes of diamond lattice cells with different strut thicknesses, (d-f) the segmented pores for lattices [93]

#### 2.4.2.2. Microstructure

SLM is characterized by a highly localized heat input in a short timeframe, and cooling of the melt pool quickly [60, 94]. This rapid solidification yields to a very fine, non-equilibrium microstructure in metallic alloys. For Ti6Al4V, an acicular martensitic structure is commonly observed in SLM lattices as well as bulk structures. The observed martensitic phase or the  $\alpha'$  phase is hexagonally packed with lattice parameters  $a = 0.293$  nm and  $c = 0.467$  nm [60].

At room temperature Ti6Al4V can exhibit equiaxed, lamellar or acicular microstructure (Figure 2. 19), which is controlled by the cooling rate and heat treatments. Figure 2. 19b shows

the solid state transformations of  $\beta$ -phase for Ti6Al4V, which was solution treated 1050 °C, at specific cooling rates. According to the graph, if the cooling rate is between 1.5-20 °C/s, 20-410 °C/s, 410-525 °C/s;  $\beta$  transforms into globular  $\alpha$ , massive  $\alpha_m$  and martensitic  $\alpha'$ , respectively. The microstructure morphology of Ti6Al4V has a direct control over the mechanical properties of Ti6Al4V. For example, hard martensite  $\alpha'$  structure causes high tensile strength and yield strength but leads to poor ductility (less than 10%) [95]. Whereas, lamellar grains are more ductile and have higher fracture toughness and fatigue strength than the acicular (Widmanstätten) structure [96, 97]. There has been a number of approaches to control the microstructure of Ti6Al4V during the SLM process by controlling the process parameters and part orientation [98-100]. However, post-process heat treatments are still the most effective way to modify the microstructure of Ti6Al4V.

Texture studies show that SLM Ti6Al4V microstructure consists of fine acicular  $\alpha'$  grains randomly located within the columnar prior  $\beta$  grain boundaries, which are aligned with the building direction [101] (Figure 2. 20). This has been attributed to the fact that heat dissipates away vertically towards the build plate [99] and is commonly observed in SLM Ti6Al4V samples.

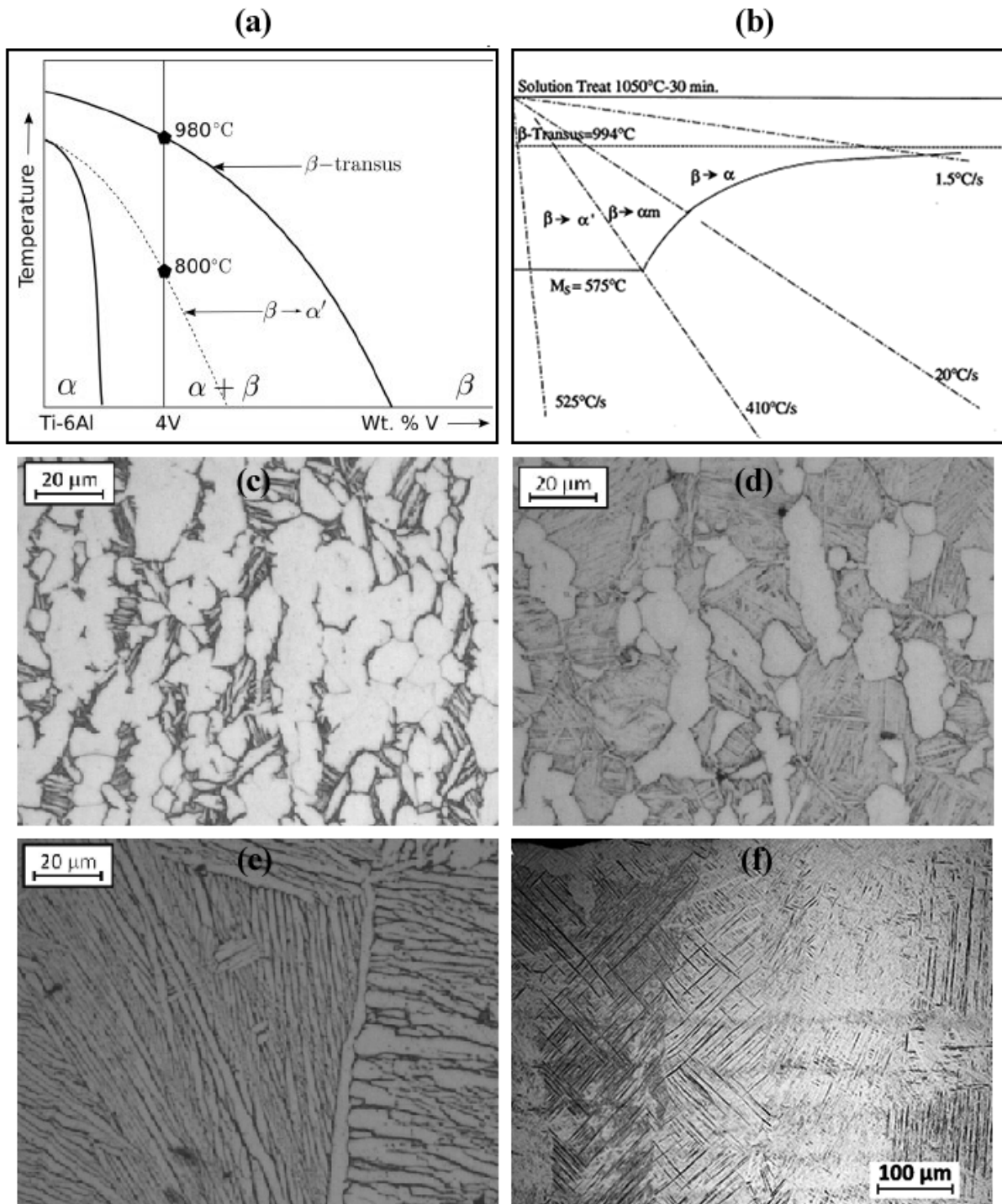


Figure 2. 19 (a) Ternary phase diagram of Ti6Al4V [102], (b) Schematic graph to show the relationship between phase selection and cooling rate during solidification (from 1050°C) [103], Optical microscope images of (c) equiaxed, (d) bi-modal, (e) lamellar [104], (f) acicular [105] Ti6Al4V microstructure morphologies.



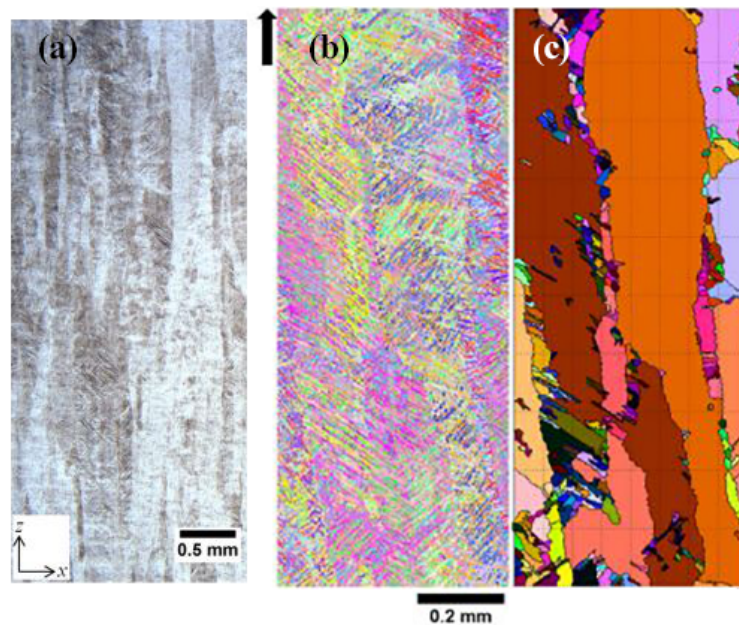


Figure 2. 20 (a) Optical microscope image of SLM Ti6Al4V, (b) EBSD  $\alpha'$  orientation map (the black arrow indicates the building direction), (c) orientation map of the reconstructed  $\beta$  phase [101]

#### 2.4.2.3. Heat Treatment

Post processing heat treatments and hot-isostatic-pressing (HIP) have been extensively studied and reported to be successful in achieving desired mechanical properties, such as increased ductility for SLM Ti6Al4V [106]. In addition, heat treatments reduce the thermal stresses that build up during the SLM process [106]. The influence of heat treatment temperature, duration and cooling rate on the final microstructure are available in literature. Below  $\beta$ -transus temperatures, since the grain growth is prevented by the mixture of  $\alpha$  and  $\beta$  phase, columnar prior  $\beta$  grains remain the same after cooling. When treated above  $\beta$ -transus, the columnar  $\beta$  grains grow extensively to form large and semi-equiaxed  $\beta$  grains [106, 107] (Figure 2. 21). The duration time and cooling rate do not have significant effect on microstructure for sub-transus treatments, but they can have an effect on the final dimensions of  $\beta$  grains for super-transus treatments.

Hot isostatic pressing (HIP) is another popular SLM post-process method to modify the microstructure and mechanical properties of as-fabricated parts. The HIP process involves a

heat treatment of the part in a high pressure containment vessel to press the part in all directions. The HIP process helps to reduce the porosity of the parts because of the isostatic pressing. Studies have shown the microstructural change of martensitic  $\alpha'$ -laths into  $\alpha+\beta$  lamellar [90, 108] after HIP of SLM samples, which increased the ductility of the structure by 10-20%, but decreased the maximum compressive strength by 15% [108]. Since the internal pores are closed during the HIP process, HIPTi6Al4V samples showed higher fatigue strengths than as-fabricated parts, which were comparable to wrought Ti6Al4V [92].

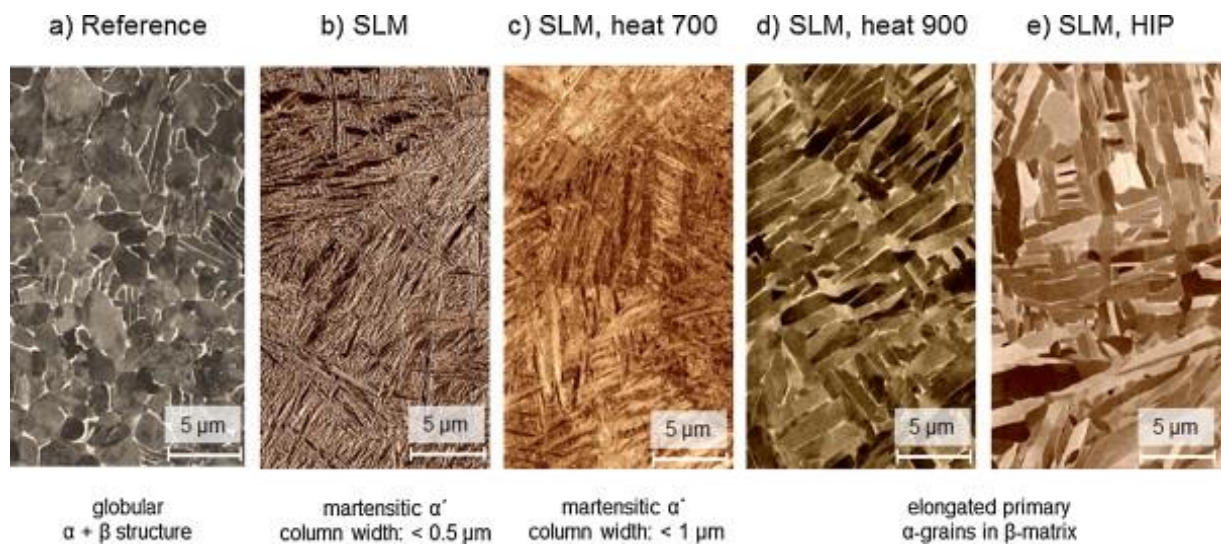


Figure 2. 21 Globular ‘Reference’ (a) and lamellar SLM (b) structures of Ti6Al4V alloy and the effect of thermomechanical treatment on the microstructure of the SLM samples (c–e) [92].

### 2.4.3. Mechanical Response of SLM Ti6Al4V lattices

#### 2.4.3.1. Quasi Static Mechanical Properties

The mechanical properties of cellular solids are dependent on three dominated factors:

- The material of which the cellular structure is made,
- The topology and shape of the cell edges and faces,
- The relative density of the cellular structure [109].

The relative density is defined as the density of cellular solid ( $\rho^*$ ) divided by the density of the solid it's made of ( $\rho^0$ ) [110].

$$Relative\ Density\ (RD) = \rho^*/\rho^0 \quad 2.2$$

The deformation of lattice structures depends on the cell topology and is either *bending-dominated* or *stretch-dominated*, based on Maxwell stability criterion [109]. The difference between a bending-dominated and a stretch-dominated structure is similar to the collapse response of a pin-jointed structure of the same morphology [10] (Figure 2. 22). The stability of a three dimensional system of a pinned frame network, which is made up of  $b$  struts and  $j$  pinned joints, is determined by the Maxwell rule, as given by equation 2.2 [111]:

$$M = b - 3j + 6 \quad 2.3$$

For pin jointed systems, if  $M < 0$  the system will collapse, while if  $M > 0$  the frame will be stable and its member will carry the load in tension or compression. Lattice structures can be thought of as a frame in which the joints are locked. When  $M < 0$ , the bars or struts of the frame will bend instead of collapsing. When  $M > 0$ , the members will carry the load as tension or compression as in the case of pin-jointed frame, but this time, they become stretch dominated structure. As shown in the following equations, stretch dominated structures have higher structural efficiency than bending dominated structures since struts are much stiffer when stretched compare to bending [109].

$$\frac{\sigma_y^*}{\sigma_y^0} \propto \left(\frac{\rho^*}{\rho^0}\right)^n \quad 2.4$$

$$\frac{\varepsilon_y^*}{\varepsilon_y^0} \propto \left(\frac{\rho^*}{\rho^0}\right)^m \quad 2.5$$

$n$  and  $m$  are 1.5 and 2, respectively, for bending dominated cell topology, and both are 1 for stretch dominated cell topology (Figure 2. 23). Where  $\sigma_y^*$  is the yield strength of the cellular structure,  $\sigma_y^0$  is the yield strength of the solid of which the structure is made,  $\epsilon_y^*$  is the elastic modulus of the cellular structure and  $\epsilon_y^0$  is the elastic modulus of the solid material.

These results show that at the same relative density, both the modulus and the initial collapse strength of a stretch-dominated structure are much greater than those of a bending dominated structure, which makes the stretch-dominated structures more ideal for lightweight and strong material applications [112].

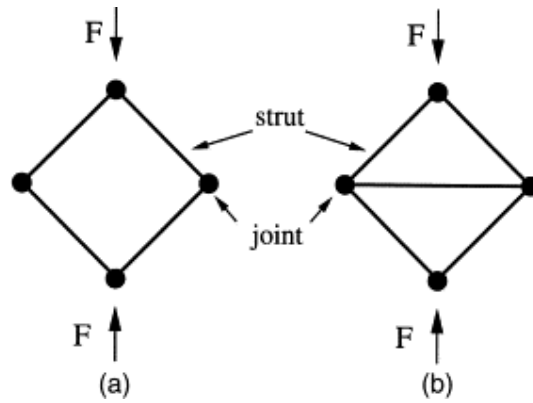


Figure 2. 22 Pin-jointed frameworks collapse when loaded (a) by struts rotating around the joints (if joints are welded together, the struts *bend*), and (b) by stretching of the struts (*stretch-dominated*) [113].

Stretch-dominated and bending-dominated structures present different stress-strain curves under compression [109]. Deformation of the stretch-dominated structures involve plastic buckling or brittle collapse (based on the material used) of the struts after the initial yield, which results in a post-yield softening (Figure 2.24). In bending-dominated structures, after the initial yield, comes a flat and extended stress plateau, which makes them a better choice for energy absorbing applications over the stretch-dominated lattices. For both structures, the last stage of stress-strain curve is the densification stage [114]. This stage involves the



neighbouring struts coming together and merging, which gives a steep rise to stress at the densification strain.

Relative density of lattice structures is another important parameter controlling the mechanical behaviour of the lattices. Relative density of a lattice can be changed by changing the strut thickness and the unit cell size. There are a number of reports in literature demonstrating the effect of relative density on different mechanical properties: stiffness [115, 116], strength [117-120], flexural strength [121] and fatigue life-cycle [122, 123]. The major findings of these studies show that the higher the relative density, the increased mechanical properties.

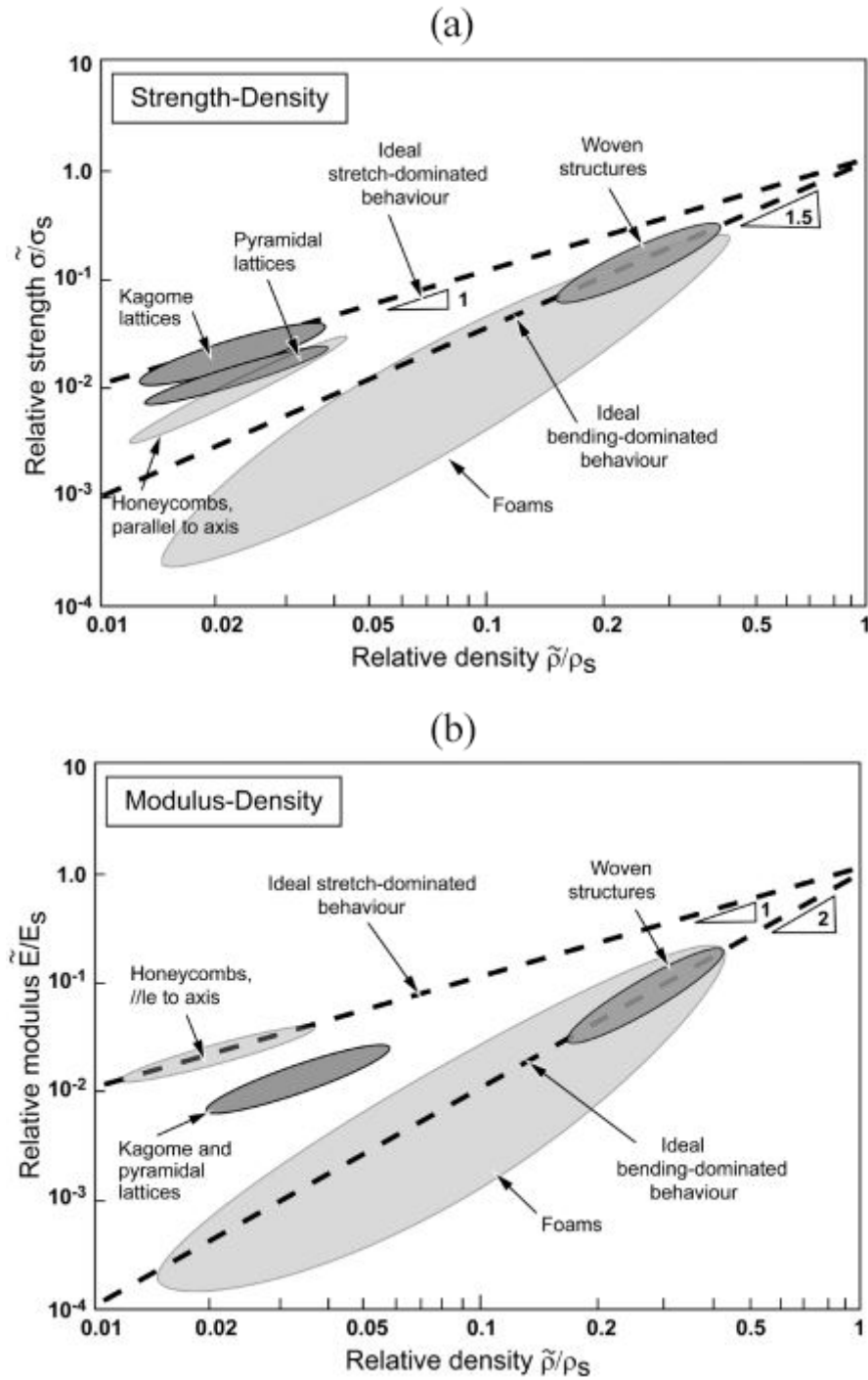


Figure 2. 23 (a) Relative strength vs Relative density on logarithmic scale for cellular structures, *bending dominated* structures follow the trajectory of slope 1.5, whereas the *stretch dominated* structures along the trajectory of slope 1. (b) Relative modulus vs Relative density on logarithmic scale, *bending dominated* line structures follow the slope of 1, and the *stretch dominated* structures follow the slope of 2 [112].

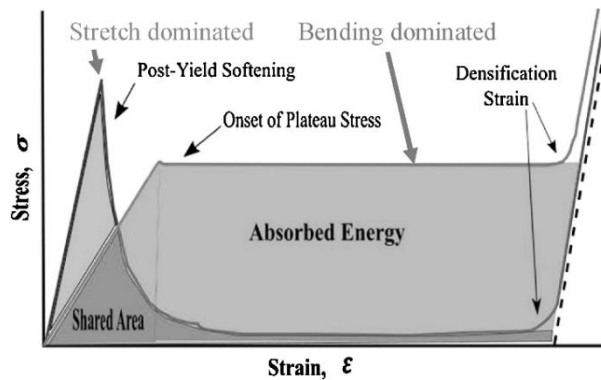


Figure 2.24 Illustrated stress-strain curves demonstrating the deformation characteristics of stretch and bending dominated structures [124].

Recently, a number of approaches have aimed to break the traditional link between relative density and mechanical properties by introducing micro and nano scale lattice structures [125-130], some of which are in an ordered hierarchical design (Figure 2. 25). These ultralight structures are labelled ‘mechanical metamaterials’ to refer to materials with certain mechanical properties defined by their geometry, rather than their composition [125]. Ultralight ‘mechanical metamaterials’ exhibit improved mechanical properties compared to macro-scale structures, including higher recoverability when compressed [127, 128], as well as higher strength and stiffness relative to density [129, 131]. However, manufacturing methods and the applications of the ultralight lattices are limited.

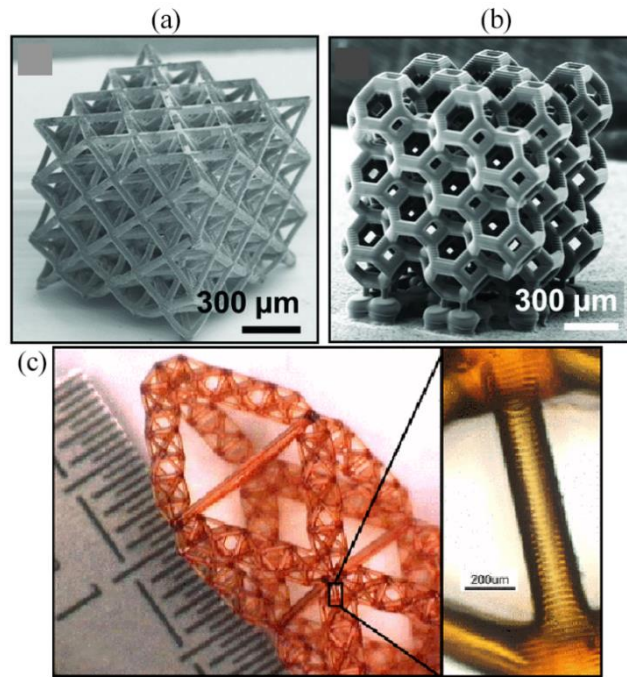


Figure 2. 25 Micro and nano scale ultralight lattice structures, (a) Octet-truss unit cells [125], and (b) Tetrakaidecahedron unit cell [125]. (c) Hierarchical hollow microstructure, combined of tetrahedron and octahedron [129].

For porous structures, literature shows that unit cell topology, porosity, pore size and distribution, as well as the mechanical properties of the base material, govern the quasi-static mechanical properties, including elastic modulus, yield strength and maximum compressive strength [132]. Many unit cell geometries have been studied and compared against each other. Mazur et al. [133] studied the failure modes of the crystalline lattice unit cells under compression. Body centred cubic (BCC), Face centred cubic with vertical struts (FCCZ), Face and Body centred cubic with vertical struts (FBCCZ), Face and Body centred cubic with horizontal and vertical struts (FBCCXYZ) were the main geometries representing bending and stretch dominated crystalline unit cells according to Maxwell stability criteria. They showed that failure mode under compression occurred by bending of diagonal struts and buckling of vertical struts (Figure 2. 26).

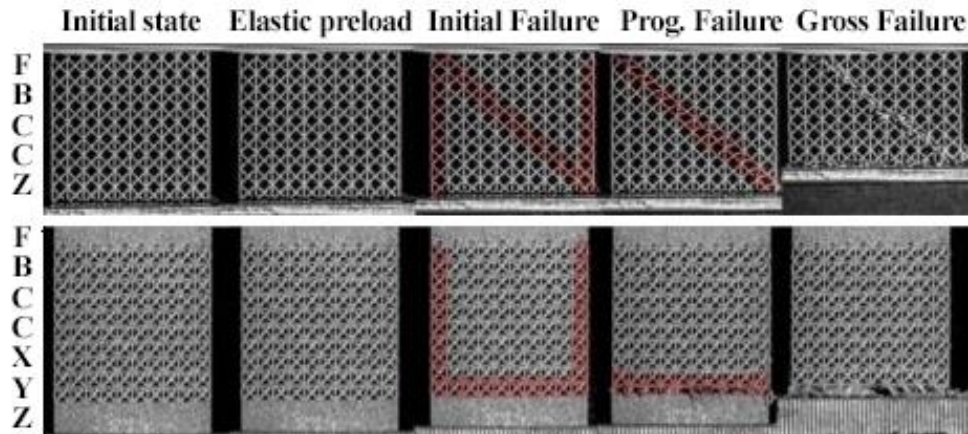


Figure 2. 26 Failure modes of FBCCZ (representing diagonal shear band collapse), and FBCCXYZ (representing horizontal layer collapse) [133]

Some of the other studied unit cells include diamond [134, 135], cubic [132, 136, 137], gyroid [138], truncated cuboctahedron [137], octahedral [139] and TPMS (primitive, I-WP, gyroid, diamond) [13]. The results show that for any given unit cell shape, the strength and modulus increase with an increase in the volume fraction (Table 2. 4). Table 2. 4 also shows that mechanical properties vary for each unit cell even at the same relative densities. Bending-dominated unit cell topologies generally fail across diagonal shear bands, whereas stretch-bending unit cells fail by horizontal sequential layer collapse [132]. Local strain analysis studied by digital image correlation [140] showed the load distribution on the single struts of bending-dominated structures consist of bending and uni-axial loads, whereas the load in stretch-dominated structures is mainly carried by struts along the loading direction (Figure 2. 27). This study also presents higher stiffness and strength in the stretch-dominated structures compared to bending-dominated ones.

Table 2. 4 Unit cell geometries and their mechanical properties, reported in literature.

Unit cell	Relative density (%)	Elastic modulus (GPa)	Yield stress (MPa)	Reference
Diamond	36	$4.3 \pm 0.1$	$90.1 \pm 2.6$	[134]
	18	$1.2 \pm 0.1$	$25.6 \pm 2.6$	[135]
Cubic	11	$1.5 \pm 0.1$	29	[132]
	22	$3.2 \pm 0.1$	48	
	35	$4.8 \pm 0.1$	118	
Truncated cuboctahedron	20	$2.2 \pm 0.1$	$41.4 \pm 2.0$	[137]
	33	$3.85 \pm 0.1$	$110.1 \pm 10.4$	
Octahedral	40	$4.2 \pm 0.1$	$174 \pm 2$	[139]
BCC	5	0.1	4	[133]
	10	0.4	18	
Honeycomb	58	14.1	692	[120]



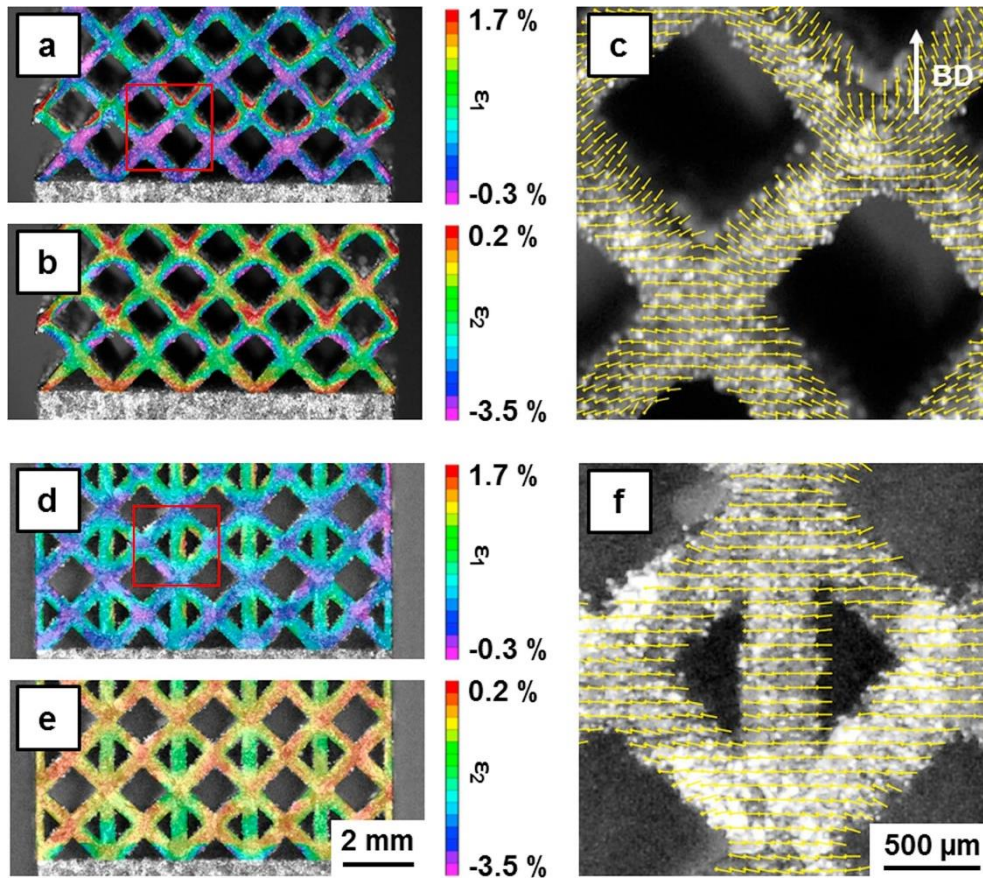


Figure 2. 27 Local distribution of maximum (a, d) and minimum (b, e) principal strains in single struts of the heat treated bcc (bending-dominated) and f2ccz (stretch-dominated) structure, respectively. The images were obtained at a macroscopic strain of  $-1.5\%$  (compressive force). The directions of the local maximum principal strains are plotted as yellow lines in the enlargements (c, f) corresponding to the areas marked by the red squares in (a) and (d), respectively [140]

An increasing number of studies reported functionally gradient structures that have various porosity distribution within a scaffold [141-148]. Early studies on functionally gradient scaffolds included gradient porous designs generated by abrupt changes between layers, by either changing strut thickness or unit cell volume [146, 147]. These designs with discontinuity between layers introduced negative effects on mechanical properties due to free nodes at the strut junctions. Recent studies aimed to overcome this problem by utilizing continuously gradient structures, which consists of gradually changing strut thickness between layers [143, 145]. Continuously gradient scaffolds showed higher stiffness (24% increase) [149] and energy absorption capacities ( $\sim 10\%$  increase) [142, 143] than the uniform designs. Functionally gradient structures also showed different failure mechanism than the uniform counterparts.

More detailed comparison between gradient and uniform porous structures are presented in chapter 4, which includes more reference to the related literature.

Auxetic designs that have negative Poisson's ratios have also gained interest from researchers in the recent years [150, 151]. Auxetic structures exhibit unusual mechanical properties, which are extremely rare in nature [152]. They undergo lateral expansion when stretched longitudinally and become thinner when compressed [151]. Auxetics also offer higher indentation resistance, shear resistance, energy absorption and fracture toughness [153-155].

The literature includes analytical models of lattice structures developed using the Euler-Bernoulli and rarely Timoshenko beam theories [152]. For each unit cell geometries, analytical models derive power-law relationship between the elastic modulus, yield strength, and buckling load with relative density and unit cell topology [19]. The exact values of the power law component and coefficient can be derived for every type of unit cell. Relative elastic modulus and yield stress values of each unit cell geometries can be different even at the same relative densities (Figure 2. 28). Developed analytical models lack accuracy since the defects and surface roughness of the struts are neglected in the models. FE models offer more accurate results to establish the property-topology relationship if the actual as-fabricated geometry is modelled by the acquired micro-computed topography (micro-CT) images of the lattice structures [152, 156]. Nevertheless, both analytical and computational models can provide access to fast calculation of the mechanical properties of lattices before manufacturing.

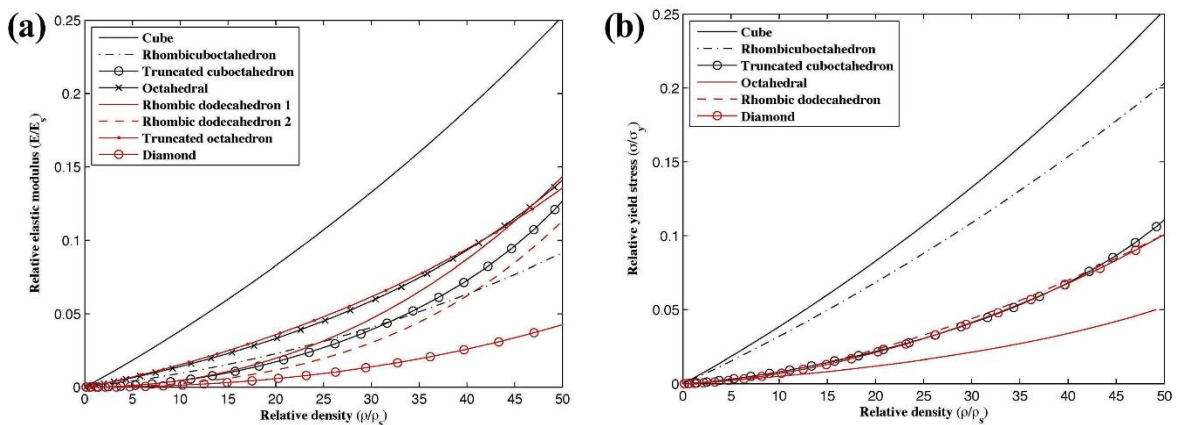


Figure 2. 28 The topology-property relationships predicted by analytical models for a variety of beam-based lattice structures. The elastic modulus (a) and yield strength (b) vs Relative density [19].



### 2.4.3.2. Fatigue Behaviour

Fatigue properties of the lattice scaffolds for medical implant applications are critical as the implants will be under musculoskeletal cyclic loading repeated millions of times per year [157]. Same as static mechanical properties, the fatigue behaviour highly depends on the unit cell geometry, relative density and the base material [158]. Unit cell topology determines how the loads are transferred to struts, i.e. compressive or tensile [137], which will eventually determine the fatigue life of the structure. It is also known that an increase in relative density or volume fraction of a porous structure increases the fatigue life [159].

Since bones and the implant bone scaffolds are generally under compressive cyclic loading [152], most of the studies reported in literature on the fatigue properties of lattices focused on compression-compression fatigue [134, 160, 161]. However, the localized stressed within the struts can be different than the global loads and either face tensile or compressive loads based on the unit cell geometry [122, 152]. Therefore, it is also important to study other fatigue behaviours.

Lietaert et al. [162] used gradient diamond structure for compression-compression, tension-tension and compression-tension fatigue tests and found that most of the fracture sites were located near the strut nodes, where the highest tensile stresses are located (Figure 2. 29). Another study [159] showed that the normalized fatigue life of SLM porous structures have lower values than the normalized fatigue life of solid Ti6Al4V under compression-compression loading. It is proposed that the rough surface of the SLM structures, which is a result of the printing process, combined with the notch sensitivity of Ti6Al4V, leads to early crack initiation and growth from multiple sites within the porous lattice structure.

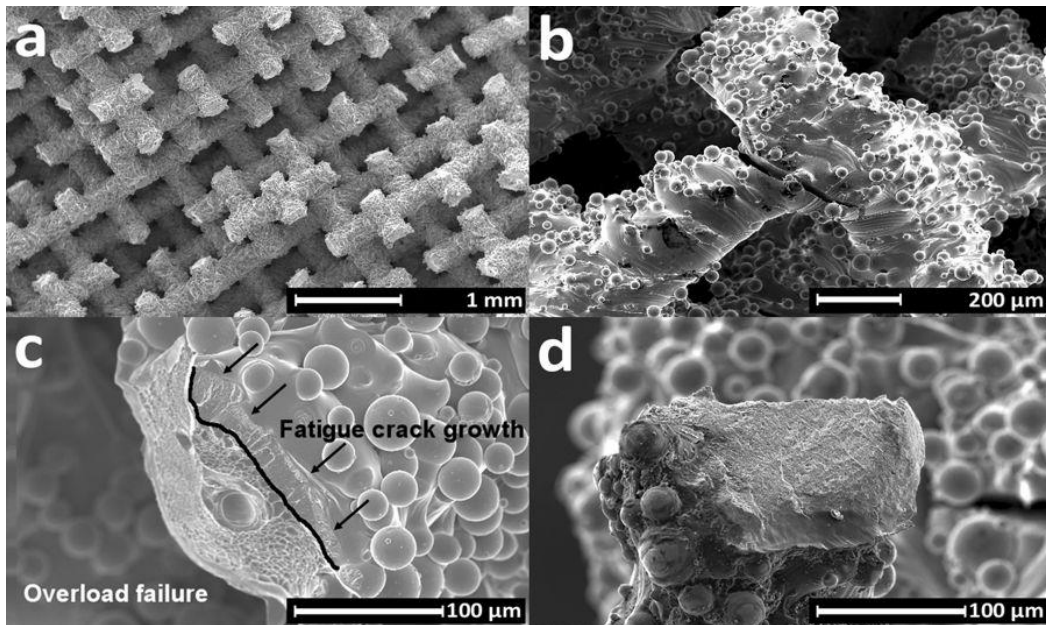


Figure 2. 29 SEM images of fracture surface after fatigue tests: (a) Samples mostly fracture close to the nodes. (b) A crack, which initiated and propagated close to a node for tension-compression fatigue. (c) The fracture surface in tension-tension fatigue showed signs of both fatigue crack propagation (upper right) and ductile overload fracture (lower left). (d) The fracture surface after compression-compression fatigue failure [162].

The fatigue behaviour of porous structures can be divided into three stages [163, 164]: the first stage includes the relative constant plastic strain accumulation, the second stage involves crack initiation and propagation on the struts, and in the third stage the fatigue crack propagation rate increases rapidly and fatigue failure occurs (Figure 2. 30). Strain accumulation in the first stage is believed to be the cyclic ratcheting of the struts, driven by the mean stress during the fatigue cycle [165]. This deformation of porous scaffolds is analogous to creep buckling in compression and creep extension in tension [123, 165].

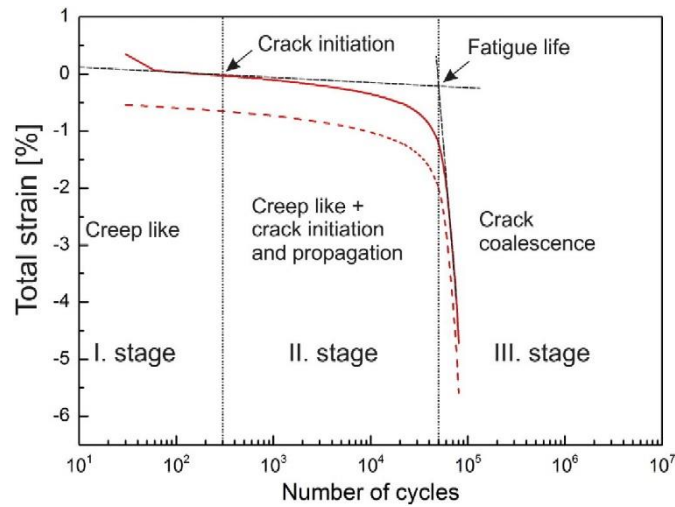


Figure 2. 30 The cyclic loading curve exhibits three different stages during compression–compression fatigue testing of porous titanium samples [163].

There are a number of studies on finite element analysis (FEA) of the lattice structures to predict fatigue properties [139, 166]. Comparison of the simulated and experimental results show that the difference in simulation results comes from surface roughness and internal defects [167].

In summary, a bone implant should exhibit similar elastic modulus and higher mechanical strength values compared to the host bone [168]. Lattice structures can provide matching elastic modulus values while offering high strength (tensile, compressive or fatigue). Bones in human skeleton have different mechanical properties based on the loading conditions (Table 2. 5). Therefore, when designing a bone implant, the specific requirements for the bone type (cortical, cancellous) and loading condition (patient's age, weight, physical activity, and bone location) must be considered. Designers should refer to the extended literature on the mechanical behaviour of different unit cell geometries and relative densities to find optimized values for each design. Zhang et al. plotted the mechanical properties of electron beam melted Ti6Al4V lattices and human bones vs. relative density. The main observations from the plotted graphs are that mechanical properties of lattice structures are comparable to bone, and these properties can be changed through adjusting porosity [168].

Table 2. 5 Compressive properties of human cancellous bone [169]

Bone	Age Gender	UCS (MPa)	Elastic Modulus(GPa)	Ultimate Strain (%)	Density (g cm <sup>-3</sup> )	Reference
Lumbar vertebra	14-89 M	4.60	0.06	6.70	0.20	[170]
	14-89 F	2.70	0.04	6.10	0.20	
Tibial head	14-89 M	3.90	0.03	8.30	0.22	[170]
	14-89 F	2.20	0.02	6.90	0.22	
Tibia	16-39	10.60	0.65	2.48	-	[171]
	40-59	9.86	0.83	2.12	-	
	60-83	7.27	0.61	2.05	-	
Proximal tibia	59-82	5.33	0.45	-	0.29	[172]
Femur	58-83	7.36	0.39	-	0.50	[173]
Lumbar spine	15-87 (vertical)	2.45	0.07	7.40	0.25	[174]
	15-87 (horizontal)	0.88	0.02	8.50	0.24	

#### 2.4.4. Biological Response of SLM Ti6Al4V lattices

The literature review on mechanical response of SLM Ti6Al4V lattice structures show that they are capable of matching the desired mechanical and morphological characteristics of bone. However, the mechanics of medical devices are not enough by itself to commercialize the medical device. Biological response, including *in-vitro* and *in-vivo* (animal tests) has to be assessed and perform well for any medical device to be considered for implantation.

When a biomaterial is exposed to cell culture environment or implanted into an organism, a sequence of physico-chemical reactions occur on the surface. Within seconds, protein adsorption onto material surface occurs, which mediates cell adhesion via integrins and provides signals to the cells regarding the biochemical and mechanical properties of the material [175]. Cells are able to adhere to the surfaces of biomaterials and release active compounds for signalling, matrix deposition, proliferation and differentiation. In addition to the surface of the biomaterial, factors including the material chemistry, mechanical properties, topography and geometry affect the cell proliferation and differentiation. Macroscopically, the biomaterial provides a structure for tissue growth, and microscopically, the biomaterial provides a capillary network for local cell and tissue organization within a controllable micro-environment [175]. Therefore, the biomaterial must be optimized to satisfy the requirement of a hierarchical level of cell-material interactions and mimic the living environment of functional cells.

*Angiogenesis* (new blood vessel formation), *vasculogenesis* (the formation of blood vessels from pre-existing vascular structures), and new bone tissue formation are important to enhance life-cycle of a bone implant [176]. Bone is a highly vascularized structure that provides adequate oxygen and nutrient transport to cells, as well as waste removal from the cells [176]. In the case of implanting a scaffold to replace the bone tissue, the remaining vascular structure of the bone attempts to remodel the removed vascular network. Therefore, the interconnected porous network is important to provide a space for vascularization. Optimal pore size values for vascularization process vary in the literature from 200-1000  $\mu\text{m}$ . [177, 178]. In addition to vascularization, bone tissue ingrowth (osseointegration) is critical for adaptability and mechanical stability of the implant. Osseointegration requires new osteoblast cells to lay down directly on the implant surface and initial interlocking to occur between alveolar bone and the implant [179]. Osseointegration includes three main stages [179]:

- Incorporation by woven bone formation,
- Adaptation of bone mass to load (lamellar and parallel-fibered bone deposition),
- Adaption of bone structure to load (bone remodelling).

Factors that determine the success or failure of osseointegration of an implant are the surface characteristics, implant biocompatibility and topographical structure. For porous implants, literature suggests minimum pore size of 300  $\mu\text{m}$  for osseointegration [3]. However, as the pore size increases, the mechanical strength of the scaffold decreases. Therefore, trade-off between strength and bone ingrowth must be considered during the implant design stage.

Other factors controlling initial cell attachment and osseointegration are surface characteristics or biocompatibility of an implant [3]. For example, average surface roughness of 1-2  $\mu\text{m}$  is reported to promote bone in-growth and mechanical interlocking shortly after implanting [180], as compared to lower roughness values. Surface topographies are also shown to effect cell attachment, which motivated researchers to study implant surface modifications including fabricating micro-patterns and nano-structures on the surfaces. Surfaces with a pattern of microdents (9  $\mu\text{m}$  in diameter and 8  $\mu\text{m}$  in spacing) were reported to have more calcified matrix than smooth surfaces [181]. In another study [182], the titanium implant surface that was nanopatterned with semispherical protrusions showed diminished inflammatory response, while enhancing mineralization during osseointegration, as compared to regular titanium implant. In addition to surface modification, coatings of surfaces with hydroxyapatite (HAp) is also reported to promote osseointegration [183]. Hydroxyapatite is a naturally occurring mineral from calcium apatite and forms 70% of human bone by weight [184]. Therefore, HAp coatings are more bioactive and compatible to bone as compared to other metals. Faster bone formation, particularly during the early stages of implantation [185], and direct bonding between the HAp-coated Ti implant and the newly formed bone [185], have been reported as compared to non-HAp-coated Ti.

A literature review revealed studies that assessed the *in-vitro* and *in-vivo* behaviour of additively manufactured lattice scaffolds in more detail, which can aid in the development of guidelines for bone scaffold design. These studies are presented separately.

### 2.4.4.1. *In-vitro* Biological Response

The effect of pore size, shape and distribution on cell survival, attachment and proliferation were studied on both osteoblasts and undifferentiated stem cells. Osteoblast cells are specialized products of mesenchymal stem cells found in bone marrow regions [176]. Primary

osteoblast cells have been found to react differently to porosity compared to osteoblast cells [186]. Therefore, it is important to consider the type of cells when reviewing the literature.

Van Bael et al. [187] studied cell growth and differentiation of human-periosteum derived cells (hPDC) on three different pore shapes (triangular, hexagonal, and rectangular) and two different pore sizes (500  $\mu\text{m}$  and 1000  $\mu\text{m}$ ). Pore size and shape effected the differentiation of hPDC whereas only pore size was found to influence the growth of hPDC cells. Interestingly, qualitative analysis showed a circular cell growth pattern independent from pore shape and size. As a result of the circular cell growth, pore occlusion was found to be highest in 500  $\mu\text{m}$  hexagonal pores due to higher curvature of the hexagonal geometry. Authors suggest that triangular pores might be beneficial for both cell proliferation and differentiation.

Pore occlusion was also observed in tissue growth studies [188]. Thickness of the tissue created by murine pre-osteoblast MC3T3-E1 cells was greater in a triangular channel, followed by square and then hexagonal channel, in the order of decreasing local curvature. Therefore, a rounding of the corners and the formation of a round opening were observed, regardless of the original pore shape (Figure 2. 31). On the other hand, Nune et al. found [189] that there was no apparent effect of pore size of 3D structures on differentiation and mineralization of MC3T3-E1 cells.

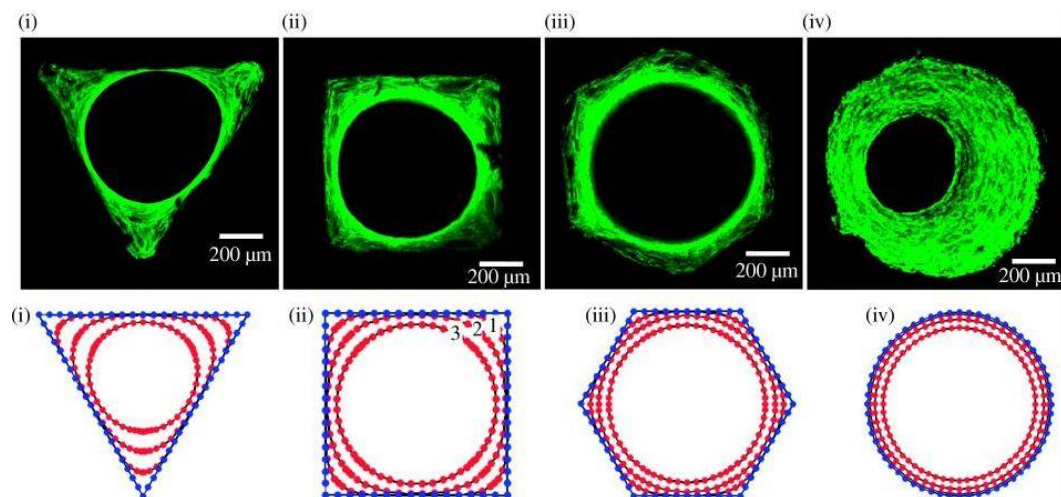


Figure 2. 31 In-vitro Biological Response Top: New tissue formation in 3D matrix channels. Actin fibres are stained with phalloidin-FITC and visualized under confocal laser scanning microscope. Tissue formation is shown in the channels of (i) triangular, (ii) square, (iii) hexagonal and (iv) round shape after culturing MC3T3-E1 cells after 21 days. Bottom: Numerical simulation of tissue formation *in-vitro* [188].



Multiple tissue formation was also observed with different pore sizes and shapes of the scaffold when human mesenchymal stem cells (hMSCs) were cultured [190]. Within the gradient construct, squared pores were found to support chondrogenic differentiation whereas rhomboidal pores showed better osteogenic differentiation. This study shows that functionally gradient scaffolds have the potential to influence hMSCs differentiation. In addition, gradient Ti6Al4V scaffolds were cultured with a pre-osteoblast MC3T3-E1 cell line to study pore size distribution effect on cell adhesion, proliferation and mineralization [191]. It is shown that when cells were seeded from large pore side, the transfer of nutrients was more efficient than seeding cells from small pore side, leading to higher proliferation. Cells also bridge the pores of the scaffold through numerous cytoplasmic extensions. This study also provides a foundation for functionally graded scaffolds with an interconnected porous network.

Stevenson et al. [186] also studied the effect of porosity on proliferation with the MG63 human osteosarcoma cell line. MG63s showed greater metabolic activity on 1.5 mm<sup>3</sup> porous lattices (lower porosity) than on 2.5 mm<sup>3</sup> porous lattices (higher porosity) at 24h, however there was no significant difference between the two lattices at 96h. Cheng et al.[192] also observed a similar cell viability of MG63 on three scaffolds with different pore sizes.

*In-vitro* studies suggest that based on the cell line, the cell-porous material interaction can be different. However, the general trend observed in porous titanium implants is that porous structures provide ample space for cell adhesion and an interconnected network for cell migration and proliferation, which promotes colonization of cells. *In-vitro* studies are good indicators of biocompatibility of the biomaterials, but they are not adequate to say the biomaterials behave well when implanted into body. Therefore, *in vivo* studies should be performed for any biomaterial to assess their behaviour in the animal models and make better assumptions before clinical trials.



### 2.4.4.2. *In-vivo* Biological Response

The environment *in-vivo*, where the osteogenesis is influenced by additional processes such as vascularization and immune response such as inflammation, is different than the environment *in-vitro* [3]. Hence, the influence of porosity might be different, or even in some cases contrasting, when implanted.

Fukuda et al. [193] implanted Ti implant with four square channels, representing pores, in sizes of 500, 600, 900 and 1200  $\mu\text{m}$  into the dorsal muscles of eight mature beagle dogs. Significant osteoinduction was observed in 500  $\mu\text{m}$  and 600  $\mu\text{m}$  size channels. The same research group worked on diamond shaped lattice structures with pore sizes of 300, 600 and 900  $\mu\text{m}$  and implanted them into the metaphysis of the tibia in mature Japanese white rabbits to evaluate bone ingrowth [194]. The implant with 600  $\mu\text{m}$  pore size demonstrated a significantly higher fixation at 2 weeks and the bone ingrowth was similar to the implant with 900  $\mu\text{m}$  pore size after 4 weeks. Because of higher mechanical strength, rapid bone ingrowth and high fixation ability, the 600  $\mu\text{m}$  pore size was recommended for orthopaedic implants manufacture by SLM.

Another study on *in-vivo* response of a diamond unit cell is the work from Wang et al [195]. They designed diamond unit cells with three different pore distributions; uniform, gradient and random, and implanted into rabbits. The *in-vivo* rabbit models showed that all groups were suitable for bone ingrowth and integration.

Arabnejad et al. [11] implanted two stretch-dominated unit cell topologies, octet and tetrahedron, into lateral cortices of canine femora. They observed more bone ingrowth in octet unit cells (56.9 %) than tetrahedron (41.3 %). However, pore sizes were different in the two cell topologies: 770  $\mu\text{m}$  and 500  $\mu\text{m}$  respectively for octet and tetrahedron. Therefore, the two topologies cannot be directly compared in regards to bone ingrowth since pore size might have also been influential.

Zhang et al. [196] showed that a diamond-shaped lattice scaffold was able to promote both cancellous and compact bone growth within the 4-months after the implantation of the scaffold into the femur of a beagle dog, and within the 6-months post-surgery, bone marrow was observed.

Combined analysis of *in-vitro* and *in-vivo* studies suggest that porous scaffolds with pore sizes larger than 300  $\mu\text{m}$  are beneficial for bone ingrowth and cell colonization, however the mechanical properties should be also be taken into consideration when designing larger pores. Having gradient pore distribution along a structure can be beneficial by offering both large and small pores at different locations to meet the contrasting requirements of biological and mechanical behaviour.

Pore shape is another influencing factor for cell activity and morphology as well as the mechanical behaviour of the structure. Other factors that are significant in biological response of porous titanium implants include surface characteristics and coatings, however they are out of the scope of the thesis.

### 2.5. Case Studies

In the last decade, additively manufactured custom-designed implants have been preferred by clinicians to treat complicated bone defects, mainly as a result of a bone sarcoma or trauma [197]. Special CAD software packages, including Mimics from Materialise and open-source 3D-Slicer, are capable of reconstructing computed-tomography (CT) and magnetic resonance imaging (MRI) images into 3D models. With the aid of these software and additive manufacturing technologies, custom-designed implants which can anatomically fit into the defected bone area are possible. The custom-designed implants are sometimes the preferred option by clinicians for complicated unusual surgeries, for which off-the-shelf implants are not feasible. There are reported clinical studies on additively manufactured custom implants with post-surgery data in literature, and the ones with porous surfaces and structure are given in Table 2.6.

## CHAPTER 2. LITERATURE REVIEW

Table 2. 6 Clinical case studies reported on custom-designed porous implants

Location Patient	Disease characteristics	Implant	Outcomes	Reference
<b>Shoulder</b> <b>52-year-old</b> <b>Female</b>	Pre-glenoid replacement surgery causing severe pain to patient after 12 years of implementation.	Custom-made porous titanium glenoid implant	At 2.5 years follow-up: no complications and good function, improved indexes for shoulder pain and disability	[198]
<b>Clavicle (Collarbone)</b> <b>21-year-old</b> <b>Female</b>	Tumor	Custom-made porous titanium prosthesis, manufactured by EBM	At 1 year follow-up, no complications and proper placement of the prosthesis	[199]
<b>Scapula</b> <b>35-year-old</b> <b>Female</b>	Tumor	Size-matched porous prosthesis	At 21 months follow-up, proper articulation	[199] (Figure 2. 32)
<b>Pelvic</b> <b>56-year-old</b> <b>Female</b>	Tumor	Partially porous titanium implant manufactured by EBM	At 18 months follow up, stable fixation and good alignment was observed.	[199]
<b>Wrist</b>	Tumor Secondary surgery	Custom CoCrMo articular implant with a porous grid part	At 9 months follow up, good functioning and recovery	[200]
<b>Hip acetabular cages</b> <b>8 Male</b> <b>16 Female</b>	Revision	Custom titanium porous implants, manufactured by direct metal sintering	At ~67 months follow up, improved hip scores, excellent mechanical stability	[201]
<b>Knee (tibia)</b> <b>1 Male</b> <b>3 Females</b> (aged 35-68 years)	Treating giant cell tumors	Custom porous titanium proximal tibia prosthesis, manufactured by EBM	At 12 months follow up, no complications and good functionality of the implant	[202] (Figure 2. 33)
<b>Spine</b> <b>12-year-old</b> <b>Male</b>	Ewing sarcoma	Titanium, highly porous implant, manufactured by EBM	At 12 months follow up, no complications and evidence of osseointegration	[203]

The reported clinical studies and feedback from both patients and clinicians demonstrate that additively manufactured porous implants offer great benefits and have the potential to reform orthopaedic practices [197]. The porous structure decreases the weight and stiffness of the implants and provides space for cell attachment and bone ingrowth. However, there are still some concerns and room to be improved for porous bone scaffolds, including regulations, ethical support, lack of long-term follow-up, the coordination between engineers and surgeons, time required to design and manufacture implants restricting the emergency cases, and biocompatibility of the material. Therefore, to further promote the use of additively manufactured porous scaffolds [197]; more research should be done on material and design, long term follow-ups should be reported with more case studies, engineers should be trained with a medical background, collaborative platforms should be developed for engineers and surgeons, and regulatory frameworks should be established.

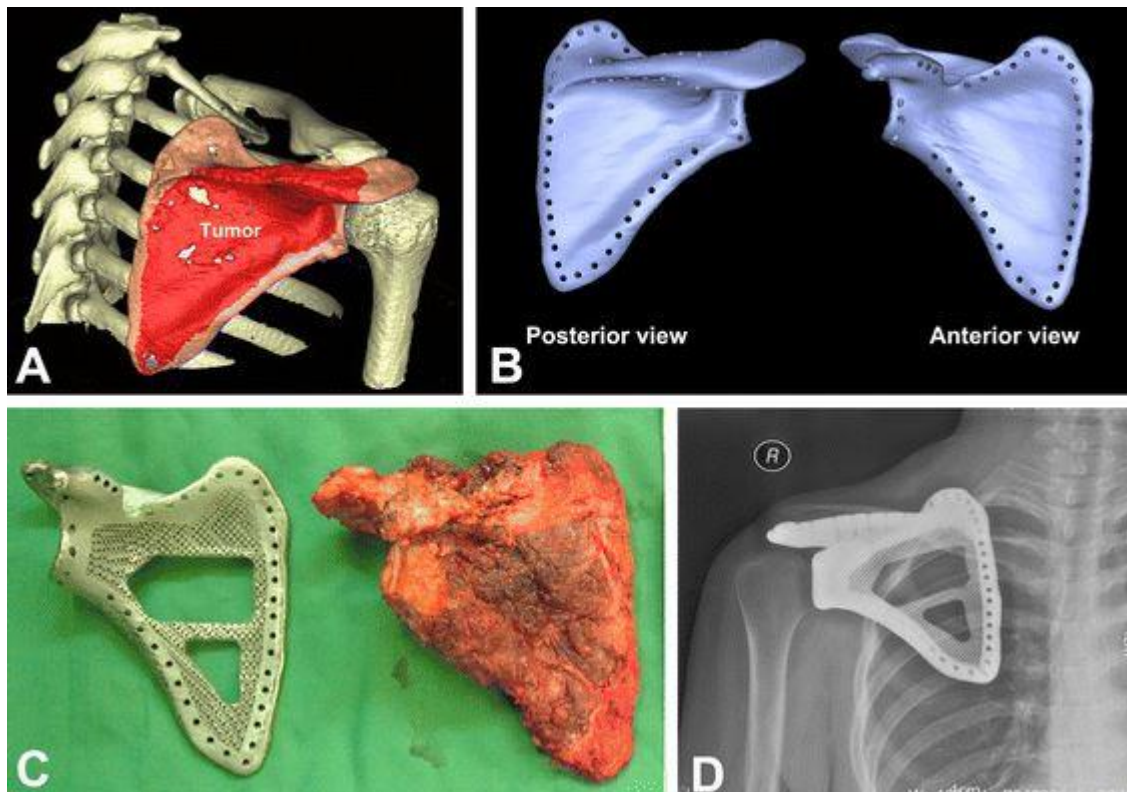


Figure 2.32 a) reconstructed 3-D scapular tumor model. b) The virtual 3-D model of scapular prosthesis. c) The size of excised tumor and prosthesis was well matched. d) X-ray showed a proper shoulder articulation at 21 months postoperatively [199]

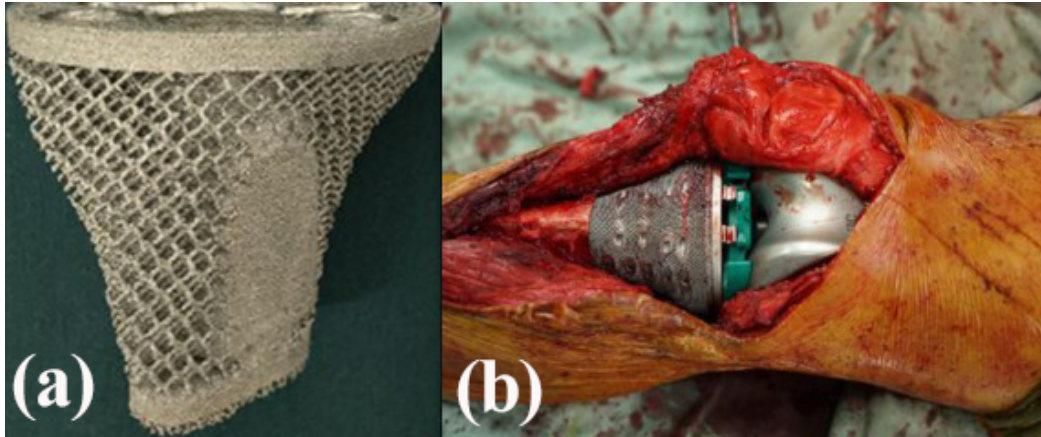


Figure 2. 33 (a) Custom designed tibia prosthesis, manufactured by EBM, (b) Successful implantation of the prosthesis, the ligaments were preserved and sutured to the proximal tibia space through porous structure [202]

## 2.6 Gaps in literature

The literature review outlines the background and recent clinical cases on additively manufactured porous implants. Porous prosthesis have reported to function well and promote osseointegration. They also benefit from adjustable mechanical strength, stiffness and structure. Additively manufactured implants are gaining their popularity among clinicians, researchers and orthopaedic companies; however, there are still some concerns and areas to be improved as it is still a new technology.

Bone tissue engineering is a multi-disciplinary area in which fundamental sciences such as chemistry, biology and engineering need to be integrated together. Without considering the elements of engineering and medicine, a successful implant design is not possible. Therefore, it is important to assess the biological and mechanical response of the orthopaedic implants in parallel. Literature review revealed studies focused either on design, material or clinical aspect and a relatively small number of studies focused on combined analysis of engineering and medical studies.

Specialized software packages for designing customized implants and additive manufacturing technologies are also improving at a rapid rate, which helps the development and increased usage of porous bone scaffolds. The advancement in manufacturing and design tools, and clinical outcomes, brings new questions and areas to improve. For example, porous scaffolds have the potential to incorporate drug delivery systems within the pores. The drug delivery systems can be helpful in osteosarcoma cases or stopping infections after surgical procedure.

The literature review helped to identify three areas to focus our studies on:

- i. The interplay between mechanical and biological behaviour of functionally gradient structures
- ii. Processability of lattices and exploring an alternative scanning strategy of SLM for lattice manufacturing
- iii. Novel lattice designs with introduced channels and pores to create spaces to place drugs or bone morphogenetic proteins

Reported design-related studies include investigation of the effects of pore size, shape, and porosity on the mechanical and biological behaviour of the implants. However, there are still largely unexplored scaffold designs and unit cell topologies, which can improve the functionality of the implant. Identified gaps indicate the need to further investigate functionally gradient porous scaffolds and hollow-beam lattice structures, which form two chapters of the thesis. In terms of manufacturing, the majority of the reported literature focused on fabrication of bulk specimens by selective laser melting technology. However, processing of complex and intricate lattice structures are quite different than processing of bulk specimens. In order to address this gap in literature, an alternative laser scanning strategy was investigated for fabricating lattice structures. This work also aims to understand the fundamentals of laser-material interaction during the SLM process. This thesis aims to contribute to advancement of lattice structures as bone scaffolds by improving their design and their processing conditions.



## 2.7. Conclusion of Literature Review

Architected structures, particularly porous lattice structures, offer unique and interesting properties, including adjustable mechanical properties, deformation behaviour, and improved biological response. Additive manufacturing technologies have enabled the manufacturing of these complex lattice structures with metallic materials at high resolutions. Selective laser melting, which is the most popular metallic AM method, works on the principle of melting and fusing of the metallic powders selectively based on the designed CAD model.

A literature review showed a growing number of papers on additively manufactured porous implants. Published works include studies on the design, manufacturing, mechanical response and *in-vitro* or *in-vivo* performance of the porous scaffolds. Clinical trial and results from follow ups at 1-2 years' timeframe are also present in literature. Reviewed works show that additively manufactured porous implants have a great potential to reform the orthopaedic industry as the next generation of implants with porous architecture offer improved functionality and stability. Problems with the current orthopaedic implants, such as stress shielding phenomena, mismatched anatomical designs and infection during the operation, can be largely eliminated by these new implant designs. The literature review included fatigue behaviour, *in-vivo* response and further post-processing of lattices. Although these studies are important to understand the lattice bone scaffolds, they are out of the scope of this thesis since this study aims to look at the interplay between processing, static mechanical behaviour and *in- vitro* response.

The current study seeks to fill the gaps identified in literature in order to optimize the design and manufacturing of lattice scaffolds. New design models, including functionally gradient porosity and hollow-beam lattices, were developed and an alternative processing method was investigated in order to enhance the performance of additively manufactured architected scaffolds for orthopaedic implant applications.

## Chapter 3. Materials and Methods



In this chapter, the equipment and techniques used to generate the data for the following chapters are explained. Manufacturing of the samples was performed by two SLM machines, Concept Laser Mlab and Realizer SLM 125. For characterisation of the samples, the equipment that was used include optical and electron microscopes, micro-computed topography machine, hardness, density and roughness measurement machines and static compression testing equipment. *In-vitro* biological testing was performed by osteoblast cells and cell attachment and proliferation were assessed by MTS assay and fluorescent imaging. These techniques and equipment are further explained.

### 3.1. Selective Laser Melting and Process Parameters

#### 3.1.1. Concept Laser MLab Cusing Machine

MLab Cusing SLM machine (Concept Laser, Lichtenfels, Germany), which is located at Woodside-Monash Innovation Lab at Monash University, was used in manufacturing the functionally gradient and hollow-beam lattice structures. This machine applied a fibre laser with a maximum power of 100 W. The build envelope is 90 x 90 x 80 mm<sup>3</sup> (x,y,z).

Ti6Al4V-ELI powder supplied by Falcon Tech Co., Ltd. (Wuxi, China) that satisfies ASTM F136 with diameter range of 15–53 µm was used for the laser melting process. The Ti6Al4V samples were fabricated using the manufacturer's recommended settings for Ti6Al4V ELI, which is given in Table 3.1.

Table 3. 1 Process Parameters used for Concept Laser Mlab Cusing with Ti6Al4V ELI powders

Laser power	95 W
Scan speed	600 mm/s
Hatch distance	0.08 mm
Beam spot size	50 (-5 +25) µm
Layer thickness	25 µm

The SLM process was carried in an argon atmosphere with oxygen content less than 0.2 %. The samples were built on top of a solid titanium plate and were removed by using Electrical Discharge Machining (EDM, AgieCharmilles CUT 30P, GF, Losone, Switzerland). After the samples were removed from the build plate, they were washed in an ultrasonic bath containing ethanol for 4 h to aid in removing the unmelted particles from the surface of the samples. No further surface modifications or heat treatments were applied to the scaffolds.

### 3.1.2. Realizer SLM 125 Machine

SLM 125 machine (Realizer GmbH, Borcheln, Germany), which is located at the Biomechanical Engineering lab at the Technical University of Delft, was used to manufacture specimens for the single point exposure study. The machine was equipped with a YLM-400-AC Ytterbium fiber laser (IPG Photonics Corporation, Oxford, USA) with a maximum power of 400 W and a wavelength of  $1.07 \pm 10 \mu\text{m}$ . The build envelope is  $125 \times 125 \times 200 \text{ mm}^3$  (x,y,z).

Ti-6Al-4V grade 23 powder supplied by AP&C (AP&C Advanced Powders and Coatings Inc., Boisbriand, Canada) with a particle size ranging from 10 to  $40 \mu\text{m}$  was used. The laser power and laser exposure times were changed for each specimen. The SLM process was carried in an argon atmosphere with oxygen content less than 0.2 %.



Figure 3. 1 SLM machines used: Concept Laser Mlab Cusing and Realizer SLM 125

## 3.2. Design of Scaffolds

### 3.2.1. Functionally Gradient Structures

Functionally gradient scaffolds were designed with Rhinoceros v5 in the RhinoPython environment. A BCC unit cell was used in a custom-made parametric script to develop continuously gradient structures. Continuous gradient was achieved by changing the strut diameter of the BCC unit cell based upon a polynomial equation, see Equation 3.1. The diameter of the strut is calculated at three locations, evenly spaced along its length based on the location of the strut, and lofted to create a smooth transition between radii.

$$Diameter = c + \sum_{n=1}^{n(x,y,z)} A_{n(x,y,z)} (|P_{(x,y,z)}| - P_{(x,y,z)_0})^n \quad 3.1$$

Here  $c$  is constant,  $A_{n(x,y,z)}$  is the gradient value in the current cardinal direction,  $|P_{(x,y,z)}|$  is the absolute current coordinate position in the relevant axis ( $x$ ,  $y$ , or  $z$ ),  $P_{(x,y,z)_0}$  is the gradient origin in each of the relevant axes, defined over  $n$  polynomial terms.

In the case of a linear gradient in a single axis, only a single term ( $A_x$ ) is required, simplifying the Equation 3.2 to the following:

$$Diameter = c + A_x(P_x - P_{x_0}) \quad 3.2$$

It should be noted that adding  $y$  and  $z$  terms into Equation 3.2 will modify the nature of the gradient and allow the design of 3D gradient scaffolds. It should be also noted that the developed script is not limited to the BCC unit cell and a large library of common unit cells was programmed, allowing the generation of a smooth gradient between layers and tailoring of their size and local and total porosity.

### 3.2.2. Hollow-beam Lattice Structures

Hollow-beam lattices were also designed with Rhinoceros v5 in the RhinoPython environment. BCC, zBCC and 2zBCC unit cells were used and hollow-tubes were achieved by Boolean

operations of subtracting the inner truss from the outer truss. zBCC is a BCC unit cell with extra trusses at the corner nodes, whereas 2zBCC is a BCC unit cell with trusses at corner and centre nodes. The outer strut diameter was 1.5 mm for all specimens, and the inner strut diameter was either 1.2 mm or 0.9 mm to achieve hollow-tube thicknesses of 0.3 and 0.6 mm. In addition, to study the process-ability of extreme dimensions, BCC hollow-beam lattices with different pore sizes and hollow-tube thicknesses were designed, which will be outlined in the related chapter.

### 3.2.3. Single Struts for Single Point Exposure Study

In this study, as the dimension of the struts were controlled by the process parameters, the struts and lattices were generated as lines in the software of the Realizer SLM machine by determining x,y,z coordinations of the lines of the building plate.

For single struts, vertical lines of 15 mm were designed and the thicknesses were controlled by a matrix of 50 conditions with exposure times ranging from 250  $\mu$ s to 1150  $\mu$ s in 100  $\mu$ s increments and laser powers of 88 W to 144W in 12 W increments, (Table 3.2). Additional struts were also printed at higher laser powers and exposure times to explore the boundaries of the single point exposure technique.

In addition to single struts, the effect of latent heat was studied by designing neighbouring struts in circular fashion. Also, the effect of double-melting was studied by locating two lines at the same point. Finally, a BCC scaffold was generated on the software to assess the ability of this scanning strategy to manufacture lattice scaffolds successfully.

Table 3. 2 The laser power and exposure time values used to manufacture struts by single point exposure strategy.

Exposure time ( $\mu$ s)	Laser power (W)										
	88	96	112	128	144	160	176	224	272	304	384
250	*	*	*	*	*						
350	*	*	*	*	*						
450	*	*	*	*	*						
550	*	*	*	*	*						
650	*	*	*	*	*						
750	*	*	*	*	*						
850	*	*	*	*	*						
950	*	*	*	*	*						
1050	*	*	*	*	*						
1150	*	*	*	*	*						
2500					*			*	*	*	*
2950					*	*	*				

### 3.3. Morphology Characterization

#### 3.3.1. Dimensional Analysis

Dimensional analysis was performed by scanning electron microscope (SEM) FEI Nova (NanoSEM, Thermo Fisher Scientific, Hillsboro, OR, USA). Dimensional analysis included strut thickness and pore size measurements, which were then assessed against the designed values. Generally, at least 5 measurements were taken to calculate the mean and standard deviation (SD) of the dimensions. In addition to SEM, a digital microscope (Keyence VHX-100, Itasca, IL, U.S.A.) was used to image the surface and internal porosities of struts.

### 3.3.2. Micro-Computed Tomography

A micro-CT scanner (Zeiss Xradia 520 Versa, Zeiss, Oberkochen, Germany) was used in hollow-beam lattice and single point exposure studies. For hollow-beam lattice structure, the micro-CT was performed to assess any residual powder or pore blockage within the tubes/channels. The following scanning parameters were used: 22.8  $\mu\text{m}$  voxel size, 140 kV source power, 72  $\mu\text{A}$ , 95 mm distance between the source and the sample, 190 mm distance between the detector and the sample.

For the single point exposure study, micro-CT was used to measure the relative density of the struts and to visualize the porosity. The following scanning parameters were used: 1.0  $\mu\text{m}$  voxel size, 60 kV source power, 84  $\mu\text{A}$ , 15 mm distance between the source and the sample, 35.5 mm distance between the detector and the sample.

In both studies, micro-CT images were reconstructed to create a 3D models, which was then further analysed using the software tools Mimics and 3-Matic (Materialise, Leuven, Belgium).

### 3.3.3. Density Measurements

The volume fraction of the samples was measured by gas pycnometry and digital densitometry, (Figure 3.2). A digital densitometry (SD-200L, AlfaMirage, Osaka, Japan) adopts the Archimedeian principle with liquid displacement. A gas pycnometry (AccuPyc 1330, Micromeritics, Norcross, GA, USA) measures the density of solid materials by employing gas displacement and Boyle's Law of gas expansion.

The volume fraction takes into account the porosity due to the design of the porous structures, whereas the relative density refers to the porosity within the total bulk volume of the scaffolds. The volume fraction values were calculated based on the following equations:

$$V = (W_a - W_e) / 0.807 \quad 3.3$$

$$V_f (\%) = V / V_t \quad 3.4$$

Here,  $V$  is the volume of the scaffolds,  $W_a$  is the weight measured in air,  $W_e$  is the weight measured in ethanol, 0.807 is the density (g /ml) of the ethanol used at 25 °C and 1 atm,  $V_f$  is the volume fraction in percent,  $V_t$  is the total volume obtained from the outer dimension of the scaffolds. Relative density values were calculated using the following equations:

$$\rho^* = W_a / V \quad 3.5$$

$$RD (\%) = (\rho^* / \rho^o) * 100 \quad 3.6$$

Here,  $\rho^*$  is the density of the scaffolds,  $\rho^o$  is the density of the Ti-6Al-4V alloy used (4.43 g/cm<sup>3</sup>, as provided by the manufacture) and RD (%) is the relative density in percent. The volume fraction values measured by gas pycnometry and digital densitometry were compared with the values obtained from the CAD designs. At least 3 measurements were taken per specimen to measure the mean and SD.

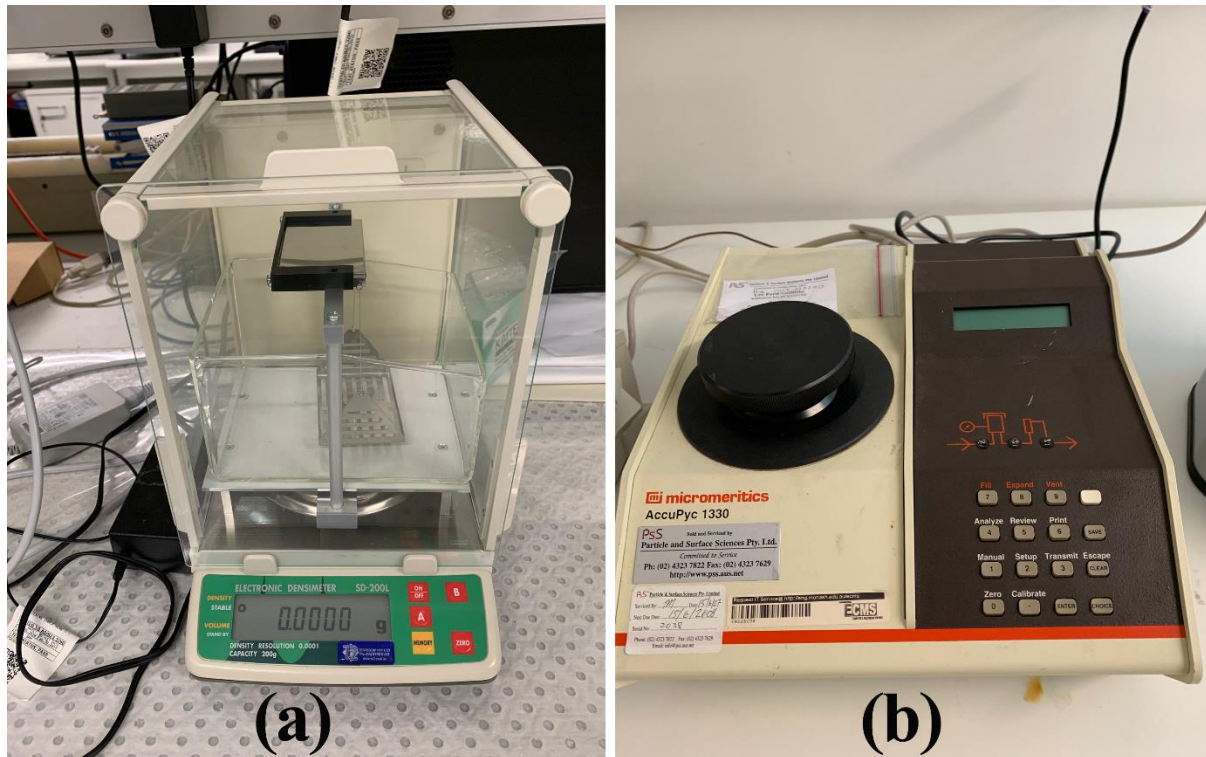


Figure 3. 2 Apparatus used for density measurements: (a) digital densitometry, (b) gas pycnometry.

### 3.3.4. Microstructure Analysis

The microstructure of the as-fabricated Ti6Al4V specimens were observed under an optical microscope (Olympus GX51, Olympus Corp., Tokyo, Japan). The specimens were grinded and polished with 3  $\mu\text{m}$  and 1  $\mu\text{m}$  diamond solutions, and with an oxide polishing suspension (OPU). Finally, the struts were etched with the Kroll's etchant for 30 s to reveal their microstructure.

A transmission electron microscope (TEM) was used in the single point exposure study to investigate the microstructure of the surface layer of the struts. The TEM foils were prepared using the in situ focused ion beam (FIB) milling and lift-out technique was performed with an FEI Quanta 3D SEM (FEI, Eindhoven, The Netherlands). FIB lamellas with a width of 4 mm and a depth of 10 mm were prepared and the microstructure was then observed with a FEI Tecnai F20 microscope (FEI, Eindhoven, The Netherlands) at an accelerating voltage of 200 kV in the TEM, STEM, and SAED modes to determine the morphology and crystal structure of the phases.

### 3.3.4. Texture Studies

EBSD analysis was performed using a JEOL 7001F SEM (JEOL, Tokyo, Japan) at an accelerating voltage of 15 kV and a probe current of 15 nA. The software package AZtecHKL (Oxford Instruments, UK) was used to acquire the EBSD data, while the software CHANNEL5 (Oxford Instruments, UK) was used for post-acquisition analysis of the data. Areas of around 90  $\mu\text{m}$   $\times$  380  $\mu\text{m}$  along the longitudinal (i.e. build) direction of the struts were scanned with a step size of 0.1  $\mu\text{m}$  to collect data from more than 5000 individual grains per condition.

## 3.4. Mechanical Testing

### 3.4.1. Compression Test

A minimum of three specimens of each functionally gradient and hollow-beam structures were mechanically tested under compression using an Instron 5982 universal testing machine with



a 100 kN load cell. In the cases where the 100 kN load cell was not enough, the structures were tested using Instron 8803 testing system with a 500 kN load cell. Following the standard for compression testing of porous and cellular metals (ISO 13314:2011), a constant cross-head velocity was utilized in accordance to a compression strain rate of  $10^{-3} \text{ s}^{-1}$ .

The engineering compressive stress was calculated by normalizing the applied compression load with the initial cross-section area of each sample ( $15 \times 15 \text{ mm}^2$ ) and the engineering strain was calculated by the displacement of the cross-heads. The stress-strain curves of each sample were analysed and the following mechanical properties were calculated based on the guidelines of the ISO Standard 13314:2011: maximum compressive strength ( $\sigma_{\max}$ ) (the first local maximum in the stress-strain curve), 0.2% offset yield stress ( $\sigma_y$ ), the elastic gradient (E). The elastic gradient (also known as the elastic modulus) was calculated between stresses of 20-70 MPa, 50-150 MPa and 100-200 MPa based on the stress-strain values that gave the best representation of the elastic straight line. A series of images were captured every 1 s during compression testing to record the deformation response of the samples.

### 3.4.2. Hardness Test

Hardness measurements were performed following the HV 0.5 protocol (DuraScan-70, Struers, Maassluis, Netherlands) using polished samples. At least five measurements were taken for each sample, which were used to find the mean and SD.

## 3.5. *In-Vitro* Assessments

MC3T3-E1, Subclone 4, preosteoblast cells (ATCC® CRL-2593™) were used for *in-vitro* biological analysis. The as-fabricated porous specimens had to be sterilized carefully before they were seeded with cells. They were cleaned by successive washes with ethanol and phosphate buffer saline (PBS) and then placed in a well plate with 3 repeats and seeded at an

optimum cell density. Positive control wells containing SLM-fabricated solid samples were also set up in parallel.

MC3T3-E1 cells were cultured in  $\alpha$ -MEM medium (Gibco, USA) supplemented with 10% fetal bovine serum (FBS, Gibco™, USA) and 1% antibiotic/antimycotic solution (Gibco, USA) in a humidified incubator at 37 °C, 5% CO<sub>2</sub>. Cell viability was assessed at 4h, 4 days and 7 days after cell culture using the MTS assay (Cell Titre 96 Aqueous One Solution Cell Proliferation Assay, Promega, Madison, WI, USA). After 2.5 h incubation with MTS reagent, 100  $\mu$ l of solution from each well were transferred into 96 multi-well plates and the optical absorbance (OD) was measured at 490 nm with a micro plate reader (Thermo Scientific™ Multiskan Spectrophotometer, Vantaa, Finland). The degree of cell attachment and spreading was studied by immunofluorescence staining. Samples were fixed with 4% paraformaldehyde (PFA) for 20 mins and stained with ActinRed™ 555 ReadyProbes® Reagent (Molecular Probes™, Gaithersburg, MD, USA) following the manufacturer's instructions and Hoechst 33342 (10 $\mu$ g/ml) (Thermo Scientific™, Rockford, IL, USA) for 30 min. After immunostaining, the top and bottom of the specimens were examined by fluorescence microscopy (Nikon Eclipse Ti, Tokyo, Japan).

Cell morphology was characterized by SEM at 4h, 4 days and 7 days of cell culture. Cells on the specimens were fixed with 2.5% glutaraldehyde in 0.1 M sodium cacodylate buffer for 2 h and postfixed in 1% osmium tetroxide for 1.5 h at room temperature. Specimens were dehydrated with a gradient series of ethanol (50%, 70%, 80%, 90%, 95% and 100%) followed by a hexamethyldisilazane (hmde) drying procedure. The specimens were sputter coated with gold and inspected using a FEI Nova NanoSEM.

# Chapter 4. Functionally Gradient Porous Structure

## 4.1. Introduction

Nature provides a great inspiration for engineers and many plants and leaves make use of lattice structures [204, 205]. Among these structures it is common to find gradient lattice structures which adopt their geometry to a particular loading condition or other functional requirement, (Figure 4. 1). Despite these observations, the majority of the 3D printed lattice structures explored so far are based on uniform lattice unit cells [206]. Recently, a number of studies have been published which focus on functionally gradient structures that have various porosity distributions within a scaffold [141-148]. The design of the functionally gradient structures presents multiple challenges and often these structures are generated through artificial joining of different unit cells [146, 147]. This design strategy was shown to negatively affect mechanical properties of the lattice structure due to free nodes at the strut junctions.

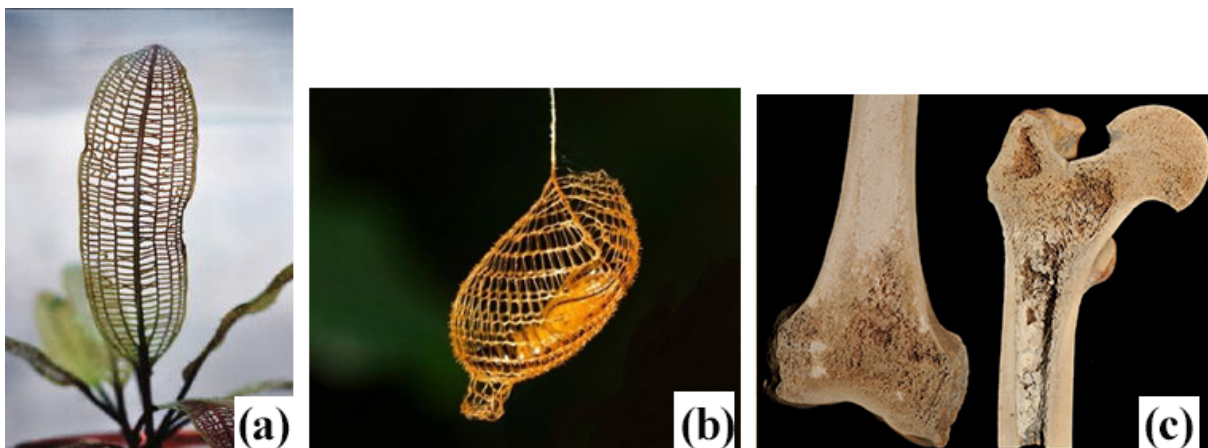


Figure 4. 1 a) Madagascar lace leaf [205], b) lattice structure cocoon [207], c) bone structure [208].

Recent studies aimed to overcome this problem utilise continuously gradient structures, which consist of gradually changing strut thickness between layers [143, 145]. It was shown that such gradient scaffolds possess higher stiffness (24% increase) [149] and energy absorption capacities (~10% increase) [142, 143] than the uniform designs. Functionally gradient structures also showed different failure mechanisms than their uniform counterparts.

This chapter of the thesis is based on the paper published in *Metals* journal [116] in 2018. In this paper the mechanical and biological behaviour of the functionally graded Ti6Al4V porous structures manufactured by SLM are studied.

While the literature review on the additively manufactured lattice structures revealed that there were a number of studies on the gradient porous structures, the majority of these studies were based on the combination of non-continuous unit cells. These designs included abrupt changes between layers, and this effected the mechanical properties in a negative way.

In order to improve the mechanical properties of the gradient structures new design strategies for the scaffolds are proposed based on gradually and continuously changing strut thicknesses along a scaffold, thus enabling a smooth transition between layers. Additionally, the need to study both biological and mechanical behaviour of the functionally gradient structures simultaneously was identified. As the requirements for improved mechanical or biological response can be conflicting, the optimized structures should be identified by considering both of the requirements. Therefore, the motivation for this study was two-fold:

- Exploring continuously gradient porous structures
- Assessing mechanical and biological properties of these structures to establishing optimised gradient structures.

### 4.2. Preliminary Study

Before deciding on using the BCC unit cell for the gradient porous design, a range of unit cell types were designed as uniform cubic scaffolds with different strut thicknesses (changing from 0.4-0.8 mm), and manufactured by Mlab SLM machine. Their mechanical properties were assessed by static compression testing. Sercombe, octet, and BFCCz unit cell types were created by Python lattice generation script within the Rhinoceros software, and dodecahedron and octahedron were created using Materialise 3-Matic STL commercial software package. Unit cell topologies are given in Figure 4. 2. 10x10x10 mm<sup>3</sup> cubes were manufactured for each unit cell with the Ti6AL4V ELI powder using the following process parameters:

- Laser power: 95 W
- Scan speed: 600 mm/s
- Layer thickness: 25  $\mu\text{m}$

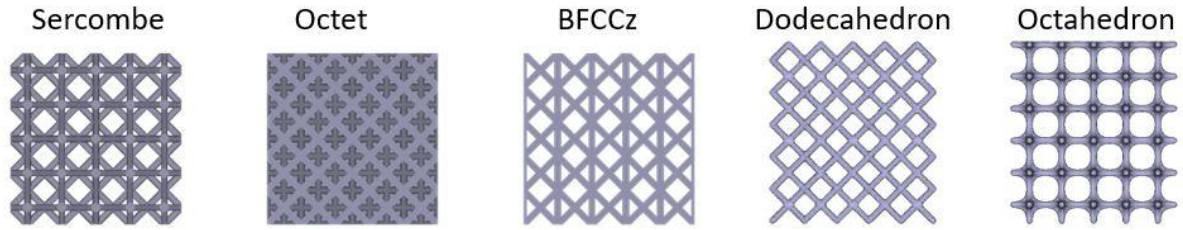


Figure 4. 2 Selected unit cell topologies to manufacture and mechanically test as a preliminary study. The compression test was performed with an Instron 5982 mechanical testing machine with a load capacity of 100 kN and compression rate of 0.06 mm/s. Elastic modulus for each sample was calculated from the initial linear-elastic region and are given in below table.

Table 4. 1 Elastic modulus of the uniform scaffolds with different unit cell geometries and strut thicknesses.

Sample Name	Relative Density (%)	Elastic Modulus (Gpa)
<b>Octet_0.4mm</b>	37	0.02
<b>Octet_0.6mm</b>	68	0.27
<b>Octet_0.8mm</b>	90	0.62
<b>Sercombe_0.4mm</b>	20	0.02
<b>Sercombe_0.6mm</b>	40	0.17
<b>Sercombe_0.8mm</b>	57	0.38
<b>zBFCC_0.6mm</b>	57	0.20
<b>zBFCC_0.8mm</b>	79	0.45
<b>Dodecahedron_0.4mm</b>	22	-
<b>Dodecahedron_0.6mm</b>	32	0.06

<b>Octahedron_0.4mm</b>	14	0.02
<b>Octahedron_0.6mm</b>	24	0.08

Elastic modulus results show that as the strut thickness or relative density increases, elastic modulus increases. Elastic modulus values also changed the unit cell topologies. This preliminary study on the mechanics and manufacturing of different unit cell topologies show that elastic modulus can be altered with the porosity and topology. The elastic modulus results are comparable to the modulus of cancellous bone, that is around 0.2-0.4 GPa [3].

For in-vitro testing, preliminary studies included assessing the cell viability and optimizing the cell seeding method. For this work, dodecahedron and octahedron were selected and manufactured in a plate form with dimensions of  $10 \times 10 \times 2 \text{ mm}^3$  that included one layer of unit cells in z-direction (Figure 4. 3). The reason for designing the samples in a plate form was to simplify the design for the initial *in-vitro* testing. Cell viability was assessed both on porous and solid plates and aimed to verify whether there are any leachable parts of the specimens affecting the cell viability. After sterilization with ethanol, the plates were placed in a multi-well plate with a complete medium for 24 hours in the incubator. In the meantime, MG63 cells were seeded in another multi-well plate with a density of  $1 \times 10^4$  cells per well and incubated for 24 h. The next day, when the multi-well plate had a confluent monolayer of cells, the medium was replaced with the medium that had been incubated with the specimens and with the control medium. The following treatment was applied in triplicate:

1. Untreated cells (fresh medium)
2. 100% conditioned medium (porous Ti6Al4V plate)
3. 50% conditioned medium (porous Ti6Al4V plate) with 50% fresh medium
4. 25% conditioned medium (porous Ti6Al4V plate) with 75% fresh medium
5. 100% conditioned medium (solid Ti6Al4V plate)
6. 50% conditioned medium (solid Ti6Al4V plate)

7. 25% conditioned medium (solid Ti6Al4V plate)

8. Dead control- cells were killed by replacing the medium with 80% EtOH for 5 min before the MTS reagent.

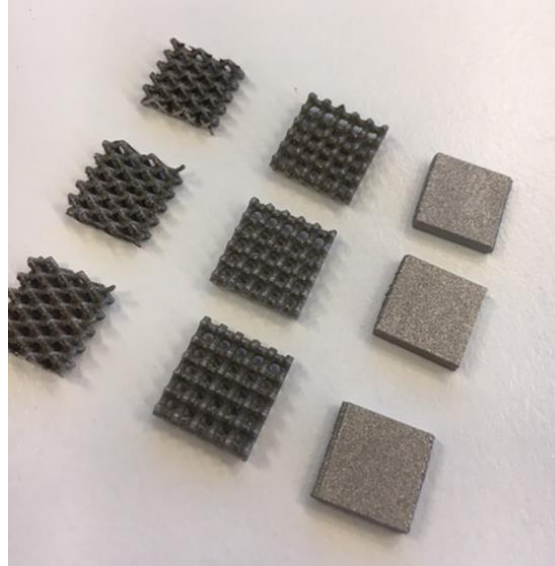


Figure 4. 3 Dodecahedron, octahedron and solid plates manufactured for preliminary *in-vitro* testing.

The treated cells were incubated for 24 h further and cell viability was assessed by MTS. Results show that there was no significant difference in terms of MG63 cell viability between conditioned mediums and the controlled medium, whereas reading from the negative control medium was significantly lower than the readings of all of the conditioned medium and the control medium. This MTS assay indicates that there is no damage to cells from the specimens or no harmful leaching from the specimens that can kill the cells.

After confirming no negative effect of the specimens on the cell viability, we aimed to optimize the cell seeding method. Cell seeding can be challenging onto porous scaffolds. Static seeding methods and several dynamic seeding methods such as spinner flasks, perfusion bioreactors have been used by many research groups [209]. Herein, two seeding methods, called Method A and Method B are proposed. For both methods, cells were seeded with a density of  $5 \times 10^4$  cells/well in the 12-well plate onto the sterilized porous and solid plates as well as onto coverslips as a control. The experiments were set up in triplicates. In method A, a highly



concentrated cell mixture was initially seeded onto the specimens and incubated for 30 mins to let the cells attach to struts of the porous specimens before they flush down to bottom of the well plate. After 30mins of incubation, enough complete medium was topped up gently and the plate was incubated for 24h. In method B, the cells and complete media were seeded at the same time and the plate was incubated for 24h. The degree of cell attachment and spreading was assessed by staining and imaging the cell nuclei and actin cytoskeleton.

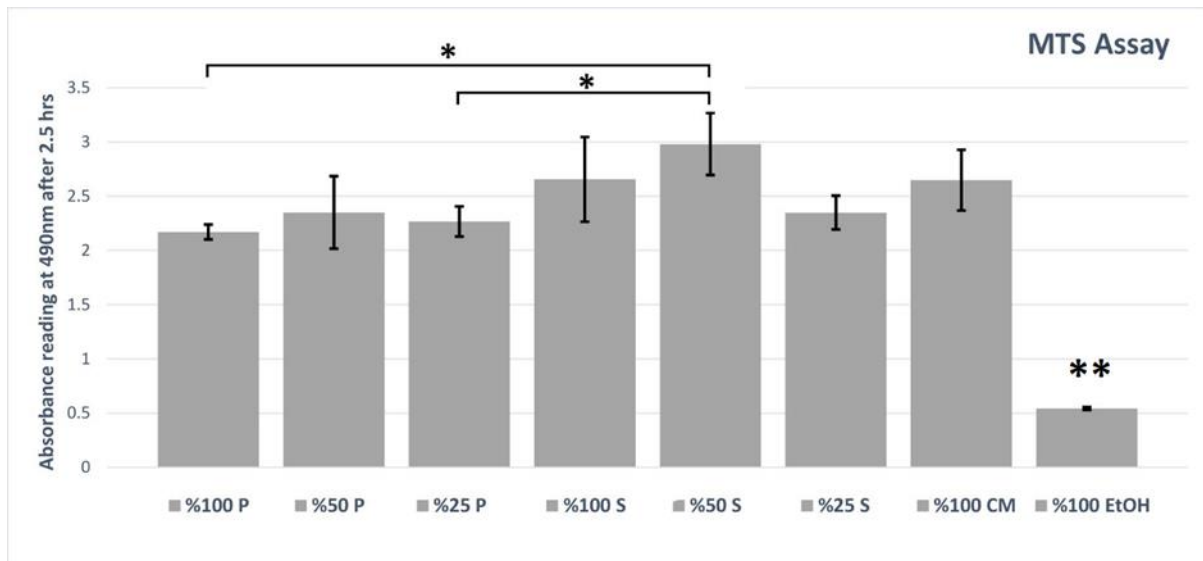


Figure 4. 4 Cell viability measured by MTS assay for the eight treatments. P refers to porous specimens, S refers to solid specimens and CM is control medium. Values presented are mean average  $\pm$  SD (n=3). Horizontal bars (\*) and (\*\*) denote the statistically difference when compared using One-Way ANOVA with Tukey-Kramer post-hoc analysis (at  $p < 0.05$ ).

As seen in Figure 4. 5, it can be said that Method A results in more efficient cell seeding than Method B. The coverslips in both methods look similar, hence, the images of two methods are comparable. The solid samples seeded with Method B showed almost no cell attachment on the top surfaces of the specimens as most of the cells attach onto the bottom of the well plate. Note that the porous (which here refers to the dodecahedron plate) and the solid plates were taken out from the initial well plate and put into the new well plate in order to avoid the signals of the cells attached to the bottom of the initial well plate.

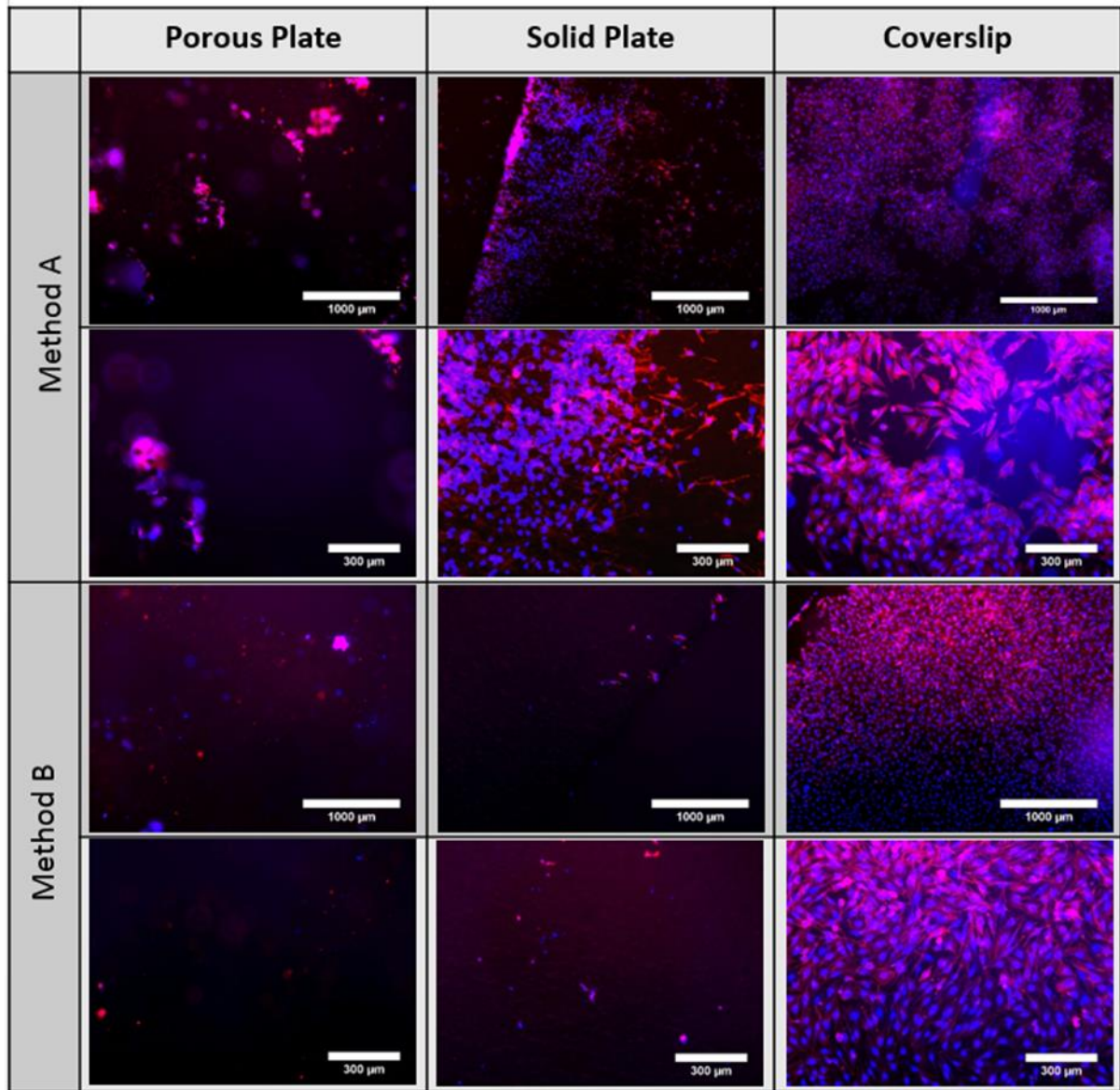


Figure 4. 5 Low and high magnification fluorescence micrographs representing cell attachment of MG63 after 24 h incubation when cells were seeded by Method A and Method B on solid and porous plates and coverslips.

Dodecahedron and octahedron plates were then seeded by following Method A to investigate the effect of pore size and shape on cell attachment. The diagonally shaped pore size of the dodecahedron unit cells were 670  $\mu\text{m}$ , whereas the spherically shaped pore size of the octahedron unit cell was 1500  $\mu\text{m}$ . Fluorescent images (Figure 4. 6) shows that there was no significant difference between the two unit cells. The reason for that can be the scale of the pore size ( $>500 \mu\text{m}$ ) being much bigger than the average cell size (10-15  $\mu\text{m}$ ). The other reason

can be due to the MG63 cell line itself, as other cell lines such as MC3T3-E1 pre-osteoblast cells showed a difference in proliferation even at mm scale pores [188].

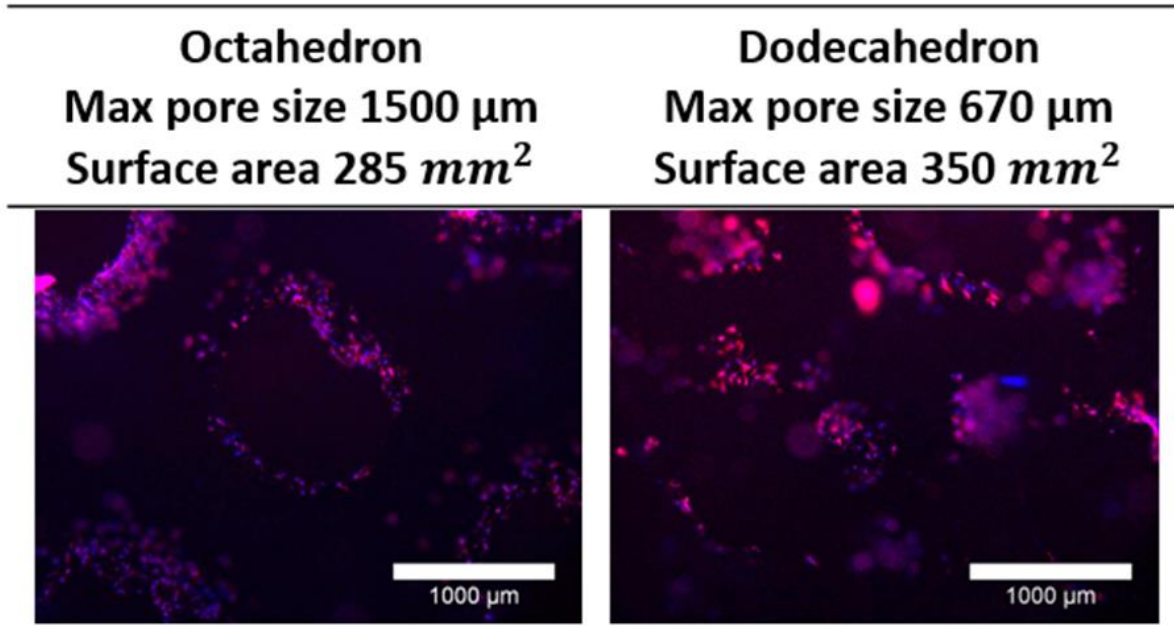


Figure 4. 6 Fluorescent micrographs showing cell attachment on the octahedron and dodecahedron plates.




The mechanical and biological results of the preliminary studies indicate that for the gradient porous study, simple unit cell geometries, such as BCC, can be chosen to eliminate complicated results and to bring the focus on the effect of the gradient porosity. As there was no difference in cell attachment between the two pore shapes, it was chosen to study only one unit cell to investigate the difference between the uniform and gradient structures. Further, the MC3T3-C1 cell line was proposed to be used in the following study as it might be more responsive to mm scale pore size [210].

Preliminary studies show a roadmap for the published paper in terms of the sample designs, cell seeding method and what type of osteoblast cells were to be used. The following subchapter presents the published paper, which includes the related literature review at the time of publication, motivation of the study, methods, study design, results and discussion.

### 4.3. Research Paper

## Article

# Mechanical Properties and In Vitro Behavior of Additively Manufactured and Functionally Graded Ti6Al4V Porous Scaffolds

Ezgi Onal <sup>1,\*</sup> , Jessica E. Frith <sup>1</sup> , Marten Jurg <sup>1</sup>, Xinhua Wu <sup>1,2</sup> and Andrey Molotnikov <sup>1,\*</sup> 

<sup>1</sup> Department of Materials Science and Engineering, Monash University, Clayton, VIC 3800, Australia; jessica.frith@monash.edu (J.E.F.); marten.jurg@monash.edu (M.J.); xinhua.wu@monash.edu (X.W.)

<sup>2</sup> Monash Centre for Additive Manufacturing, Monash University, Clayton, VIC 3800, Australia

\* Correspondence: ezgi.onal@monash.edu (E.O.); andrey.molotnikov@monash.edu (A.M.); Tel.: +61-3-9905-0398 (E.O.); +61-3-9905-9996 (A.M.)

Received: 15 February 2018; Accepted: 19 March 2018; Published: 21 March 2018



**Abstract:** Functionally graded lattice structures produced by additive manufacturing are promising for bone tissue engineering. Spatial variations in their porosity are reported to vary the stiffness and make it comparable to cortical or trabecular bone. However, the interplay between the mechanical properties and biological response of functionally graded lattices is less clear. Here we show that by designing continuous gradient structures and studying their mechanical and biological properties simultaneously, orthopedic implant design can be improved and guidelines can be established. Our continuous gradient structures were generated by gradually changing the strut diameter of a body centered cubic (BCC) unit cell. This approach enables a smooth transition between unit cell layers and minimizes the effect of stress discontinuity within the scaffold. Scaffolds were fabricated using selective laser melting (SLM) and underwent mechanical and in vitro biological testing. Our results indicate that optimal gradient structures should possess small pores in their core (~900 µm) to increase their mechanical strength whilst large pores (~1100 µm) should be utilized in their outer surface to enhance cell penetration and proliferation. We suggest this approach could be widely used in the design of orthopedic implants to maximize both the mechanical and biological properties of the implant.

**Keywords:** selective laser melting; gradient structure; porous biomaterial; Ti6Al4V; mechanical properties; osteoblast

## 1. Introduction

Recent advances in additive manufacturing have revealed new possibilities for the design of the next generation of metallic biomedical implants based on lattice structures. Generally, a bone scaffold should possess four essential characteristics [1,2]: (i) biocompatibility; (ii) mechanical properties matching those of the host tissue; (iii) an interconnected porous structure for cell migration and proliferation and nutrient–waste transportation; (iv) suitable surface characteristics for cell attachment. Traditionally, large bone defects are treated with metallic implants. Several metals have been shown to fulfil the requirement of biocompatibility including cobalt-based alloys, stainless steels as well as titanium alloys [3]. However, metallic implants possess higher elastic moduli than bone, e.g., Ti6Al4V and 316 L stainless steel have a modulus of around 110 GPa and 210 GPa [4] respectively, whereas the modulus of cortical bone is in the range of 3–20 GPa [5]. The mismatch between the modulus of the bone and the implant results in the failure of the implant in the long-term due to the stress-shielding problem [6]. Therefore, matching the mechanical properties of the implant to the host bone and simultaneously providing the implant with biological performance remains a challenge. One potential

strategy is to create porous metallic scaffolds where the porosity, the pore size and shape are optimized collectively to reduce the modulus while maintaining the strength of the scaffold [7].

Porous Ti6Al4V scaffolds are ideal candidates as bone scaffolds since they comply with the aforementioned requirements: they are biocompatible [8,9] and their mechanical properties can be adjusted by porosity [10]. Porous structures with an interconnected pore network are of particular interest for promoting cell migration and colonization [11] as well as tissue in-growth [12,13]. Interconnected pore network enables the flow of nutrients and oxygen to cells and tissue and promotes the formation of blood capillaries [14]. When the vascular network is not sufficient, nutrient and oxygen deficiencies cause hypoxia or necrosis [15,16]. Therefore, open-porous structures with adequate pore sizes are critical for vascularization and tissue growth. However, the optimum porous structure for orthopedic scaffolds is yet to be established and there is conflicting information regarding an optimum pore size for both enhanced bone ingrowth and mechanical strength of the scaffold. Recent reviews [17–19] summarize that optimum pore size should be 300  $\mu\text{m}$  or larger for bone ingrowth and vascularization. However, whilst high porosity and/or large pore size ( $>800\text{ }\mu\text{m}$ ) promotes flow of nutrients, vascularization and tissue growth [14,15,20], highly porous structures lack the required mechanical strength and integrity and decrease the cell seeding efficiency [15,21]. At the same time, in vitro studies have shown that scaffolds with small pore sizes ( $<500\text{ }\mu\text{m}$ ) or low porosities are prone to pore occlusions [22].

Gradient structures present a potential solution to the opposing requirements of an optimal pore size for biological response and mechanical properties. Given an optimal pore size distribution, there is potential to develop structures that exhibit both adequate mechanical strength and tissue in-growth rate. In addition, gradient structures can mimic the natural bone in terms of its structure and mechanical properties [23]. The structure of the bone changes with the amount and direction of the applied stress [24] resulting in differences in the internal structure (porosity and composition) and mechanical properties of the bone along its dimensions. For example, the elastic modulus of trabecular bone at the ends of long bones or within the interior of vertebrae is around 0.5 GPa [25]. This variation in elastic modulus depending on the location in the bone indicates the need for development of gradient structures in bone scaffolds.

The gradient and uniform porous scaffolds can be designed using traditional CAD (Computer Aided Design) and include the use of open cellular foams [26,27] and periodic uniform unit cells based on platonic solids [28–30]. Other techniques, such as implicit surface modelling [31–33] and topology optimized scaffolds [18,34], are also gaining in popularity. The fabrication of such complex structures has recently become feasible with the advances in additive manufacturing [35]. Traditional manufacturing of porous metals such as solid or liquid state processing has limited control over the shape and size of the pores achievable through adaptation of the processing parameters. These shortcomings can be overcome through additive manufacturing which builds a three-dimensional object in layer-by-layer fashion. Selective laser melting (SLM) and electron beam melting (EBM) have both been utilized to successfully fabricate porous scaffolds [36]. Both methods rely on a computer-controlled high power energy source to selectively melt a metallic powder on each layer.

A number of studies have investigated the mechanical or biological response of metallic-based gradient porous designs produced by additive manufacturing [37–45]. The majority of these studies focused on gradient structures generated by abrupt changes between layers based on change in strut diameter or unit cell volume. For instance, Li et al. [37] studied the deformation behavior of radial dual-density rhombic dodecahedron Ti6Al4V scaffolds fabricated by EBM. They achieved radial dual-density by altering the rhombic dodecahedron unit volume between two layers which resulted in discontinuity between layers. Their finite volume method simulations revealed that the inherent discontinuity between layers resulted in stress concentration and maximum stresses at the interfaces. They concluded that continuous variation between layers are ideal to minimize the stress concentration at the interface. Nune et al. [38,39] investigated the osteoblastic functions of the scaffolds designed



using Li et al. [37] work, based on gradient rhombic dodecahedron created by changing the unit volume between layers. Although their work showed promising results on cellular activity when cells were seeded from large pore side (1000  $\mu\text{m}$ ), there was no complementary study on the mechanical properties and therefore the adverse effect of discontinuity between layers on the mechanical properties were not covered.

Another study [40] of multiple-layer gradient structures based on changing unit cell volume also showed the mismatch between two layers. They designed gradient BCC and diamond cylinders where two different unit cell volumes were used in the outer and inner parts of the cylinder. This design approach resulted in free nodes of outer layers that are not connected to inner layers, which caused a negative effect on the mechanical properties. Another approach frequently used to generate gradient structures is based on a sharp change in strut diameter between layers [41,42]. This design principle also results in a mismatch between layers negatively affecting the mechanical properties as well as tissue ingrowth and mineralization [42].

Recently, there have been a few investigations aiming to overcome the problem of a mismatch between layers by designing continuous gradient structures which consists of gradually changing strut diameters between layers. For example, Han et al. [43] reported the mechanical properties of SLM-fabricated pure titanium Schwartz diamond unit cell and demonstrated the layer-by-layer sequential failure of these gradient scaffolds. Maskery et al. [44] also showed the layer-by-layer gradual collapse of gradient scaffolds using SLM-fabricated AlSi10Mg gradient BCC structures. These two studies highlighted that the deformation and energy absorption of gradient lattices is more predictable than the uniform lattices due to the lack of diagonal shear band formation during deformation. In another study Ti6Al4V cubic and honeycomb lattice structures [45] were combined to a gradient structure with a continuous density change and it was shown that this design had a superior energy absorption properties compared to their uniform counterparts. Although the aforementioned studies on the mechanical properties of continuous gradient structures indicate promising results; the selection of unit cells, materials as well as their in vitro and in vivo response need to be better understood.

In this work, we introduce a concept of generating continuous gradient structures by changing the strut diameter linearly across cell layers which enables a smooth transition between layers. To demonstrate the benefit of this design principle, we apply it to the BCC unit cell and create gradient structures with rising or decreasing pores sizes. These gradient structures were mirrored from the central horizontal axis to obtain a symmetrical sample. Their mechanical properties were obtained by uniaxial compression tests and cell attachment and proliferation were assessed with murine pre-osteoblast cells. It will be shown that gradient scaffold can be tailored to fulfil the mechanical properties required and simultaneously improve biological response.

## 2. Materials and Methods

### 2.1. Design and Fabrication of Ti6Al4V Gradient Cellular Structures

The lattice structures were designed with Rhinoceros v5 in the RhinoPython environment. A custom-made parametric script was developed to create the lattice models with continuous gradient structures. The scaffold structure is defined by its type (BCC) (Figure 1a) and size in each of the cardinal directions, and has a changing strut diameter based upon a polynomial equation, see Equation (1). The diameter of the strut is calculated at a minimum or three locations, evenly spaced along its length based on the location of the strut, and lofted to create a smooth transition between radii.

$$Diameter = c + \sum_{n=1}^{n,(x,y,z)} A_{n,(x,y,z)} \left( \left| P_{(x,y,z)} \right| - P_{(x,y,z)_0} \right)^n \quad (1)$$

Here  $c$  is constant,  $A_{n(x,y,z)}$  is the gradient value in the current cardinal direction,  $|P_{(x,y,z)}|$  is the absolute current coordinate position in the relevant axis ( $x$ ,  $y$ , or  $z$ ),  $P_{(x,y,z)_0}$  is the gradient origin in each of the relevant axes, defined over  $n$  polynomial terms.

In the case of linear gradient in a single axis, only a single term ( $A_x$ ) is required, simplifying the Equation (1) to following:

$$\text{Diameter} = c + A_x(P_x - P_{x_0}) \quad (2)$$

It should be noted that by adding  $y$  and  $z$  terms in Equation (2) will modify the nature of the gradient and allow to produce 3D gradient scaffolds.

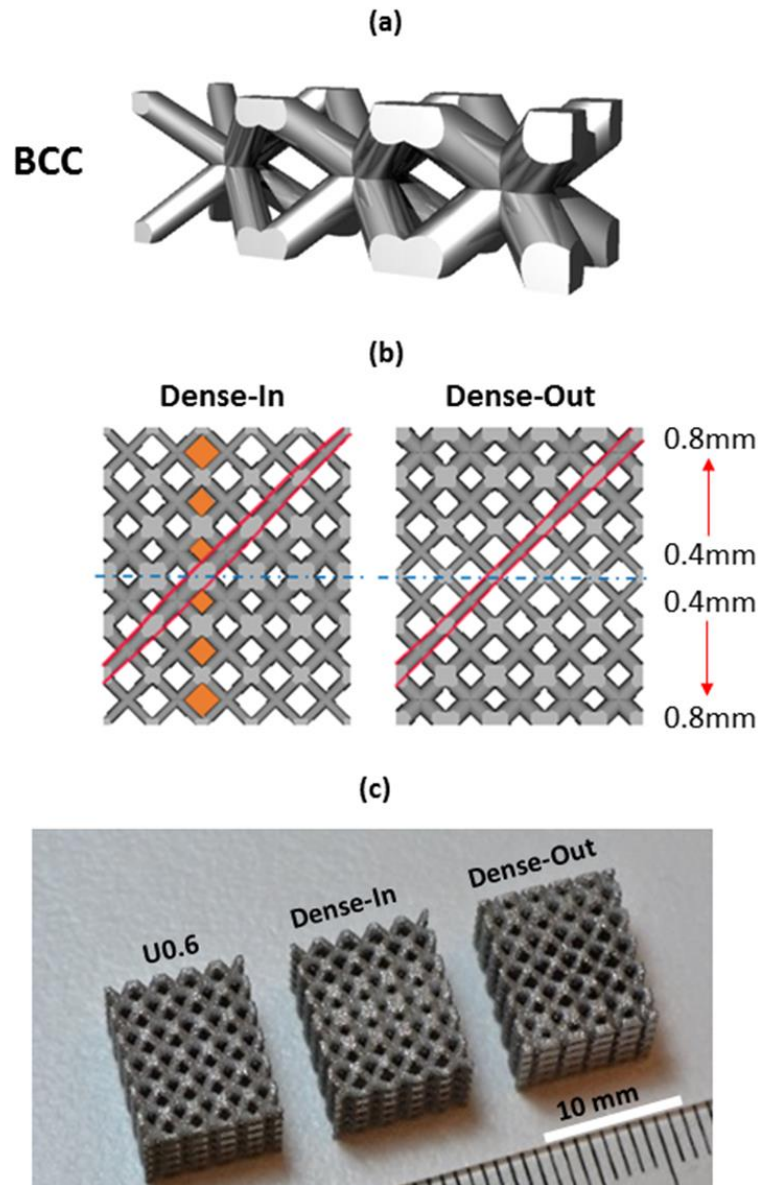


**Figure 1.** (a) Gradient BCC unit cell showing continuous transition at the unit cell junctions, (b) CAD view of the gradient BCC lattice scaffold; the arrows show the gradual increase in strut diameter and the highlighted areas show the gradually changing pore size and strut diameter along the scaffolds' height; Dense-In scaffold has increasing strut diameter towards the center, whereas Dense-Out follows the opposite trend; (c) SLM-fabricated specimens with dimensions of  $10 \times 10 \times 12 \text{ mm}^3$ , from left to right: uniform BCC lattice scaffold with 0.6 mm strut diameter, Dense-In and Dense-Out scaffolds.



To demonstrate the benefit of this concept, we designed two gradient structures with dimensions of  $6 \times 10 \times 10 \text{ mm}^3$ , mirrored in the  $x$ -axis to create lattices of  $12 \times 10 \times 10 \text{ mm}^3$ . In this case a gradient value  $A_x$  was set to 0.07 (mm/mm) and a constant  $c$  equal to 0.4 mm. The choice of the parameters is motivated by manufacturability of the struts and leads to a minimum diameter of 0.4 mm and a maximum of 0.82 mm over the 6-mm lattice. When gradient design was mirrored from the thinner strut plane, it is named as Dense-Out and when mirrored from the thicker strut plane, it is named as Dense-In. For comparison of the mechanical and biological response of gradient structures, we also created three uniform BCC structures which utilize the same strut diameters as present in the gradient structure, namely 0.4, 0.6, 0.8 mm. These uniform BCC structures are denoted U0.4, U0.6 and U0.8, respectively.

It should be noted that the developed script is not limited to the BCC unit cell and a large library of common unit cells was programmed allowing us to generate a smooth gradient between layers and tailor their size and local and total porosity.

The uniform and gradient BCC structures were fabricated by selective laser melting (SLM) process, described in [46], using a MLab Cusing machine (Concept Laser, Lichtenfels, Germany). Ti6Al4V-ELI powder supplied by Falcon Tech Co., Ltd. (Wuxi, China) that satisfies ASTM F136 with diameter range of 15–53  $\mu\text{m}$  was used for laser melting process. The Ti6Al4V samples were fabricated using a laser power of 95 W, scan speed of 600 mm/s with a hatch distance of 0.08 mm, the beam spot size of 50 (–5, +25)  $\mu\text{m}$ , with oxygen content less than 0.2% in an argon atmosphere and the layer thickness of 25  $\mu\text{m}$ . The samples were built on top of a solid titanium plate and were removed by using Electrical Discharge Machining (EDM, AgieCharmilles CUT 30P, GF, Losone, Switzerland). All samples were 12 mm in height with a cross-section of  $10 \times 10 \text{ mm}^2$ . After the samples were removed from the build plate, they were washed in an ultrasonic bath containing ethanol for 4 h to aid in removing the unmelted particles from the surface of the samples. No further surface modifications or heat treatments were applied to the scaffolds.

## 2.2. Morphological Analysis

Morphological properties were characterized by three methods: scanning electron microscope (SEM), digital densitometry and gas pycnometry. Pore size and strut diameter were measured using SEM (FEI Nova NanoSEM, Thermo Fisher Scientific, Hillsboro, OR, USA) images. The average of four pore sizes and strut diameters was calculated for each specimen. The volume fraction of the samples was measured by both gas pycnometry and digital densitometry. A digital densitometry (SD-200L, AlfaMirage, Osaka, Japan) adopts the Archimedean principle with liquid displacement. Three specimens of each sample were used to measure the volume fraction. In addition to densitometry measurements, the volume fraction of each sample were measured by a gas pycnometry (AccuPyc 1330, Micromeritics, Norcross, GA, USA) with helium gas in 3 repeats. The pycnometry measures the density of solid materials by employing gas displacement and Boyle's Law of gas expansion. The volume fraction values measured by gas pycnometry were compared with the values obtained from the CAD designs.

## 2.3. Measurement of Mechanical Properties

A minimum of five specimens of each uniform and gradient structure were mechanically tested under compression using an Instron 5982 universal testing machine with a 100 kN load cell. Following the standard for compression test for porous and cellular metals (ISO 13314:2011), a constant cross-head velocity of 0.72 mm/min was utilized corresponding to a compression strain rate of  $10^{-3} \text{ s}^{-1}$ . The measurements were recorded after a preload of 50–70 N to avoid the initial settling of the samples between plates. A series of images were captured every 1 s during compression testing to record the deformation response of the samples.

The engineering compressive stress was calculated by normalizing the applied compression load with the initial cross-section area of each sample ( $10 \times 10 \text{ mm}^2$ ) and the engineering strain

was calculated by the displacement of the cross-heads. The stress-strain curves of each sample were analyzed and the following mechanical properties were calculated based on the guidelines of the ISO Standard 13314:2011: first maximum compressive strength ( $\sigma_{\max}$ ) (the first local maximum in the stress-strain curve), 0.2% offset yield stress ( $\sigma_y$ ), the elastic gradient ( $E_{(\sigma_{20}-\sigma_{50})}$ ) (the gradient of the elastic straight line between stresses of 20 and 50 MPa). The ISO Standard recommends determining the elastic gradient between stresses of 20 and 70 MPa; however, since 70 MPa was higher than the 0.2% yield stress point for some of the samples, 50 MPa was adopted for all samples.

#### 2.4. Cell Viability, Proliferation and Morphology

MC3T3-E1, Subclone 4, preosteoblast cells (ATCC® CRL-2593™, Manassas, VA, USA) were cultured in  $\alpha$ -MEM medium (Gibco) supplemented with 10% fetal bovine serum (FBS, Gibco) and 1% antibiotic/antimycotic solution (Gibco) in a humidified incubator at 37 °C, 5% CO<sub>2</sub>. As-fabricated Ti6Al4V uniform and gradient porous structures were cleaned by successive washes with ethanol and phosphate buffer saline (PBS). Subsequently, specimens with dimensions of 10 × 10 × 12 mm<sup>3</sup> were placed in a 24-multiwell plate with 3 repeats and seeded at a density of 1 × 10<sup>5</sup> cells per specimen. In parallel, positive control wells containing SLM-fabricated solid samples were set up. Before any evaluation, all scaffolds were transferred into a new 24-multiwell plate.

Cell viability was assessed at 4 h, 4 days and 7 days after cell culture using the MTS assay (Cell Titre 96 Aqueous One Solution Cell Proliferation Assay, Promega, Madison, WI, USA). After 2.5 h incubation with MTS reagent, 100  $\mu$ L of solution from each well were transferred into a 96-multiwell plate and the optical absorbance (OD) was measured at 490 nm with a microplate reader (Thermo Scientific™ Multiskan Spectrophotometer, Vantaa, Finland). The degree of cell attachment and spreading was studied by immunofluorescence staining. Samples were fixed with 4% paraformaldehyde (PFA) for 20 min and stained with ActinRed™ 555 ReadyProbes® Reagent (Molecular Probes™, Gaithersburg, MD, USA) following the manufacturer's instructions and Hoechst 33342 (10  $\mu$ g/mL) (Thermo Scientific™, Rockford, IL, USA) for 30 min. After immunostaining, the top and bottom of the specimens were examined by fluorescence microscopy (Nikon Eclipse Ti, Tokyo, Japan).

Cell morphology was characterized by scanning electron microscope (SEM) at 4 h, 4 days and 7 days of cell culture. Cells on the specimens were fixed with 2.5% glutaraldehyde in 0.1 M of sodium cacodylate buffer for 2 h and postfixed in 1% osmium tetroxide for 1.5 h at room temperature. Specimens were dehydrated with a gradient series of ethanol (50%, 70%, 80%, 90%, 95% and 100%) followed by a hexamethyldisilazane (hmde) drying procedure. The specimens were sputter coated with gold and inspected using a FEI Nova NanoSEM.

#### 2.5. Statistical Analysis

Statistical analyses were performed using SPSS Statistics 20.0 (SPSS, Inc., Chicago, IL, USA). Data were presented as mean  $\pm$  standard deviation (SD). One-way analysis of variation (ANOVA) together with Tukey–Kramer post-hoc analysis were used to identify significant differences (significance threshold:  $p < 0.05$ ).

### 3. Results

#### 3.1. Morphology of Porous Scaffolds

The key morphological parameters of the scaffolds, such as pore size and strut diameter, were measured by SEM and presented in Table 1. The measured strut diameters were larger than the original designs for all samples due to the adhesion of the semimolten powder on the surface (Figure 2b). We measured average surface roughness,  $R_a$ , using a Mitutoyo SurfTest SJ400 and found it to be around 10  $\mu$ m. This is in agreement with the reported values of surface roughness of SLM printed lattice structures [47]. In addition, volume fraction was quantified using the gas pycnometry and

densitometry (Table 1). The volume fraction values were derived directly from the pycnometry and calculated from the densitometry, based on the following equations:

$$V = (W_a - W_w)/0.9971 \quad (3)$$

$$V_f(\%) = V/V_t \quad (4)$$

**Table 1.** The morphometric parameters of uniform and gradient BCC structures based on CAD designs, gas pycnometry, digital densitometry and SEM.

Scaffold Name	Porosity (%)				Pore Size (mm)		Strut Diameter (mm)	
	Design	Gas Pycnometry	Densitometry	Difference (%)	Design	SEM	Design	SEM
U0.4	82	71.87 ± 0.01	71.45 ± 0.02	13	1.51	1.14 ± 0.03	0.40	0.57 ± 0.01
U0.6	64	53.06 ± 0.01	51.11 ± 0.01	17	1.26	0.94 ± 0.05	0.60	0.77 ± 0.01
U0.8	44	33.78 ± 0.01	31.86 ± 0.01	23	1.02	0.73 ± 0.03	0.80	1.06 ± 0.02
Dense-In	62	50.73 ± 0.01	49.38 ± 0.01	18	1.33	1.04 ± 0.02	0.40	0.59 ± 0.01
					1.13	0.83 ± 0.01	0.61	0.72 ± 0.01
					0.94	0.74 ± 0.07	0.82	0.92 ± 0.03
Dense-Out	62	51.90 ± 0.02	50.01 ± 0.01	16	0.94	0.62 ± 0.02	0.82	0.91 ± 0.02
					1.13	0.82 ± 0.02	0.61	0.74 ± 0.01
					1.33	0.98 ± 0.03	0.40	0.59 ± 0.01

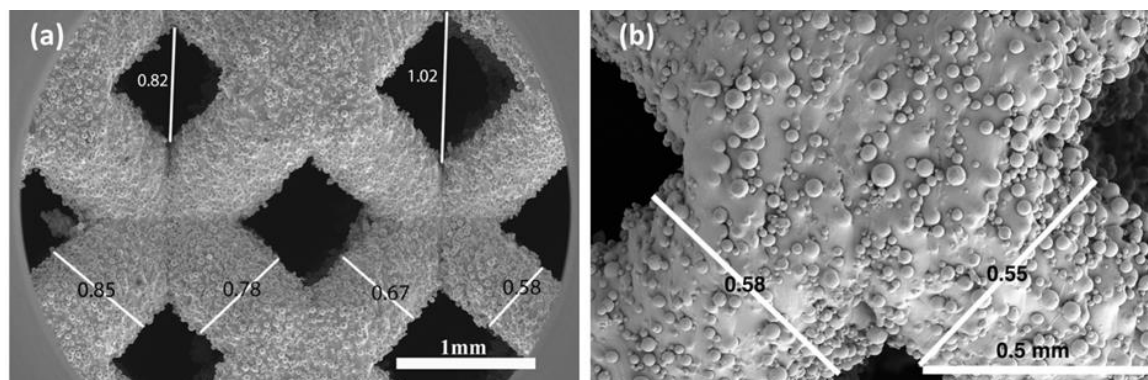


**Figure 2.** SEM image of (a) a gradient Dense-Out structure, demonstrating the change in strut diameter and pore size along the scaffold, (b) higher magnification view of the struts showing attached semi-molten powders.

Here,  $V$  is the volume of the scaffolds,  $W_a$  is the weight measured in air,  $W_w$  is the weight measured in water, 0.9971 is the density ( $\text{g cm}^{-3}$ ) of distilled water at 25 °C and 1 atm,  $V_f$  is the volume fraction in percent,  $V_t$  is the total volume obtained from the outer dimension of the scaffolds, which is  $1.2 \text{ cm}^3$  for all. The porosity of the scaffolds is defined as 100-Volume fraction (%).

The measured values of volume fraction were smaller than the designed volume fraction values for all samples. The difference between the original designs and pycnometry results was around 13–23%. These deviations are as expected since the as-fabricated strut diameters were larger than the original designs, resulting in smaller pore sizes than the intended geometry. This difference is characteristic to SLM process and is caused by effects such as staircase stepping due to layered manufacturing and melt pool variation due to residual stresses [48].

Strut diameter change along the gradient BCC scaffolds was noticeable in SEM images, (Figure 2a), confirming that the desired graded porosity was successfully achieved by the SLM process. The pore size of gradient Dense-In scaffold was varied from 1.14 mm to 0.74 mm, whereas it was between

0.62 mm to 0.98 mm for gradient Dense-Out scaffold. Measured porosity of the gradient Dense-In and Dense-Out scaffolds were almost identical due to symmetric design along the horizontal center plane.

### 3.2. Mechanical Properties of Porous Scaffolds

The compressive nominal stress–strain plots of uniform and gradient BCC structures are presented in Figure 3. The stress–strain curves exhibit characteristic stages of deformation for cellular solids [10,49], including linear elastic region, followed by plateau region with fluctuating stresses. The uniform structures showed similar behavior under compression; however, they reached different levels of maximum stress and possess different elastic moduli. The stress–strain curves for gradient structures also showed initially similar behavior to the uniform scaffolds. After the onset of plasticity an abrupt structural collapse was observed in uniform scaffolds, but not in the gradient scaffolds. Furthermore, the fluctuating degree of plateau region was more distinguished for the uniform scaffolds than the gradient scaffolds.

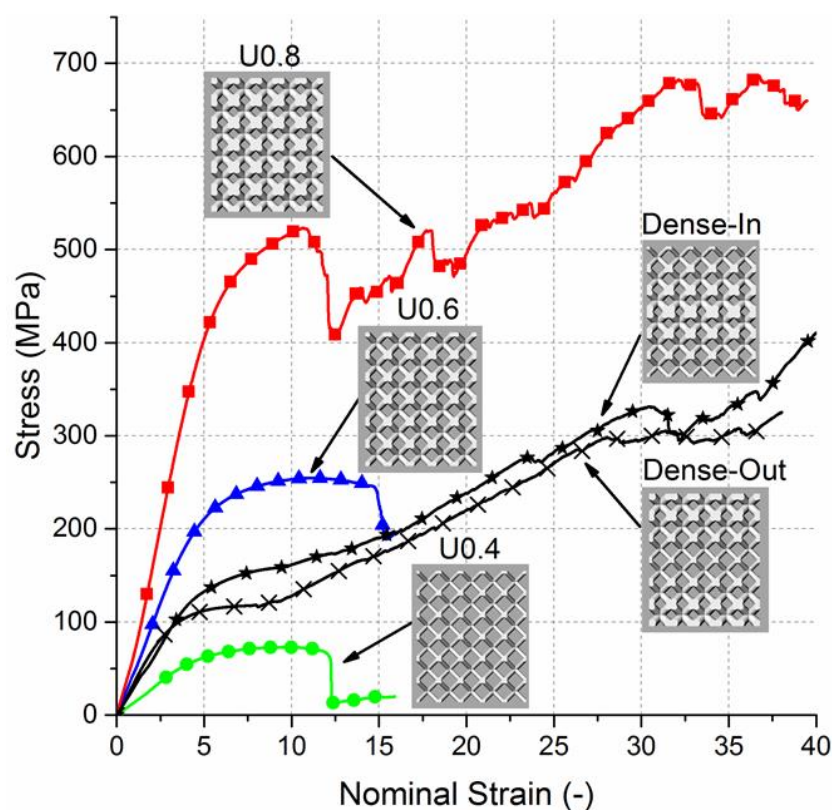


**Figure 3.** Nominal stress–strain curves for uniform and gradient structures.

The elastic gradient between stresses of 20 MPa and 50 MPa ( $E_{(\sigma_{20}-\sigma_{50})}$ ), the 0.2% offset yield stress ( $\sigma_y$ ) and the first maximum compressive strength ( $\sigma_{max}$ ) of the scaffolds are summarized (Table 2). Elastic modulus, yield stress and compressive strength increases with extension in strut diameter of the uniform structures or decrease in porosity. Aligned with the expectations of composite rule of mixtures [50], the values of elastic modulus, compressive strength and yield stress of gradient structures lie between those values of the uniform structures. No significant difference between elastic modulus of gradient structures and Uniform 0.6 sample was observed (Supplementary document Figure S1).

**Table 2.** The summary of the mechanical properties of uniform and gradient BCC structures measured by compression tests. (Mean  $\pm$  SD).

Scaffold Name	$E_{\sigma 20-\sigma 50}$ (GPa)	$\sigma_y$ (MPa)	$\sigma_{max}$ (MPa)
U0.4	$1.6 \pm 0.2$	$53 \pm 4$	$74 \pm 2$
U0.6	$4.6 \pm 0.4$	$192 \pm 14$	$256 \pm 4$
U0.8	$9.0 \pm 0.6$	$392 \pm 14$	$532 \pm 11$
Dense-In	$3.9 \pm 0.8$	$114 \pm 8$	$150 \pm 17$
Dense-Out	$3.5 \pm 0.5$	$86 \pm 11$	$128 \pm 8$

Relative modulus ( $E/E_0$ ) against the measured volume fraction (%) is plotted in Figure 4. Elastic modulus was normalized relative to the values of solid Ti6Al4V (110 GPa). The observed average trend shows a positive power relation with the volume fraction and this trend corresponds to theoretically expected behavior of bending-dominated structures [10,51]. Results of a similar study from the literature were used to support our data [52]. The gradient structures were not considered for the power law curve since their volume fraction is similar to U0.6 specimen.

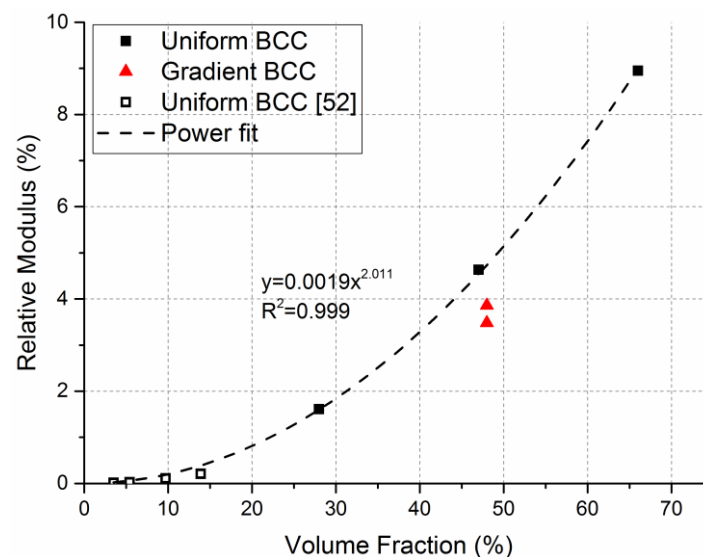


**Figure 4.** Relative elastic modulus vs volume fraction (%) of uniform and gradient BCC structures. Power law curve and equation was fitted on the uniform BCC structure data and demonstrates bending-dominated behavior.

Images of the initial stage and the progressive failure of uniform and gradient structures recorded during the compression tests (Figure 5) show that the major failure bands were formed at a  $45^\circ$  angle from the loading direction for all uniform BCC structures. For the gradient structures, the fracture initiated from the thinnest struts, that is at the top and bottom plane for Dense-In and in the middle for Dense-Out. This diagonal shear collapse of uniform structures is typical behavior of BCC structures [52–54] and other structures with different cell geometries [55,56] owing to strut bending at lattice joints [51].



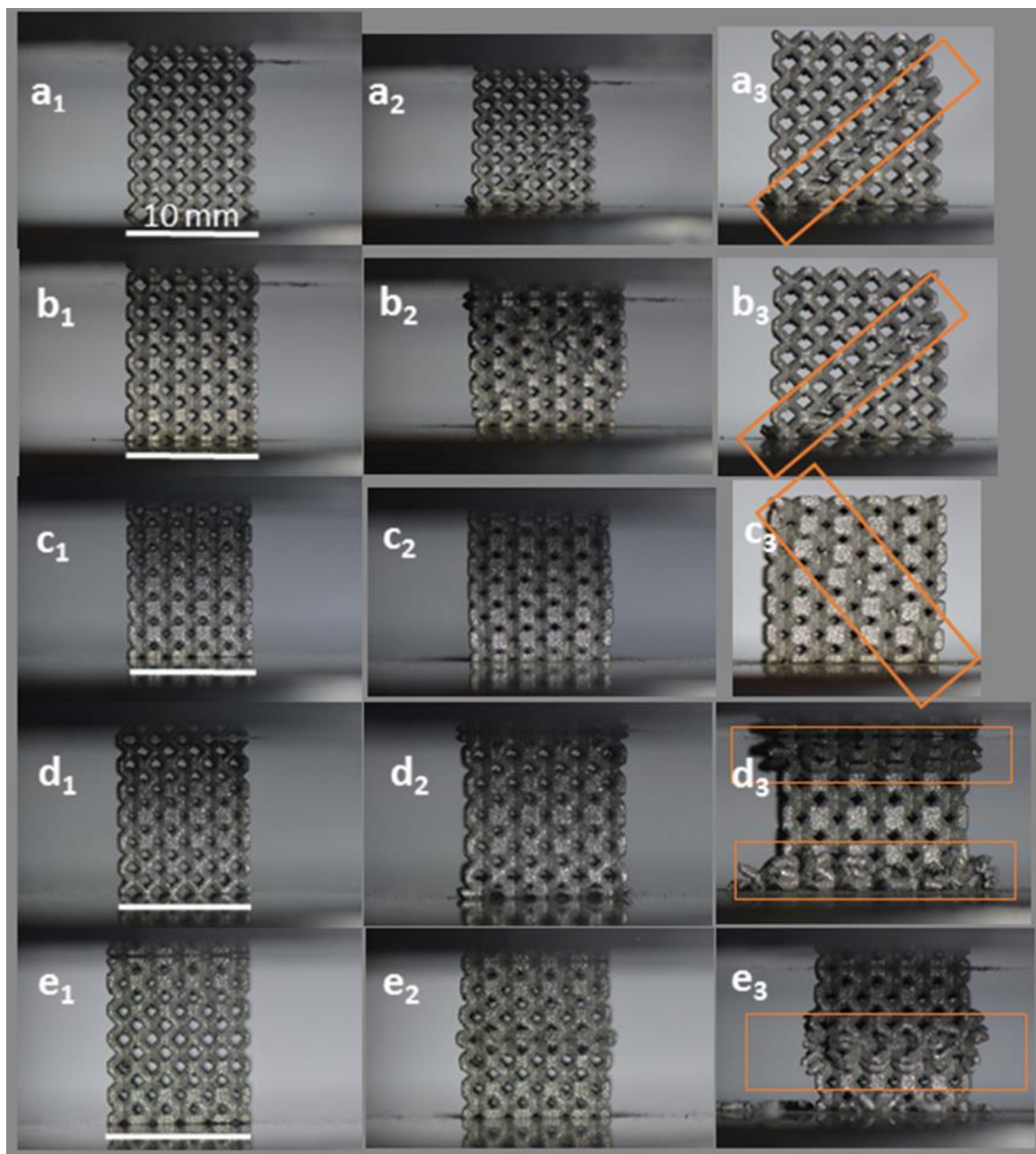


**Figure 5.** Failure modes of (a) U0.4, (b) U0.6, (c) U0.8, (d) Dense-In, (e) Dense-Out structures. Left images (subscript 1) represent the initial state and middle (subscript 2) and last right images (subscript 3) present the progressive failure. Highlights represent the observed regions of deformation and failure. (Scale bars = 10 mm).

### 3.3. Cellular Response to Porous Scaffolds

In order to determine the ability of the scaffolds to interact with cells, the adhesion of MC3T3-E1 preosteoblast cells on the gradient, uniform and solid scaffolds were determined by MTS assay after 4 h of incubation and showed no significant difference in cell seeding between the scaffolds (Figure 6).

In order to determine the extent of cell proliferation on the scaffolds, an MTS assay was performed after 4 and 7 days of culture. The uniform scaffolds showed a trend of decreasing cell number with increasing strut diameter at both days 4 and 7 (Figure 7). For the U0.4 and U0.6 scaffolds the number of cells approximately doubled across this time period whilst there was only a 70% increase on the

U0.8 scaffold (Figure 8), further extending the difference in cell number between the samples. For the gradient scaffolds, there were no significant differences in cell number on day 4. However, from day 4 to day 7, there was almost a 400% increase in cell numbers on the Dense-In scaffold but only 20% increase in cell numbers on the Dense-Out scaffold, resulting in significantly fewer cells on the Dense-Out scaffold as compared to the Dense-In scaffold on day 7. Although solid control sample showed the highest cell number at day 7, the percentage increase from day 4 to day 7 was largest for Dense-In scaffold. The final cell number on the Dense-Out scaffold was comparable to that of the U0.8, with both scaffolds having similar diameter of the outermost struts of the design. These results suggest that the scaffolds having thinner struts or larger pores on their outside surface (such as U0.4 and Dense-In) were more favorable for cell proliferation than the scaffolds having thicker struts or smaller pores on their outer surface. Given that the surface area of Dense-In and Dense-Out is identical as a result of their symmetrical design, it can be said that the cell viability was independent of surface area in this study.

Further to cell proliferation, cell distribution on the uniform and gradient scaffolds was studied by staining and imaging the cell nuclei and actin cytoskeleton. After 4 h of incubation, all of the scaffolds had similar cell distribution on their top surface (i.e., the surface onto which the cells were seeded) (Figure 9). The lack of cells at the bottom of the scaffolds suggests that most of the initial attachment was on the top surface. After 4 days, substantially more cells were observed both on the top and bottom surfaces of the U0.4 and Dense-In scaffolds, whereas there were no noticeable differences on the other scaffolds between 4 h and day 4 time points (Figure 10). At day 7, all the scaffolds had high density of cells on their top surface; whilst, the bottom surface of U0.6, U0.8 and Dense-Out scaffolds had almost no cells. In contrast, the bottom surface of U0.4 and Dense-In scaffolds had visibly higher cell densities.

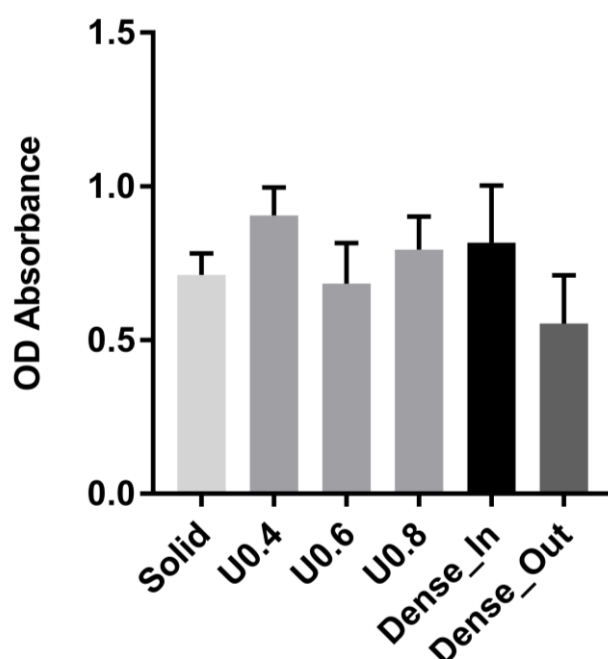


**Figure 6.** Adhesion of cells to uniform and gradient porous structures and to solid control sample as measured by MTS assay after 4 h. The optical absorbance (OD) was measured at 490 nm. Data are presented as mean  $\pm$  SD ( $n = 3$ ). No statistically significant differences were observed between scaffolds.

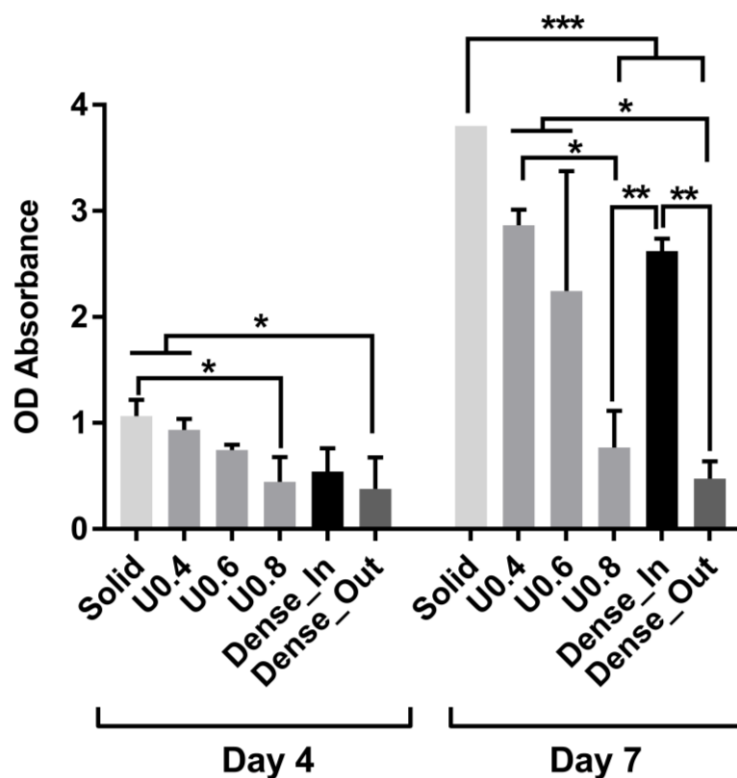


**Figure 7.** Cell proliferation measured by MTS assay after culturing 4 and 7 days on the uniform and gradient porous structures. The optical absorbance (OD) was measured at 490 nm. Data were presented as mean  $\pm$  SD ( $n = 3$ ). (\*  $p < 0.05$ , \*\*  $p < 0.01$ , \*\*\*  $p < 0.001$  when compared using ANOVA Tukey–Kramer post-hoc test).

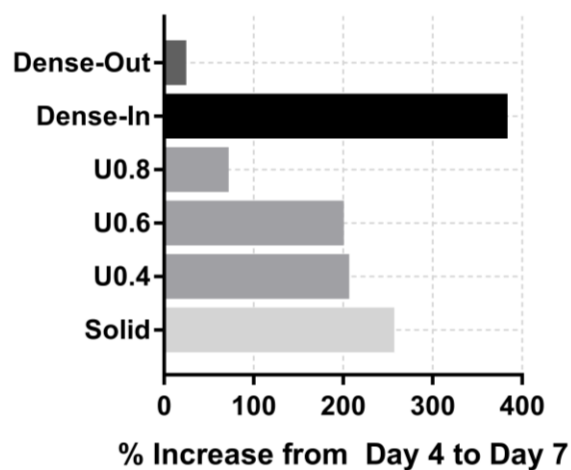


**Figure 8.** Percentage increase in od absorbance of the scaffolds from day 4 to day 7.



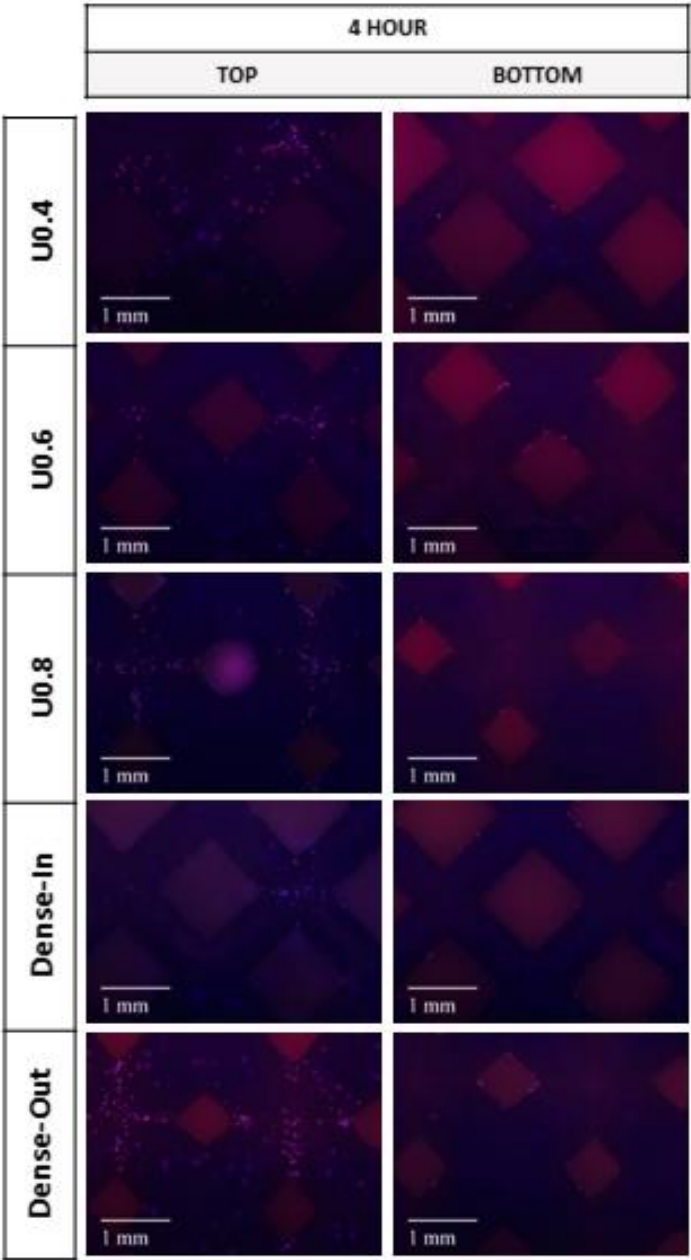


**Figure 9.** Fluorescence micrographs representing merged Hoechst stained nucleus (blue) and actin cytoskeleton (red) of MC3T3-E1 preosteoblast cells on the uniform and gradient BCC structures after culturing for 4 h. Top represents the side where cells were seeded onto the samples.

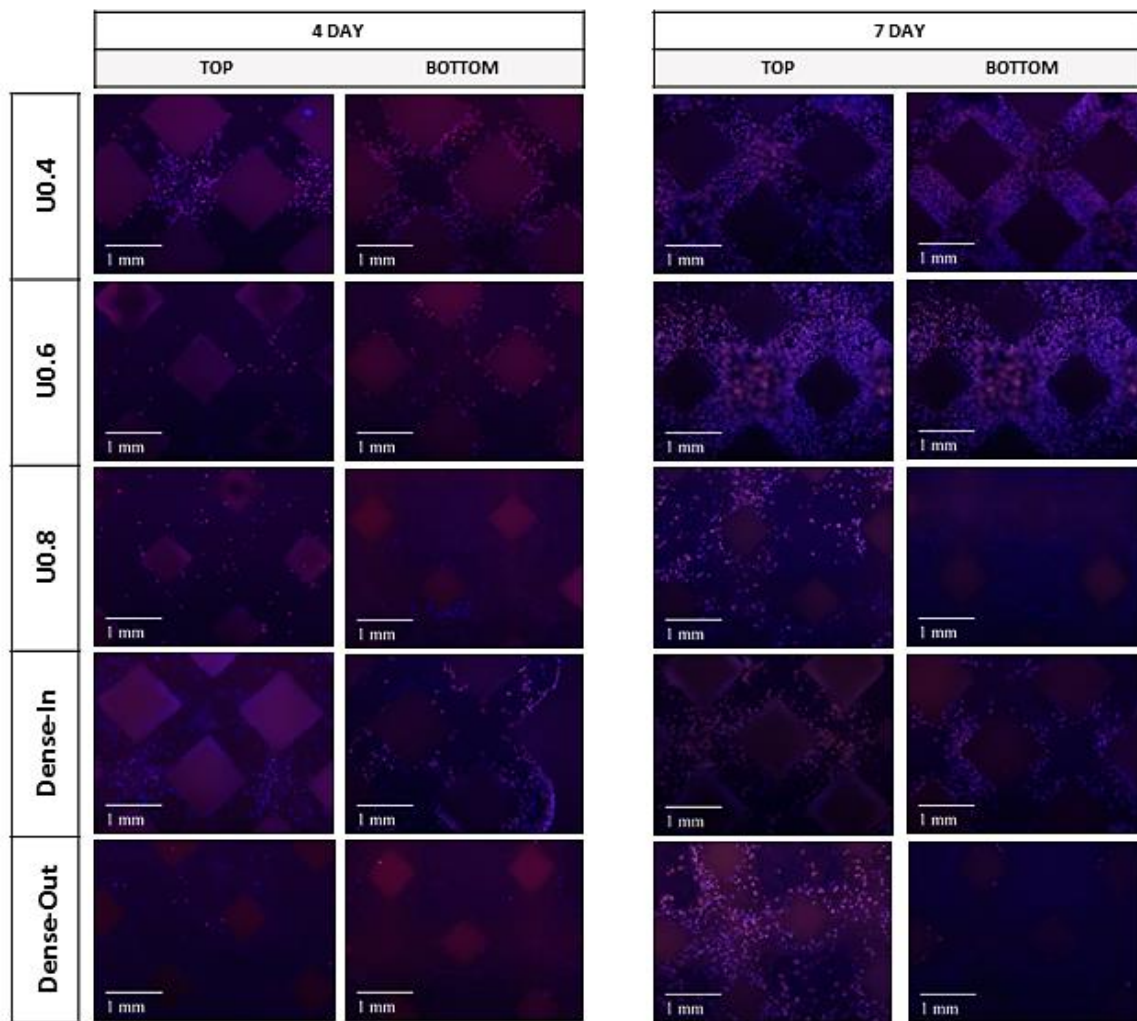


**Figure 10.** Fluorescence micrographs representing merged Hoechst stained nucleus (blue) and actin cytoskeleton (red) of MC3T3-E1 preosteoblast cells on the uniform and gradient BCC structures after culturing for 4 days and 7 days. Top represents the side where cells were seeded onto the samples.

Despite the difference in cell proliferation and migration on the different scaffolds, cell morphology was similar for the scaffolds when the images were taken from the top surface (Figure 9). SEM images taken from the middle and bottom part of the scaffolds supported the findings of fluorescent images showing differing cell penetration depth profiles for the varying scaffold structures (Supplementary document Figures S2–S6). The number of cells decreased in the middle and bottom parts of the U0.8 and Dense-Out scaffolds, as compared to U0.4 and Dense-In scaffolds. Cells were noticed to form a sheet-like elongated matrix (dashed line) (Figure 9). Moreover, the morphology of cells presented a high density of filopodia-like projections (red arrows) extending from the leading edges of cells and interacting with the substrate. The interaction between cells and substrate observed by SEM (Figure 11) shows that cells attach both on and between the unmelted powders, indicating that SLM process are beneficial to cell attachment and colonization.

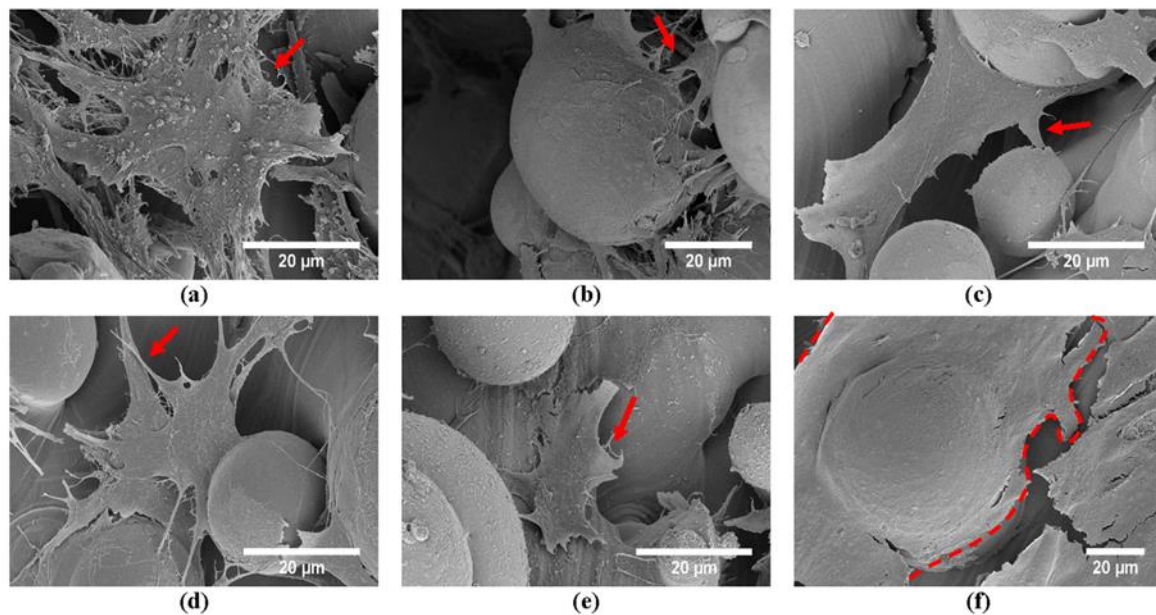


**Figure 11.** SEM images of the MC3T3 preosteoblast cells after culturing for 7 days on the top surfaces of (a) U0.4, (b) U0.6, (c) U0.8, (d) Dense-In, (e) Dense-Out, (f) solid scaffolds.

#### 4. Discussion

In this work, the effect of gradient porous structures on both biological response and mechanical behavior is investigated. The generated gradient structures, denoted as Dense-In and Dense-Out, utilize gradual change in diameter and therefore minimize the stress concentration at the lattice junctions. The designed pore sizes changed from 940 µm to 1330 µm for the gradient scaffolds. The deviation of pore size and strut diameter between CAD design and fabricated scaffolds were within an expected range [57] and was attributed to surface irregularities [58]. The deviation for each scaffold was similar, demonstrating the consistency of the SLM fabrication process. Porosities of the uniform scaffolds varied from 32% to 72%, and both gradient structures had a porosity of 50%. SEM images revealed that all scaffolds had unmelted powder attached to the surface of the struts due to layered manufacturing and melt pool variation during the SLM process.

The stiffness of the tested scaffolds varied in the range of 1.6 to 9.0 GPa, which aligns with the stiffness range of the trabecular (0.4 GPa [59,60]) and cortical bones (3–20 GPa [5,24]). The yield stress values of the scaffolds were in the range of 53 to 392 MPa, which lies in the range of cortical bones (33–193 MPa [24,61]), but it is not suitable for a replacement of trabecular bone, 2–17 MPa [60]. Considering the scaffolds presented in this study aim to be used as load-bearing implants for replacement of cortical bones, the yield stress and elastic modulus values satisfy the mechanical property requirements.

Table 2 shows that the elastic modulus, yield stress and maximum compressive strength values increase as the strut diameter increases or porosity decreases. The mechanical properties of gradient structures lie in the range of representative values of uniform structures and can be predicted based on an assumption that gradient structures are composites of uniform layers of the same diameter struts. Based on this assumption, the elastic modulus of gradient structure in uniaxial compression can be calculated through the general rule of mixtures [42,50]:

$$\frac{1}{E_{Gradient}} = \frac{1}{3E_{U0.4}} + \frac{1}{3E_{U0.6}} + \frac{1}{3E_{U0.8}} \quad (5)$$

Using Equation (1), elastic modulus of gradient structure was calculated to be 3.2 GPa, which is comparable to the measured values of 3.9 and 3.5 GPa for Dense-In and Dense-Out scaffolds, respectively.

The deformation response of uniform BCC structures follows the bending-dominated behavior with diagonal shear collapse. Interestingly, the failure mechanism of gradient structures was different due to sequential layer collapse and various deformation stages occurring simultaneously. Thinner struts reached the densification stage (when two opposite cell walls come together as the pore size decreases) while the thicker struts were still in the plateau region during the compression test. The predominant fracture band of gradient structures was initiated at the thinnest struts due to high stress concentrations on the thin strut junctions. This failure mechanism has also been noted in other studies [44,45].

Further to mechanical behavior studies, we analyzed the *in vitro* response of the scaffolds with preosteoblast cells. The degree of cell attachment was similar for all scaffolds, but cell proliferation and colonization were significantly different. Scaffolds with a thin strut diameter on the periphery (U0.4 and Dense-In) allowed cells to populate throughout the scaffold whereas those with a thicker outer strut (U0.6, U0.8 and Dense-Out) did not allow cells to migrate to the bottom surface, suggesting that cells were entrapped at the smaller pore size region (top surface). Consequently, the proliferation rate of cells on these scaffolds was markedly less. Although this immobilization behavior of the preosteoblast cells when seeded from small pore size region was observed in the previous studies of Nune et al. [38,39], the underlying reason for this behavior is still unknown. The smallest pore size in our scaffolds were 940  $\mu\text{m}$  which is larger than the suggested pore size (100–300  $\mu\text{m}$ ) for cell colonization and migration [62,63]. In addition, the smallest pore size is much larger than an average size of a MC3T3-E1 pre-osteoblast cells (20–40  $\mu\text{m}$ , Figure 9). It is not yet clear why thicker struts on the scaffold periphery inhibit cell activity whilst the thick struts on the interior of the Dense-In scaffold did not deter colonization of cells through the whole structure.

Our results suggest that the surface area does not affect the cell attachment and proliferation. The large surface area of the U0.8 scaffold, due to its large strut diameters, was expected to promote cell attachment and growth; however, it showed the lowest cell number at day 7. Similar behavior was observed for the gradient structures, which possessed equal surface area but showed a large difference in cell number. It is therefore likely that, parameters other than the surface area of the scaffold affected the cell colonization. Identification of the specific factors would require further clarification but could include the flow conditions and cellular aggregation [39]. In addition, it would be interesting to assess whether vascularization happens more quickly or easily with larger pores on the periphery than the smaller pores on the periphery.

In recent years, additively manufactured gradient structures for tissue engineering have been studied [37–39,41,44,64,65]; however these studies either focused on the mechanical properties or biological response independently. In this work, the biological and mechanical responses were assessed simultaneously allowing us to study the overall impact of the designed geometry of the scaffolds. Our results suggest that when designing a porous gradient structure, both biological and mechanical requirements must be considered concurrently, since their requirements are opposing. The compression test results demonstrate the benefit of utilizing smaller pore size in increasing the stiffness and strength of the porous scaffolds; whereas, the cell proliferation data suggests that scaffolds with larger pore size in their outer surface favors cell proliferation. Therefore, it can be concluded that gradient scaffolds provide a possible solution for overcoming the conflicting requirements of bone tissue implants. Gradient structures with decreasing pore size towards their center can provide the required strength and stiffness, while simultaneously promoting cell colonization throughout the whole scaffold. The Dense-In scaffold fabricated in this study has an elastic modulus of 3.9 GPa which is in the range for those of cortical bone [5]. Furthermore, this scaffold has a varying pore size ranging from 1330  $\mu\text{m}$  on the outside to 940  $\mu\text{m}$  at the core. These values have been previously reported to be favorable for cell colonization as well as bone ingrowth and vascularization [66–68].



In summary, an ideal scaffold for bone regeneration should facilitate cell attachment, infiltration and matrix deposition to guide bone formation [69] as well as providing initial mechanical support to the surrounding bone [70]. Porous titanium scaffolds can meet the mechanical strength and bone formation requirements without osseoinductive biomolecules [68]; however, the pore size of the scaffolds needs to be high for bone-ingrowth whereas, as the porosity increases, the mechanical strength and integrity of the structure decreases [71]. Gradient structures represent an ideal candidate to overcome these opposing requirements of high porosity and mechanical strength.

Our study demonstrated the benefit of the gradient scaffold with larger pores in its outer surface in terms of gaining optimum mechanical strength and promoting cell attachment and colonization. In addition, this framework demonstrates that mechanical properties can be tailored through gradient structure design and simultaneously improve the biological response. This approach therefore holds significant promise in the development of orthopedic implants, where the location of the implant and the corresponding loading condition can dictate the implant topology.

## 5. Conclusions

This work combined and assessed the in vitro behavior and mechanical response of gradient and uniform porous scaffolds for bone tissue engineering. For this purpose, five different BCC structures were fabricated using selective laser melting technology. Static mechanical properties of the gradient structures followed the rule of mixtures and the obtained values are in the range of those corresponding values for uniform structures. The mechanical properties of all studied scaffolds are comparable to the reported mechanical properties of the cortical bone. Quantitative analysis of cell viability showed higher cell colonization and proliferation rates for scaffolds with large pores (1000–1100 µm) in their outer surface after 4 and 7 days of culturing. However, when comparing the mechanical properties of structures with this comparable biological activity, the uniform U0.4 scaffold showed less than half of the respective mechanical properties for the Dense-In scaffold. The combined results of compression tests and in vitro biological analyses indicate that the Dense-In scaffold is an ideal porous structure to balance mechanical and biological performances to meet the requirements of load-bearing implants. Based on the results presented in this work, optimal gradient structures should possess small pores in their core in order to increase their mechanical integrity and strength while large pores should be utilized in their outer surface to avoid pore occlusion. We suggest that this approach could be widely used in the design of orthopedic implants to maximize both the mechanical and biological properties of the implant.

**Supplementary Materials:** The following are available online at <http://www.mdpi.com/2075-4701/8/4/200/s1>, Figure S1: Mechanical properties of the scaffolds; Figures S2–S6: Observation of cell morphology and distribution along the scaffolds by SEM.

**Acknowledgments:** Ezgi Onal would like to acknowledge The Clive and Vera Ramaciotti Centre for Structural Cryo-Electron Microscopy. This project is funded by the ARC Research Hub for Transforming Australia's Manufacturing Industry through High Value Additive Manufacturing (IH130100008) and Jessica E. Frith is supported by an ARC DECRA (DE130100986).

**Author Contributions:** E.O. and A.M. conceived and designed the experiments; E.O. performed the experiments; E.O., J.E.F., X.W. and A.M. analyzed the data; M.J. contributed generating Python scripts to design structures; all authors contributed to the writing of the paper.

**Conflicts of Interest:** The authors declare no conflicts of interest.

## References

1. Hutmacher, D.W. Scaffolds in tissue engineering bone and cartilage. *Biomaterials* **2000**, *21*, 2529–2543. [CrossRef]
2. Hutmacher, D.W.; Schantz, J.T.; Lam, C.X.F.; Tan, K.C.; Lim, T.C. State of the art and future directions of scaffold-based bone engineering from a biomaterials perspective. *J. Tissue Eng. Regen. Med.* **2007**, *1*, 245–260. [CrossRef] [PubMed]

3. Niinomi, M.; Nakai, M.; Hieda, J. Development of new metallic alloys for biomedical applications. *Acta Biomater.* **2012**, *8*, 3888–3903. [[CrossRef](#)] [[PubMed](#)]
4. Andani, M.T.; Shayesteh Moghaddam, N.; Haberland, C.; Dean, D.; Miller, M.J.; Elahinia, M. Metals for bone implants. Part 1. Powder metallurgy and implant rendering. *Acta Biomater.* **2014**, *10*, 4058–4070. [[CrossRef](#)] [[PubMed](#)]
5. Bayraktar, H.H.; Morgan, E.F.; Niebur, G.L.; Morris, G.E.; Wong, E.K.; Keaveny, T.M. Comparison of the elastic and yield properties of human femoral trabecular and cortical bone tissue. *J. Biomech.* **2004**, *37*, 27–35. [[CrossRef](#)]
6. Moghaddam, N.S.; Andani, M.T.; Amerinatanzi, A.; Haberland, C.; Huff, S.; Miller, M.; Elahinia, M.; Dean, D. Metals for bone implants: Safety, design, and efficacy. *Biomanuf. Rev.* **2016**, *1*, 1. [[CrossRef](#)]
7. Al-Tamimi, A.A.; Fernandes, P.R.A.; Peach, C.; Cooper, G.; Diver, C.; Bartolo, P.J. Metallic bone fixation implants: A novel design approach for reducing the stress shielding phenomenon. *Virtual Phys. Prototyp.* **2017**, *12*, 141–151. [[CrossRef](#)]
8. Long, M.; Rack, H.J. Titanium alloys in total joint replacement—A materials science perspective. *Biomaterials* **1998**, *19*, 1621–1639. [[CrossRef](#)]
9. Abdel-Hady Gepreel, M.; Niinomi, M. Biocompatibility of Ti-alloys for long-term implantation. *J. Mech. Behav. Biomed. Mater.* **2013**, *20*, 407–415. [[CrossRef](#)] [[PubMed](#)]
10. Ashby, M.F. The properties of foams and lattices. *Philos. Trans. R. Soc. A Math. Phys. Eng. Sci.* **2006**, *364*, 15–30. [[CrossRef](#)] [[PubMed](#)]
11. Alvarez, K.; Nakajima, H. Metallic scaffolds for bone regeneration. *Materials* **2009**, *2*, 790. [[CrossRef](#)]
12. Heinel, P.; Müller, L.; Körner, C.; Singer, R.F.; Müller, F.A. Cellular Ti–6Al–4V structures with interconnected macro porosity for bone implants fabricated by selective electron beam melting. *Acta Biomater.* **2008**, *4*, 1536–1544. [[CrossRef](#)] [[PubMed](#)]
13. Marin, E.; Fusi, S.; Pressacco, M.; Paussa, L.; Fedrizzi, L. Characterization of cellular solids in Ti6Al4V for orthopedic implant applications: Trabecular titanium. *J. Mech. Behav. Biomed. Mater.* **2010**, *3*, 373–381. [[CrossRef](#)] [[PubMed](#)]
14. Rouwkema, J.; Rivron, N.C.; van Blitterswijk, C.A. Vascularization in tissue engineering. *Trends Biotechnol.* **2008**, *26*, 434–441. [[CrossRef](#)] [[PubMed](#)]
15. Kumar, A.; Nune, K.C.; Murr, L.E.; Misra, R.D.K. Biocompatibility and mechanical behaviour of three-dimensional scaffolds for biomedical devices: Process–structure–property paradigm. *Int. Mater. Rev.* **2016**, *61*, 20–45. [[CrossRef](#)]
16. Bramfeld, H.; Sabra, G.; Centis, V.; Vermette, P. Scaffold vascularization: A challenge for three-dimensional tissue engineering. *Curr. Med. Chem.* **2010**, *17*, 3944–3967. [[CrossRef](#)]
17. Perez, R.A.; Mestres, G. Role of pore size and morphology in musculo-skeletal tissue regeneration. *Mater. Sci. Eng. C* **2016**, *61*, 922–939. [[CrossRef](#)] [[PubMed](#)]
18. Wang, X.; Xu, S.; Zhou, S.; Xu, W.; Leary, M.; Choong, P.; Qian, M.; Brandt, M.; Xie, Y.M. Topological design and additive manufacturing of porous metals for bone scaffolds and orthopedic implants: A review. *Biomaterials* **2016**, *83*, 127–141. [[CrossRef](#)] [[PubMed](#)]
19. Sing, S.L.; An, J.; Yeong, W.Y.; Wiria, F.E. Laser and electron-beam powder-bed additive manufacturing of metallic implants: A review on processes, materials and designs. *J. Orthop. Res.* **2016**, *34*, 369–385. [[CrossRef](#)] [[PubMed](#)]
20. Li, J.P.; Habibovic, P.; van den Doel, M.; Wilson, C.E.; de Wijn, J.R.; van Blitterswijk, C.A.; de Groot, K. Bone ingrowth in porous titanium implants produced by 3D fiber deposition. *Biomaterials* **2007**, *28*, 2810–2820. [[CrossRef](#)] [[PubMed](#)]
21. Warnke, P.H.; Douglas, T.; Wollny, P.; Sherry, E.; Steiner, M.; Galonska, S.; Becker, S.T.; Springer, I.N.; Wiltfang, J.; Sivananthan, S. Rapid prototyping: Porous titanium alloy scaffolds produced by selective laser melting for bone tissue engineering. *Tissue Eng. Part C Methods* **2008**, *15*, 115–124. [[CrossRef](#)] [[PubMed](#)]
22. Van Bael, S.; Chai, Y.C.; Truscetto, S.; Moesen, M.; Kerckhofs, G.; Van Oosterwyck, H.; Kruth, J.P.; Schrooten, J. The effect of pore geometry on the in vitro biological behavior of human periosteum-derived cells seeded on selective laser-melted Ti6Al4V bone scaffolds. *Acta Biomater.* **2012**, *8*, 2824–2834. [[CrossRef](#)] [[PubMed](#)]
23. Leong, K.F.; Chua, C.K.; Sudarmadji, N.; Yeong, W.Y. Engineering functionally graded tissue engineering scaffolds. *J. Mech. Behav. Biomed. Mater.* **2008**, *1*, 140–152. [[CrossRef](#)] [[PubMed](#)]

24. Karageorgiou, V.; Kaplan, D. Porosity of 3D biomaterial scaffolds and osteogenesis. *Biomaterials* **2005**, *26*, 5474–5491. [[CrossRef](#)] [[PubMed](#)]
25. Li, G.; Wang, L.; Pan, W.; Yang, F.; Jiang, W.; Wu, X.; Kong, X.; Dai, K.; Hao, Y. In vitro and in vivo study of additive manufactured porous Ti6Al4V scaffolds for repairing bone defects. *Sci. Rep.* **2016**, *6*, 34072. [[CrossRef](#)] [[PubMed](#)]
26. Murr, L.E.; Gaytan, S.M.; Medina, F.; Martinez, E.; Martinez, J.L.; Hernandez, D.H.; Machado, B.I.; Ramirez, D.A.; Wicker, R.B. Characterization of Ti–6Al–4V open cellular foams fabricated by additive manufacturing using electron beam melting. *Mater. Sci. Eng. A* **2010**, *527*, 1861–1868. [[CrossRef](#)]
27. Murr, L.E.; Gaytan, S.M.; Medina, F.; Lopez, H.; Martinez, E.; Machado, B.I.; Hernandez, D.H.; Martinez, L.; Lopez, M.I.; Wicker, R.B.; et al. Next-generation biomedical implants using additive manufacturing of complex, cellular and functional mesh arrays. *Philos. Trans. R. Soc. Lond. A Math. Phys. Eng. Sci.* **2010**, *368*, 1999–2032. [[CrossRef](#)] [[PubMed](#)]
28. Arabnejad, S.; Burnett Johnston, R.; Pura, J.A.; Singh, B.; Tanzer, M.; Pasini, D. High-strength porous biomaterials for bone replacement: A strategy to assess the interplay between cell morphology, mechanical properties, bone ingrowth and manufacturing constraints. *Acta Biomater.* **2016**, *30*, 345–356. [[CrossRef](#)] [[PubMed](#)]
29. Wettergreen, M.A.; Bucklen, B.S.; Starly, B.; Yuksel, E.; Sun, W.; Liebschner, M.A.K. Creation of a unit block library of architectures for use in assembled scaffold engineering. *Comput.-Aided Des.* **2005**, *37*, 1141–1149. [[CrossRef](#)]
30. Parthasarathy, J.; Starly, B.; Raman, S. A design for the additive manufacture of functionally graded porous structures with tailored mechanical properties for biomedical applications. *J. Manuf. Process.* **2011**, *13*, 160–170. [[CrossRef](#)]
31. Bobbert, F.S.L.; Lietaert, K.; Eftekhari, A.A.; Pouran, B.; Ahmadi, S.M.; Weinans, H.; Zadpoor, A.A. Additively manufactured metallic porous biomaterials based on minimal surfaces: A unique combination of topological, mechanical, and mass transport properties. *Acta Biomater.* **2017**, *53*, 572–584. [[CrossRef](#)] [[PubMed](#)]
32. Giannitelli, S.M.; Accoto, D.; Trombetta, M.; Rainer, A. Current trends in the design of scaffolds for computer-aided tissue engineering. *Acta Biomater.* **2014**, *10*, 580–594. [[CrossRef](#)] [[PubMed](#)]
33. Kapfer, S.C.; Hyde, S.T.; Mecke, K.; Arns, C.H.; Schröder-Turk, G.E. Minimal surface scaffold designs for tissue engineering. *Biomaterials* **2011**, *32*, 6875–6882. [[CrossRef](#)] [[PubMed](#)]
34. Zhang, X.-Y.; Fang, G.; Zhou, J. Additively manufactured scaffolds for bone tissue engineering and the prediction of their mechanical behavior: A review. *Materials* **2017**, *10*, 50. [[CrossRef](#)] [[PubMed](#)]
35. Horn, T.J.; Harrysson, O.L.A. Overview of current additive manufacturing technologies and selected applications. *Sci. Prog.* **2012**, *95*, 255–282. [[CrossRef](#)] [[PubMed](#)]
36. Sidambe, A. Biocompatibility of advanced manufactured titanium implants—A review. *Materials* **2014**, *7*, 8168–8188. [[CrossRef](#)] [[PubMed](#)]
37. Li, S.; Zhao, S.; Hou, W.; Teng, C.; Hao, Y.; Li, Y.; Yang, R.; Misra, R.D.K. Functionally graded Ti-6Al-4V meshes with high strength and energy absorption. *Adv. Eng. Mater.* **2016**, *18*, 34–38. [[CrossRef](#)]
38. Nune, K.; Kumar, A.; Misra, R.; Li, S.; Hao, Y.; Yang, R. Osteoblast functions in functionally graded Ti-6Al-4V mesh structures. *J. Biomater. Appl.* **2016**, *30*, 1182–1204. [[CrossRef](#)] [[PubMed](#)]
39. Nune, K.C.; Kumar, A.; Misra, R.D.K.; Li, S.J.; Hao, Y.L.; Yang, R. Functional response of osteoblasts in functionally gradient titanium alloy mesh arrays processed by 3D additive manufacturing. *Colloids Surf. B Biointerfaces* **2017**, *150*, 78–88. [[CrossRef](#)] [[PubMed](#)]
40. Surmeneva, M.A.; Surmenev, R.A.; Chudinova, E.A.; Koptioug, A.; Tkachev, M.S.; Gorodzha, S.N.; Rännar, L.-E. Fabrication of multiple-layered gradient cellular metal scaffold via electron beam melting for segmental bone reconstruction. *Mater. Des.* **2017**, *133*, 195–204. [[CrossRef](#)]
41. Limmahakhun, S.; Oloyede, A.; Sithiseripratip, K.; Xiao, Y.; Yan, C. Stiffness and strength tailoring of cobalt chromium graded cellular structures for stress-shielding reduction. *Mater. Des.* **2017**, *114*, 633–641. [[CrossRef](#)]
42. Van Grunsven, W.; Hernandez-Nava, E.; Reilly, G.; Goodall, R. Fabrication and mechanical characterisation of titanium lattices with graded porosity. *Metals* **2014**, *4*, 401–409. [[CrossRef](#)]

43. Han, C.; Li, Y.; Wang, Q.; Wen, S.; Wei, Q.; Yan, C.; Hao, L.; Liu, J.; Shi, Y. Continuous functionally graded porous titanium scaffolds manufactured by selective laser melting for bone implants. *J. Mech. Behav. Biomed. Mater.* **2018**, *80*, 119–127. [[CrossRef](#)] [[PubMed](#)]
44. Maskery, I.; Aboulkhair, N.T.; Aremu, A.O.; Tuck, C.J.; Ashcroft, I.A.; Wildman, R.D.; Hague, R.J.M. A mechanical property evaluation of graded density Al-Si10-Mg lattice structures manufactured by selective laser melting. *Mater. Sci. Eng. A* **2016**, *670*, 264–274. [[CrossRef](#)]
45. Choy, S.Y.; Sun, C.-N.; Leong, K.F.; Wei, J. Compressive properties of functionally graded lattice structures manufactured by selective laser melting. *Mater. Des.* **2017**, *131*, 112–120. [[CrossRef](#)]
46. Yap, C.Y.; Chua, C.K.; Dong, Z.L.; Liu, Z.H.; Zhang, D.Q.; Loh, L.E.; Sing, S.L. Review of selective laser melting: Materials and applications. *Appl. Phys. Rev.* **2015**, *2*, 041101. [[CrossRef](#)]
47. Pyka, G.; Kerckhofs, G.; Papantoniou, I.; Speirs, M.; Schrooten, J.; Wevers, M. Surface Roughness and Morphology Customization of Additive Manufactured Open Porous Ti6Al4V Structures. *Materials* **2013**, *6*, 4737–4757. [[CrossRef](#)] [[PubMed](#)]
48. Wang, D.; Yang, Y.; Liu, R.; Xiao, D.; Sun, J. Study on the designing rules and processability of porous structure based on selective laser melting (SLM). *J. Mater. Process. Technol.* **2013**, *213*, 1734–1742. [[CrossRef](#)]
49. Rashed, M.G.; Ashraf, M.; Mines, R.A.W.; Hazell, P.J. Metallic microlattice materials: A current state of the art on manufacturing, mechanical properties and applications. *Mater. Des.* **2016**, *95*, 518–533. [[CrossRef](#)]
50. Nemat-Nasser, S.; Hori, M. *Micromechanics: Overall Properties of Heterogeneous Materials*, 2nd ed.; Elsevier: Amsterdam, The Netherlands, 1998.
51. Mazur, M.; Leary, M.; Sun, S.; Vcelka, M.; Shidid, D.; Brandt, M. Deformation and failure behaviour of Ti-6Al-4V lattice structures manufactured by selective laser melting (SLM). *Int. J. Adv. Manuf. Technol.* **2016**, *84*, 1391–1411. [[CrossRef](#)]
52. Smith, M.; Guan, Z.; Cantwell, W.J. Finite element modelling of the compressive response of lattice structures manufactured using the selective laser melting technique. *Int. J. Mech. Sci.* **2013**, *67*, 28–41. [[CrossRef](#)]
53. Gorny, B.; Niendorf, T.; Lackmann, J.; Thoene, M.; Troester, T.; Maier, H.J. In situ characterization of the deformation and failure behavior of non-stochastic porous structures processed by selective laser melting. *Mater. Sci. Eng. A* **2011**, *528*, 7962–7967. [[CrossRef](#)]
54. Cansizoglu, O.; Harrysson, O.; Cormier, D.; West, H.; Mahale, T. Properties of Ti-6Al-4V non-stochastic lattice structures fabricated via electron beam melting. *Mater. Sci. Eng. A* **2008**, *492*, 468–474. [[CrossRef](#)]
55. Zhao, S.; Li, S.J.; Hou, W.T.; Hao, Y.L.; Yang, R.; Misra, R.D.K. The influence of cell morphology on the compressive fatigue behavior of Ti-6Al-4V meshes fabricated by electron beam melting. *J. Mech. Behav. Biomed. Mater.* **2016**, *59*, 251–264. [[CrossRef](#)] [[PubMed](#)]
56. Li, S.J.; Xu, Q.S.; Wang, Z.; Hou, W.T.; Hao, Y.L.; Yang, R.; Murr, L.E. Influence of cell shape on mechanical properties of Ti-6Al-4V meshes fabricated by electron beam melting method. *Acta Biomater.* **2014**, *10*, 4537–4547. [[CrossRef](#)] [[PubMed](#)]
57. Van Bael, S.; Kerckhofs, G.; Moesen, M.; Pyka, G.; Schrooten, J.; Kruth, J.P. Micro-CT-based improvement of geometrical and mechanical controllability of selective laser melted Ti6Al4V porous structures. *Mater. Sci. Eng. A* **2011**, *528*, 7423–7431. [[CrossRef](#)]
58. Parthasarathy, J.; Starly, B.; Raman, S.; Christensen, A. Mechanical evaluation of porous titanium (Ti6Al4V) structures with electron beam melting (EBM). *J. Mech. Behav. Biomed. Mater.* **2010**, *3*, 249–259. [[CrossRef](#)] [[PubMed](#)]
59. Linde, F.; Hvid, I. The effect of constraint on the mechanical behaviour of trabecular bone specimens. *J. Biomech.* **1989**, *22*, 485–490. [[CrossRef](#)]
60. Morgan, E.F.; Keaveny, T.M. Dependence of yield strain of human trabecular bone on anatomic site. *J. Biomech.* **2001**, *34*, 569–577. [[CrossRef](#)]
61. Cullinane, D.M.; Einhorn, T.A. Biomechanics of bone. In *Principles of Bone Biology*, 2nd ed.; Raisz, L.G., Rodan, G.A., Eds.; Academic Press: San Diego, CA, USA, 2002.
62. Murphy, C.M.; Haugh, M.G.; O'Brien, F.J. The effect of mean pore size on cell attachment, proliferation and migration in collagen-glycosaminoglycan scaffolds for bone tissue engineering. *Biomaterials* **2010**, *31*, 461–466. [[CrossRef](#)] [[PubMed](#)]
63. Simske, S.J.; Ayers, R.A.; Bateman, T.A. Porous materials for bone engineering. *Mater. Sci. Forum* **1997**, *250*, 151–182. [[CrossRef](#)]



64. Dumas, M.; Terriault, P.; Brailovski, V. Modelling and characterization of a porosity graded lattice structure for additively manufactured biomaterials. *Mater. Des.* **2017**, *121*, 383–392. [[CrossRef](#)]
65. Sudarmadji, N.; Tan, J.Y.; Leong, K.F.; Chua, C.K.; Loh, Y.T. Investigation of the mechanical properties and porosity relationships in selective laser-sintered polyhedral for functionally graded scaffolds. *Acta Biomater.* **2011**, *7*, 530–537. [[CrossRef](#)] [[PubMed](#)]
66. De Wild, M.; Zimmermann, S.; Rüegg, J.; Schumacher, R.; Fleischmann, T.; Ghayor, C.; Weber, F.E. Influence of microarchitecture on osteoconduction and mechanics of porous titanium scaffolds generated by selective laser melting. *3D Print. Addit. Manuf.* **2016**, *3*, 142–151. [[CrossRef](#)]
67. Taniguchi, N.; Fujibayashi, S.; Takemoto, M.; Sasaki, K.; Otsuki, B.; Nakamura, T.; Matsushita, T.; Kokubo, T.; Matsuda, S. Effect of pore size on bone ingrowth into porous titanium implants fabricated by additive manufacturing: An in vivo experiment. *Mater. Sci. Eng. C* **2016**, *59*, 690–701. [[CrossRef](#)] [[PubMed](#)]
68. Fukuda, A.; Takemoto, M.; Saito, T.; Fujibayashi, S.; Neo, M.; Pattanayak, D.K.; Matsushita, T.; Sasaki, K.; Nishida, N.; Kokubo, T.; et al. Osteoinduction of porous Ti implants with a channel structure fabricated by selective laser melting. *Acta Biomater.* **2011**, *7*, 2327–2336. [[CrossRef](#)] [[PubMed](#)]
69. Khan, W.S.; Rayan, F.; Dhinsa, B.S.; Marsh, D. An osteoconductive, osteoinductive, and osteogenic tissue-engineered product for trauma and orthopedic surgery: How far are we? *Stem Cells Int.* **2012**, *2012*, 236231. [[CrossRef](#)] [[PubMed](#)]
70. Van der Stok, J.; Van der Jagt, O.P.; Amin Yavari, S.; De Haas, M.F.P.; Waarsing, J.H.; Jahr, H.; Van Lieshout, E.M.M.; Patka, P.; Verhaar, J.A.N.; Zadpoor, A.A.; et al. Selective laser melting-produced porous titanium scaffolds regenerate bone in critical size cortical bone defects. *J. Orthop. Res.* **2013**, *31*, 792–799. [[CrossRef](#)] [[PubMed](#)]
71. Hollister, S.J. Porous scaffold design for tissue engineering. *Nat. Mater.* **2006**, *5*, 590. [[CrossRef](#)]



© 2018 by the authors. Licensee MDPI, Basel, Switzerland. This article is an open access article distributed under the terms and conditions of the Creative Commons Attribution (CC BY) license (<http://creativecommons.org/licenses/by/4.0/>).

#### 4.4. Supplementary Data

The supplementary data file was submitted and published together with the manuscript and includes extra images and graphs to represent the data presented in the paper in other forms. Figure 4. 7 shows the mechanical properties of the structures in bar graphs to present statistical difference between the structures. The real values of compressive mechanical properties are given in the manuscript (Table 2). Figure 4. 7 shows that there is no significant difference in elastic modulus of Uniform 0.6 and gradient BCC structures.

##### Mechanical properties of the Scaffolds

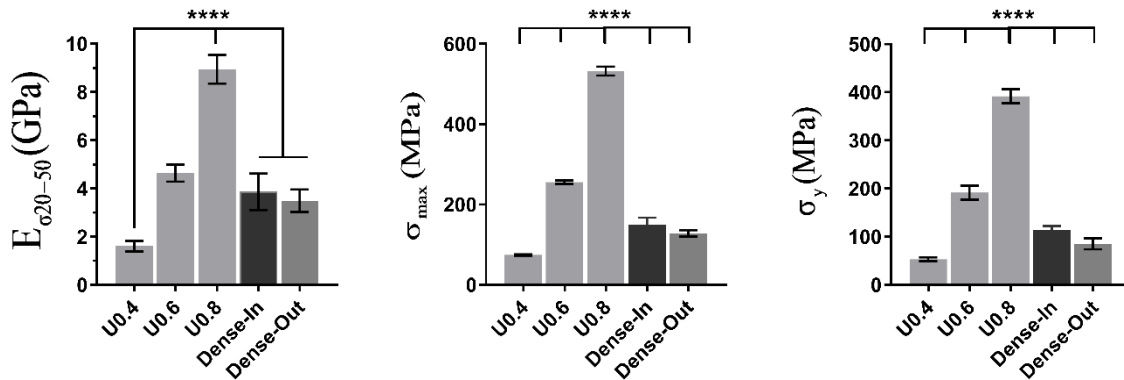


Figure 4. 7 Compressive mechanical properties of uniform and gradient BCC structures. Data were presented as mean  $\pm$  SD (n=5). (\*\*\*\*  $p < 0.0001$  when compared using ANOVA Tukey-Kramer Post-Hoc) (Supplementary Figure 1).

##### Cell Morphology and Distribution along the Scaffolds

SEM images taken from the top, middle and bottom surfaces of all of the structures supported the findings about the cell penetration profiles presented in Figure 10 of the manuscript. However, as the SEM images needed to be presented in larger size for better visibility of the attached cells, these SEM images were found to be more suitable to be included in Supplementary data. These images shows that cell penetration is deeper in U0.4 and Dense-In scaffolds, supporting the idea that scaffolds with thinner struts in their outer surface allow higher cell migration throughout the scaffold.

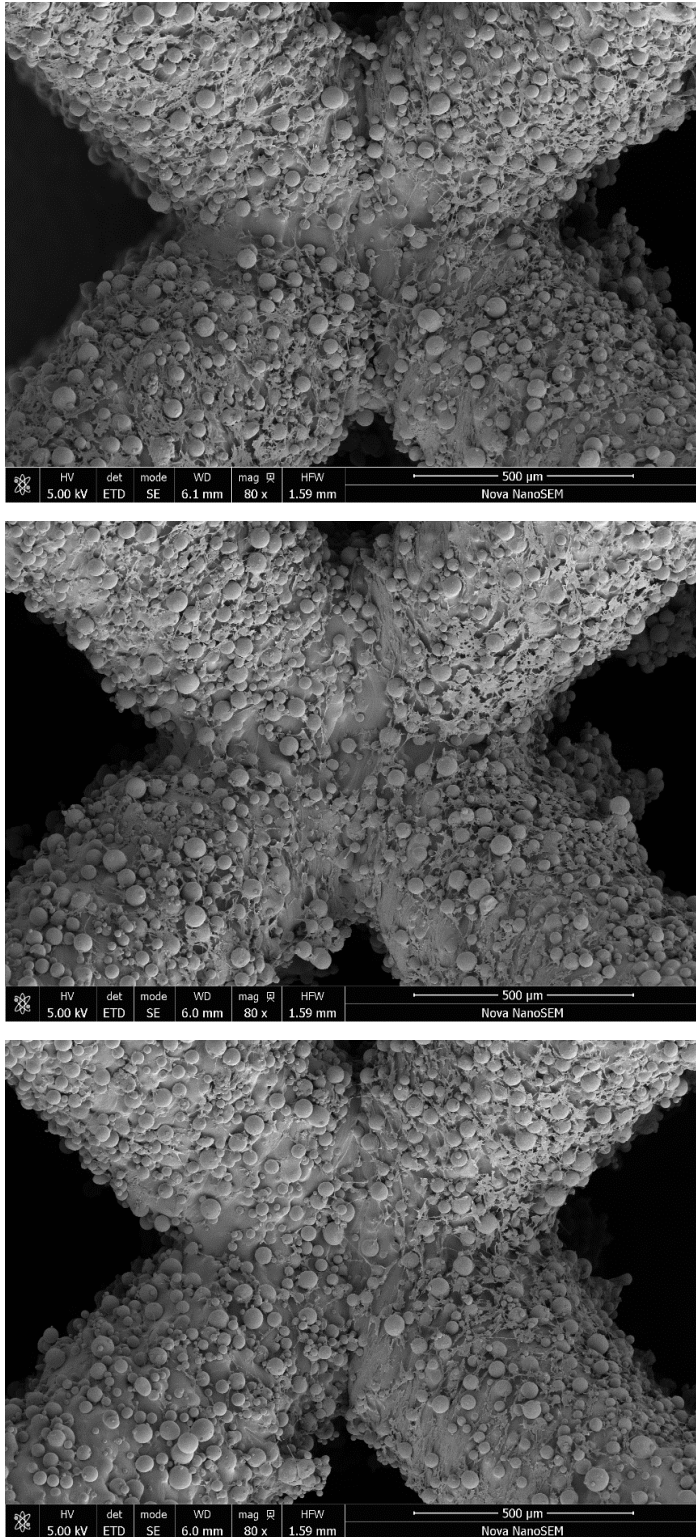


Figure 4. 8 SEM images of U0.4 scaffold incubated with MC3T3-E1 cells for 7 days. Images from top to bottom refers to respectively the top, middle and bottom surface of the scaffold along the vertical plane. Sells were seeded from the top surface. Cells were observed in all surfaces (Supplementary Figure 2).



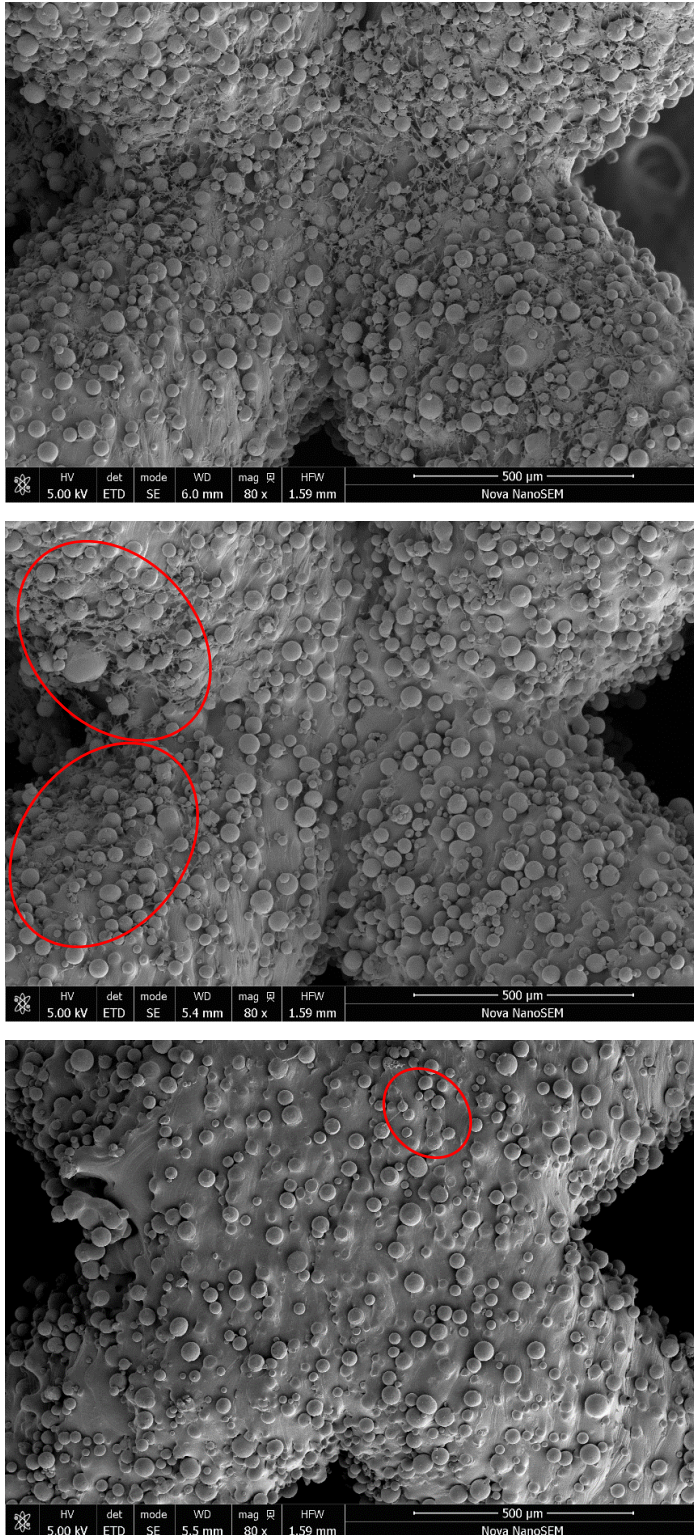


Figure 4. 9 SEM images of U0.6 scaffold incubated with MC3T3-E1 cells for 7 days. Images from top to bottom refers to respectively the top, middle and bottom surface of the scaffold along the vertical plane. Sells were seeded from the top surface. The number of cells decreased towards to the bottom surface. Highlights were used to point out cells when they are not visible (Supplementary Figure 3).

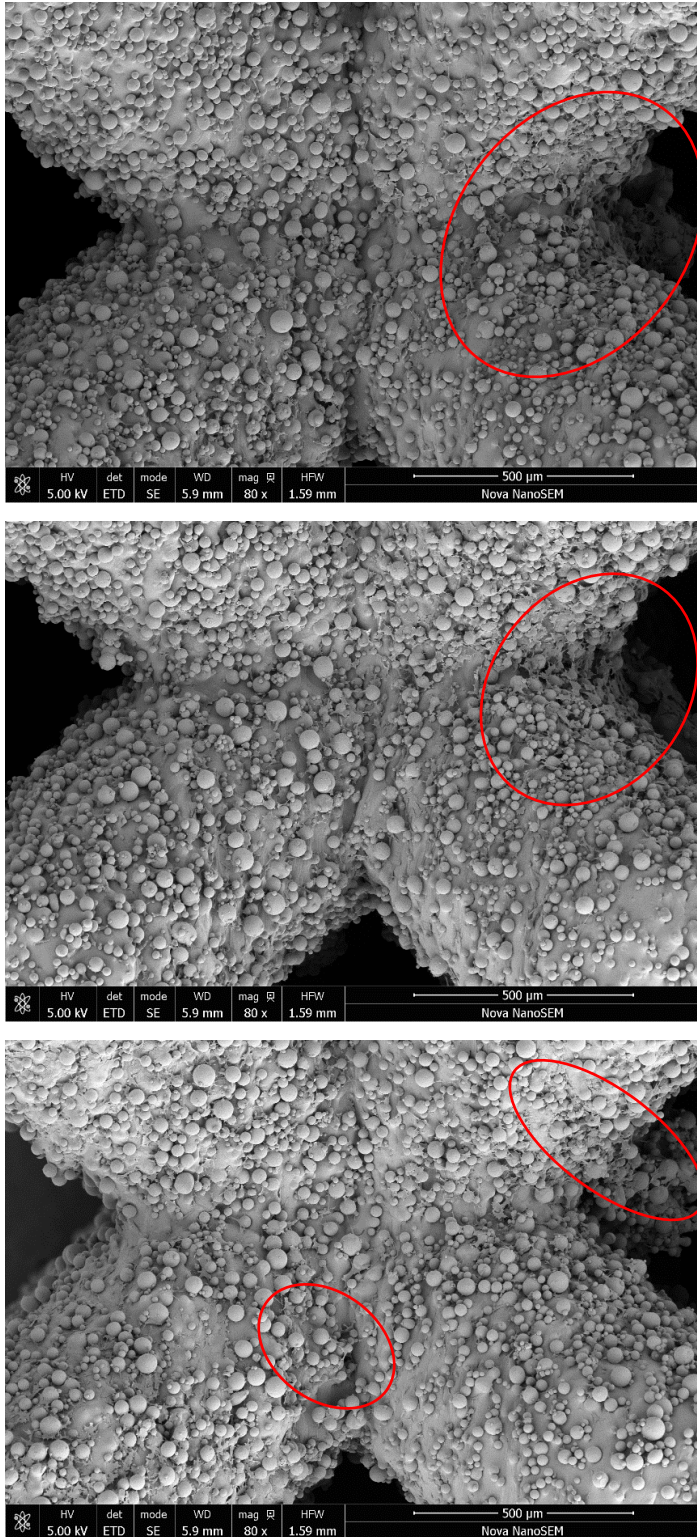


Figure 4. 10 SEM images of U0.8 scaffold incubated with MC3T3-E1 cells for 7 days. Images from top to bottom refers to respectively the top, middle and bottom surface of the scaffold along the vertical plane. Sells were seeded from the top surface. The cell distribution was non-uniform in all surfaces and there were less number of observed cells throughout the scaffold (Supplementary Figure 4).



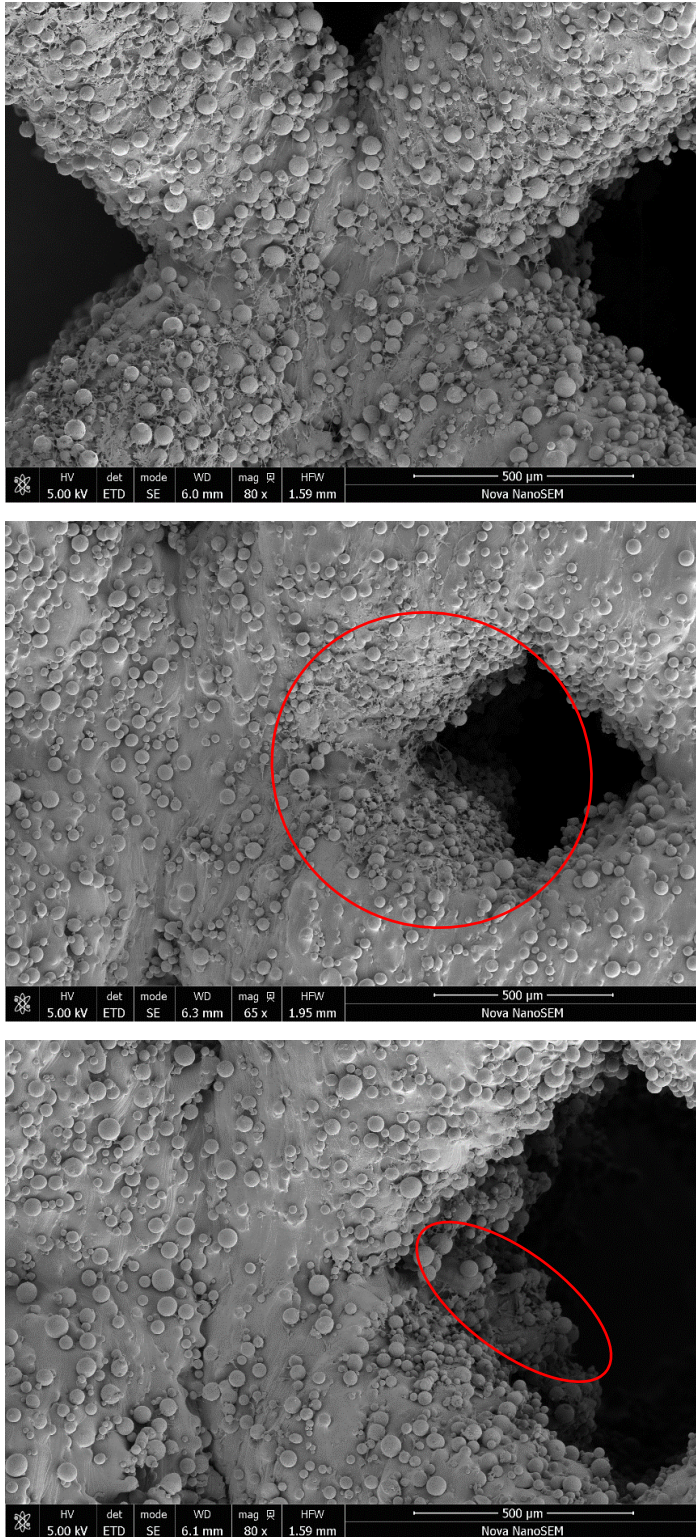


Figure 4. 11 SEM images of Dense-In scaffold incubated with MC3T3-E1 cells for 7 days. Images from top to bottom refers to respectively the top, middle and bottom surface of the scaffold along the vertical plane. Cells were seeded from the top surface. Cells were observed in all surfaces, but the distribution of cells was non-uniform on the bottom surface (Supplementary Figure 5).

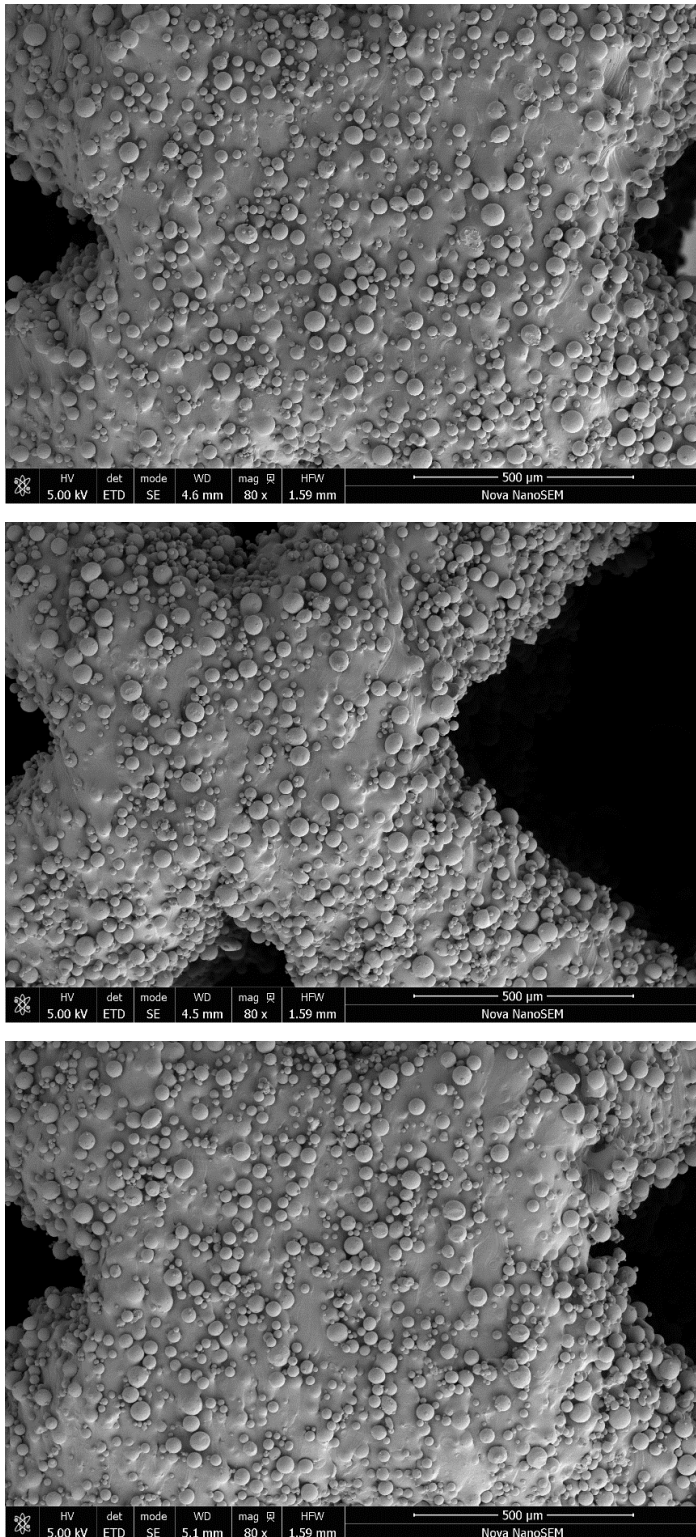


Figure 4. 12 SEM images of Dense-Out scaffolds incubated with MC3T3-E1 cells for 7 days. Images from top to bottom refers to respectively the top, middle and bottom surface of the scaffold along the vertical plane. Cells were seeded from the top surface. There were no visible cells in the scanned regions (Supplementary Figure 6).



## 4.5. Conclusion of the Chapter

In this work, the effect of gradient porous structures on both biological response and mechanical behaviour was investigated. The gradient designs were termed “Dense-In” and “Dense-Out”. Both designs had gradually changed pore sizes from 940  $\mu\text{m}$  to 1330  $\mu\text{m}$ . The mechanical properties, stiffness and strength of these scaffolds were found to be comparable to the properties of cortical bone. The rule of mixture was proposed to calculate the mechanical properties of gradient designs based on an assumption that gradient structures are composites of uniform layers of the same diameter struts. The deformation mechanism of gradient structures was by sequential layer collapse, whereas uniform BCC scaffolds failed by diagonal shear collapse.

*In-vitro* tests with MC3T3 preosteoblast cells showed that the degree of cell attachment was similar for all scaffolds, however cell proliferation and colonization were significantly different. Scaffolds with a thin strut diameter on the periphery (U0.4 and Dense-In) allowed cells to populate throughout the scaffold whereas those with a thicker outer strut (U0.6, U0.8 and Dense-Out) did not allow cells to migrate to the bottom surface, suggesting that cells were entrapped at the smaller pore size region (top surface).

Combined results of biological and mechanical studies suggest that optimal gradient designs for bone implant use should have decreasing pore size towards their centre, which can provide the required strength and stiffness, while simultaneously promoting cell colonization throughout the whole scaffold. This study also demonstrates the importance of assessing the biological and mechanical performance of the bone scaffolds simultaneously.

In summary, this work provides important insights into the design and manufacturing of functionally gradient porous bone scaffolds. Following this work several new studies adopted gradient designs with continuous and gradual change. For example, Zhang et al. [211, 212] investigated the effect of functionally graded structure on permeability and mechanical properties of the scaffolds for bone tissue engineering. Functionally graded diamond structures exhibited a low density (1.9  $\text{g/cm}^3$ ), a moderate Young’s modulus (10.44 GPa), a high yield stress (170.6 MPa), a high maximum stress (201 MPa) and favourable ductility, being superior

to the uniform diamond structures in comprehensive mechanical properties [212]. Functionally gradient structures were also found to show comparable permeability values to those of human proximal tibia [211].

Mahmoud et al. [213] investigated the manufacturability of porosity-graded triply periodic minimal surfaces (TPMS) lattice structures and looked at different laser scanning strategies. They showed that the effect of different scanning strategies on the morphological quality relies highly on the design volume fraction of the unit cell design. Liu et al. [214] manufactured gradient scaffolds based on the gyroid and diamond unit cells and suggested that with gradient designs, the porous surface area can be altered without sacrificing the relative density and mechanical properties.

Overall, it can be concluded that the functionally gradient structures with continues gradient change are promising candidates for bone scaffolds. Future work in this field can be extended to investigate *in-vivo* performance of the gradient scaffolds to assess their osseointegration and mechanical performance.

# Chapter 5. Single Point Exposure Scanning Strategy for SLM

## 5.1. Introduction

As presented in Chapter 1, lattice structures offer unique benefits to a part, including high stiffness-to-weight ratio, superior energy absorption capability, open porous network for tissue growth, enhanced thermal management and many more. AM technologies have made it possible to fabricate the complex lattice scaffolds with high-performance materials, *i.e.* Ti6Al4V. Most of the research literature on additive manufacturing of lattice structures have focused on topology optimisation, porosity and mechanical properties [133, 159, 215-217]. Static mechanical and fatigue behaviour characterisation are among the most popular studies due to their importance for biomedical and aerospace products. These studies on the lattice structures, as well as Chapter 4 and 6 of this thesis, show that unit cell shape, size and porosity distribution are important design parameters controlling the mechanical response of lattice properties. However, other parameters such as manufacturability, quality and microstructure are as significant as topology and density in controlling the mechanical properties. The limited understanding between manufacturing process parameters, defects and microstructure of lattice structures motivated us to study SLM process optimisation for lattice structures and formed the basis of this chapter.

In literature, the most common utilized scanning strategy for SLM is contour and hatching [60, 218, 219], in which the laser beam scans a pre-defined contour and hatches the area inside the contour to achieve a given geometry based on the 2D slice. Contour and hatching strategy is proven to work well for fabricating solid parts and lattice structures. However, there are several problems observed with this scanning strategy. The laser scan may jump and bypass some hatching scans randomly, which might result in lack of fusion of the powder and pore formation, and therefore lower part quality. Furthermore, contour and hatching strategy can be computationally costly for large builds with lattice structures and can cause delays in the file preparation stage [76].

Alternative strategies such as the single point exposure strategy are largely unexplored in the literature. A small number of studies [72, 74-76] reported the use of the single point exposure strategy for fabrication of lattice structures. While these studies have focused on the relationship between process parameters and mechanical properties, a better understanding of

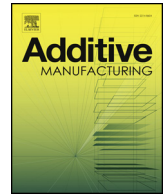
some fundamental phenomena such as laser-power interaction, process parameter-microstructure relationship, and defect formation, is lacking for the SLM of porous structures with single point exposure strategy. Therefore, this study aims to investigate the influence of single point exposure strategy on the microstructure formation in Ti6Al4V struts fabricated by SLM. The work focused on two major points:

- Understanding of laser-powder interaction through a series of >50 sets of processing parameters for the SLM fabrication of vertical struts made of Ti6Al4V, and
- The effects of (partial) re-melting and latent heat on hardness and developed microstructure. Re-melting occurs at the strut junctions during SLM and strut junctions are critical in controlling the mechanical properties of the scaffolds.

The presented work was partially performed at Delft University of Technology, Delft, Netherlands. Realizer SLM125 was utilised in a point exposure mode to produce vertical struts. The result of this study is published in *Additive Manufacturing* journal [220]. Some of the preliminary work which was not included in the manuscript is presented in Chapter 5.4.2.

### 5.3. Research Paper





## Full Length Article

# Novel microstructural features of selective laser melted lattice struts fabricated with single point exposure scanning

E. Onal<sup>a,\*</sup>, A.E. Medvedev<sup>a</sup>, M.A. Leeftang<sup>b</sup>, A. Molotnikov<sup>a,\*</sup>, A.A. Zadpoor<sup>b,\*</sup>

<sup>a</sup> Department of Materials Science and Engineering, Monash University, Clayton, VIC, 3800, Australia

<sup>b</sup> Department of Biomechanical Engineering, Delft University of Technology, Delft, the Netherlands

## ARTICLE INFO

## Keywords:

Selective laser melting  
Microstructure  
Texture  
High performance titanium alloys  
Lattice structure

## ABSTRACT

Single point exposure scanning strategy is a largely unexplored selective laser melting (SLM) technique to fabricate lattice structures without an STL file. In this work, we used a series of > 50 sets of processing parameters to systematically study the SLM fabrication of vertical struts made of Ti-6Al-4 V. In addition, the effects of (partial) re-melting and latent heat on hardness and developed microstructure were investigated. We demonstrate that the strut dimensions could be controlled by the processing parameters with higher energy inputs, resulting in larger strut diameters up to a saturation point (i.e. 520  $\mu\text{m}$  corresponding to 0.5 J energy). The single point exposure method yielded keyhole shaped pores that were up to 4 times smaller than those observed, typically when the hatching and contour technique is used. Transmission electron microscopy (TEM) images revealed ultrafine ( $\sim 200\text{--}300\text{ nm}$ ) and homogeneous microstructure in the double-melted specimens as compared to the classic microstructure of SLM Ti6Al4V observed in the single melted strut: hierarchical  $\alpha'$ -laths with varying sizes (0.1–1  $\mu\text{m}$ ). Finally, we investigated the texture and identified the retained  $\beta$  phase, which enabled us to check the Burgers orientation relationship (BOR) between  $\alpha'$  and  $\beta$  phases. This is the first attempt to systematically study the microstructural features resulting from the single point exposure SLM technique for lattice structures made from Ti6Al4V, and exhibits the processability window that could be used to engineer the microstructure of such structures.

## 1. Introduction

The rational design principles [1,2] and advanced additive manufacturing (AM) techniques [3–5] have enabled the emergence of a new class of designer materials [6] where complex topological designs at smaller scales are used to create unusual properties at larger scales. These types of designer materials are sometimes collectively referred to as metamaterials and usually target very specific values of the mechanical [7–10], acoustic [11–13], or biomedical [14–17] properties. Materials with negative values of mechanical and physical properties (i.e. negative Poisson's ratio [18,19] or negative stiffness [20–22]), ultralight materials exhibiting ultrastiff behavior [23], bone-mimicking mechanical and material properties [24,25], and programmable mechanical behavior [26,27] are all examples of such rare properties and, thus, functionalities.

The topological design of a large number of mechanical metamaterials, acoustic metamaterials, and meta-biomaterials are based on lattice structures. It is thus crucial to be able to additively manufacture complex lattice structures from high-performance materials such as

high strength metallic alloys. The fact that the porous structure of lattice structures translates into significantly reduced elastic modulus [28–31] and fatigue life [32–36] highlights the importance of an effective and defect-free AM process. Many groups are therefore intensively researching AM of metallic lattices made using a variety of AM technologies, including powder bed fusion techniques such as selective laser melting [37–42] and electron beam melting [3,34,43–45]. One of the most widely used materials is the high strength titanium alloy Ti-6Al-4 V, which has many applications in the aerospace and biomedical industries due to its exceptional properties, such as biocompatibility, corrosion resistance, and excellent fatigue behavior [46]. In this study, we will focus on the lattice structures made from Ti-6Al-4 V using the selective laser melting (SLM) process.

SLM processes could be categorized into two major categories depending on the type of laser source and scanning strategy. While the first category (contour and hatching) is based on continuous laser scanning of a pre-defined contour and hatching the area inside the contour [47–50], the second category of SLM processes works on the basis of pulsed exposure to the energy source and is sometimes called

\* Corresponding authors.

E-mail addresses: [ezgi.onal@monash.edu](mailto:ezgi.onal@monash.edu) (E. Onal), [andrey.molotnikov@monash.edu](mailto:andrey.molotnikov@monash.edu) (A. Molotnikov), [a.a.zadpoor@tudelft.nl](mailto:a.a.zadpoor@tudelft.nl) (A.A. Zadpoor).

<https://doi.org/10.1016/j.addma.2019.100785>

Received 29 December 2018; Received in revised form 17 June 2019; Accepted 6 July 2019

Available online 08 July 2019

2214-8604/© 2019 Elsevier B.V. All rights reserved.

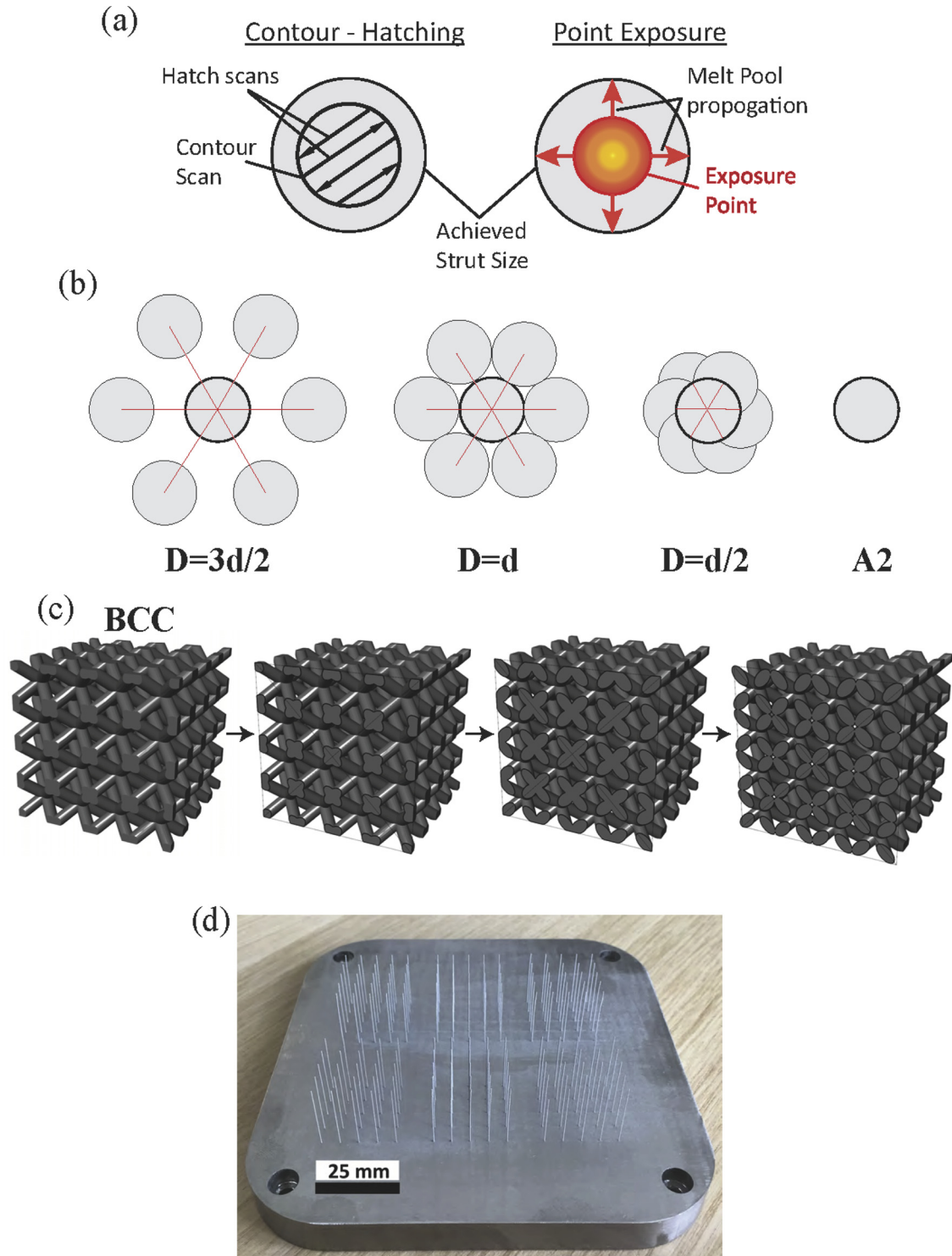


**Fig. 1.** (a) Laser scanning strategies for the SLM process: Contour hatching and point exposure; (b) A schematic view of the struts in a circular arrangement; (c) consecutive slices of a BCC scaffold show how individual struts come closer and eventually some overlapped areas form; (d) The fabricated single struts on the build plate.

the single point exposure method (Fig. 1a). There is evidence suggesting that for both of those categories the density, microstructure, and mechanical properties of the resulting metallic parts are dependent on the laser processing parameters and build direction [41,51–54]. However, the vast majority of the studies investigating the microstructure and mechanical properties of SLM Ti-6Al-4 V [49,55] are focused on the first category. While bulk parts made by the first category of SLM techniques have received the most attention [46,56], there are also

some studies [47,53,57,58] on the lattice structures made by the contour and hatching technique.

The relationship between the processing parameters and the resulting density, microstructure, and mechanical properties of the lattice structures made with the single point exposure technique are mostly unexplored, save for a handful of studies [59–62]. This lack of understanding is a major limiting factor hindering the practical applications of the single point exposure technique for fabrication of lattice

structures, despite the inherent advantages of low computational cost and increased productivity. Most importantly, it is relatively straightforward to establish a direct relationship between the parameters of the SLM process on the one hand and the spatial distribution of energy within the individual struts of the lattice structure on the other. Such direct relationships open up the possibility of producing lattice structures with arbitrarily complex topological designs. For example, the complex geometry of penta-mode mechanical metamaterials was recently realized for the first time through careful planning of the spatial distribution of energy enabled by the single point exposure method [63].

Here, we take a systematic approach to study the effects of the processing parameters in the single point exposure SLM process on the geometry, density, microstructure, and hardness of the resulting materials. Separate studies analyzing the fatigue performance and strength are out of the scope of this work and will be presented in a follow-up publication. We fabricate single struts with different laser powers and exposure times to precisely control the temperature profiles, while isolating the effects of involved parameters as much as possible. A number of strut arrays are also used to study the effects of (partial) re-melting and latent heat on the morphology and microstructure of the resulting materials.

## 2. Materials and methods

### 2.1. Study design

We designed a matrix of 50 conditions with exposure times ranging from 250  $\mu$ s to 1150  $\mu$ s in 100  $\mu$ s increments and laser powers of 88 W to 144 W in 12 W increments (Table 1). Additional struts were also printed at higher laser powers and exposure times (Table 1) to explore the boundaries of the single point exposure technique.

In addition to single struts, and to simulate the effects of strut proximity, latent heat, and (partial) re-melting, three conditions (96W-1150 $\mu$ s, 128W-750 $\mu$ s and 144 W-1150 $\mu$ s) representing low, medium, and high energy inputs were selected from Table 1 to fabricate arrays of struts ( $d$  = strut diameter) with different distances between them in a circular arrangement ( $D$  = distance between the center of the middle strut and the center of the surrounding struts) (Fig. 1b). In the case of  $D = 3d/2$ , the center strut is surrounded by six other single struts with a distance of  $3d/2$ . When  $D = d$ , the surrounding struts are touching each other and the center strut. With  $D = d/2$ , the surrounding struts and the center strut have an overlapping length of  $d/2$ . In addition to the three conditions mentioned above, the laser beam was fired twice to achieve double-melted struts (called A2 struts). Double-melted struts represent the neighboring struts in lattice structures that overlap with each other in some areas and are therefore double-melted (e.g., strut junctions)

**Table 1**

The laser power and exposure time values used to manufacture struts by single point exposure strategy.

Exposure time ( $\mu$ s)	Laser power (W)										
	88	96	112	128	144	160	176	224	272	304	384
250	*	*	*	*	*						
350	*	*	*	*	*						
450	*	*	*	*	*						
550	*	*	*	*	*						
650	*	*	*	*	*						
750	*	*	*	*	*						
850	*	*	*	*	*						
950	*	*	*	*	*						
1050	*	*	*	*	*						
1150	*	*	*	*	*						
2500					*			*	*	*	*
2950					*	*	*				

(Fig. 1c).

### 2.2. Materials and additive manufacture (AM) method

All specimens were fabricated on an SLM 125 machine (Realizer GmbH, Borcheln, Germany) equipped with a YLM-400-AC Ytterbium fiber laser (IPG Photonics Corporation, Oxford, USA) (max. 400 W,  $\lambda = 1070 \pm 10$  nm) using Ti-6Al-4 V grade 23 powder supplied by AP & C (AP&C Advanced Powders and Coatings Inc., Boisbriand, Canada) with a particle size ranging from 10 to 40  $\mu$ m. The build chamber was vacuumed and filled with argon gas to maintain the oxygen level < 0.2% while manufacturing the specimens. The length of the struts was 15 mm, while their diameter was controlled by the energy input (Fig. 1d). The energy input (J) was defined by the product of the laser power (W) and exposure time (s).

### 2.3. Morphological characterization

The single struts were cleaned in an ultrasonic bath with ethanol and were then imaged with a scanning electron microscope (SEM) (FEI Nova NanoEM, Eindhoven, The Netherlands) to measure their diameters. A total of 10 measurements were taken along the length of each strut to find the mean and standard deviation (SD) of their diameters (Fig. 2a).

### 2.4. Hardness

Hardness measurements were performed following the HV 0.5 protocol (DuraScan-70, Struers, Maassluis, Netherlands) using polished samples. At least five measurements were taken for each sample along the build direction, which were used to find the mean and SD.

### 2.5. Micro-computed tomography (micro-CT)

A micro-CT scanner (Zeiss Xradia 520 Versa, Zeiss, Oberkochen, Germany) was used to measure the relative density of the strut and to visualize the porosity. A single strut fabricated with 144 W and 1150  $\mu$ s was scanned over a height of 3.7 mm with a voxel size of  $1.0 \times 1.0 \times 1.0 \mu\text{m}^3$ . The following scanning parameters were used: 60 kV/84  $\mu$ A source power, 1  $\mu\text{m}^3$  voxel size, 15 mm distance of the source from the sample, 35.5 mm distance of the detector from the sample. CT images were reconstructed to create a 3D model of the strut, which was then further analyzed using the software tools Mimics and 3-Matic (Materialise, Leuven, Belgium). The 3D model was segmented out using an automatic segmentation function available in Mimics. The inner pores were then segmented using the segmentation and Boolean functions available in the same software. The volumes of the part,  $V_{\text{part}}$ , and the inner pores,  $V_{\text{pores}}$ , were taken from the software to calculate the approximate porosity of the struts using  $V_{\text{pores}}/(V_{\text{pores}} + V_{\text{part}}) \times 100\%$ . Moreover, a digital microscope (Keyence VHX-100, Itasca, IL, U.S.A.) was used to scan the surface of the polished struts along the build direction to observe the internal porosity of the struts. In the case of extremely low masses (i.e., < 0.01 g), measuring porosity according to the Archimedes principle requires special means, which were not available.

### 2.6. Optical microscopy (OM)

The microstructure of the single struts, the middle struts in the circular arrangements, and the double-melted struts were observed under an optical microscope (Olympus GX51, Olympus Corp., Tokyo, Japan). The struts were ground along the build direction and were polished with 3  $\mu$ m, 1  $\mu$ m diamond solutions and with oxide polishing suspension. Finally, the struts were etched with the Kroll's etchant for 30 s to reveal their microstructure.

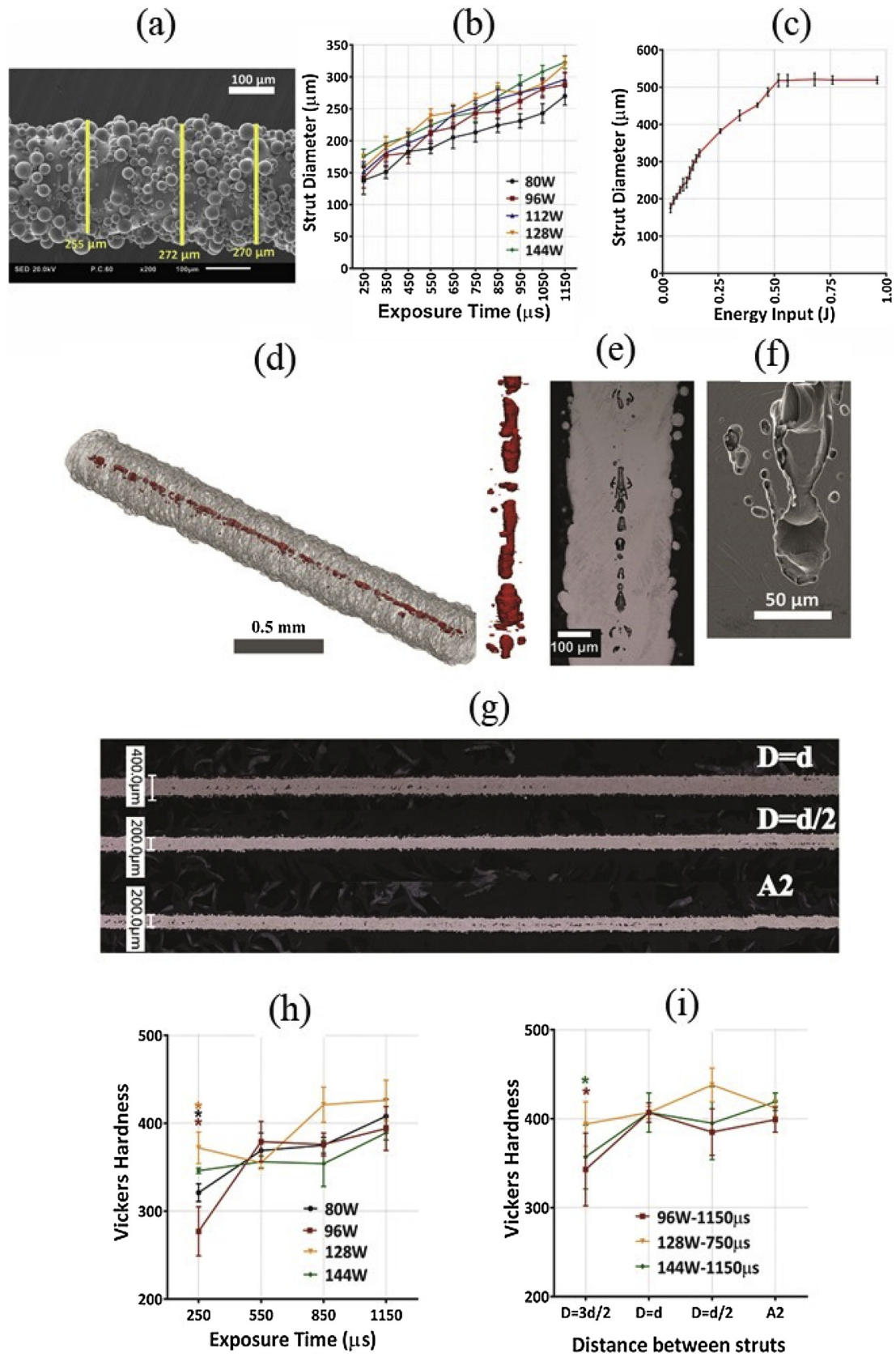


**Fig. 2.** (a) An SEM image demonstrating the measurement of the diameter of the struts; Strut diameters for (b) laser powers of 80–144 W and exposure times of 250–1150  $\mu\text{s}$ , (c) for the higher energy inputs (Energy input (J) = Laser power (W)  $\times$  Exposure time (s)); (d) a strut reconstructed from  $\mu\text{CT}$  images (grey) and the pores within the struts (red); (e) a digital microscope image of the double-melted strut showing the pores in the center; (f) a SEM image revealing a keyhole-shaped pore; (g) Digital microscope images of the struts to show the distribution of the pores along their lengths; The Vickers hardness values (h) of the struts for the given laser power and exposure time, (i) of the struts in circular arrangement and for the double-melted one.



## 2.7. Transmission electron microscopy (TEM)

The TEM foils were prepared using the *in situ* focused ion beam (FIB) milling and lift-out technique performed with an FEI Quanta 3D SEM (FEI, Eindhoven, The Netherlands) to study the microstructure of the surface layer of the struts (transverse direction). FIB lamellas with a width of 4 mm and a depth of 10 mm were prepared for two conditions of single and double-melted struts fabricated with 144 W and 1150  $\mu$ s. The microstructure was then observed with an FEI Tecnai F20 microscope (FEI, Eindhoven, The Netherlands) at an accelerating voltage of 200 kV in the TEM, scanning transmission electron microscopy (STEM), and selected area electron diffraction (SAED) modes to determine the morphology and crystal structure of the phases.

## 2.8. Electron backscattered diffraction (EBSD) analysis

EBSD analysis was performed using a JEOL 7001 F SEM (JEOL, Tokyo, Japan) at an accelerating voltage of 15 kV and a probe current of 15 nA. The software package AZtechKL (Oxford Instruments, UK) was used to acquire the EBSD data, while the software CHANNEL5 (Oxford Instruments, UK) was used for post-acquisition analysis of the data. Areas of around  $90 \mu\text{m} \times 380 \mu\text{m}$  along the longitudinal (*i.e.* build) direction of the struts were scanned with a step size of 0.1 mm to collect data from more than 5000 individual grains per condition.

## 2.9. Analysis of the orientation relationship between $\alpha$ and prior $\beta$ phase

We also studied the characteristics of  $\alpha'$ -laths precipitation in the prior  $\beta$ -grains. In AM materials, such an analysis is complicated by the fact that the amount of the residual beta in most cases is negligible and not sufficient for a meaningful analysis. The methodological challenge was addressed, as originally proposed by Humbert et al. [64], and later adopted by other researchers [55,65–67], by converting the orientation of the  $\alpha$ -platelets into a possible  $\beta$ -phase orientation based on the well-known Burgers orientation relationship [68]:

$$\langle 111 \rangle_{\beta} \parallel \langle 11\bar{2}0 \rangle_{\alpha}$$

$$\{110\}_{\beta} \parallel \{0001\}_{\alpha}$$

This orientation relationship (OR) theoretically allows for only 12 different variants that  $\alpha$ -phase can precipitate within a single  $\beta$  grain, all of which are characterized by five specific misorientation angles between each other [69] (Table 2). In practice, it may be challenging to discern between  $60^\circ$  and  $63^\circ$  misorientation angles (particularly in pole figures) due to a certain degree of local lattice orientation variability. It is therefore useful to reduce the number of possible groups to three (*i.e.*,  $10^\circ$ ,  $60$ – $63^\circ$ , and  $90^\circ$ ).

## 3. Results

### 3.1. Morphological characterization

The strut diameter increased with exposure time and laser power (Fig. 2b). However, the increasing trend saturated for delivered

**Table 2**

Possible misorientation angles between neighboring  $\alpha$ -platelets within an individual prior- $\beta$  grain.

Misorientation angle	Rotation axis
$10^\circ 529$	$\vec{c} = [0001]$
$60^\circ$	$\vec{a}_2 = [1\bar{2}10]$
$60^\circ 832$	$\vec{d}_1$ at $80^\circ 97$ from $\vec{c}$ in $(\vec{d}_3, \vec{c})$ plane
$63^\circ 262$	$\vec{d}_2$ at $72^\circ 73$ from $\vec{c}$ in $(\vec{a}_2, \vec{c})$ plane
$90^\circ$	$\vec{d}_3$ at $5^\circ 26$ from $\vec{c}$ in $\vec{a}_2$ in basal plane

energies above 0.5 J (Fig. 2c). The maximum achievable strut size with the single point exposure scanning strategy was therefore around  $520 \mu\text{m}$  (Fig. 2c). The 3D model reconstructed from the micro-CT scans revealed a continuous pore formation at the center of a single strut (fabricated with 144 W–1150  $\mu$ s) along the build direction (BD) (Fig. 2d). The average pore size was  $\approx 25 \pm 5 \mu\text{m}$ , while the relative density of the bulk material constituting the struts of the BCC cubic scaffold was  $\approx 96.7\%$ . The variability observed in the porosity of the models created using the micro-CT images of the struts was within  $\sim 0.5\%$  (Table S2). The pore size, pore shape, and pore distribution were also inspected by a digital microscope (Fig. 2e) and SEM (Fig. 2f) images. Frequent pore formation at the center of struts was also observed with a digital microscope for the double-melted struts as well as for  $D = d$  and  $d/2$  struts, all of which were fabricated with the same processing parameters (Fig. 2g) (144 W, 1150  $\mu$ s).

### 3.2. Hardness

The struts fabricated with an exposure time of 250  $\mu$ s exhibited smaller microhardness values (270–340 HV) as compared to the rest of the single struts (350–420 HV) (Fig. 2h). Struts that were double-melted ( $A_2$ ), overlapped ( $D = d/2$ ), and touching struts ( $D = d$ ) showed higher values of microhardness (400–440 HV) than the middle strut in a circular arrangement with  $D = 3d/2$  (340–400 HV) (Fig. 2i).

### 3.3. Optical microscopy

The optical microscopy images of the single struts fabricated with different energy inputs revealed martensitic  $\alpha'$ -laths (Fig. 3a). The microstructure of the struts fabricated with 144 W and 1150  $\mu$ s in a circular arrangement with a distance of  $d$  and  $d/2$ , as well as of the double-melted struts, showed the martensitic  $\alpha'$ -phase (Fig. 3b). The energy input and the spacing between the struts did not affect the main characteristics of the microstructure. However, the prior  $\beta$  grain alignment was more pronounced for the overlapping struts ( $D = d/2$ ) and double-melted struts (Fig. 3b).

### 3.4. Microstructure of the surface of the struts with a single and a double-melting cycle

Some uncharacteristic relief was observed on the surface of the struts that resembled basket-weave morphology, with interleaving  $\alpha$  laths exhibiting a quadrangular symmetry [70] (Fig. 4a). These structures were observed on the surface of unpolished, as-fabricated struts. These features have been reported in SLM bulk Ti-6Al-4 V [71]; however, have never been observed in SLM Ti-6Al-4 V lattice struts. To investigate this further, we prepared a cross-section lamella from the surface of the strut to determine the underlying structure of the surface layer and estimate its uniformity. We also studied the structure of double-melted struts, since it also exhibited similar surface features (Fig. 4b).

The microstructure of the struts made with the single point exposure technique was represented by martensitic  $\alpha'$ -laths of varying sizes (Fig. 5a). Selected area diffraction confirmed the formation of a hexagonal martensitic crystal structure (Fig. 5c, inset). In addition, twinning seemed to be present within the martensite laths, particularly in the regions annotated by red arrows (Fig. 5c). The size of separate  $\alpha'$ -platelets decreased from  $1 \mu\text{m}$  (A and B in Fig. 5a) to almost 100 nm in diameter (A in Fig. 5c) when moving towards the surface of a single strut.

The structure of the surface layer of the double melted struts was notably more uniform (Fig. 5b). The lath size across the area of interest was very consistent regardless of the depth. At the same time, the actual size of the laths was somewhere between the extrema observed in the first sample, having an average thickness of 200–300 nm (Fig. 5d). Similar to the single strut, the phase was identified as hexagonal  $\alpha'$

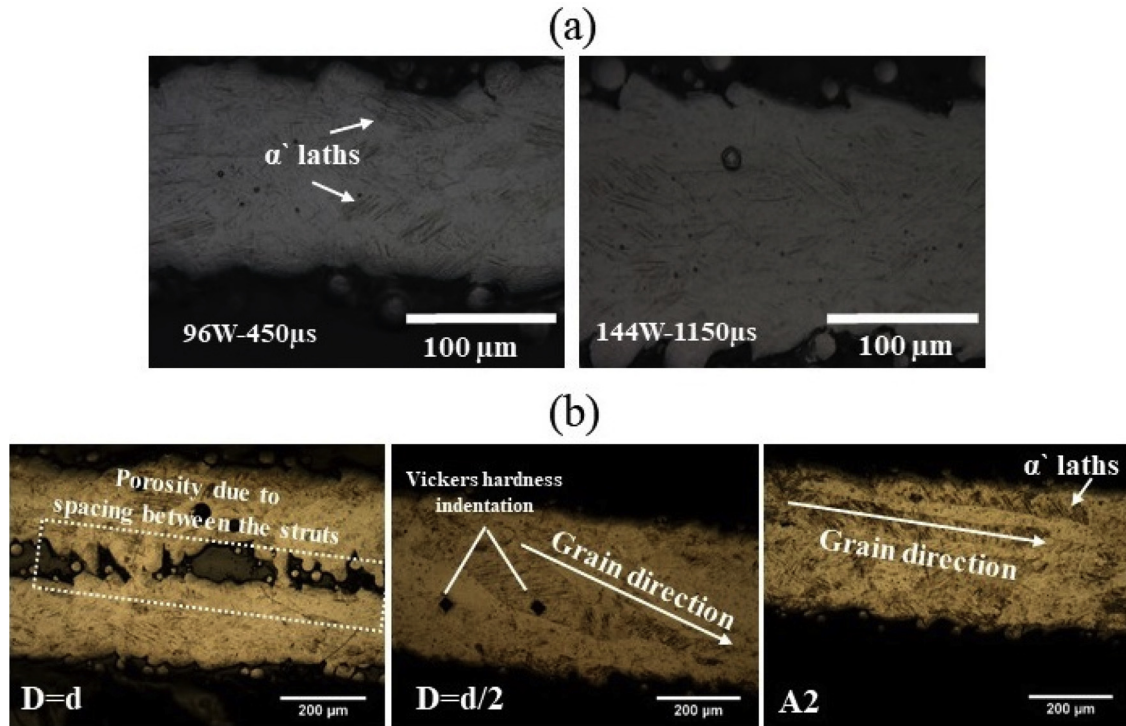


Fig. 3. The microstructure of (a) the single struts fabricated with laser powers of 96W-450 μs and exposure times of 144 W-1150 μs, (b) circularly arranged struts ( $D = d$  and  $d/2$ ), and double-melted struts (A2).

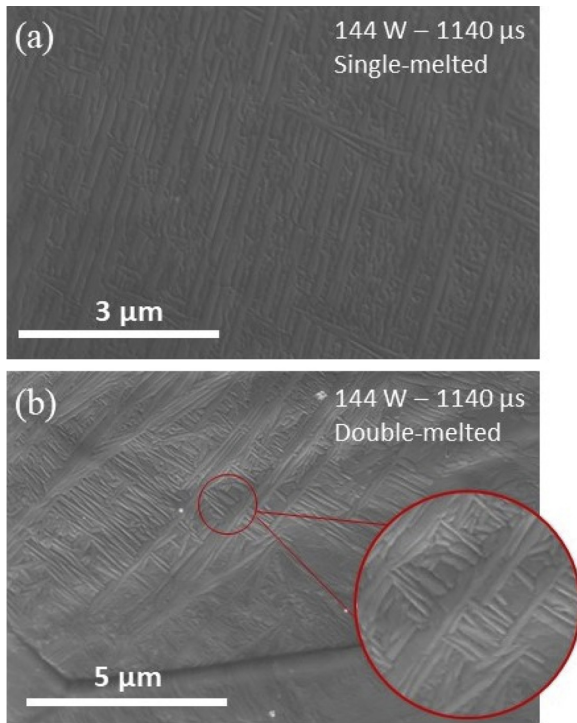


Fig. 4. SEM images presenting the surface microstructure of the (c) single-melted and (d) double-melted struts. The red circle shows the magnified image of a basket-weave like structure, observed on the surface of unpolished as-fabricated double-melted struts.

(Fig. 5d, inset).

### 3.5. Effects of re-melting on the crystallographic texture in the struts

In single struts, several prior  $\beta$ -grains could be discerned (based on the acicular  $\alpha'$  pattern) with a size varying between 70 and 150–200 μm (Fig. 6a). The majority of  $\alpha'$ -platelets within the prior- $\beta$  grains were either 45° inclined or perpendicular to the building direction (BD). The pole figures of the hexagonal lattice indicated very weak  $\alpha'$ -texture in all directions, including the BD (Fig. 6b). Residual  $\beta$ -phase was detected within some of the prior  $\beta$ -grains (see Section 3.6). The pole figures built based on this data showed that there is a strong  $\{100\}$  texture component directed at approximately 15–20° to the BD (Fig. 6c).

The double-melted struts shared many of their microstructural features with the single-melted struts (Fig. 6d). The overall shape and orientation of  $\alpha'$ -laths were very similar in both processing conditions (Fig. 6a, d). The overall texture of the  $\alpha'$  phase did not exhibit any preferential orientation (Fig. 6e), which is consistent with observations for the single-melted struts. There were several prior- $\beta$  grains that could be discerned in the map and were inclined at an angle with respect to the BD as well as coincided with a  $\{100\}$  orientation of the residual  $\beta$  texture (Fig. 6f). The overall  $\beta$  phase texture appeared to be very similar to that of the single-melted struts.

We also performed additional mapping along the strut length to clarify the homogeneity of texture and microstructure (Fig. 7). For both single- and double-melted struts, the crystal texture was similar in all the mapped areas (Fig. 7a and b, respectively), indicating that the structure shown in Fig. 6 represents the entire strut.

### 3.6. Orientation relationship between $\alpha$ and prior $\beta$ phase

Residual  $\beta$ -phase was detected in some of the prior- $\beta$  grains in single- and double-melted struts. EBSD map of a single prior- $\beta$  grain, taken from the region in Fig. 6a (single-melted strut), showed a combined data for  $\alpha'$ -laths (Fig. 8a) and residual  $\beta$ -phase (Fig. 8b). A comparison between the texture plot in Fig. 8a and b shows identical

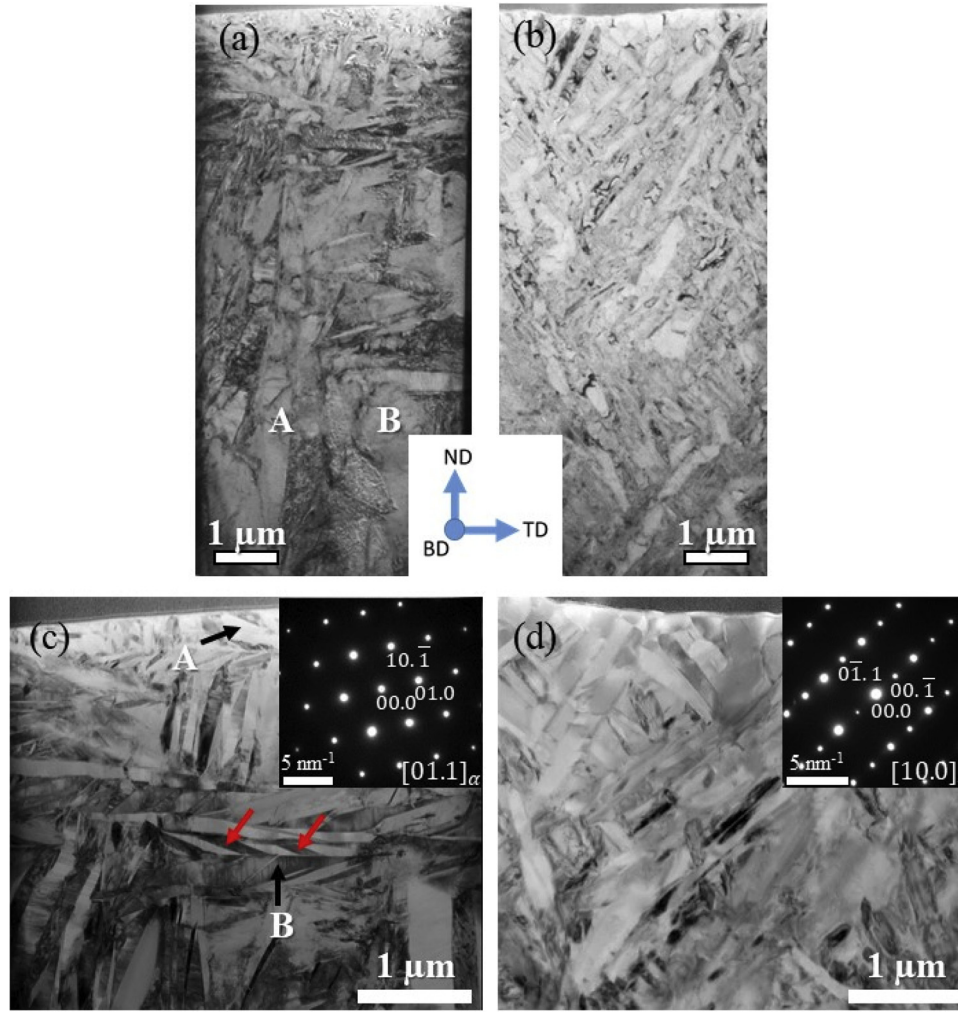


**Fig. 5.** TEM analysis of the surface layer of (a) single strut and (b) double-melted strut, showing the size and uniformity of individual  $\alpha'$ -laths. Detailed view of the surface layer of (c) single strut and (d) double-melted strut, with insets showing zone axis diffraction patterns consistent with  $\alpha/\alpha'$  phase. ND – normal direction; BD – building direction; TD – transverse direction.

pole figures for  $\{0001\}_\alpha$  and  $\{110\}_\beta$ , indicating that the  $\alpha'$ -laths precipitation strictly follows the Burgers orientation relationship [68]:

$$\langle 111 \rangle_\beta \parallel \langle 11\bar{2}0 \rangle_\alpha$$

$$\{110\}_\beta \parallel \{0001\}_\alpha.$$

The analysis of individual  $\alpha'$ -laths orientation within the prior- $\beta$  grain revealed that three major values of misorientation were present, namely, around  $10^\circ$  (shown by arrows in the intensity plot in Fig. 8a),  $60^\circ$  (circled in  $\{0001\}_\alpha$  plot) and  $90^\circ$  (marked by an oval) degrees. The misorientation angle histogram (Fig. 8e) showed prominent peaks at respective angle values, which were similar to previously reported results [69,72].

The EBSD map of the double-melted struts also showed a single prior  $\beta$ -grain map with  $\alpha'$ -laths (Fig. 8c) and  $\beta$ -grain (Fig. 8d). The pole figures for both phases looked very similar to those of the single-melted strut (Fig. 8a,b). The position (Fig. 8c) and distribution of misorientation values between separate  $\alpha'$ -laths (Fig. 8f) was also consistent with the single-melted strut.

Despite similarities between both conditions, the characteristic BOR-related correlation between  $\{0001\}_\alpha$  and  $\{110\}_\beta$  was no longer apparent in the case of double-melted specimens. Furthermore, there was no relationship between the pole figures (and orientation) of both phases, suggesting that the formation of  $\alpha'$  in this case may not have been related to the orientation of the observed residual  $\beta$ -phase.

#### 4. Discussion

We studied the microstructural features resulting from an alternative scanning strategy, namely single point exposure scanning method, used for AM of metallic lattice structures. Another approach that is widely adopted in the literature is the contour and hatching scan strategy, in which the melt-pool is controlled by the laser power, scanning speed, and hatch spacing [73]. Conversely, in single-point exposure method, the melt-pool is controlled by laser power and exposure time. Although both methods are based on the similar thermal processing principle of melting the powder using a laser and creating a melt pool interaction [60], the single point exposure has a number of advantages over the commonly used contour-hatching technique. For example, the long file preparation times and high computational cost of complex STL files could be avoided while preventing the bypassing of laser scans in random places. Moreover, it might be possible to decrease the minimum achievable strut size. Finally, a direct relationship between the processing parameters and the geometry of the resulting struts and, thus, the lattice structure, could be established. A similar relationship was also recognized for contour-hatching using statistical approaches [74,75]. However, these studies have mainly focused on dimensional accuracy, since the geometry is mainly controlled by the CAD model in this technique. Due to the aforementioned reasons, the single point exposure can be considered as an ideal scanning strategy for the fabrication of lattice structures. The systematic study reported



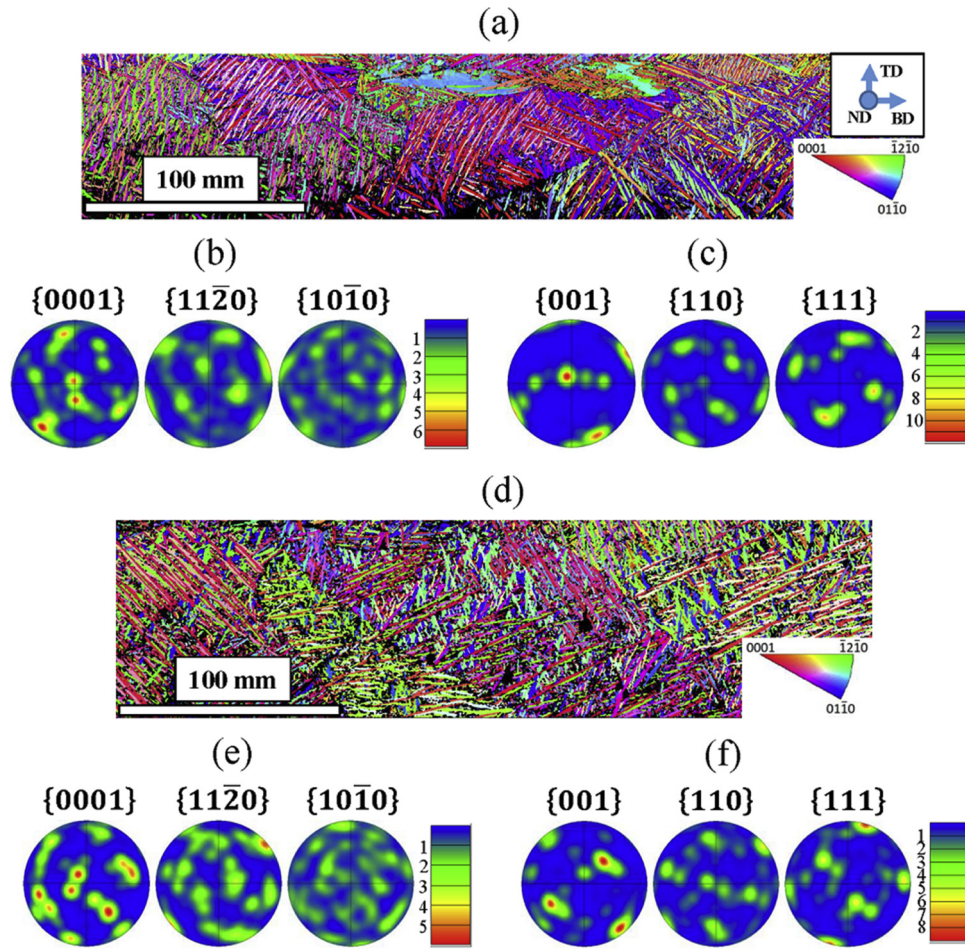


**Fig. 6.**  $\alpha'$  EBSD IPF maps and pole figures for major plane families in  $\alpha'$ - and  $\beta$ -phases of single (a, b, c) and double (d, e, f) exposure struts. (a,d) IPF maps of  $\alpha'$ -phase; (b,e) texture contour plots for  $\alpha'$ -phase; (c,f) texture contour plots for residual  $\beta$ -phase. TD – transverse direction; ND – normal direction; BD – building direction.

here enabled us to reveal some important microstructural features of the vertical AM fabricated struts resulting from this scanning strategy. Varying the building angle typically results in struts with increased diameter and higher roughness [73,76], as well as increased porosity. These behaviors have been reported for both hatch-contouring [73] and single point exposure [60] scanning methods. In this work, we demonstrate that single point exposure can produce complex scaffolds such as cubic scaffolds with BCC unit cells (Figure S.1 in the Supplementary document). A more detailed study of the effects of the building angle with the single point exposure is outside the scope of the current study and will be presented in a follow-up publication.

#### 4.1. Morphological characterization of single struts

Our study covered a wide range of laser power and exposure times, thereby allowing us to determine the relationship between the processing parameters and the dimension of the single vertical struts. It was observed that there is a limit to the maximum achievable strut size that could be obtained with the single point exposure strategy using only one scanning line of the laser beam. It should be noted that this is not an inherent limitation of the single point exposure technique, as more complex designs of laser scanning lines could be used to create struts with very complex shapes (e.g., struts with a varying thickness [63]) and arbitrarily large thicknesses. For one single beam, however, we observed a saturation point of 520  $\mu\text{m}$  in the strut diameter approximately at 0.5 J laser beam energy. Similar trends have been reported in the literature [60] for 316L stainless steel where the strut diameter starts to saturate around 420  $\mu\text{m}$  at a laser energy of 0.35 J. As the strut

diameter is directly linked to the diameter of the melt pool, the saturation point in the diameter indicates that the width of the melt pool does not change when the laser beam energy exceeds 0.5 J. Further increase in the laser beam energy can therefore only yield an increase in the melt-pool depth. A similar behavior has been also observed in the contour-hatching strategy, whereby the weld pool shape at a slow scanning speed (2000 mm/s), hence higher energy density, was deeper than at a higher scanning speed of 4000 mm/s [77]. Excessive energy in the melt pool depth may cause a keyhole-mode melting [78] and pore formation. Keyhole-mode melting occurs when the excessive energy causes evaporation of the material and formation of plasma. Evaporated material yields a vapor cavity, which increases the laser absorption of the melt-pool [79]. Therefore, the laser beam reaches higher depths of the melting pool. This unstable condition eventually causes the collapse of the cavity walls, which are named keyhole pores [79]. We also observed keyhole pores in the micro-CT scans, SEM, and OM images. The pores were irregular in shape, continuous and located in the middle of the struts, which are the attributes of keyhole porosity [46,80]. However, the observed size of the pores was 25  $\mu\text{m}$ , which is much smaller than the expected size of the keyhole pores (> 100  $\mu\text{m}$ ) [37]. This might be due to the morphology and scanning strategy of the samples reported in the literature, which are usually bulk samples fabricated through the hatching-contour strategy. The fact that keyhole pores are significantly (i.e. by a factor of four) smaller in the case of the single point exposure scanning strategy is an advantage of this technique as compared to the hatching-contour technique. In general, not only the total volume of the pores, but also their absolute size, is expected to affect the mechanical properties of the struts, with smaller pores

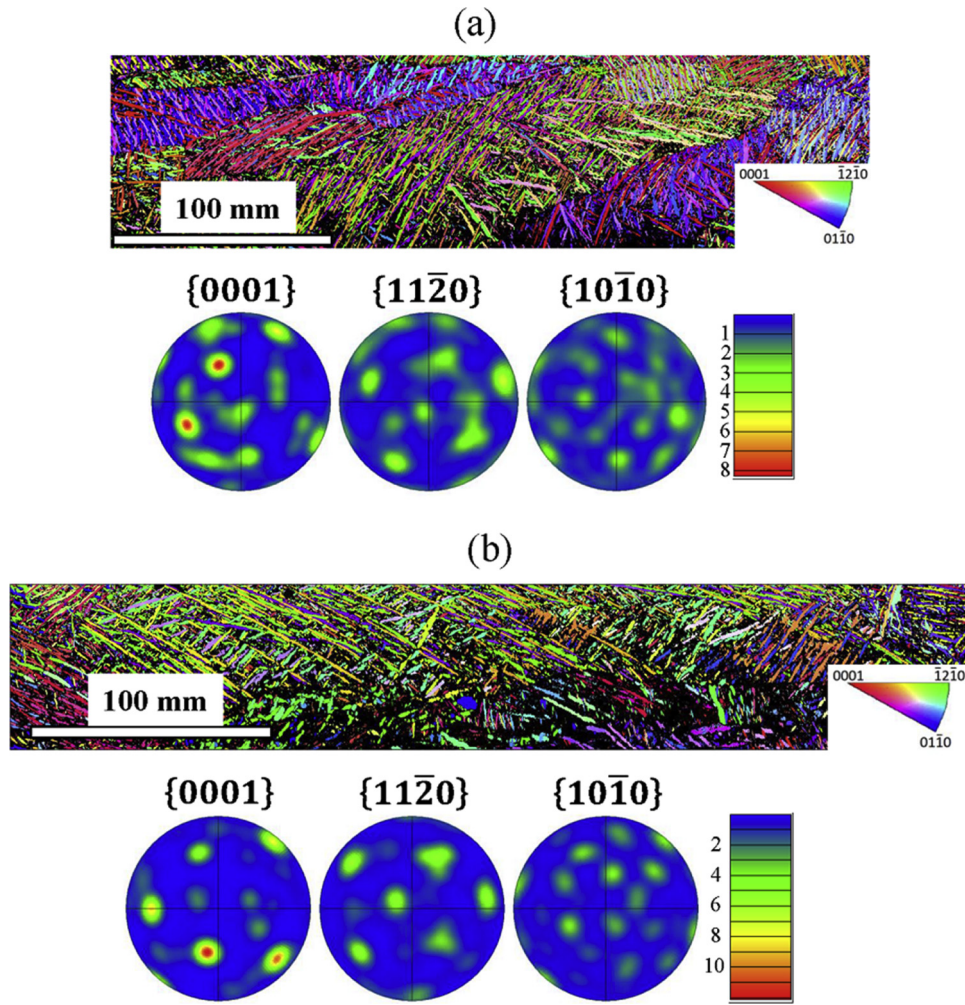


Fig. 7. EBSD  $\alpha'$ -phase IPF map and pole figures for an additional scanning along the strut length for single (a) and double (b) melted samples.

favorable over large pores that could span a large fraction of the strut diameter.

#### 4.2. Effect of laser parameters and latent heat on hardness

The hardness of SLM Ti-6Al-4V usually varies between 350 and 500 HV, depending on the processing parameters [49,81]. We observed hardness values of 350–450 HV, which confirms the processability of Ti-6Al-4V with the single point exposure method. The only exception (270–340 HV) to the stated range of microhardness values was observed when the struts were fabricated with an exposure time of 250  $\mu$ s, at any laser power. This might be due to insufficient energy input causing localized unmolten regions and less integrity in the overall structure, and therefore decreased hardness values. The hardness values increased slightly with an increase in the exposure time for the given laser powers, suggesting that a higher energy input results in a higher hardness value. Similar observations have also been reported by Ahmadi et al. [62] for the single point exposure method, where lower microhardness values were observed when the exposure time was 350  $\mu$ s or lower. This relationship between the energy input and hardness has also been established in some previous studies [49,82] where the contour-hatching scanning technique was applied.

We also observed differences in the microhardness values between the single-melted and re-melted regions for the same energy inputs. Struts that were double-melted (A2), overlapped ( $D = d/2$ ), and touching ( $D = d$ ), all of which had re-melted regions, showed higher values of the microhardness (400–440 HV) than the middle strut in a

circular arrangement with  $D = 3d/2$  (340–400 HV), which had only single-melted regions and minimum latent heat effect. Yasa et al. [83] also observed higher microhardness values in the laser re-melted zones as compared to single-melted regions. They concluded that the higher microhardness values in the re-melted regions are due to a finer and more homogeneous microstructure. We also observed finer microstructures in the STEM images of the double-melted struts (Fig. 5b), compare with the microstructure of single-melted struts in Fig. 5a). As the finer microstructure contains more  $\alpha'$ -laths, which are harder structures, than higher hardness values are expected in the finer microstructures [81,84]. Moreover, according to the Hall-Petch relationship, a finer grain structure increases the yield stress and, thus, the microhardness of the material (the grain boundary strengthening phenomenon).

#### 4.3. Effect of laser processing parameters and latent heat on microstructure

Optical microscope analysis of all samples with a wide range of energy inputs (0.02–1 J) revealed the similar microstructure of the martensitic  $\alpha'$ -laths. This suggests that the energy input does not fundamentally change the type of the microstructure in SLM Ti-6Al-4V material processed with the single point exposure technique.

As lattice structures consist of numerous individual struts that are close enough to heat each other, it is important to understand the effects of the latent heat on the morphological parameters and microstructural features of the AM material. Mullen et al. [59] have shown that the latent heat increases the strut diameter due to the fact that the



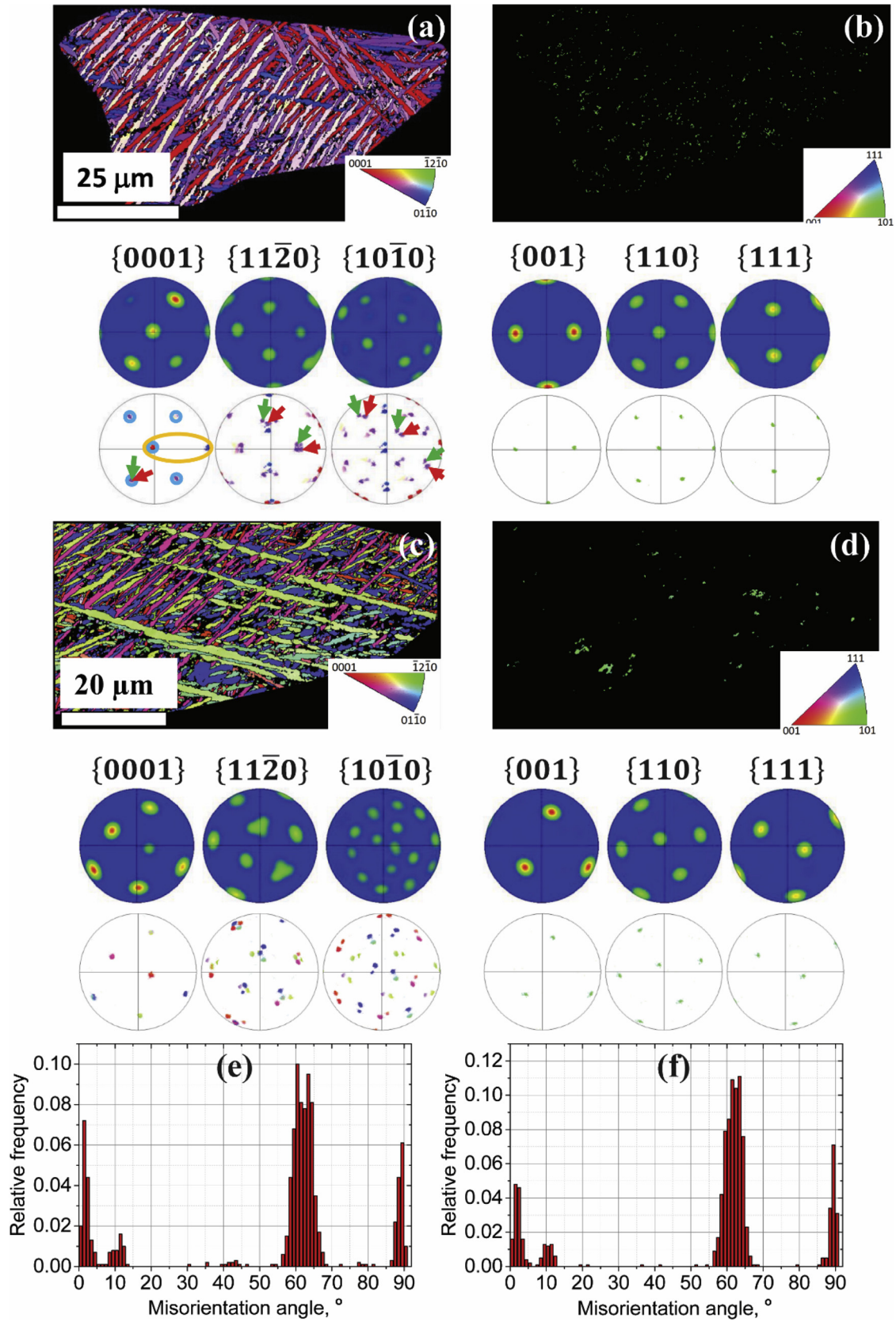


**Fig. 8.** Analysis of  $\alpha'$ - $\beta$  orientation relationship in single and double-melted struts. EBSD maps coupled with pole Figure and IPF colored intensity plots of (a,c)  $\alpha'$ -laths and (b,d) residual  $\beta$ -phase within a single prior- $\beta$  grain for single strut (a,b) and double-melted strut (c,d). (e,f) Misorientation angles frequency for  $\alpha'$ -laths in single (e) and double (f) melted struts. Prominent peaks are visible at  $\approx 10^\circ$ ,  $\approx 60$ - $63^\circ$  and  $90^\circ$ .

latent heat can heat the powder bed sufficiently to reduce the required energy to melt the powder, hence increasing the strut diameter. However, there have been no studies in the literature investigating the effects of the latent heat on the microstructure. To study the effects of the latent heat, we arranged a number of struts in circular arrays with different interspacing. The microstructures of the circular arrays with different sizes of interspacing were generally similar, re-affirming the observation that the general microstructure of SLM Ti-6Al-4 V remains the same regardless of the processing and design parameters. However, given that the number of the struts present in each array was limited, one could argue that the latent heat was not sufficient to alter the temperature of the powder bed and the surrounding struts.

#### 4.4. Microstructure of single and double-melted struts: the homogenization effect

Due to the high proximity of the adjacent melt pools, there are many re-melted zones in lattice structures particularly close to the strut junctions. Moreover, strut junctions play a key role in controlling the mechanical properties of the lattice structures because they are usually the stress concentration points [85]. It is therefore important to understand the possible effects of re-melting on the microstructure of SLM Ti-6Al-4 V.

In general, TEM images revealed more homogeneous microstructure, regarding  $\alpha'$ -lath sizes, in double-melted struts as compared to single-melted struts. In the single strut, the prior  $\beta$ -grain consists of a hierarchical acicular  $\alpha'$ -laths, with the thickness of secondary  $\alpha'$ -laths (A in Fig. 5c) and length of the primary  $\alpha'$ -laths (B in Fig. 5c) varied from 0.1  $\mu\text{m}$  to 1  $\mu\text{m}$ , respectively. In contrast to the hierarchical structure in single-melted struts, the homogeneous packets of fine  $\alpha$ -lamellae (thickness 200–300 nm) were observed in double-melted struts.

The more homogenous microstructure observed here is consistent with what has been reported elsewhere for the re-melted regions made using the contour-hatching scanning technique [83]. The homogeneity of the double-melted struts can be explained by the additional thermal effect of the second laser pulse. Usually SLM of Ti-6Al-4 V powder results in martensitic  $\alpha'$ -laths within prior- $\beta$  grains due to the fast cooling rates ( $10^3$ – $10^8$  K/s [86,87]) during the solidification stage. This type of microstructure is composed of hierarchical martensite with a high density of dislocations and twins [88] and tends to promote intergranular failure [89], anisotropic mechanical behavior [90], and lower ductility [71]. In the literature, there are a few studies [71,91] on the *in-situ* transformation of martensitic  $\alpha'$  to lamellar  $\alpha + \beta$  during the SLM process to improve the ductility and isotropic mechanical behavior of the resulting material. However, all these studies have been focused on bulk Ti-6Al-4 V samples made using the contour-hatching scanning technique. Due to the smaller melted area and limited latent heat, the cooling of lattice structures during SLM occurs at a faster rate than bulk specimens, and the resulting microstructure could be very different. There is currently no study on the microstructural transformations occurring during SLM of lattice structures. Here, we demonstrated that with double exposure, uniform ultrafine (200–300 nm) lamellar  $\alpha$  microstructure can be achieved in lattice structures.

#### 4.5. Grain alignment and the effects of remelting on texture

Analysis of the microstructure of the single- and double-melted struts revealed that, for the most part, the microstructure formation follows similar rules, including prior- $\beta$  grains growing along their  $\langle 100 \rangle_\beta$  direction. The  $\alpha'$  laths within the prior  $\beta$  grains were randomly oriented with no significant texture observed for both single- and double-melted struts.

Most grains were angled (18–20°) towards the BD for both types of struts, which is a usual outcome of SLM processes for lattice structures [58]. It is known that the columnar prior- $\beta$  grains tend to tilt with

respect to the hatching scanning direction [55]. It is, however, surprising to observe such behavior in the process where the scanning is replaced by static single point laser exposure. Since grain growth is controlled by the temperature gradient and melt pool evolution [92], this deviation of the columnar grains from the BD during the single point exposure of laser suggests that maximum heat flow is 18–20° off from the BD (based on the melt pool boundary). It is also shown that the high-energy laser causes a directional heat transfer and therefore directional solidification [93]. Other researchers have shown that a  $\langle 100 \rangle$  grain texture can result from repeating the deposition of layers upon layers also for other materials [94].

#### 4.6. Burgers orientation relationship for the double-melted struts

The effects of double laser exposure on the microstructure of materials can primarily be studied based on the microstructural properties of  $\alpha'$ -martensite. However, given that the re-melting process causes several combinations of  $\alpha' \leftrightarrow \beta$  and  $\beta \leftrightarrow L$  transformations within a short timeframe, it is also important to study the effects of such processing on the properties of  $\beta$ -phase, as well as on the specifics of the transformations. Such analysis is complicated by the fact that the amount of  $\beta$ -phase available for the analysis is, in most cases, insufficient. In the literature, this complication has been resolved by converting the orientation of  $\alpha'$ -platelets into a possible  $\beta$ -phase orientation based on the Burgers orientation relationship (OR):

$$\langle 111 \rangle_\beta \parallel \langle 11\bar{2}0 \rangle_\alpha;$$

$$\{110\}_\beta \parallel \{0001\}_\alpha$$

Unlike the previous works, in this study we were able to observe the  $\beta$ -phase directly in the form of residual  $\beta$ -phase between  $\alpha'$ -laths. Assuming the residual  $\beta$  inherited the orientation from the prior- $\beta$  grains, this allowed us to directly check the validity of the Burgers OR under the severe conditions of melting and solidification during the laser processing.

In single point exposure strut all major three groups of  $\alpha'$ -laths misorientation were observed within the prior- $\beta$  grain (Fig. 8a). Laths with 10.53° misorientation were characterized by a common  $\{0001\}_\alpha$  plane and a rotation around  $\vec{c} = [0001]_\alpha$ , which could be seen in  $\{11\bar{2}0\}_\alpha$  and  $\{10\bar{1}0\}_\alpha$  plots. The other two groups (60–63° and 90°), which were due to the mutual misorientation of  $\{110\}$  planes in  $\beta$ -phase, were also present.

To summarize, we confirmed the validity of OR for the single point exposure strut, which is evidenced by an ideal correlation of  $\alpha'$ -laths orientation with respect to the parent  $\beta$ , with evidence of all 12 possible  $\alpha'$ -variants with different mutual orientation that could theoretically occur.

At the same time, the analysis of a double-melted specimen indicated a lack of a correlation between  $\alpha'$ - and  $\beta$ -phases that is characteristic of the Burgers OR – similarity of the  $\{0001\}_\alpha$  and  $\{110\}_\beta$  pole figures. However, there were no indications that any other type of OR is possible between these phases due to the lattice geometry and the correlation between them. In fact, a more detailed analysis of the grain orientations showed no meaningful correlation between the phases. There are two possible explanations for this. The first explanation suggests that the data is of low quality and/or is misinterpreted. This seems unlikely since the fit of the experimental data to the simulated  $\beta$ -phase data was found to be high. A more probable explanation is that the double laser exposure has occurred at different times during the solidification/ $\beta \rightarrow \alpha'$  transformation processes. This might have disrupted the natural way in which the microstructure is formed and have resulted in unconventional arrangements of the phases with respect to each other. It can be hypothesized that the single exposure technique might provide a new avenue for local microstructure control in the SLM process.

## 5. Conclusions

This study is the first of its kind to understand the fundamentals of the single point exposure method and the microstructure of SLM Ti-6Al-4V lattice structures fabricated using this technique. Struts with over 50 processing conditions were fabricated to study the effects of the processing parameters in the single point exposure SLM process on the final geometry, density, microstructure, and hardness of the struts. The major findings of this research are:

- 1 We found that the strut dimensions can be controlled through the SLM processing parameters, with higher energy inputs resulting in a larger strut diameter up to a saturation point (*i.e.*, 520  $\mu\text{m}$  corresponding to 0.5 J energy).
- 2 The single point exposure method yielded a keyhole shaped pores that were up to 4 times smaller than those observed in the hatching and contour technique. The holes were positioned in the middle of the struts and had an average size of 25  $\mu\text{m}$ . The pores were observed for all specimens, regardless of the process parameters and conditions. The relative density of the BCC cubic scaffold calculated by Archimedes principle was around 96.7%.
- 3 The general microstructure of the specimens remained the same regardless of the processing parameters, the amount of the latent heat, and the number of exposures (*i.e.*, single vs. double). That said, re-melting resulted in a finer, more uniform, microstructure and, thus, higher hardness values. In particular, the STEM images of the cross-section of the single and double-melted struts revealed that while classic hierarchical  $\alpha'$ -laths with varying lath sizes (0.1–1  $\mu\text{m}$ ) are observed in the single-melted struts, ultrafine (200–300 nm) homogeneous  $\alpha$ -lamellar microstructure could be achieved after re-melting, which could be beneficial for improving the mechanical properties of the lattice structures.
- 4 The textures of single- and double-melted struts were similar, with randomly oriented  $\alpha'$ -laths within the prior columnar  $\beta$  grains. The  $\beta$  grains were angled 18–20° off the build direction as dictated by the maximum heat flow during the solidification process.
- 5 Finally, we were able to observe the  $\beta$ -phase directly in the form of residual  $\beta$ -phase between  $\alpha'$ -laths, which allowed us to check the validity of the Burgers orientation relationship for the single- and double-melted struts. Although single-melted struts showed the expected BOR between the  $\alpha'$  and  $\beta$  phases, there was a lack of correlation between both phases for the double-melted struts. This suggests the occurrence of a disruptive change during the second melting and solidification process.

## Author declaration

None.

## Acknowledgements

E.O. would like to acknowledge Monash X-Ray computed tomography facility and Dr. Asadul Haque for the assistance with micro CT scans. A.E.M. would like to acknowledge Monash Centre for Electron Microscopy and Dr. Emily Chen for assistance with TEM analysis. This project is funded by the ARC Research Hub for Transforming Australia's Manufacturing Industry through High Value Additive Manufacturing (IH130100008).

## Appendix A. Supplementary data

Supplementary material related to this article can be found, in the online version, at doi:<https://doi.org/10.1016/j.addma.2019.100785>.

## References

- [1] M. Mirzaali, R. Hedayati, P. Vena, L. Vergani, M. Strano, A. Zadpoor, Rational design of soft mechanical metamaterials: independent tailoring of elastic properties with randomness, *Appl. Phys. Lett.* 111 (5) (2017) 051903.
- [2] J.T. Overvelde, J.C. Weaver, C. Hoberman, K. Bertoldi, Rational design of reconfigurable prismatic architected materials, *Nature* 541 (7637) (2017) 347.
- [3] C. Körner, Additive manufacturing of metallic components by selective electron beam melting—a review, *Int. Mater. Rev.* 61 (5) (2016) 361–377.
- [4] X. Wang, S. Xu, S. Zhou, W. Xu, M. Leary, P. Choong, M. Qian, M. Brandt, Y.M. Xie, Topological design and additive manufacturing of porous metals for bone scaffolds and orthopaedic implants: a review, *Biomaterials* 83 (2016) 127–141.
- [5] A.A. Zadpoor, J. Malda, Additive manufacturing of biomaterials, tissues, and organs, *Ann. Biomed. Eng.* 45 (1) (2017) 1–11.
- [6] P.M. Reis, H.M. Jaeger, M. Van Hecke, Designer matter: a perspective, *Extreme Mech. Lett.* 5 (2015) 25–29.
- [7] J. Berger, H. Wadley, R. McMeeking, Mechanical metamaterials at the theoretical limit of isotropic elastic stiffness, *Nature* 543 (7646) (2017) 533.
- [8] J. Christensen, M. Kadic, O. Kraft, M. Wegener, Vibrant times for mechanical metamaterials, *MRS Commun.* 5 (3) (2015) 453–462.
- [9] J.H. Lee, J.P. Singer, E.L. Thomas, Micro-/nanostructured mechanical metamaterials, *Adv. Mater.* 24 (36) (2012) 4782–4810.
- [10] A.A. Zadpoor, Mechanical meta-materials, *Mater. Horiz.* 3 (5) (2016) 371–381.
- [11] S.A. Cummer, J. Christensen, A. Alù, Controlling sound with acoustic metamaterials, *Nat. Rev. Mater.* 1 (3) (2016) 16001.
- [12] M.-H. Lu, L. Feng, Y.-F. Chen, Phononic crystals and acoustic metamaterials, *Mater. Today* 12 (12) (2009) 34–42.
- [13] G. Ma, P. Sheng, Acoustic metamaterials: from local resonances to broad horizons, *Sci. Adv.* 2 (2) (2016) e1501595.
- [14] R. Hedayati, M. Sadighi, M. Mohammadi-Aghdam, A. Zadpoor, Mechanical behavior of additively manufactured porous biomaterials made from truncated cuboctahedron unit cells, *Int. J. Mech. Sci.* 106 (2016) 19–38.
- [15] R. Hedayati, M. Sadighi, M. Mohammadi-Aghdam, A. Zadpoor, Mechanical properties of regular porous biomaterials made from truncated cube repeating unit cells: analytical solutions and computational models, *Mater. Sci. Eng. C* 60 (2016) 163–183.
- [16] H.M. Kolken, S. Janbaz, S.M. Leeflang, K. Lietaert, H.H. Weinans, A.A. Zadpoor, Rationally designed meta-implants: a combination of auxetic and conventional meta-biomaterials, *Mater. Horiz.* 5 (1) (2018) 28–35.
- [17] A.A. Zadpoor, R. Hedayati, Analytical relationships for prediction of the mechanical properties of additively manufactured porous biomaterials, *J. Biomed. Mater. Res. A* 104 (12) (2016) 3164–3174.
- [18] S. Babaei, J. Shim, J.C. Weaver, E.R. Chen, N. Patel, K. Bertoldi, 3D soft metamaterials with negative Poisson's ratio, *Adv. Mater.* 25 (36) (2013) 5044–5049.
- [19] T.A. Hewage, K.L. Alderson, A. Alderson, F. Scarpa, Double-negative mechanical metamaterials displaying simultaneous negative stiffness and negative Poisson's ratio properties, *Adv. Mater.* 28 (46) (2016) 10323–10332.
- [20] Z.G. Nicolaou, A.E. Motter, Mechanical metamaterials with negative compressibility transitions, *Nat. Mater.* 11 (7) (2012) 608.
- [21] L. Wu, B. Li, J. Zhou, Isotropic negative thermal expansion metamaterials, *ACS Appl. Mater. Interfaces* 8 (27) (2016) 17721–17727.
- [22] J.N. Grima, D. Attard, R. Caruana-Gauci, R. Gatt, Negative linear compressibility of hexagonal honeycombs and related systems, *Scr. Mater.* 65 (7) (2011) 565–568.
- [23] X. Zheng, H. Lee, T.H. Weisgraber, M. Shusteff, J. DeOtte, E.B. Duoss, J.D. Kuntz, M.M. Biener, Q. Ge, J.A. Jackson, Ultralight, ultrastiff mechanical metamaterials, *Science* 344 (6190) (2014) 1373–1377.
- [24] F. Bobbert, K. Lietaert, A.A. Eftekhari, B. Pourn, S. Ahmadi, H. Weinans, A. Zadpoor, Additively manufactured metallic porous biomaterials based on minimal surfaces: a unique combination of topological, mechanical, and mass transport properties, *Acta Biomater.* 53 (2017) 572–584.
- [25] R. Wauthle, S.M. Ahmadi, S.A. Yavari, M. Mulier, A.A. Zadpoor, H. Weinans, J. Van Humbeeck, J.-P. Kruth, J. Schrooten, Revival of pure titanium for dynamically loaded porous implants using additive manufacturing, *Mater. Sci. Eng. C* 54 (2015) 94–100.
- [26] J.L. Silverberg, A.A. Evans, L. McLeod, R.C. Hayward, T. Hull, C.D. Santangelo, I. Cohen, Using origami design principles to fold reprogrammable mechanical metamaterials, *Science* 345 (6197) (2014) 647–650.
- [27] Y. Tang, G. Lin, S. Yang, Y.K. Yi, R.D. Kamien, J. Yin, Programmable Kiri-Kirigami metamaterials, *Adv. Mater.* 29 (10) (2017) 1604262.
- [28] R. Hedayati, S. Ahmadi, K. Lietaert, B. Pourn, Y. Li, H. Weinans, C. Rans, A. Zadpoor, Isolated and modulated effects of topology and material type on the mechanical properties of additively manufactured porous biomaterials, *J. Mech. Behav. Biomed. Mater.* 79 (2018) 254–263.
- [29] R. Hedayati, M. Sadighi, M. Mohammadi-Aghdam, A. Zadpoor, Mechanics of additively manufactured porous biomaterials based on the rhombicuboctahedron unit cell, *J. Mech. Behav. Biomed. Mater.* 53 (2016) 272–294.
- [30] J. Kadkhodapour, H. Montazerian, A.C. Darabi, A. Anaraki, S. Ahmadi, A. Zadpoor, S. Schmauder, Failure mechanisms of additively manufactured porous biomaterials: effects of porosity and type of unit cell, *J. Mech. Behav. Biomed. Mater.* 50 (2015) 180–191.
- [31] E. Onal, J.E. Frith, M. Jurg, X. Wu, A. Molotnikov, Mechanical properties and in vitro behavior of additively manufactured and functionally graded Ti6Al4V porous scaffolds, *Metals* 8 (4) (2018) 200.
- [32] S. Ahmadi, R. Hedayati, Y. Li, K. Lietaert, N. Tümer, A. Fatemi, C. Rans, B. Pourn, H. Weinans, A. Zadpoor, Fatigue performance of additively manufactured meta-



- biomaterials: the effects of topology and material type, *Acta Biomater.* 65 (2018) 292–304.
- [33] N.W. Hrabie, P. Heinel, B. Flinn, C. Körner, R.K. Bordia, Compression-compression fatigue of selective electron beam melted cellular titanium (Ti-6Al-4V), *J. Biomed. Mater. Res. Part B Appl. Biomater.* 99 (2) (2011) 313–320.
- [34] S. Li, L.E. Murr, X. Cheng, Z. Zhang, Y. Hao, R. Yang, F. Medina, R. Wicker, Compression fatigue behavior of Ti-6Al-4V mesh arrays fabricated by electron beam melting, *Acta Mater.* 60 (3) (2012) 793–802.
- [35] K. Lietaert, A. Cutolo, D. Boey, B. Van Hooreweder, Fatigue life of additively manufactured Ti6Al4V scaffolds under tension-tension, tension-compression and compression-compression fatigue load, *Sci. Rep.* 8 (1) (2018) 4957.
- [36] A. Zargarian, M. Esfahanian, J. Kadkhodapour, S. Ziaei-Rad, Numerical simulation of the fatigue behavior of additive manufactured titanium porous lattice structures, *Mater. Sci. Eng. C* 60 (2016) 339–347.
- [37] N.T. Aboulkhair, N.M. Everitt, I. Ashcroft, C. Tuck, Reducing porosity in AlSi10Mg parts processed by selective laser melting, *Addit. Manuf.* 1–4 (2014) 77–86.
- [38] B. AlMangour, D. Grzesiak, J.-M. Yang, Selective laser melting of TiB2/316L stainless steel composites: the roles of powder preparation and hot isostatic pressing post-treatment, *Powder Technol.* 309 (2017) 37–48.
- [39] H. Attar, M. Calin, L. Zhang, S. Scudino, J. Eckert, Manufacture by selective laser melting and mechanical behavior of commercially pure titanium, *Mater. Sci. Eng. A* 593 (2014) 170–177.
- [40] M. Badrossamay, T. Childs, Further studies in selective laser melting of stainless and tool steel powders, *Int. J. Mach. Tools Manuf.* 47 (5) (2007) 779–784.
- [41] T. Bormann, R. Schumacher, B. Müller, M. Mertmann, M. de Wild, Tailoring selective laser melting process parameters for NiTi implants, *J. Mater. Eng. Perform.* 21 (12) (2012) 2519–2524.
- [42] S. Dadbakhsh, B. Vrancken, J.-P. Kruth, J. Luyten, J. Van Humbeeck, Texture and anisotropy in selective laser melting of NiTi alloy, *Mater. Sci. Eng. A* 650 (2016) 225–232.
- [43] A. Ataee, Y. Li, D. Fraser, G. Song, C. Wen, Anisotropic Ti-6Al-4V gyroid scaffolds manufactured by electron beam melting (EBM) for bone implant applications, *Mater. Des.* 137 (2018) 345–354.
- [44] X. Cheng, S. Li, L. Murr, Z. Zhang, Y. Hao, R. Yang, F. Medina, R. Wicker, Compression deformation behavior of Ti-6Al-4V alloy with cellular structures fabricated by electron beam melting, *J. Mech. Behav. Biomed. Mater.* 16 (2012) 153–162.
- [45] P. Heinel, A. Rottmair, C. Körner, R.F. Singer, Cellular titanium by selective electron beam melting, *Adv. Eng. Mater.* 9 (5) (2007) 360–364.
- [46] H. Gong, K. Rafi, H. Gu, T. Starr, B. Stucker, Analysis of defect generation in Ti-6Al-4V parts made using powder bed fusion additive manufacturing processes, *Addit. Manuf.* 1–4 (2014) 87–98.
- [47] R. Stamp, P. Fox, W. O'Neill, E. Jones, C. Sutcliffe, The development of a scanning strategy for the manufacture of porous biomaterials by selective laser melting, *J. Mater. Sci.* 20 (9) (2009) 1839–1848.
- [48] L.N. Carter, C. Martin, P.J. Withers, M.M. Attallah, The influence of the laser scan strategy on grain structure and cracking behaviour in SLM powder-bed fabricated nickel superalloy, *J. Alloys. Compd.* 615 (2014) 338–347.
- [49] L. Thijs, F. Verhaeghe, T. Craeghs, J.V. Humbeeck, J.-P. Kruth, A study of the microstructural evolution during selective laser melting of Ti-6Al-4V, *Acta Mater.* 58 (9) (2010) 3303–3312.
- [50] C. Zhang, H. Zhu, Z. Hu, L. Zhang, X. Zeng, A comparative study on single-laser and multi-laser selective laser melting AlSi10Mg: defects, microstructure and mechanical properties, *Mater. Sci. Eng. A* 746 (2019) 416–423.
- [51] S. Ahmadi, R. Hedayati, R.A.K. Jain, Y. Li, S. Leeftang, A. Zadpoor, Effects of laser processing parameters on the mechanical properties, topology, and microstructure of additively manufactured porous metallic biomaterials: a vector-based approach, *Mater. Des.* 134 (2017) 234–243.
- [52] P. Wang, W.J. Sin, M.L.S. Nai, J. Wei, Effects of processing parameters on surface roughness of additive manufactured Ti-6Al-4V via electron beam melting, *Materials* 10 (10) (2017) 1121.
- [53] R. Wauthle, B. Vrancken, B. Beynaerts, K. Jorissen, J. Schrooten, J.-P. Kruth, J. Van Humbeeck, Effects of build orientation and heat treatment on the microstructure and mechanical properties of selective laser melted Ti6Al4V lattice structures, *Addit. Manuf.* 5 (2015) 77–84.
- [54] B. Wysocki, J. Idaszek, J. Zdunek, K. Rożniatowski, M. Pisarek, A. Yamamoto, W. Świążkowski, The influence of selective laser melting (SLM) process parameters on in-vitro cell response, *Int. J. Mol. Sci.* 19 (6) (2018).
- [55] M. Simonelli, Y.Y. Tse, C. Tuck, On the texture formation of selective laser melted Ti-6Al-4V, *Metall. Mater. Trans. A* 45 (6) (2014) 2863–2872.
- [56] J. Stef, A. Poulon-Quintin, A. Redjaimia, J. Ghanbaja, O. Ferry, M. De Sousa, M. Gouné, Mechanism of porosity formation and influence on mechanical properties in selective laser melting of Ti-6Al-4V parts, *Mater. Des.* 156 (2018) 480–493.
- [57] B. Van Hooreweder, Y. Apers, K. Lietaert, J.-P. Kruth, Improving the fatigue performance of porous metallic biomaterials produced by Selective Laser Melting, *Acta Biomater.* 47 (2017) 193–202.
- [58] T. Niendorf, F. Brenne, M. Schaper, Lattice structures manufactured by SLM: on the effect of geometrical dimensions on microstructure evolution during processing, *Metall. Mater. Trans.* 45 (4) (2014) 1181–1185.
- [59] L. Mullen, R.C. Stamp, W.K. Brooks, E. Jones, C.J. Sutcliffe, Selective Laser Melting: a regular unit cell approach for the manufacture of porous, titanium, bone in-growth constructs, suitable for orthopedic applications, *J. Biomed. Mater. Res. Part B Appl. Biomater.* 89B (2) (2009) 325–334.
- [60] S. Tsoupanos, R.A.W. Mines, S. McKown, Y. Shen, W.J. Cantwell, W. Brooks, C.J. Sutcliffe, The influence of processing parameters on the mechanical properties of selectively laser melted stainless steel microlattice structures, *J. Manuf. Sci. Eng.* 132 (4) (2010) 041011–041011-12.
- [61] S. Ghose, S. Babu, R.J. Van Arkel, K. Nai, P.A. Hooper, J.R.T. Jeffers, The influence of laser parameters and scanning strategies on the mechanical properties of a stochastic porous material, *Mater. Des.* 131 (2017) 498–508.
- [62] S.M. Ahmadi, R. Hedayati, R.K. Ashok Kumar Jain, Y. Li, S. Leeftang, A.A. Zadpoor, Effects of laser processing parameters on the mechanical properties, topology, and microstructure of additively manufactured porous metallic biomaterials: A vector-based approach, *Mater. Des.* 134 (2017) 234–243.
- [63] R. Hedayati, A. Leeftang, A. Zadpoor, Additively manufactured metallic pentamode meta-materials, *Appl. Phys. Lett.* 110 (9) (2017) 091905.
- [64] M. Humbert, H. Moustahfid, F. Wagner, M.J. Philippe, Evaluation of the high temperature texture of the  $\beta$  phase of a TA6V sample from the individual orientations of grains of the low temperature  $\alpha$  phase, *Scr. Metall. Mater.* 30 (3) (1994) 377–382.
- [65] P.S. Davies, B.P. Wynne, W.M. Rainforth, M.J. Thomas, P.L. Threadgill, Development of microstructure and crystallographic texture during stationary shoulder friction stir welding of Ti-6Al-4V, *Metall. Mater. Trans. A* 42 (8) (2011) 2278–2289.
- [66] A.A. Antony, J. Meyer, P.B. Prangnell, Effect of build geometry on the  $\beta$ -grain structure and texture in additive manufacture of Ti6Al4V by selective electron beam melting, *Mater. Charact.* 84 (2013) 153–168.
- [67] M. Simonelli, Y.Y. Tse, C. Tuck, Further understanding of Ti-6Al-4V selective laser melting using texture analysis, *Annual International Solid Freeform Fabrication Symposium* (2012) 480–491.
- [68] E. Lee, R. Banerjee, S. Kar, D. Bhattacharyya, H.L. Fraser, Selection of  $\alpha$  variants during microstructural evolution in  $\alpha/\beta$  titanium alloys, *Philos. Mag.* 87 (24) (2007) 3615–3627.
- [69] N. Gey, M. Humbert, Characterization of the variant selection occurring during the  $\alpha \rightarrow \beta \rightarrow \alpha$  phase transformations of a cold rolled titanium sheet, *Acta Mater.* 50 (2) (2002) 277–287.
- [70] B. Baufeld, O. van der Biest, Mechanical properties of Ti-6Al-4V specimens produced by shaped metal deposition, *Sci. Technol. Adv. Mater.* 10 (1) (2009) 015008.
- [71] W. Xu, M. Brandt, S. Sun, J. Elambasseril, Q. Liu, K. Latham, K. Xia, M. Qian, Additive manufacturing of strong and ductile Ti-6Al-4V by selective laser melting via in situ martensite decomposition, *Acta Mater.* 85 (2015) 74–84.
- [72] S.C. Wang, M. Aindow, M.J. Starink, Effect of self-accommodation on  $\alpha/\alpha$  boundary populations in pure titanium, *Acta Mater.* 51 (9) (2003) 2485–2503.
- [73] S.L. Sing, F.E. Wiria, W.Y. Yeong, Selective laser melting of lattice structures: a statistical approach to manufacturability and mechanical behavior, *Robot. Comput. Manuf.* 49 (2018) 170–180.
- [74] S.L. Sing, W.Y. Yeong, F.E. Wiria, B.Y. Tay, Characterization of titanium lattice structures fabricated by selective laser melting using an adapted compressive test method, *Exp. Mech.* 56 (5) (2016) 735–748.
- [75] C. Qiu, S. Yue, N.J.E. Adkins, M. Ward, H. Hassanin, P.D. Lee, P.J. Withers, M.M. Attallah, Influence of processing conditions on strut structure and compressive properties of cellular lattice structures fabricated by selective laser melting, *Mater. Sci. Eng. A* 628 (2015) 188–197.
- [76] Z. Dong, Y. Liu, W. Li, J. Liang, Orientation dependency for microstructure, geometric accuracy and mechanical properties of selective laser melting AlSi10Mg lattices, *J. Alloys. Compd.* 791 (2019) 490–500.
- [77] C. Panwisawas, C.L. Qiu, Y. Sovani, J.W. Brooks, M.M. Attallah, H.C. Basoalto, On the role of thermal fluid dynamics into the evolution of porosity during selective laser melting, *Scr. Mater.* 105 (2015) 14–17.
- [78] R. Rai, J.W. Elmer, T.A. Palmer, T. DebRoy, Heat transfer and fluid flow during keyhole mode laser welding of tantalum, Ti-6Al-4V, 304L stainless steel and vanadium, *J. Phys. D Appl. Phys.* 40 (18) (2007) 5753–5766.
- [79] W.E. King, H.D. Barth, V.M. Castillo, G.F. Gallegos, J.W. Gibbs, D.E. Hahn, C. Kamath, A.M. Rubenchik, Observation of keyhole-mode laser melting in laser powder-bed fusion additive manufacturing, *J. Mater. Process. Technol.* 214 (12) (2014) 2915–2925.
- [80] R. Xiao, X. Zhang, Problems and issues in laser beam welding of aluminum–lithium alloys, *J. Manuf. Process.* 16 (2) (2014) 166–175.
- [81] I. Yadroitsev, P. Krakhmalev, I. Yadroitsava, Selective laser melting of Ti6Al4V alloy for biomedical applications: temperature monitoring and microstructural evolution, *J. Alloys. Compd.* 583 (2014) 404–409.
- [82] K. Kempen, E. Yasa, L. Thijs, J.P. Kruth, J. Van Humbeeck, Microstructure and mechanical properties of Selective Laser Melted 18Ni-300 steel, *Phys. Procedia* 12 (2011) 255–263.
- [83] E. Yasa, J. Deckers, J.P. Kruth, The investigation of the influence of laser re-melting on density, surface quality and microstructure of selective laser melting parts, *Rapid Prototyp. J.* 17 (5) (2011) 312–327.
- [84] L.E. Murr, S.M. Gaytan, F. Medina, H. Lopez, E. Martinez, B.I. Machado, D.H. Hernandez, L. Martinez, M.I. Lopez, R.B. Wicker, J. Bracke, Next-generation biomedical implants using additive manufacturing of complex, cellular and functional mesh arrays, *Philos. Trans. Math. Phys. Eng. Sci.* 368 (2010) (1917) 1999–2032.
- [85] M. Smith, Z. Guan, W.J. Cantwell, Finite element modelling of the compressive response of lattice structures manufactured using the selective laser melting technique, *Int. J. Mech. Sci.* 67 (2013) 28–41.
- [86] P.A. Kobryn, S.L. Semiatin, The laser additive manufacture of Ti-6Al-4V, *JOM* 53 (9) (2001) 40–42.
- [87] N.E. Hodge, R.M. Ferencz, J.M. Solberg, Implementation of a thermomechanical model for the simulation of selective laser melting, *Comput. Mech.* 54 (1) (2014) 33–51.
- [88] J. Yang, H. Yu, J. Yin, M. Gao, Z. Wang, X. Zeng, Formation and control of martensite in Ti-6Al-4V alloy produced by selective laser melting, *Mater. Des.* 108



- (2016) 308–318.
- [89] S.S. Al-Bermani, M.L. Blackmore, W. Zhang, I. Todd, The origin of microstructural diversity, texture, and mechanical properties in Electron beam melted Ti-6Al-4V, *Metall. Mater. Trans. A* 41 (13) (2010) 3422–3434.
- [90] T. Vilaro, C. Colin, J.D. Bartout, As-fabricated and heat-treated microstructures of the Ti-6Al-4V alloy processed by selective laser melting, *Metall. Mater. Trans. A* 42 (10) (2011) 3190–3199.
- [91] P. Barriobero-Vila, J. Gussone, J. Haubrich, S. Sandlöbes, J.C. Da Silva, P. Cloetens, N. Schell, G. Requena, Inducing stable  $\alpha + \beta$  microstructures during selective laser melting of Ti-6Al-4V using intensified intrinsic heat treatments, *Materials* 10 (3) (2017) 268.
- [92] J. Yin, G. Peng, C. Chen, J. Yang, H. Zhu, L. Ke, Z. Wang, D. Wang, M. Ma, G. Wang, X. Zeng, Thermal behavior and grain growth orientation during selective laser melting of Ti-6Al-4V alloy, *J. Mater. Process. Technol.* 260 (2018) 57–65.
- [93] G.P. Dinda, A.K. Dasgupta, J. Mazumder, Evolution of microstructure in laser deposited Al–11.28%Si alloy, *Surf. Coat. Technol.* 206 (8) (2012) 2152–2160.
- [94] L. Thijs, K. Kempen, J.-P. Kruth, J. Van Humbeeck, Fine-structured aluminium products with controllable texture by selective laser melting of pre-alloyed AlSi10Mg powder, *Acta Mater.* 61 (5) (2013) 1809–1819.

## 5.4. Supplementary Data

### 5.4.1. Supplementary Data to the Published Paper

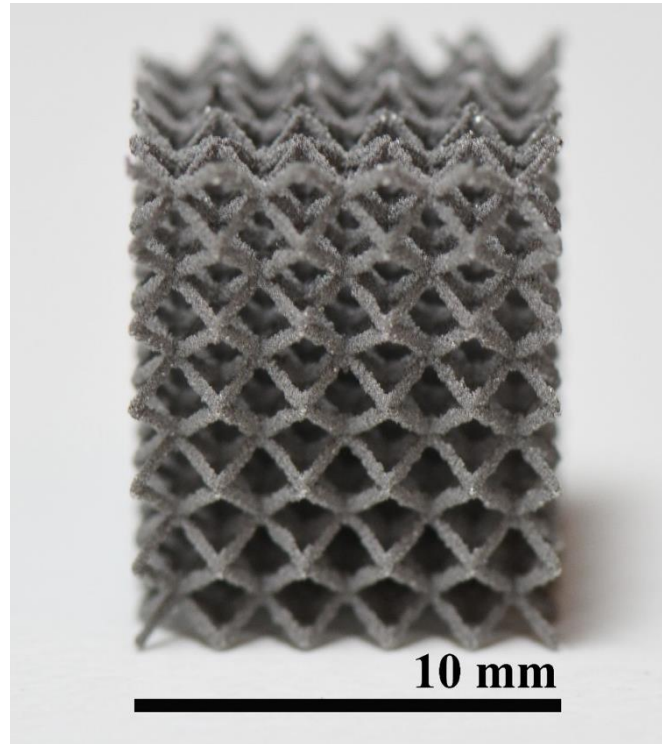


Figure 5. 1 A lattice cubic specimen with BCC unit cells was fabricated to demonstrate the capability of the single point exposure strategy to make angled struts and complex lattices (Figure S1).

Table 5. 1 Relative density calculation of the of the bulk material constituting the struts of the BCC cubic scaffold using Archimedes principle (Table S1).

Weight in Air ( $W_a$ ) g	Weight in Ethanol ( $W_e$ ) g	Density of Ethanol ( $\rho_e$ ) g/cm <sup>3</sup>	Density of BCC scaffold* ( $\rho_s$ ) g/cm <sup>3</sup>	Density of reference Ti64 [221] ( $\rho_{Ti64}$ ) g/cm <sup>3</sup>	True density of BCC scaffold (( $\rho_s / \rho_{Ti64}$ )*100) (%)
1.082	0.8827	0.789	4.28	4.43	96.7

$$* \rho_s = \frac{(\rho_e * W_a)}{(W_a - W_e)}$$

Table 5. 2 Porosity measurements calculated from the micro-CT images of the specimens. The values do not represent the real volume values as they are based on the 3D model. The ratio of the volumes should be taken into consideration (Table S2).

Sample ID	Pore volume ( $V_p$ )	Solid volume ( $V_s$ )	Total volume ( $V_t$ )	$V_p/V_t$	$V_p/V_t \times 100$ (%)
144W_1100us	4051681	770485076	774536757	0.005231	0.52311
144W_950 us	30956	5667144	5698100	0.005433	0.543269
144W_550us	27401	5965992	5993393	0.004572	0.457187
144W_350us	22801	3254902	3277703	0.006956	0.69564

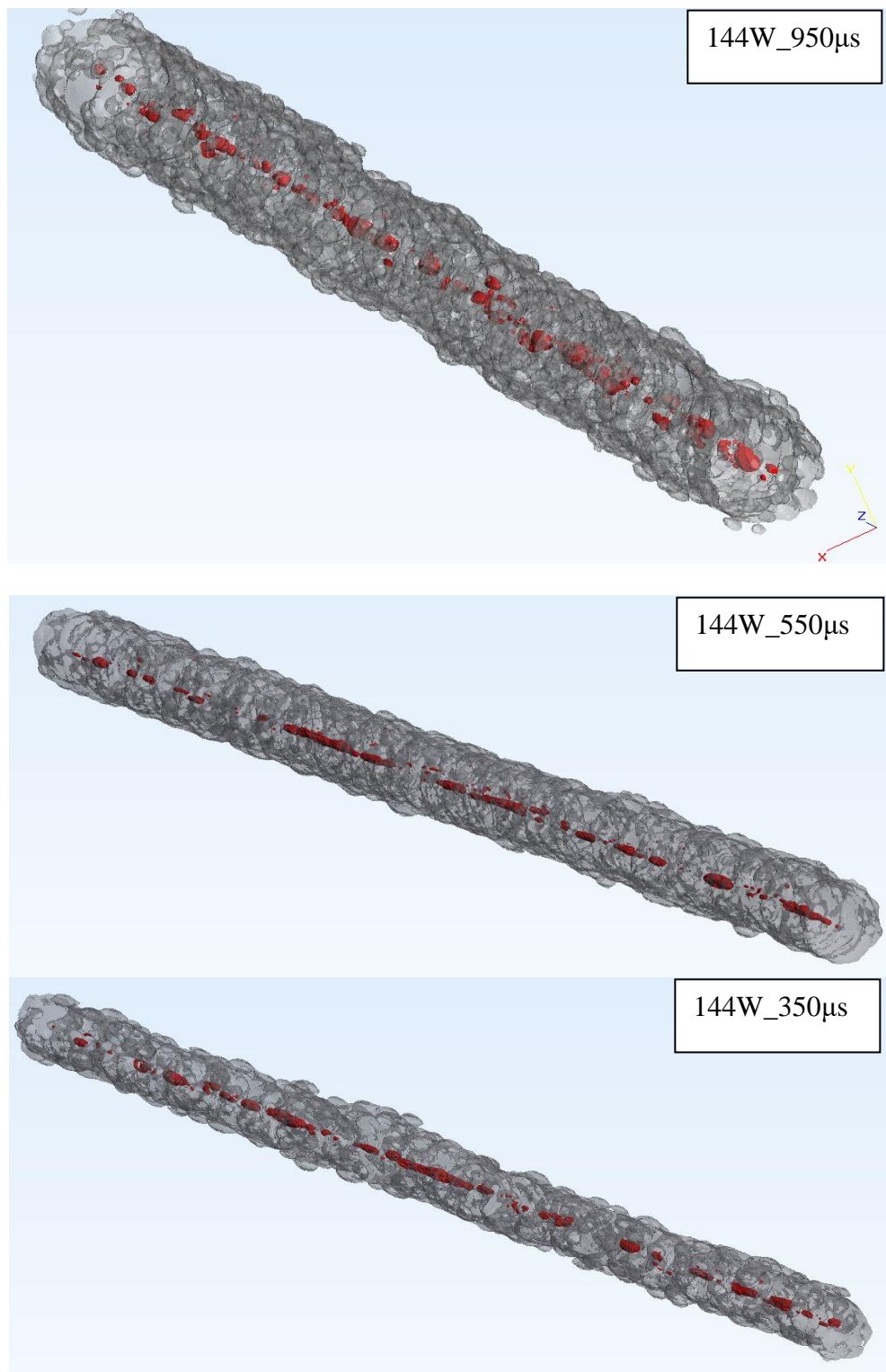


Figure 5. 2 The 3D models of the struts reconstructed using the micro-CT images. The red colored parts are the internal pores and the grey parts are the specimens (Figure S2).

### 5.4.2. Additional Supplementary Data

In addition to the data presented in the publication and the supplementary data published with the original paper, we performed other experimental work to study roughness of struts and chemical composition near the internal pores.

A Mitutoyo Surftest SJ400 machine was used to measure the surface roughness. The data obtained by this measurement includes surface roughness parameters (e.g.  $R_a$ ,  $R_q$ ,  $R_z$ ,  $R_{sk}$ ,  $R_{ku}$ ) and surface height profile over the measurement length (2.5 mm). A cut-off length ( $\lambda_c$ ) of 2.5 mm is chosen for all the roughness measurements. For each sample, 5 different measurements were taken to calculate mean  $\pm$  SD. Figure 5. 3 presents the surface profile of the single struts fabricated with laser powers of 128 W and 144 W, respectively, as well as the surface profile of the neighbouring struts fabricated at process parameters of 128 W-750  $\mu$ s and 96W-1150  $\mu$ s. Average values of Surface Roughness ( $R_a$ ), Kurtosis ( $R_{ku}$ ) and Skewness ( $R_{sk}$ ) showed no significant difference between the struts fabricated at different laser powers and process parameters. Surface height profiles of the neighbouring struts are shown in Figure 5. 4. Although there was no significant difference in the data obtained, SEM images of the neighbouring struts showed different surface profiles, *i.e.* the number of attached un-melted particles (Figure 5. 5). For example, the number of attached un-molten particles on the single strut (with a lateral difference of 'd' to another strut ( $d=d$ )) and on the double-melted struts (A2 and B2) are observed to be different in the SEM images (Figure 5. 5). It is therefore hypothesised that the Mitutoyo Surftest machine is not capable of measuring small features ( $< 5 \mu$ m). Further investigation on the surface roughness of the struts fabricated by single point exposure strategy is proposed to understand the effect of process parameters and build angle on the surface roughness.

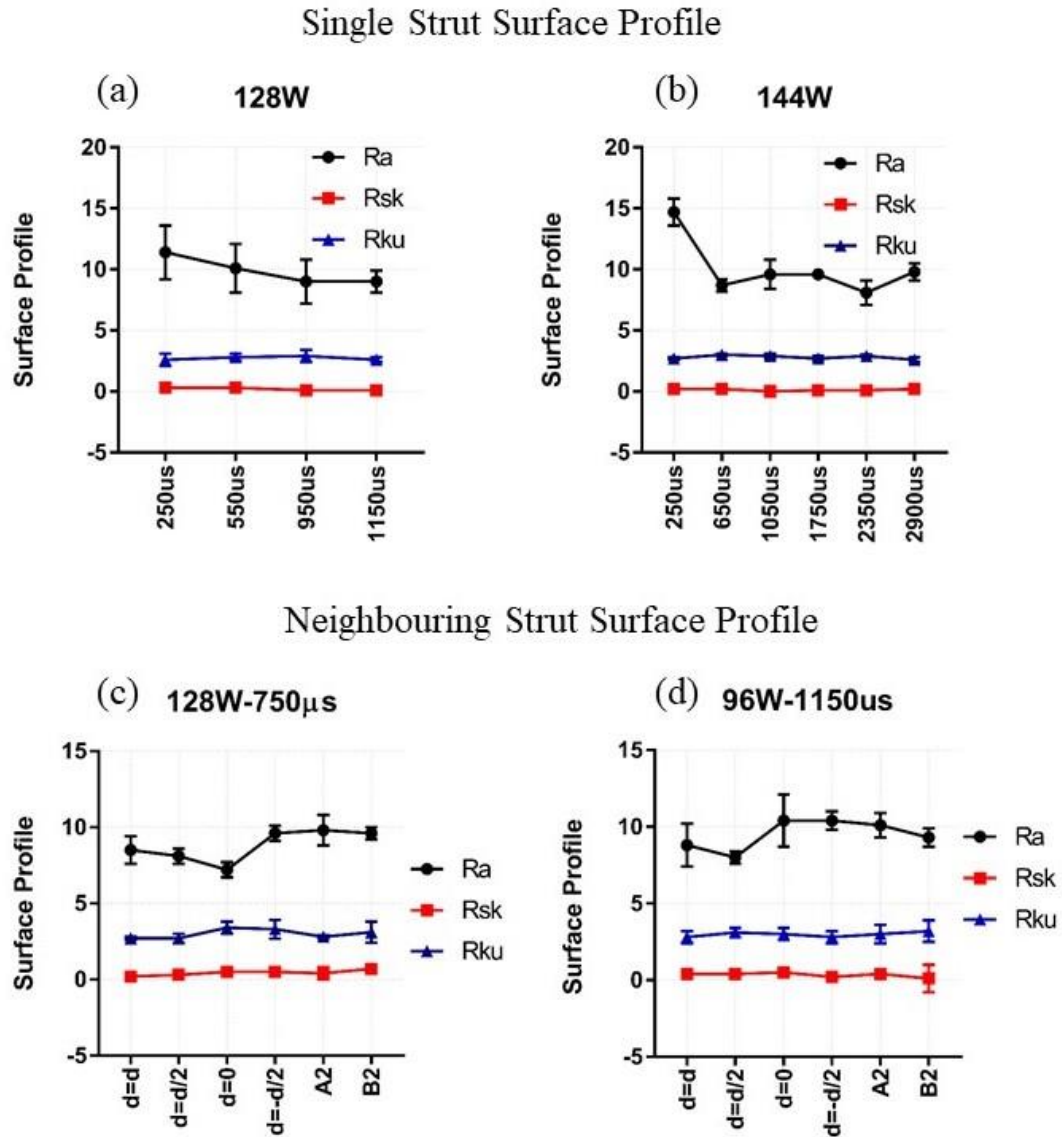


Figure 5. 3 Surface profile of the single struts fabricated at the laser power of (a) 128 W and (b) 144 W, and neighbouring struts at the process parameters of (c) 128 W-750  $\mu$ s and (d) 96W-1150  $\mu$ s. Here A2 and B2 refers to double-melted struts.



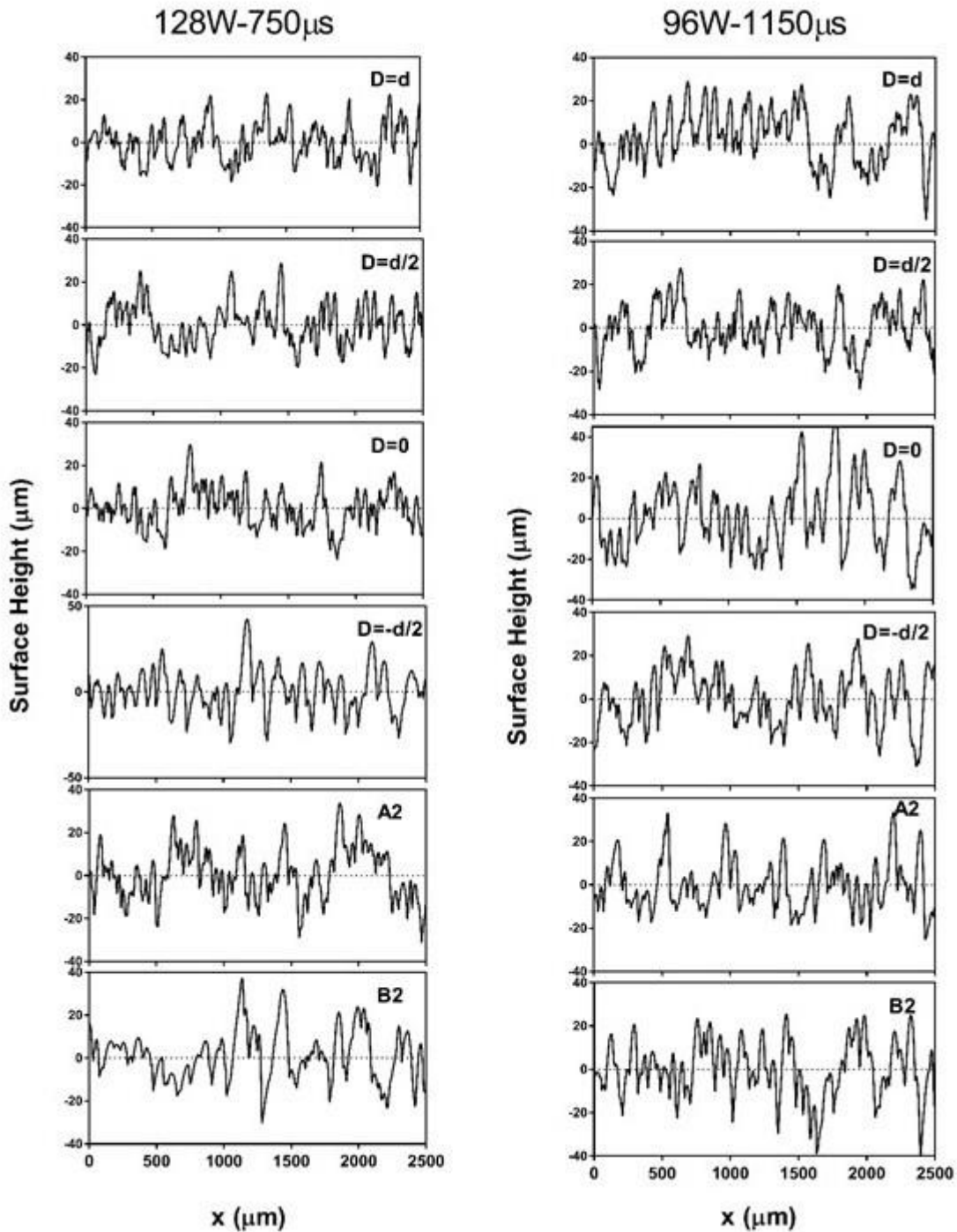


Figure 5. 4 Surface height profiles of neighbouring struts fabricated at 128W-750 µs and 96W-1150 µs. The profiles were obtained by the Mitutoyo SurfTest equipment. A2 and B2 refer to double-melted struts.

**96W-1150 $\mu$ s**

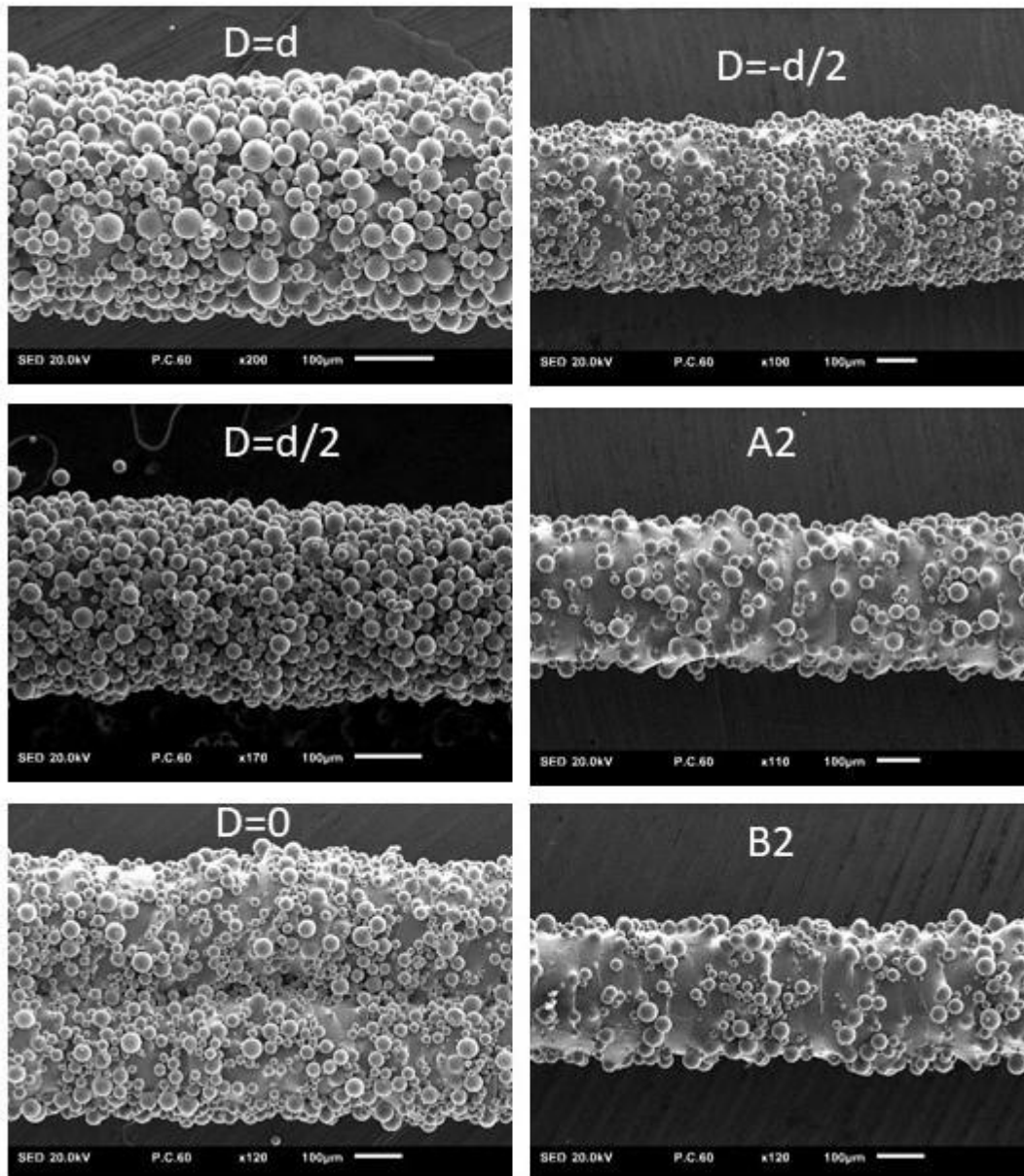


Figure 5. 5 The surface of the neighbouring struts and double-melted struts (A2 and B2), fabricated at 96W-1150  $\mu$ s, observed under the SEM.

Additionally, EDX elemental analysis was performed on one of the fabricated struts to analyse chemical composition near the pore. Figure 5. 6 shows the SEM image of the area mapped, and the elemental mapping (Ti, Al and V), as well as a line analysis. These images show that there is significantly less Ti, Al and V inside the pores and Al values almost drops to zero. This is most likely due to the evaporation of Al near and inside the pores. However, EDX analysis may not be reliable near the pores but can still provide indicative values. Further investigation of the chemical analysis of pores can provide insights into the causes of pore formation.

Figure 5. 7 shows a SEM image of unpolished surfaces from a Ti6Al4V bulk sample and strut. The bulk cube was fabricated prior to this study with contour-hatching scanning strategy. The SEM image of the bulk sample shows similarity of features observed on the surfaces of both bulk and strut samples. Although these features resemble the topology of basketwave Ti6Al4V microstructure, there is no additional data to support whether the observed microstructure is Widmanstätten  $\alpha$ . A study on these features observed on the unpolished surfaces of SLM Ti6Al4V is proposed as future work, which could be beneficial to understand the laser-material interaction.

In summary, the additional supplementary data on the surface roughness, EDX analysis and surface SEM image from a bulk sample unfolded questions around the laser-material interaction, pore formation and un-molten particles on the surface. These questions will be presented as future work in Chapter 7.

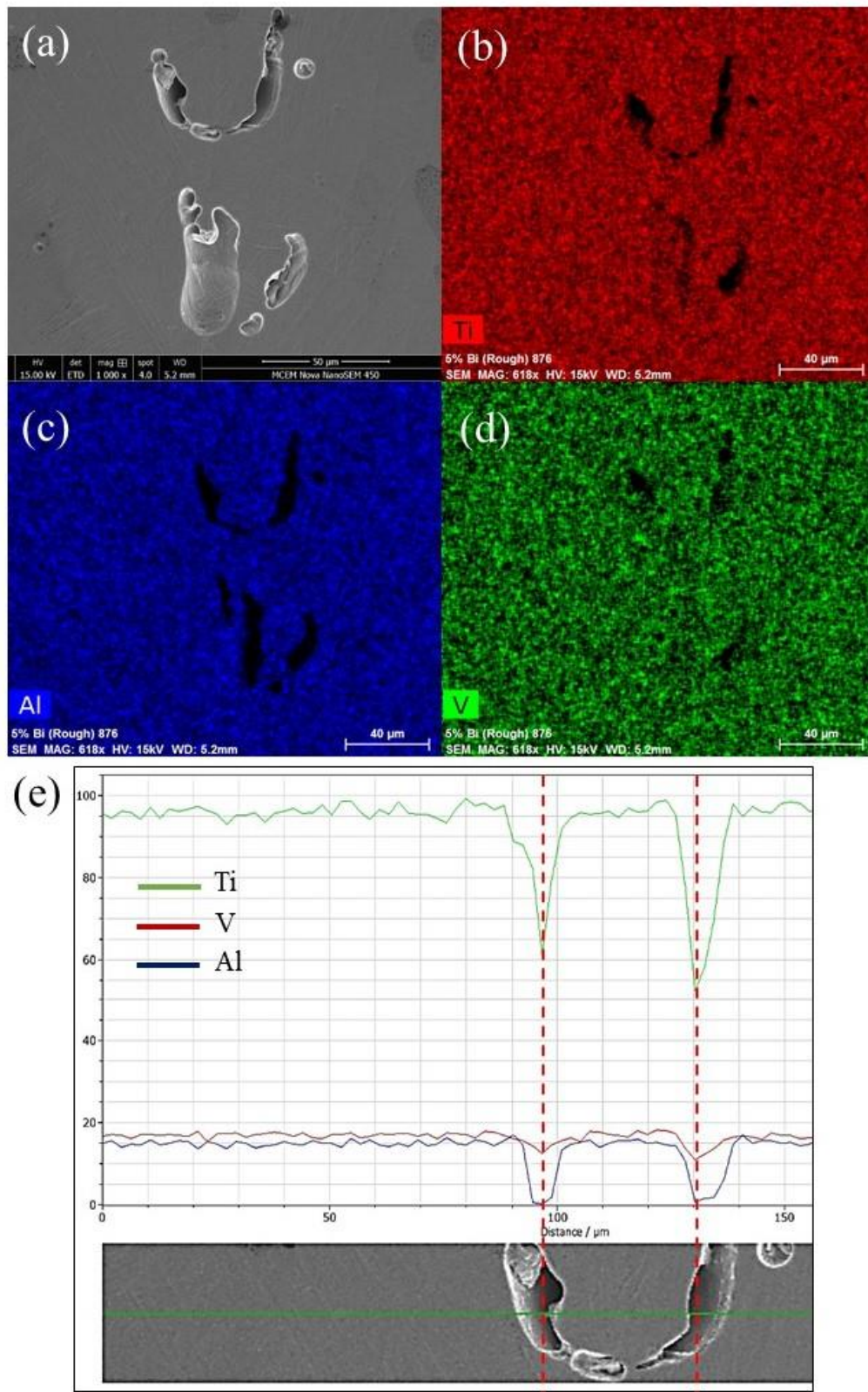


Figure 5. 6 (a) SEM image of internal pore in the double-melted strut, (b-d) EDX elemental mapping, (e) EDX line analysis of the same area.



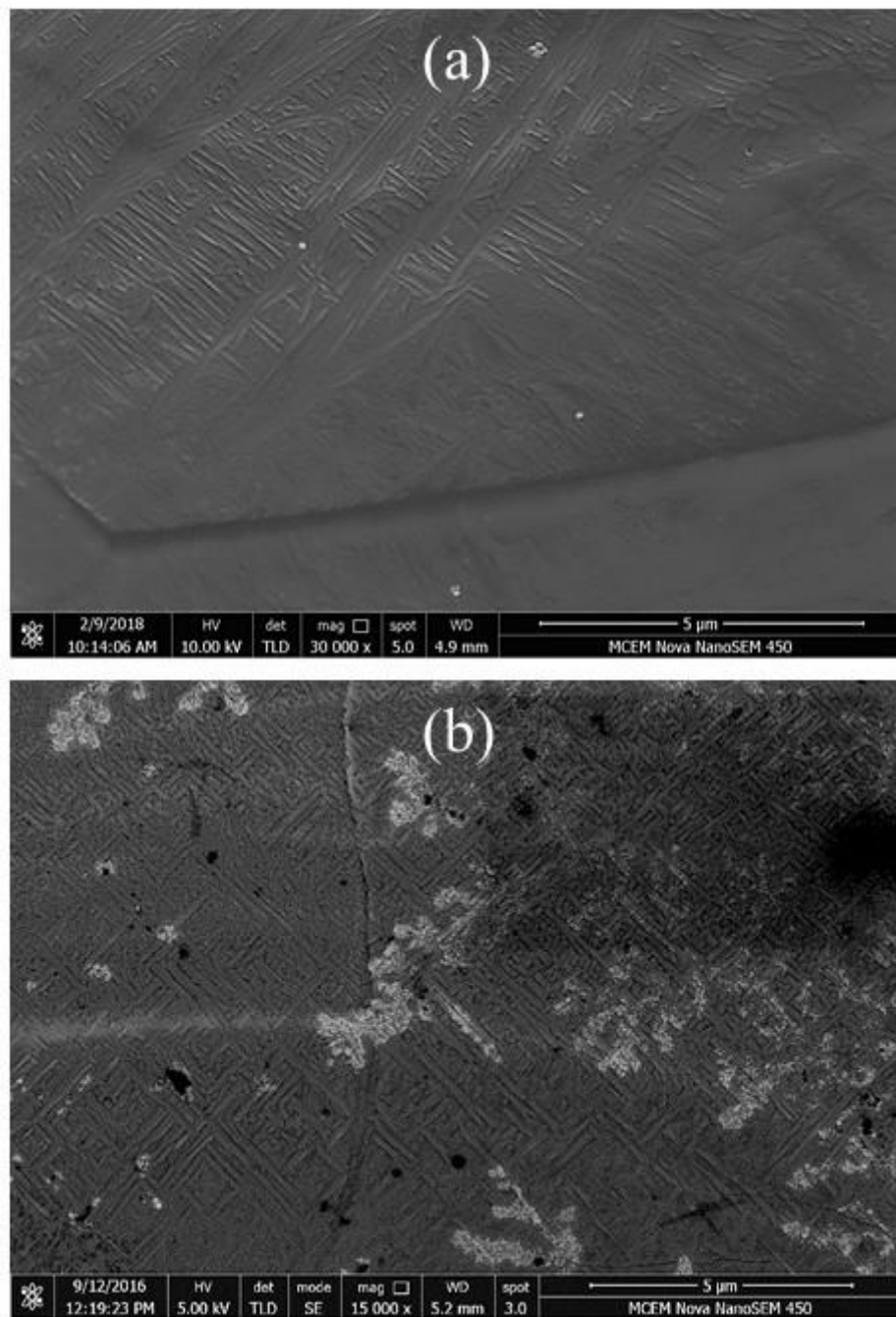


Figure 5. 7 Ultra-High-Resolution mode under the SEM, images of unpolished (a) single strut and (b) bulk Ti6Al4V cube.

## 5.4. Conclusion of the Chapter

In this chapter, single point exposure strategy was investigated as an alternative strategy to fabricate lattice structures. Single vertical struts were produced by testing more than 50 process conditions by varying laser power and exposure time. Furthermore, lateral heat effect and double-melting effect were studied by manufacturing struts in circular arrangements. The major findings of this work can be summarised as follows:

- The strut diameter increases with energy input up to a saturation point with single point exposure strategy. It is demonstrated that a maximum achievable strut size of 520  $\mu\text{m}$  is achieved at 0.5 J energy input. Changing the processing parameters can help tailor the size of a strut.
- Continuous pore formation was observed in the centre of the struts along the build direction. The morphology and the consistency of the pores suggest that they are keyhole pores.
- The amount of energy input and latent heat did not affect the microstructure of the struts; they all had martensitic  $\alpha$ -laths. However, some unusual relief, resembling basketweave microstructure, was observed on the unpolished surfaces of the struts when analysed with SEM. These features were further investigated by performing TEM on a cross-sectional area of the surface. TEM images showed that a more uniform structure with consistent  $\alpha$ -lath sizes (200-300 nm) were observed in double-melted struts, whereas single-melt struts had varying size  $\alpha$ -laths. (10nm to 1 $\mu\text{m}$ ). The homogeneity of the double-melted struts can be explained by the additional thermal effect of the second laser pulse.
- The overall shape and orientation of  $\alpha'$ -laths (randomly oriented) and prior  $\beta$ -columns (18-20° off the build direction) were very similar in both double and single-melted struts. However, the characteristic BOR-related correlation between  $\{0001\}_{\alpha}$  and  $\{110\}_{\beta}$  was no longer apparent in the case of double-melted specimens. It is hypothesised that double laser exposure has occurred at different times during the solidification/ $\beta \rightarrow \alpha'$  transformation processes. This might have disrupted the natural way in which the microstructures were



formed, thus resulting in unconventional arrangements of the phases with respect to each other.

This study investigated microstructural features of struts fabricated by single-point exposure strategy. The results of the study contribute to the existing literature by exhibiting novel microstructural features observed on the surfaces of the struts and by demonstrating the maximum achievable strut (or melt-pool) size with this strategy. The findings of this work can be used to tailor the processability to engineer the microstructure and morphology of the struts.

## Chapter 6. Hollow-tube Lattice Structures

## 6.1. Introduction

The results from Chapter 4 highlighted that functionally gradient designs can be tailored to possess suitable mechanical and biological properties. Specifically, it was shown that large pores ( $>1000\ \mu\text{m}$ ) at the surface support effective migration of the cells. Examples from nature, such as vasculature systems in humans and animals (arteries, veins, capillaries), make an effective use of tubular structures, see Figure 6. 1. These tubular structures have been successfully adopted in the field of architecture [222] and are a hot topic in tissue engineering [223].

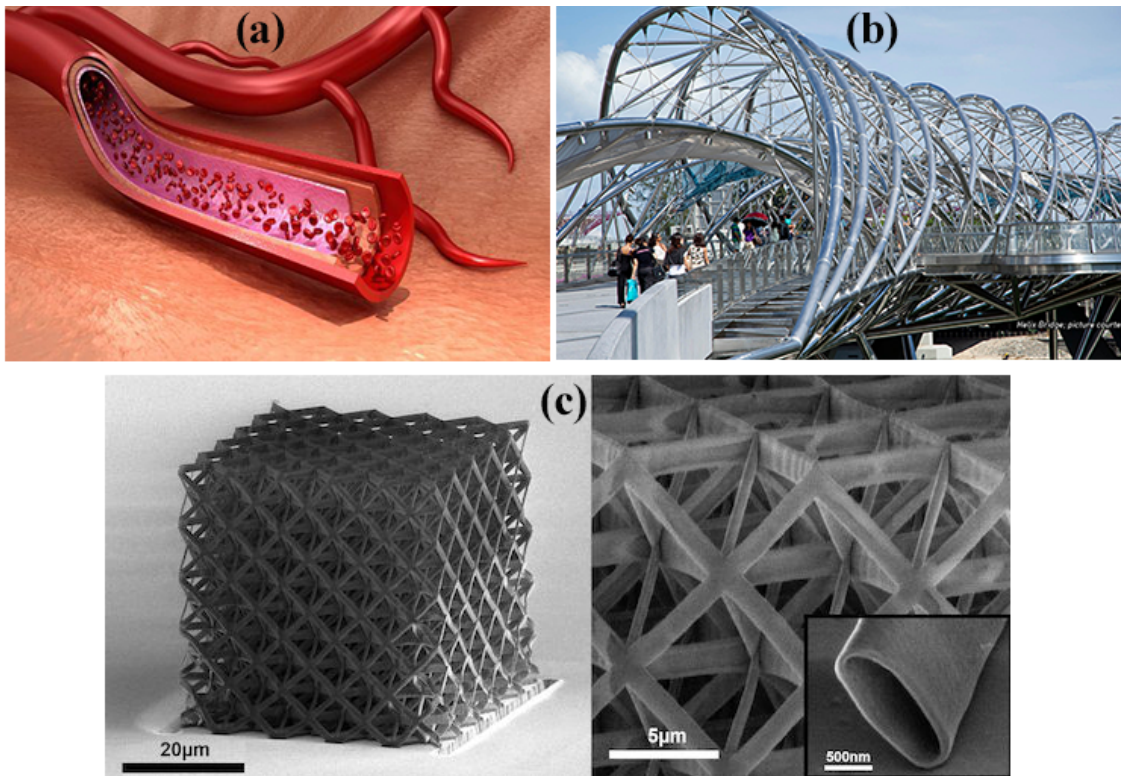


Figure 6. 1 Hollow lattice structures in (a) biology [224], (b) architecture [222] ,and (c) micro/nano size [225].

Here, we propose to incorporate the hollow-tube lattices for functional implants, and have adopted the knowledge on the size of the struts and internal channels from our results reported in Chapter 4. Designing hollow-tube lattice structures have been reported previously in

literature [127, 128, 226]. However, most of these studies are focused on either micro/nano size hollow lattices based on electroplating of polymer tubes [127, 128, 226], or on analytical and simulation models [227-229]. Some recent studies investigated the manufacturing of hollow-tube lattice designs using selective laser melting or sintering [230-233], focusing on their mechanical properties. Specifically, these structures have improved energy absorption capacities and strength compared to their solid counterparts at the same relative densities [230]. It should be noted that the use of hollow lattice structured manufactured by selective laser melting process for bone scaffold application is new and has not been fully explored yet.

Hollow-tube lattices are also referred to as shell-based lattices and referenced to triply periodic minimal surfaces in literature [233-235], due to their topology. Hollow-tube lattices and TPMS's are found to be stretch-dominated; whereas most of the strut-beam lattices tend to be bending-dominated structures [236]. According to the Gibson-Ashby model [110], stretch-dominated porous structures exhibit higher stiffness and strength than the bending-dominated structures for the same weight. Bonatti et al. [235] investigated the mechanical performance of SC, BCC and FCC shell- and truss- lattices and found that shell-lattices (which are similar to TPMS) exhibit substantially higher stiffness and strength than the truss-lattices of equal mass. They also exhibit high specific energy absorption for large strain compression. Yan et al. [237] and Bobbert et al. [13] fabricated Ti6Al4V TPMS structures and showed that their mechanical performance and structure mimic the human bones and offer potential to be used in orthopaedic implants.

Al-Ketan et al. [232] examined the effect of architecture on mechanical properties of SLM printed maraging steel. They studied BCC, primary, secondary and sheet-based IWP structures. Since sheet-based IWP structures resemble hollow-beam BCC structure, this study gives insights into comparison of the solid and hollow-beam BCC unit cells. They found that sheet-based IWP structure had the highest stress distribution when compressed due to absence of connecting nodes or sharp edges compared to other structures. Therefore, it can be concluded that hollow-beam structures have good stress transferring capabilities as they are free from nodes or stress concentrations. Sheet-based IWP, or hollow BCC, was also found to have significantly higher stiffness values (1.2 GPa) than the BCC structure (0.8 GPa) at 21% relative density. Bonatti et al. [235] also compared solid- and hollow-BCC structure and referred the

hollow-BCC to Schoen's IWP, as they share the same boundary conditions and symmetries as triply periodic minimal surfaces. The main difference between hollow-beam BCC and TPMS IWP structure was the local curvature measure, which is always zero for any TPMS, but found to be 14% for the hollow-BCC shell. They also reported that TPMS, like hollow-BCC, had 40% higher stiffness than the strut-based BCC at relative density of 30%; however, the pronounced stiffness advantage was diminished at lower densities (<10% relative density).

Another study on the effect of unit cell topology in terms of hollow vs. solid beams or strut vs. sheet-based lattices on the mechanical properties and deformation was reported by Bonatti et al. [230]. In this work, FEA and experiment testing were performed on the solid and hollow FCC structures, which were manufactured by SLM using stainless steel 316L. Both simulations and experimental work showed higher strength and stiffness values for the hollow FCC when compared to solid FCC of the same density. This work highlighted the difference in failure mechanisms between the solid and hollow-beam structures. The solid FCC lattice structure showed an oscillating stress-strain curve when compressed, and failed by shear collapsing of the unit cells. On the other hand, the hollow FCC lattice structure showed a monotonically increasing stress-strain curve. The deformation response for hollow-FCC included a concentration of plastic deformation at the spherical nodes. These nodes which were compacted by folding that resulted in macroscopically a smoother deformation.

Micro and nanofabrication techniques are also emerging for fabrication of sheet-based (or hollow-beam) lattices in addition to aforementioned AM technologies. Schaedlar et al. produced nickel thin hollow octahedral scaffolds with strut lengths of a few millimetres (1-4 mm) and hollow-tube thicknesses of a few hundred micrometres (100-500  $\mu\text{m}$ ) using combined techniques of self-propagating photopolymer waveguide (SPPW), electroless nickel plating and polymer etching [226]. This technique enables manufacturing of ultralight structures with a relative densities of  $10^{-4}$ - $10^{-1}$  %. Another emerging process method for micro and nano fabrication is multiphoton lithography (or direct laser writing), which relies on multi-photon absorption of photosensitive material that is transparent at the wavelength of the laser used. Hollow nanolattices with dimensions spanning from 100 nm to 1000 nm were reported in literature for cubic [238], kagome [239], octahedron and octet forms [240]. The ultralight hollow micro or nano lattices have exceptional mechanical properties. For example, Jang et al.

[239] reported tensile strength of 1.75 GPa for nano and hollow TiN structure at relative density of 0.013, and Bauer et al. [238] showed compressive strengths of 280 MPa for hollow nano alumina structure at relative densities below 1,000 kg/m<sup>3</sup>. Although micro and nano fabrication techniques offer multi-scale manufacturing, they are still under development and their applications are limited. AM is still the most promising method to manufacture the complex lattices for industrial or clinical applications.

The literature review demonstrates that hollow-beam lattices can offer higher stiffness, strength and energy absorption capacity compared to the strut-based lattices with the same relative density. In addition, due to absence of nodes which act as stress concentration points, hollow-lattices fail by folding of the hollow beam junctions and exhibit a monotonous and smooth stress-strain curve, which is associated with their high energy absorption capacity. Whereas, solid-beam lattices fail suddenly by diagonal shear collapse and have a fluctuating stress-strain curve after yield point.

The advantages of hollow-beam lattices also include use of the additional pores for biological purposes, including targeted drug-delivery. For example, Mueller et al. [241] showed a femoral stem implant with inner channels that was manufactured by SLM. The channels within this implant can be loaded with antibiotics to treat possible infections after surgery. According to Bezuidenhout et al. [242], infections acquired from the implant are difficult to treat, and the antibiotics administrated orally or intravenously do not always reach the implant area. To solve this problem, implants can be functionalized by incorporating antibiotics inside the channels of the implant, so as to administer the antibiotic directly to the site of infection. Burton et al. [243] developed a lattice structure that could be used in the design of therapeutically loaded orthopaedic hip implant, which can be used as an alternative to the commercially available traditional cement spacer.

Although lattice structures and inner channel designs were studied and proposed to be used in therapeutically loaded implant designs, there has been no effort to combine channel designs in lattice structures. In this chapter, hollow-beam lattice structures that can be functionalised by therapeutic agents and used in implant designs, are investigated. It includes the study on the processability and mechanical and biological response of hollow-beam lattice structures and aims to establish design guidelines for functional implants.



## 6.2. Methods and Materials

### 6.2.3. Study Design

We designed hollow-beam lattice structures based on BCC, zBCC and 2zBCC unit cells. BCC structure is selected for the sake of simplicity and consistency with designs in Chapter 4. The other two are selected since zBCC is a BCC unit cell with extra trusses at the corner nodes; whereas 2zBCC is a BCC unit cell with trusses at corner and centre nodes. Hollow-tube designs were achieved by Boolean operations by subtracting the inner truss from the outer truss. Therefore, the hollow tube thickness can be found by finding the difference of the outer and inner truss radius. The outer truss radius of 1.5mm was kept same for all samples and the inner truss radius' values were 1.2 mm and 0.9 mm, generating hollow-tube thicknesses of 0.3 and 0.6 mm, respectively (Figure 6. 2c,b). The inner to outer radius ratios for the designs with hollow-beam thicknesses of 0.3 and 0.6 mm were 0.8 and 0.6, respectively. The solid counterparts of all of the lattice structures were also generated (Figure 6. 2a). The inner to outer radius ratios for solid lattice structures were zero. Cubic scaffolds were constructed by merging an array of 4 unit cells in x-, y- and z-directions (Figure 6. 2d). The dimensions of the cubic scaffolds were 15x15x15 mm since the edge length of each unit cell was 3.75 mm.

In addition to the given scaffold designs, we designed hollow-tube BCC lattice structures with different values of hollow-beam thicknesses and inner/outer radii to study the processability of extreme dimensions. The unit cell size was kept the same and the edge length was selected to be 3.75 mm. The first scaffold had hollow-tube thickness of 0.2 mm to study the minimum achievable tube thickness, the second scaffold had inner channel radius of 0.5 mm and the third scaffold had outer channel radius of 1.8 mm to assess if there is any pore blockage. These values are summarised in Table 6. 1, which also includes the dimensions of the scaffolds from the original study.

Table 6. 1 Hollow-beam lattice structure design parameters

Scaffold ID	Outer Truss Radius ( $R_0$ ) (mm)	Inner Truss Radius ( $R_i$ ) (mm)	Hollow-tube thickness (t) (mm)
Original Study (BCC-zBCC-2zBCC)	1.5	1.2	0.3
	1.5	0.9	0.6
Process-ability	1.3	1.1	<b>0.2</b>
Study (BCC)	1.3	<b>0.5</b>	0.8
	<b>1.8</b>	1.0	0.8

All specimens were fabricated on a Mlab Cusing machine (Concept Laser, Lichtenfels, Germany) equipped with a fibre laser 100 W using Ti-6Al-4V-ELI powder supplied by Falcon Tech (Falcon Tech. Co., Ltd. Wuxi, China) with a particle size ranging from 15 to 50  $\mu\text{m}$ . The specimens were fabricated using a 95W laser power, 600 mm/s scan speed with a 0.08mm hatch distance, 50 (-5,+25)  $\mu\text{m}$  beam spot size and 25  $\mu\text{m}$  layer thickness. After the specimens were removed by electrical discharge machining, they were washed in ultrasonic bath for 2 h to aid in removing the residual particles from the pores. No further surface modifications and heat treatments were applied to the specimens.

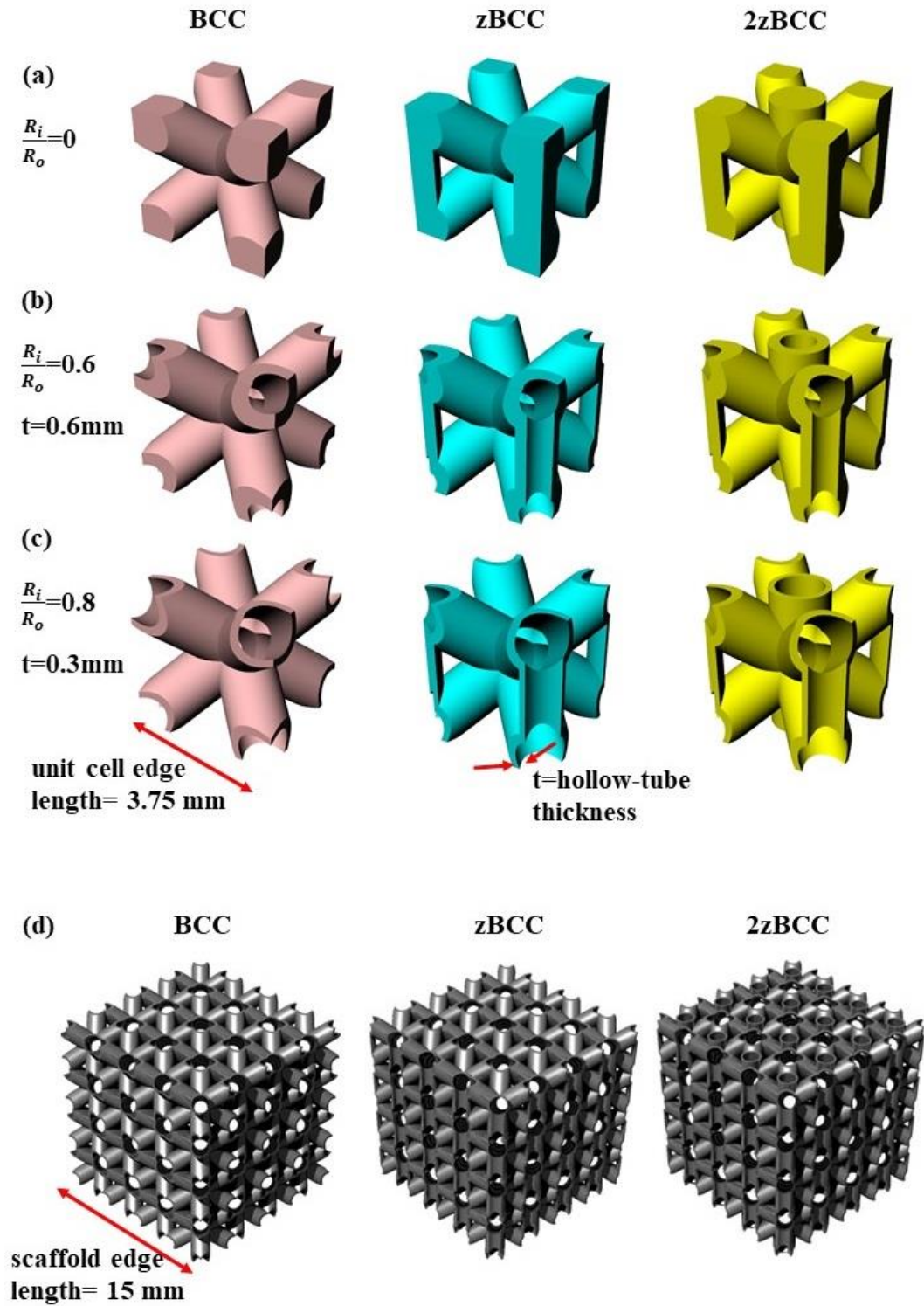


Figure 6.2 CAD illustrations of (a) solid unit cells and unit cells with hollow-tube thickness of (b) 0.6 mm and (c) 0.3 mm for the BCC, zBCC and 2zBCC topologies. (d) Cubic scaffolds made of  $4 \times 4 \times 4$  unit cells with scaffold edge length of 15mm.

### 6.2.3. Morphological properties

The specimens were photographed by Nikon D5200 digital single-lens reflex camera with macro lens (AF-S micro-nikkor 105mm 1:2.8G ED) to visually inspect the channels and make an initial assessment whether the pores were blocked or were free after the manufacturing process. In addition to imaging, several specimens were investigated by a micro-CT scanner (Zeiss Xradia 520 Versa, Zeiss, Oberkochen, Germany) to visualize the inner channels. The BCC and 2zBCC specimens with hollow-tube thicknesses of 0.6 mm were scanned with a voxel size of 22.8  $\mu\text{m}$ . The scanning parameters used were: 140 kV/72  $\mu\text{A}$  source power, 22.8  $\mu\text{m}$  voxel size, 95 mm distance between the source and the sample, and 190 mm distance between the detector and the sample. CT images were reconstructed to create a 3D model of the specimen using Mimics 21.0 (Materialise, Leuven, Belgium). Moreover, the 2zBCC specimen was scanned with a voxel size of 5  $\mu\text{m}$  to inspect the internal porosity within the trusses, which is a characteristic result of the additive manufacturing process. For this scan, the source power was 140 kV/71  $\mu\text{A}$ , the distance from of the source from the detector was 55 mm and, and the distance of the detector from the sample was 320 mm.

The volume fraction and relative density of the specimens were measured by digital densitometry (SD-200L, AlfaMirage, Osaka, Japan), which adopts the Archimedean principle. Three samples for each specimen were used to measure the volume fraction and relative density.

As-fabricated morphology of the specimens were inspected using SEM (FEI Nova NanoSEM, Thermo Fisher Scientific, Hillsboro, OR, USA) imaging to observe the pores and beam-wall thicknesses. The microstructure of one of the specimens was observed under optical microscope (Olympus GX51, Olympus Corp., Tokyo, Japan). The specimen was grinded from the top section perpendicular to the building direction and was polished with 3  $\mu\text{m}$ , 1  $\mu\text{m}$  diamond solutions and with an oxide polishing suspension. Finally, the struts were etched with the Kroll's etchant for 30 s to reveal the microstructure.

#### 6.2.4. Mechanical Properties and Deformation Response

A minimum of three specimens of each hollow-beam structure were tested under compression using an Instron 5982 universal testing machine with a 100 kN load cell. The solid-beam structures were tested using an Instron 8803 testing system with a 500 kN load cell. Following the standard for compression tests for porous and cellular metals (ISO 13314:2011), a constant cross-head velocity of 0.9 mm/min was utilised corresponding to a compression strain rate of  $10^{-3} \text{ s}^{-1}$ . The engineering compressive stress was calculated by normalizing the applied compression load with the initial cross-section area of each sample ( $15 \times 15 \text{ mm}^2$ ) and the engineering strain was calculated by the displacement of the cross-heads. The stress-strain curves of each sample were analysed and the following mechanical properties were calculated based on the guidelines of the ISO Standard 13314:2011: maximum compressive strength ( $\sigma_{\max}$ ) (the first local maximum in the stress-strain curve), 0.2% offset yield stress ( $\sigma_y$ ), and the elastic gradient ( $E$ ). The elastic gradient was calculated between stresses of 20-70 MPa, 50-150 MPa and 100-200 MPa for the hollow-beam structures with tube thickness of 0.3 mm, 0.6mm and solid-beam structures, respectively. The range of stresses was chosen according to the best representation of the elastic straight line. A series of images were captured every 1 s during compression testing to record the deformation response of the samples.

#### 6.2.5. *In-Vitro* Study

In this study, MG63 mouse osteoblast cells were used to assess cell viability and proliferation in solid BCC and 2zBCC, and hollow BCC and 2zBCC with hollow-beam thickness of 0.3 mm. These four designs are chosen to compare solid vs. hollow structures as well as BCC vs. 2zBCC structures, so that both the effect of hollow-beams and z-vertical channels on the cell migration can be assessed. The hollow structures are named and used as hBCC and h2zBCC, whereas BCC and 2zBCC represent the solid-beam lattices. MG63 cell line was used instead of MC3T-E1 cells. We anticipated that there is no significant difference between the two cell lines for the planned study.

The scaffolds were seeded with  $1 \times 10^5$  cells/scaffold by using Method A, as explained in Chapter 4.2, in 12 multi-well plate. Empty wells were also seeded with cells as positive controls. MTS assay was performed at 24 hour and 7-day time points, following the

experimental method given in Chapter 3.5. Fluorescent images were taken from the bottom and top of the scaffolds at two time points, following the same procedure described in Chapter 3.5. The scaffolds and controls were set in triplicates. One-way analysis of variation (ANOVA), together with Tukey–Kramer post-hoc analysis, were used to identify significant differences (significance threshold:  $p < 0.05$ ).

## 6.3. Results

### 6.3.1. Morphological Properties

Initial images taken by digital camera showed that all of the hollow-specimens including the trial ones for the processability study, have unblocked clear channels (Figure 6. 3a). Fusing of the neighbouring struts was not observed at the designed dimensions. In addition to digital imaging, micro-CT scans showed no blockage of the hollow tubes and pores were free of residual powder after ultrasonic washing (Figure 6. 3b). The micro-CT scans were used to create a 3D model of the 2zBCC\_t0.3 scaffold (Figure 6. 3c), and sliced at random layers to observe the inside of the hollow-tubes (Figure 6. 3d). The combined results of digital camera imaging and micro-CT scanning proved that SLM is capable of manufacturing hollow-tube lattices with pores as small as 0.5 mm and hollow-tube thicknesses of 0.2 mm.



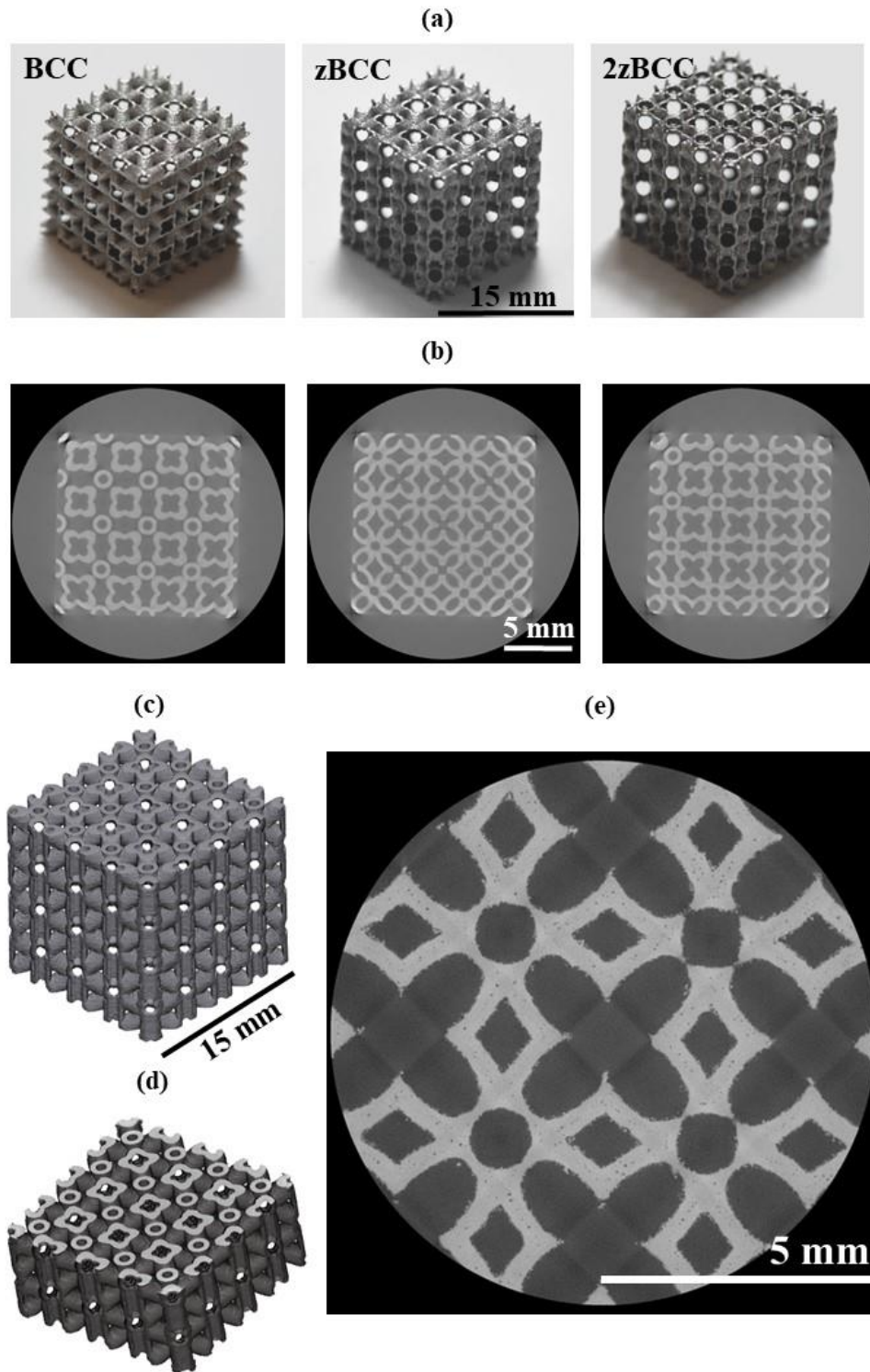


Figure 6. 3 (a) As-fabricated cubis scaffolds imaged by digital camera, (b) micro-CT images of 2zBCC with voxel size of  $22.8 \mu\text{m}$  from different locations, (c) constructed into a 3D model, (d) and sliced in the half. (e) Micro-CT image of 2zBCC with voxel size of  $5 \mu\text{m}$ , showing internal porosity.

Micro-CT images with voxel size of 5  $\mu\text{m}$  showed the internal pores that are smaller than the voxel size. Pores were located in the middle of the struts/ sheets, which is an expected characteristic of SLM lattices [244]. Pores were observed to be micron size and less than 0.5% of the overall structure (Table 6. 2). Table 6. 2 also presents the difference between designed and measured volume fractions of the structures. The observed difference was found to be 5-10% and is consistent with our previously reported studies and literature.

Table 6. 2 The volume fraction and relative density of the specimens.

Scaffold ID	Volume Fraction (%)			Relative Density (%)
	CAD Design	Experiment	Difference	
BCC(t0.3)	16.0	26.7 $\pm$ 0.2	10.7	99.7 $\pm$ 0.2
zBCC(t0.3)	16.6	27.5 $\pm$ 0.2	10.9	98.0 $\pm$ 2.2
2zBCC(t0.3)	17.3	27.5 $\pm$ 0.4	10.2	99.9 $\pm$ 0.2
BCC(t0.6)	31.1	44.0 $\pm$ 0.2	12.9	96.5 $\pm$ 3.4
zBCC(t0.6)	32.9	44.0 $\pm$ 0.2	11.1	98.9 $\pm$ 0.7
2zBCC(t0.6)	34.7	43.4 $\pm$ 0.3	8.7	99.2 $\pm$ 0.1
BCC	55.7	60.1 $\pm$ 0.2	4.3	99.6 $\pm$ 0.5
zBCC	60.3	65.2 $\pm$ 0.3	4.9	99.7 $\pm$ 0.4
2zBCC	64.9	68.6 $\pm$ 0.2	3.7	99.9 $\pm$ 0.1

SEM images (Figure 6. 4a-c) also show that the pores are free from residual powder and not blocked. The pore shapes can be also distinguished by SEM images. The additional vertical z-struts to the BCC structure introduce spherical pores to the structure, as well as diamond and square-shaped pores. These pores are identified by lines that are color-coded. It is known that pore shape controls the cell attachment [188] and it will be interesting to investigate *in-vitro* cell behaviour of BCC, zBCC and 2zBCC to assess the extent of pore shape effect on cell proliferation. SEM images also reveals the surface characteristics of as-fabricated structures, which is similar to the surface of functionally gradient scaffolds that were manufactured on the

same SLM machine with the same powder. The surface roughness can be attributed to the attached non-molten particles. The microstructure of all the specimens (Figure 6. 4d) included martensitic  $\alpha'$ -laths, which is characteristics to SLM Ti6Al4V lattices.

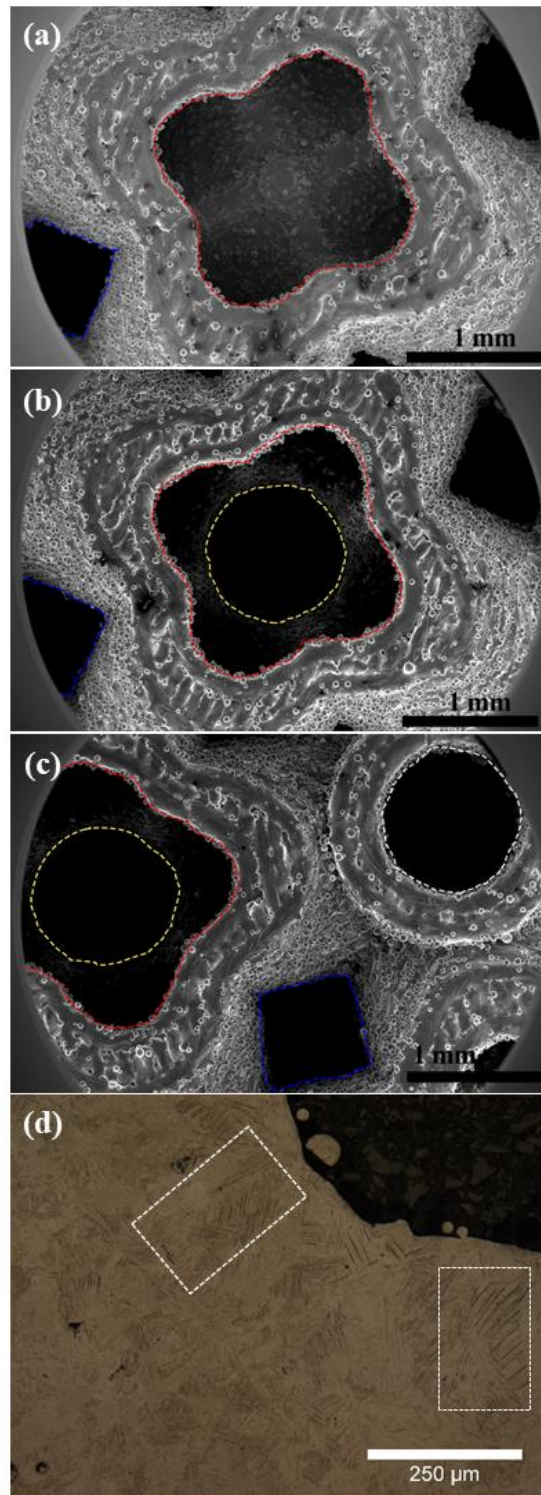


Figure 6. 4 SEM images of hollow (a) BCC, (b) zBCC, (c) 2zBCC scaffolds. Each coloured line represents different pores, introduced by the design. (d) Optical microscope image of hollow BCC scaffold, the white boxes show the martensitic  $\alpha$ -laths.

### 6.3.2. Mechanical Properties

The compressive nominal stress-strain plots of hollow-beam and strut-based lattice structures are presented in Figure 6. 5. The stress-strain curves of strut-based BCC, zBCC and 2zBCC lattices exhibit characteristic stages of deformation for cellular solids, including a linear-elastic region, followed by a plateau region with fluctuating stresses. Although these strut-based lattices showed similar deformation behaviour, they reached different levels of maximum stress and possessed different elastic moduli due to additional z-struts. For example, zBCC structure exhibited elastic moduli and yield stress values of almost twice that of the BCC structure (Table 6. 3). This shows that vertical corner columns carried as much load as the BCC structure. The additional centre z-strut in 2zBCC structure also increased the stiffness and strength as compared to zBCC.

The stress-strain curves for hollow-beam structures initially showed similar behaviour to the uniform scaffolds; however, they didn't have the fluctuating plateau region. Instead, the deformation continued monotonously and smoothly (Figure 6. 5).

Elastic moduli, yield stress and maximum compressive stress values of the hollow-beam lattices were lower than those of solid-beam lattices for any unit cell topology due to the difference in relative densities. However, when they were compared to each other at the same relative densities, the hollow-beam lattices showed higher stiffness and strength. For example, literature reported [116, 245] elastic moduli of 1.6 GPa and 1.9 GPa, and yield stresses of 53 MPa and 42 MPa, for BCC structures with relative densities around 26%. Here, hollow-BCC structures with relative density of 26% exhibited elastic moduli of 2.3 GPa and yield stress of 102 MPa. At the same relative density, the hollow BCC showed 30% higher elastic modulus and 110% higher yield stress.

The elastic moduli, the 0.2% offset yield stress ( $\sigma_y$ ) and the first maximum compressive strength ( $\sigma_{max}$ ) of the scaffolds are summarised in Table 6. 3. Elastic modulus, yield stress and compressive strength increases with hollow tube thickness from 0.3 mm to 0.6 mm for all of the unit cells.



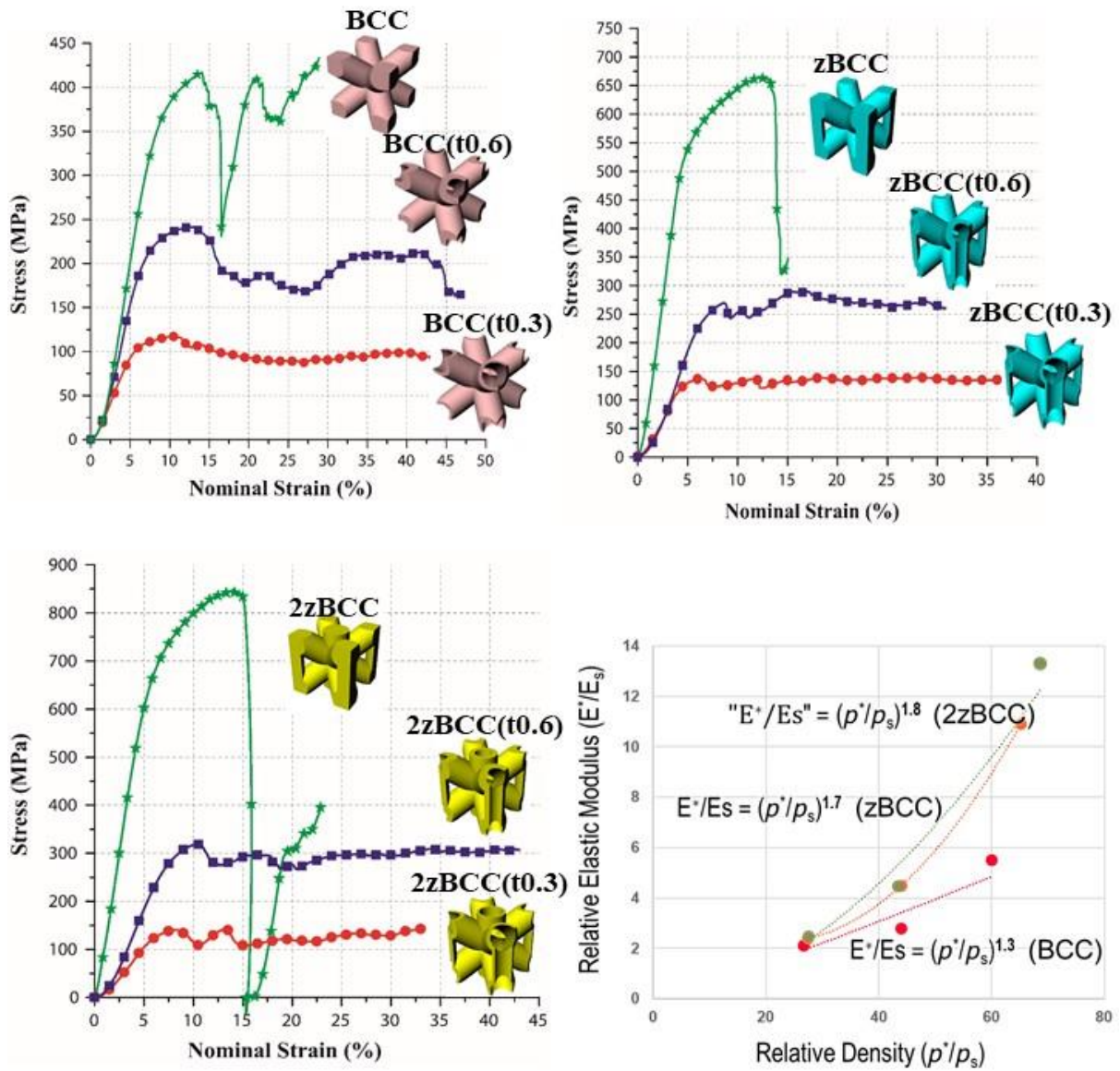


Figure 6. 5 Stress-strain curves of (a) BCC, (b) zBCC and (c) 2zBCC hollow and solid lattices. (d) Relative density vs Relative Elastic Modulus of all the structures with fitted power law curves.

Table 6. 3 The summary of the mechanical properties of hollow and solid beam structures measured by compression tests (Mean  $\pm$  SD).

Scaffold ID	$E$ (GPa)	$\sigma_y$ (MPa)	$\sigma_{max}$ (MPa)
BCC(t0.3)	2.3 $\pm$ 0.1	102 $\pm$ 4	121 $\pm$ 3



zBCC(t0.3)	2.6±0.4	107±15	128±12
2zBCC(t0.3)	2.7±0.3	112±10	135±7
BCC(t0.6)	3.1±0.1	176±1	233±7
zBCC(t0.6)	5.0±0.1	207±19	261±14
2zBCC(t0.6)	5.0±0.1	258±10	315±4
BCC	6.1±0.2	275±6	413±8
zBCC	12.0±1.3	407±11	657±11
2zBCC	14.6±1.1	530±31	853±9

In order to provide a better comparison between different lattice unit cells, relative elastic modulus ( $E/E_s$ ) is plotted against the measured relative density ( $p^*/p_s$ ) (or volume fraction) (%) in Figure 6. 5d. Elastic modulus was normalized relative to the values of solid Ti6Al4V (110 GPa). The observed average trend shows a positive power law relation with volume fraction. This trend corresponds to theoretically expected behaviour of bending-dominated structures for the BCC structure and stretch-dominated structure behaviour for the zBCC and 2zBCC structures [109]. Similar results are also reported in literature [133].

Images of the initial stage and the progressive failure of hollow-beam and strut-based structures recorded during the compression tests (Figure 6. 6) show that the major failure bands were formed at a  $45^\circ$  angle from the loading direction for all strut-based unit cell topologies. For the hollow-beam structures, buckling of the hollow-beams were observed either horizontally (BCC) or diagonally (zBCC and 2zBCC), which lead to a more stable and smoother failure as compared to sudden failure of strut-based lattices. Due to lack of nodes or stress concentration in hollow-beam lattices, the beams failed by folding of the hollow-beam junctions, as shown with red arrows.

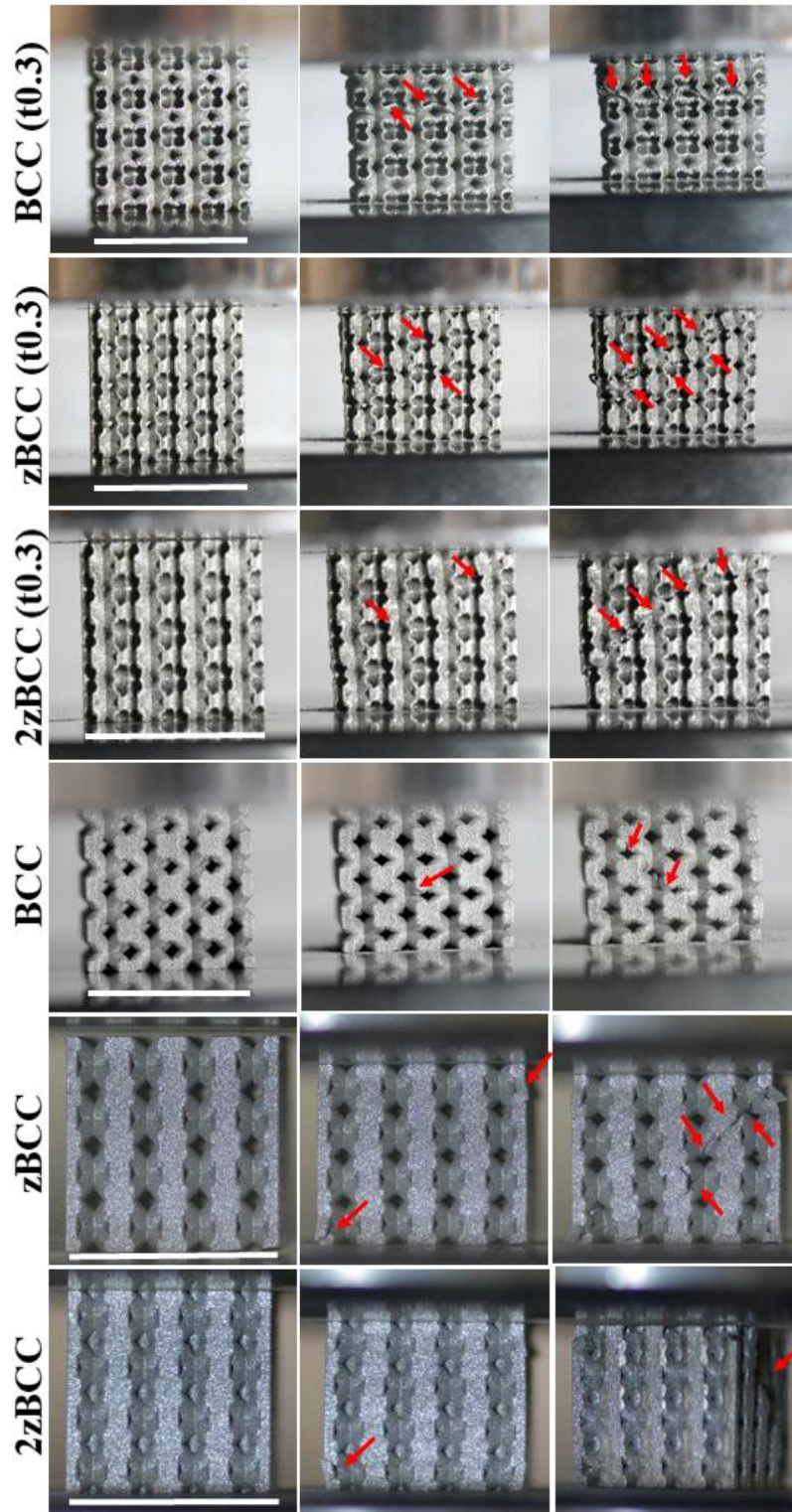


Figure 6. 6 Failure modes of BCC, zBCC and 2zBCC structures with hollow-tubes (0.3mm thickness) and solid-beams. Left images represent the initial state, middle and right images present the progressive failure. Arrows point the regions of deformation and failure (Scale bars = 15mm).

### 6.3.3. *In-vitro* Response

The degree of the cell adhesion and viability of the MG63 cells on the scaffolds were determined using MTS assay, which was performed after 24 hours (1 day) of cell seeding. Further, the extent of cell proliferation on the scaffolds was assessed by performing the MTS assay after 7 days of cell seeding. There was no significant difference in cell numbers between the scaffolds at both of the time points. The difference between the scaffolds and the positive control at Day 1 is due to the fact that the scaffolds are porous and some of the cells could not attach to the scaffolds, whereas the positive control had all of the seeded cells. However, the difference in cell numbers between the positive controls and the scaffolds diminished after 7 days. This shows the ability of cells to proliferate on the scaffolds increased from day 1 to day 7. This can be also seen in Figure 6. 7, whereby the OD absorbance is shown to almost double for all of the scaffolds. The number of the cells on the positive control wells did not change much due to a confluent layer of cells and the limited space (only the bottom of the well plate) for cells to proliferate.

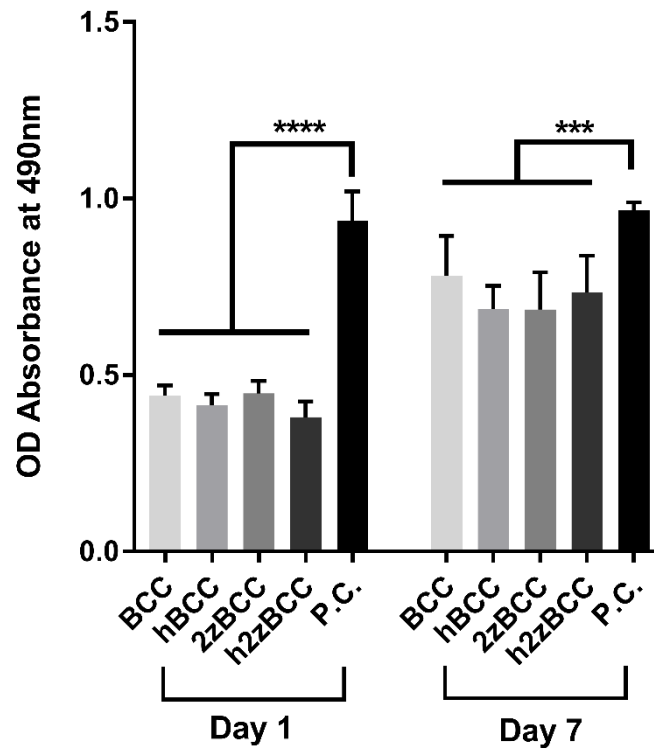


Figure 6. 7 Cell proliferation measured by MTS assay after culturing 1 and 7 days on the solid and hollow lattice structures. Data were presented as mean  $\pm$  SD (n=3). (\*\* $p < 0.001$  and \*\*\*\* $p < 0.0001$  when compared using ANOVA Tukey-Kramer post-hoc test).

Further to cell proliferation assay, cell distribution and migration on the solid and hollow-beam lattice structures were studied by staining and imaging the cell nuclei and actin cytoskeleton. Based on the images in Figure 6. 8, there are more cells on the bottom of the hollow-beam lattices as compared to the solid lattices at both time points. Although, this doesn't appear to be reflected in the MTS data. Since the MTS assay results suggest that the number of cells on the overall scaffolds are similar, these images suggest that the distribution throughout the hollow-beam lattice structure is more uniform as compared to solid ones. The number of the cells on the top of all of the scaffolds look increased from day 1 to day 7, which aligns with the results of the MTS assay. This shows that MG63 cells proliferated on the scaffolds.

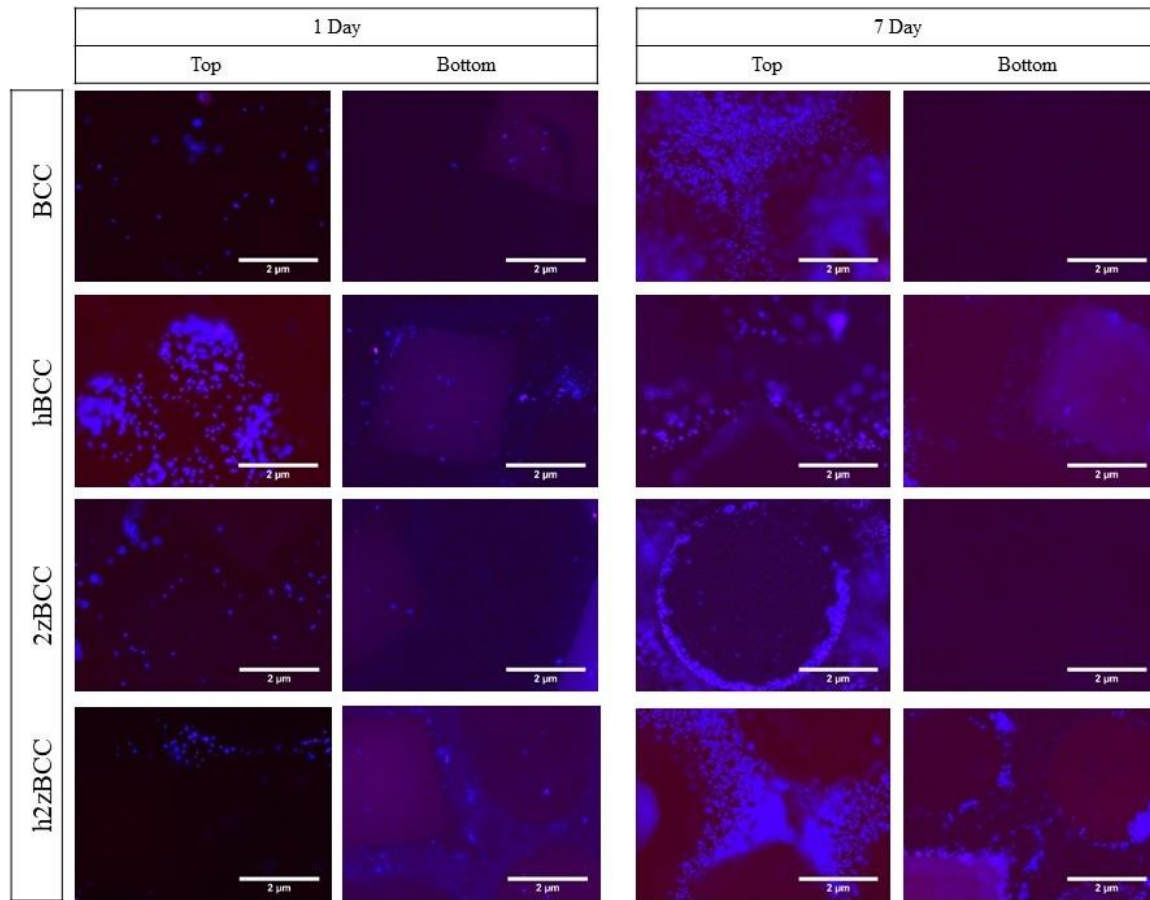


Figure 6. 8 Fluorescence micrographs representing merged Hoechst stained nucleus (blue) and actin cytoskeleton (red) of MC3T3-E1 preosteoblast cells on the solid and hollow-beam BCC and 2zBCC structures after culturing for 1 day and 7 days. Top represents the side where cells were seeded onto the samples.

## 6.6. Discussion

In this chapter, the hollow-tube lattice structures were investigated. This study includes the SLM processability, mechanical properties and biological response of these structures. The generated hollow-structures were based on BCC, zBCC and 2zBCC unit cells. Further, solid-beam versions of these unit cells were also included in the study for comparison. The hollow-tube thicknesses for all of the scaffolds were 0.3 mm and 0.6 mm. To explore the critical design

dimension limits, additional hollow-beam lattices were also manufactured. It is shown that SLM is able to manufacture hollow-tube lattices with a wall-thickness of 0.2 mm and inner-channel pore size of 0.5 mm. Digital camera and SEM images, as well as the micro-CT scans, revealed that the channels and pores were free of residual process powders and there was no blockage or un-desirable fusion of the struts. Although a deviation in the dimension of the structures compared to their CAD models was observed, this deviation did not cause overlapping of the struts or blocked pores. The difference in strut sizes and pores between the designed and as-fabricated structures was within an expected range [86] (around 5-10 %), and was attributed to surface irregularities.

Table 6. 3 shows that the elastic modulus and yield stress values of the solid-beam based lattices are higher than the hollow-beam lattices. However, when these values are normalised with the relative density of the structures, the stiffness and strength of hollow-beam lattices are higher than the solid-beam lattices. For example, at the same relative density (26%), hollow-BCC structure exhibited elastic moduli of 2.3 GPa and yield stress of 102 MPa; whereas, solid-BCC structures had an average elastic moduli of 1.7 GPa and yield stress of 47 MPa. Our results complement the findings of the literature and show that hollow-beam lattices offer higher (30-60% higher) stiffness, strength and energy absorption capacities at the same relative densities [231, 235].

Deformation behaviour of the hollow-beam lattices were more monotonous and smooth than the solid-beam lattices, as observed in their stress-strain diagrams (Figure 6. 5) and the images taken during the compression testing (Figure 6. 6). The geometrical smoothness of the hollow-tubes, as well as the absence of strut junctions, prevented the abrupt failure and oscillating stress-strain curve, which is characteristic of solid-beam lattice structures. This smooth deformation characteristic can be beneficial in an orthopaedic implant design to prevent the sudden failure and undesirable material removal from the implant. Shell-based lattice (hollow-beam) structures were also reported to have substantial advantages over the truss-based lattices in regards to fatigue life [235]. Overall, our results and literature show that hollow-beam structures have superior mechanical properties and behaviour compared to the solid-beam lattices.



Further to the mechanical behaviour studies, we analysed the *in-vitro* biological response of the hollow and solid-beam structures with MG63 preosteoblast cells. MTS assay results indicated similar degree of cell attachment and cell proliferation for hollow and solid BCC and 2zBCC structures at day 1 and 7. However, fluorescent images show more cells at the bottom of the hollow-beam lattices than the solid ones. This suggests that more cells were able to migrate from the seeding point to the other end of the hollow-beam scaffolds. Since the MTS assay results show that the number of cells attached on all the scaffolds are the same, the fluorescent images suggest that the distribution of the cells are more even in the hollow-beam lattices. This is in agreement with our reported study on the functionally gradient scaffolds, which also showed that scaffolds with large pores or higher porosity had more uniformly distributed cells throughout the scaffold.

The channels created within the struts due to hollow-beam lattice design can be loaded with therapeutic agents, such as antibiotics, to allow targeted drug release. Or, alternatively, they can be loaded with bone morphogenetic proteins to promote bone in-growth [243, 246]. Targeted drug release system within an orthopaedic implant is a promising research avenue and can solve the post-operational infection problems. With the right design of the channels and pores, the release rate of the drug can be controlled. A study investigating the effect of design and channel size on the drug release rate of the implants will help the design of the next-generation medical devices in the future.

In summary, we showed that hollow-beam lattices offer both mechanical and biological advantages. Hollow-beam lattices, sometimes referred to as shell-based lattice structures, offer higher energy absorption, stiffness and strength than solid lattice structures. The smooth deformation behaviour observed in hollow-structures due to absence of stress-concentrations can be beneficial in the use of orthopaedic implants. Another advantage of these structures are shown in our *in-vitro* studies. Hollow channels enabled better cell migration, which resulted in more homogenous distribution of the cells within the overall scaffold. Hollow-channels offer ample space for loading of the therapeutic agents to functionalise the implants. Due to the aforementioned benefits, hollow-lattice structures offer promising properties and functionality in next-generation orthopaedic implants. Future studies on the hollow-beam lattices should include the effect of channel size on the drug release rate.

## 6.8. Conclusion of the Chapter

This chapter includes the study on the processability, mechanical behaviour and in-vitro biological response of the hollow-beam lattice structures. Hollow-beam structures with wall thicknesses of 0.3 and 0.6 mm, as well as solid-beam BCC, zBCC and 2zBCC structures, were successfully fabricated using selective laser melting technology. Our preliminary study on the processability of the hollow-beam lattices with SLM method revealed that SLM is capable of fabricating structures with minimum hollow-tube thickness of 0.2 mm and inner channel size of 0.5 mm without any blockage. Static mechanical properties of the hollow-structures show that they are stiffer and stronger than their solid counterparts at the same relative densities. Quantitative analysis of cell viability show similar cell colonisation and proliferation rates for both hollow and solid-beam scaffolds. However, fluorescent images suggest that the distribution of the cells are more uniform in the hollow-beam structures. The combined results of compression tests and *in vitro* biological performances suggest that hollow-beam lattices can be beneficial in the use of orthopaedic implants. Furthermore, the channel space provided within the struts can be incorporated with therapeutic agents to aid in targeted drug treatment. We suggest that the next-generation implants can be functionalised with this approach of incorporating additional channels and therapeutic agents within the porous scaffolds, without compromising the mechanical properties.

## Chapter 7. Conclusions and Future Work

## 7.2. Conclusions

The aim of this thesis was to study the mechanical and biological properties of lattice scaffolds manufactured by selective laser melting and establish a better understanding of their relationship. This was achieved by proposing new designs of the scaffolds and simultaneously assessing the mechanical and biological properties.

A particular target of this work was to study a functionally gradient porous scaffolds and their mechanical and biological response. For this purpose, two gradient designs, so called Dense-In and Dense-Out, were fabricated by SLM. Both gradient designs were based on the BCC unit cell and had pore sizes changing from 940  $\mu\text{m}$  to 1330  $\mu\text{m}$ . The uniform BCC structures were also manufactured for comparison. The mechanical properties of gradient and uniform scaffolds were found to be comparable to the values of cortical bone. The rule of mixture was proposed to calculate the mechanical properties of gradient designs based on an assumption that gradient structures are composites of uniform layers of the same diameter struts. The deformation mechanism of gradient structures was observed to follow a sequential layer collapse, whereas uniform BCC scaffolds failed by diagonal shear collapse. The sequential layer collapse has an advantage of retaining the mechanical properties of a scaffold over a large degree of deformation. *In-vitro* tests with MC3T3 preosteoblast cells showed that the degree of cell attachment was similar for all scaffolds. However, the cell colonization and migration were significantly higher on the scaffolds having thinner struts on their periphery (*i.e.*, Uniform 0.4 and Dense-In) than the scaffolds with thick struts on their outer surface (*i.e.*, Uniform 0.8 and Dense-Out). The *in-vitro* results combined with the mechanical properties show that the optimal gradient designs for bone implant use should have decreasing pore size towards their centre, which can provide the required strength and stiffness, while simultaneously promoting cell colonization throughout the whole scaffold. This study has also demonstrated the importance of assessing the biological and mechanical properties together when designing an implant as the two properties have contradicting requirements.

The other target of the thesis was to study alternative exposure strategy for the SLM process to improve the processability of the lattice structures and understand the formation of the resulting microstructure. Here, single point exposure strategy is investigated as an alternative method to

the contour-hatching strategy. This method involves exposing the laser at a certain exposure time to reach the desired dimensions. With this method, the dimensions of the parts are directly controlled by the laser power and exposure time, without the need of 3D modelling. This also diminishes the computational costs and steps required from design to fabrication. In this work, single vertical struts were fabricated with >50 process parameters to investigate the effect of process parameters and the basics of laser-material interaction during the single point exposure.

The characterisation results of the single vertical struts show that the strut diameter increases with energy input up to a saturation point with single point exposure strategy. The maximum achievable strut size is shown to be 520  $\mu\text{m}$  at the saturation point (0.5 J energy input). Continuous pore formation was observed in the centre of the struts along the build direction. The morphology and the location of these pores suggest that they were produced due to excessive energy delivery in the core of the struts and resulted in a keyhole pore formation. The microstructure of all of the struts included martensitic  $\alpha$ -laths.

In addition to single vertical struts, the effects of (partial) re-melting was investigated by placing two struts in the same location; hence leading to a double laser exposure at the same location. Furthermore, the effect of latent heat was studied by designing struts in circular arrangements and assessing the middle strut. It was shown that the latent heat did not effect the microstructure of the struts and they all had martensitic  $\alpha$ -laths. However, some unusual relief was observed on the unpolished surfaces of the double-melted struts under the SEM, that resembled the basketweave microstructure. This was further characterised by performing TEM on the cross-sectional area from the surface of double and single-melted struts. TEM images revealed that a more uniform structure with consistent  $\alpha$ -lath sizes (200-300 nm) was observed in double-melted struts. On the other hand the single-melt struts had varying size  $\alpha$ -laths (10 nm to 1  $\mu\text{m}$ ). This homogeneity effect on the microstructure of the double-melted struts can be explained by the additional thermal effect of the second laser pulse; and further investigations are proposed in the future work. Another difference observed between the double and single-melted struts was in the texture results. The characteristic BOR-related correlation between  $\{0001\}_{\alpha}$  and  $\{110\}_{\beta}$  was no longer apparent in the case of double-melted specimens. It is hypothesised that double laser exposure has occurred at different times during the solidification  $\beta \rightarrow \alpha'$  transformation processes. This might have disrupted the natural way in which the

microstructure is formed and have resulted in unconventional arrangements of the phases with respect to each other. However, the overall shape and orientation of  $\alpha'$ -laths (randomly oriented) and prior  $\beta$ -columns ( $18-20^\circ$  off the build direction) were very similar in both double and single-melted struts.

This work contributes to the field of processing lattice structures by selective laser melting by introducing the single point exposure strategy and the processing window to alter the microstructure. The lattice scaffolds include both single and double melted areas (i.e., strut junctions). Therefore, the microstructure of these regions have an effect on the mechanical properties of the overall scaffold. The future work is suggested to further investigate the mechanical properties of the single and double-melted struts and establish a direct correlation between the process parameters and mechanical properties.

The final part of this thesis, Chapter 6, includes the work on the processability, mechanical behaviour and *in-vitro* biological response of the hollow-beam lattice structures. Hollow-beam scaffolds with wall thicknesses of 0.3 and 0.6 mm based on the unit cells of BCC, zBCC and 2zBCC, as well as the solid-beam scaffolds, were successfully fabricated using selective laser melting technology. Previous work in literature included micro and nano size hollow-beam lattices; therefore, our study on the SLM hollow-lattices contributes to the field by exploring the process-ability of these structures with SLM. The limitation of the hollow-beam designs without any pore blockage include a minimum hollow-tube thickness of 0.2 mm and an inner channel size of 0.5 mm for SLM Ti6Al4V. The mechanical testing of the hollow-structures show that they are stiffer and stronger than their solid counterparts at the same relative densities. For example, at the same relative density (26%), hollow-BCC structure exhibited elastic moduli of 2.3 GPa and yield stress of 102 MPa; whereas, solid-BCC structures had an average elastic moduli of 1.7 GPa and yield stress of 47 MPa. Deformation behaviour of the hollow-beam lattices were more monotonous and smooth than the solid-beam lattices. The geometrical smoothness of the hollow-tubes, as well as the absence of strut junctions, prevented the abrupt failure and oscillating stress-strain curve (that is characteristic of solid-beam lattice structures). This smooth deformation characteristic can be beneficial in an orthopaedic implant design to prevent the sudden failure and undesirable material removal from the implant.



Quantitative *in-vitro* biological performance, assessed by using MG63 pre-osteoblast cells, show that the cell colonisation and proliferation rates for both hollow and solid-beam scaffolds. However, fluorescent images show that distribution of the cells being more uniform in the hollow-beam structures as compared to solid-beam lattices.

In summary, this thesis presents the results around the processability and properties of SLM Ti6Al4V lattice structures to be used in the orthopaedic implants. The related literature, which mainly involves the recent decade publications, was presented. An important conclusion following from our results is that mechanical and biological properties should be considered simultaneously and gradient structures and hollow lattice are promising candidates for future orthopaedic implants.

### 7.2. Future Work

A number of research gaps were addressed in this thesis including mechanical, morphological and biological assesment of lattice structures for an orthopaedic implant use. However, further research is required to improve the surface and design of lattice structures for orthopaedic implants.

Foremost, the surface of SLM Ti6Al4V lattice structures is a major concern for biomedical applications due to the risk of detachment of the partially-melted particles. Although there are reported studies on electrochemical polishing and etching of surface of the SLM Ti6Al4V implants [82, 247], there is no standard optimum procedure to follow. Further research might include developing surface modifications techniques specifically for the lattice implants and assessing the effect of etching on the mechanical and biological performance of the structures. The other important factor to consider for AM lattice orthopaedic implants is their fatigue properties. It is therefore proposed that the fatigue performance of hollow-beam lattices and functionally-gradient lattice structures should be studied next. Moreover, *in-vivo* testing will be required required for any translational research or commercialisation. The literature demonstrates the benefit of lattice SLM scaffolds in animal models, such as increased osseointegration [193, 248].

Another important aspect of the future work is to investigating different titanium alloys for additively manufactured implants. Although  $\alpha+\beta$  Ti6Al4V is still the most widely used material for orthopaedic implants, several reports argue that V is toxic both in the elemental state and in the form of oxide. Furthermore, V and Al ions released from the alloy can have an effect on the long-term health such as Alzheimer disease and neuropathy [249]. Therefore, there is a growing interest in the research community to develop different alloys for AM orthopaedic implants. Some of the titanium alloys which were reported include TiTa alloys [250],  $\beta$ -type titanium alloys such as Ti-24Nb-4Zr-8Sn (TNZS) or Ti-Nb-Z (TNZ) [251, 252]. Challenges with developing new alloys for AM include homogeneous distribution of alloying elements and vaporisation of low-melting temperature constituents. The process optimisation of these new alloys and characterisation of the properties are recommended as a future work.

Finally, it was demonstrated that the hollow-tube lattices are beneficial in terms of their mechanical properties and cell colonisation. In addition to these benefits, the hollow-channels can be incorporated with therapeutic agents to have targeted drug-release function. There are a number of recent studies in literature suggesting a similar future work direction for hollow-lattices [242, 243]. Yet, there is no detailed study on the drug-release rate and effect *in-vitro* and *in-vivo* in literature for the hollow-lattices. The drug-release rate will have a great impact on the effectiveness of antibiotic on the postsurgery infections. Therefore, smart designs such as hollow-lattices can be a key to control the drug-release rate by design. Future work might include designing hollow-tube lattice scaffolds with different channel-sizes and loading these channels with an industry-standard therapeutic agent (such as tobramycin, gentamicin, vancomycin [253]) to establish a relationship between channel-size and drug-release rate and find an optimum channel-size based on the bacterial inhibition experiments.

In summary, additive manufacturing is been enabling the rapid transition of novel ideas to prototype building, but further research and developments in this field are required to transition to a qualified and certified medical implants.

## REFERENCES

1. Brandt, M., *The role of lasers in additive manufacturing*, in *Laser Additive Manufacturing*, M. Brandt, Editor. 2017, Woodhead Publishing. p. 1-18.
2. Mantripragada, V.P., et al., *An overview of recent advances in designing orthopedic and craniofacial implants*. Journal of biomedical materials research. Part A, 2013. **101**(11): p. 3349-3364.
3. Karageorgiou, V. and D. Kaplan, *Porosity of 3D biomaterial scaffolds and osteogenesis*. Biomaterials, 2005. **26**(27): p. 5474-5491.
4. Stevens, M.M., *Biomaterials for bone tissue engineering*. Materials Today, 2008. **11**(5): p. 18-25.
5. Amini, A.R., C.T. Laurencin, and S.P. Nukavarapu, *Bone tissue engineering: recent advances and challenges*. Critical reviews in biomedical engineering, 2012. **40**(5): p. 363-408.
6. Dyrda, L. *Number of Orthopedic Surgeries to Reach 6.6M by 2020*. Orthopedic, Spine & Pain Management-Driven ASCs, 2011.
7. GlobalData *Global Orthopedics Market to Grow to \$66.2 Billion by 2023*. 2018.
8. Guerado, E. and E. Caso, *Challenges of bone tissue engineering in orthopaedic patients*. World journal of orthopedics, 2017. **8**(2): p. 87-98.
9. Ashby, M., *Designing architected materials*. Scripta Materialia, 2013. **68**(1): p. 4-7.
10. Fleck, N.A., V.S. Deshpande, and M.F. Ashby, *Micro-architected materials: past, present and future*. Proceedings of the Royal Society A: Mathematical, Physical and Engineering Sciences, 2010. **466**(2121): p. 2495-2516.
11. Arabnejad, S., et al., *High-strength porous biomaterials for bone replacement: A strategy to assess the interplay between cell morphology, mechanical properties, bone ingrowth and manufacturing constraints*. Acta Biomaterialia, 2016. **30**: p. 345-356.
12. Wettergreen, M.A., et al., *Creation of a unit block library of architectures for use in assembled scaffold engineering*. Computer-Aided Design, 2005. **37**(11): p. 1141-1149.
13. Bobbert, F.S.L., et al., *Additively manufactured metallic porous biomaterials based on minimal surfaces: A unique combination of topological, mechanical, and mass transport properties*. Acta Biomaterialia, 2017. **53**: p. 572-584.

## REFERENCES

---

14. Kapfer, S.C., et al., *Minimal surface scaffold designs for tissue engineering*. Biomaterials, 2011. **32**(29): p. 6875-6882.
15. Zhang, X.-Y., G. Fang, and J. Zhou, *Additively Manufactured Scaffolds for Bone Tissue Engineering and the Prediction of their Mechanical Behavior: A Review*. Materials, 2017. **10**(1): p. 50.
16. Wang, X., et al., *Topological design and additive manufacturing of porous metals for bone scaffolds and orthopaedic implants: A review*. Biomaterials, 2016. **83**: p. 127-141.
17. Karcher, H. and K. Polthier, *Construction of Triply Periodic Minimal Surfaces*. Philosophical Transactions: Mathematical, Physical and Engineering Sciences, 1996. **354**(1715): p. 2077-2104.
18. Mahmoud, D. and M. Elbestawi, *Lattice Structures and Functionally Graded Materials Applications in Additive Manufacturing of Orthopedic Implants: A Review*. Journal of Manufacturing and Materials Processing, 2017. **1**(2): p. 13.
19. Zadpoor, A.A. and R. Hedayati, *Analytical relationships for prediction of the mechanical properties of additively manufactured porous biomaterials*. Journal of Biomedical Materials Research Part A, 2016. **104**(12): p. 3164-3174.
20. Yoo, D.J., *Porous scaffold design using the distance field and triply periodic minimal surface models*. Biomaterials, 2011. **32**(31): p. 7741-7754.
21. Huang, X., A. Radman, and Y.M. Xie, *Topological design of microstructures of cellular materials for maximum bulk or shear modulus*. Computational Materials Science, 2011. **50**(6): p. 1861-1870.
22. Helou, M. and S. Kara, *Design, analysis and manufacturing of lattice structures: an overview*. International Journal of Computer Integrated Manufacturing, 2018. **31**(3): p. 243-261.
23. Dong, L., V. Deshpande, and H. Wadley, *Mechanical response of Ti–6Al–4V octet-truss lattice structures*. International Journal of Solids and Structures, 2015. **60-61**: p. 107-124.
24. Wadley, H.N.G., N.A. Fleck, and A.G. Evans, *Fabrication and structural performance of periodic cellular metal sandwich structures*. Composites Science and Technology, 2003. **63**(16): p. 2331-2343.

## REFERENCES

25. Groover, M.P., *Fundamentals of Modern Manufacturing : Materials Processes, and Systems*. 2nd ed. 2007: John Wiley & Sons Inc.
26. Chiras, S., et al., *The structural performance of near-optimized truss core panels*. International Journal of Solids and Structures, 2002. **39**(15): p. 4093-4115.
27. International, A., *ASTM F2792-10, Standard Terminology for Additive Manufacturing Technologies*. 2010: West Conshohocken, PA.
28. Wohlers, T., *Wohlers report 2014: 3D printing and additive manufacturing state of the industry annual worldwide progress report*. 2014, Fort Collins: Wohlers Associates.
29. <https://www.ge.com/additive/additive-manufacturing> accessed on 8/1/2019.
30. <https://www.sculpteo.com/en/glossary/additive-manufacturing-definition/> accessed on 8/1/2019.
31. Wohlers, T., *Wohlers Report 2010: Additive Manufacturing state of the industry annual worldwide progress report*. 2010.
32. Plewa, K., *3D printing pioneers: Top 10 industries utilizing Additive Manufacturing*. 2019: <https://www.sculpteo.com/blog/2019/02/01/3d-printing-pioneers-top-10-industries-utilizing-additive-manufacturing/> accessed on 8/1/2019.
33. Dutta, B., et al., *Additive Manufacturing by Direct Metal Deposition*. ADVANCED MATERIALS & PROCESSES, 2011.
34. Lewis, G.K. and E. Schlienger, *Practical considerations and capabilities for laser assisted direct metal deposition*. Materials & Design, 2000. **21**(4): p. 417-423.
35. Wang, F., X.H. Wu, and D. Clark, *On direct laser deposited Hastelloy X: dimension, surface finish, microstructure and mechanical properties*. Materials Science and Technology, 2011. **27**(1): p. 344-356.
36. Mazumder, J., *1 - Laser-aided direct metal deposition of metals and alloys*, in *Laser Additive Manufacturing*, M. Brandt, Editor. 2017, Woodhead Publishing. p. 21-53.
37. *Isfahan University of technology, Additive Manufacturing Lab*. 2012.
38. Murr, L.E., et al., *Metal Fabrication by Additive Manufacturing Using Laser and Electron Beam Melting Technologies*. Journal of Materials Science & Technology, 2012. **28**(1): p. 1-14.
39. Biamino, S., et al., *Electron beam melting of Ti–48Al–2Cr–2Nb alloy: Microstructure and mechanical properties investigation*. Intermetallics, 2011. **19**(6): p. 776-781.

## REFERENCES

---

40. Körner, C., *Additive manufacturing of metallic components by selective electron beam melting—a review*. International Materials Reviews, 2016. **61**(5): p. 361-377.
41. Zhong, Y., et al., *Additive manufacturing of ITER first wall panel parts by two approaches: Selective laser melting and electron beam melting*. Fusion Engineering and Design, 2017. **116**: p. 24-33.
42. Gong, H., et al., *Influence of defects on mechanical properties of Ti-6Al-4V components produced by selective laser melting and electron beam melting*. Materials & Design, 2015. **86**: p. 545-554.
43. Chastand, V., et al., *Comparative study of fatigue properties of Ti-6Al-4V specimens built by electron beam melting (EBM) and selective laser melting (SLM)*. Materials Characterization, 2018. **143**: p. 76-81.
44. Liu, Y.J., et al., *Microstructure, defects and mechanical behavior of beta-type titanium porous structures manufactured by electron beam melting and selective laser melting*. Acta Materialia, 2016. **113**: p. 56-67.
45. Rafi, H.K., et al., *Microstructures and Mechanical Properties of Ti6Al4V Parts Fabricated by Selective Laser Melting and Electron Beam Melting*. Journal of Materials Engineering and Performance, 2013. **22**(12): p. 3872-3883.
46. Gokuldoss, P.K., S. Kolla, and J. Eckert, *Additive Manufacturing Processes: Selective Laser Melting, Electron Beam Melting and Binder Jetting—Selection Guidelines*. Materials, 2017. **10**(6): p. 672.
47. Rauch, E., M. Unterhofer, and P. Dallasega, *Industry sector analysis for the application of additive manufacturing in smart and distributed manufacturing systems*. Manufacturing Letters, 2018. **15**: p. 126-131.
48. Shipley, H., et al., *Optimisation of process parameters to address fundamental challenges during selective laser melting of Ti-6Al-4V: A review*. International Journal of Machine Tools and Manufacture, 2018. **128**: p. 1-20.
49. Gokuldoss, P.K., S. Kolla, and J. Eckert, *Additive Manufacturing Processes: Selective Laser Melting, Electron Beam Melting and Binder Jetting-Selection Guidelines*. Materials (Basel, Switzerland), 2017. **10**(6): p. 672.
50. Yap, C.Y., et al., *Review of selective laser melting: Materials and applications*. Applied Physics Reviews, 2015. **2**(4): p. 041101.



## REFERENCES

---

51. Sutton, A.T., et al., *Powder characterisation techniques and effects of powder characteristics on part properties in powder-bed fusion processes*. Virtual and Physical Prototyping, 2017. **12**(1): p. 3-29.
52. Kashapov, R.N., L.N. Kashapov, and N.F. Kashapov, *Analysis and development of methods for obtaining metallic powders for selective laser melting*. IOP Conference Series: Materials Science and Engineering, 2017. **240**: p. 012071.
53. Li, R., et al., *Densification behavior of gas and water atomized 316L stainless steel powder during selective laser melting*. Applied Surface Science, 2010. **256**(13): p. 4350-4356.
54. Olakanmi, E.O., *Effect of Mixing Time on the Bed Density, and Microstructure of Selective Laser Sintered (SLS) Aluminium Powders*. Materials Research-Ibero-american Journal of Materials, 2012. **15**(2): p. 167-176.
55. Cleary, P.W. and M.L. Sawley, *DEM modelling of industrial granular flows: 3D case studies and the effect of particle shape on hopper discharge*. Applied Mathematical Modelling, 2002. **26**(2): p. 89-111.
56. Lee, Y.S. and W. Zhang, *Mesosopic simulation of heat transfer and fluid flow in laser powder bed additive manufacturing*. International Solid Free Form Fabrication Symposium, 2015: p. 1154-1165.
57. Yadroitsev, I., et al., *Factor analysis of selective laser melting process parameters and geometrical characteristics of synthesized single tracks*. Rapid Prototyping Journal, 2012. **18**(3): p. 201-208.
58. Ciurana, J., L. Hernandez, and J. Delgado, *Energy density analysis on single tracks formed by selective laser melting with CoCrMo powder material*. The International Journal of Advanced Manufacturing Technology, 2013. **68**(5): p. 1103-1110.
59. Peng, T. and C. Chen, *Influence of energy density on energy demand and porosity of 316L stainless steel fabricated by selective laser melting*. International Journal of Precision Engineering and Manufacturing-Green Technology, 2018. **5**(1): p. 55-62.
60. Thijs, L., et al., *A study of the microstructural evolution during selective laser melting of Ti-6Al-4V*. Acta Materialia, 2010. **58**(9): p. 3303-3312.
61. Scipioni Bertoli, U., et al., *On the limitations of Volumetric Energy Density as a design parameter for Selective Laser Melting*. Materials & Design, 2017. **113**: p. 331-340.

## REFERENCES

---

62. Chua, C.K. and Z.L. Dong, *An effective analytical model of selective laser melting AU - Yap, C. Y. Virtual and Physical Prototyping*, 2016. **11**(1): p. 21-26.
63. Wang, J.-H., et al., *Effect of Selective Laser Melting Process Parameters on Microstructure and Properties of Co-Cr Alloy*. Materials (Basel, Switzerland), 2018. **11**(9): p. 1546.
64. Laohaprapanon, A., et al., *Optimal Scanning Condition of Selective Laser Melting Processing with Stainless Steel 316L Powder*. Advanced Materials Research, 2012. **341-342**: p. 816-820.
65. Buchbinder, D., et al., *High Power Selective Laser Melting (HP SLM) of Aluminum Parts*. Physics Procedia, 2011. **12**: p. 271-278.
66. Mishra, P., et al., *Energy efficiency contributions and losses during selective laser melting*. Journal of Laser Applications, 2018. **30**(3): p. 032304.
67. <https://www.eos.info/material-m> accessed on 9/1/2019.
68. Sufiiarov, V.S., et al., *The Effect of Layer Thickness at Selective Laser Melting*. Procedia Engineering, 2017. **174**: p. 126-134.
69. Dadbakhsh, S. and L. Hao, *Effect of Layer Thickness in Selective Laser Melting on Microstructure of Al/5 wt.%Fe<sub>2</sub>O<sub>3</sub> Powder Consolidated Parts*. The Scientific World Journal, 2014. **2014**: p. 10.
70. Sun, J., Y. Yang, and D. Wang, *Parametric optimization of selective laser melting for forming Ti6Al4V samples by Taguchi method*. Optics & Laser Technology, 2013. **49**: p. 118-124.
71. Shi, X., et al., *Performance of High Layer Thickness in Selective Laser Melting of Ti6Al4V*. Materials, 2016. **9**(12): p. 975.
72. Ahmadi, S.M., et al., *Effects of laser processing parameters on the mechanical properties, topology, and microstructure of additively manufactured porous metallic biomaterials: A vector-based approach*. Materials & Design, 2017. **134**: p. 234-243.
73. Sames, W.J., et al., *The metallurgy and processing science of metal additive manufacturing*. International Materials Reviews, 2016. **61**(5): p. 315-360.
74. Mullen, L., et al., *Selective Laser Melting: A regular unit cell approach for the manufacture of porous, titanium, bone in-growth constructs, suitable for orthopedic*

## REFERENCES

---

- applications*. Journal of Biomedical Materials Research Part B: Applied Biomaterials, 2009. **89B**(2): p. 325-334.
75. Tsopanos, S., et al., *The Influence of Processing Parameters on the Mechanical Properties of Selectively Laser Melted Stainless Steel Microlattice Structures*. Journal of Manufacturing Science and Engineering, 2010. **132**(4): p. 041011-041011-12.
76. Ghouse, S., et al., *The influence of laser parameters and scanning strategies on the mechanical properties of a stochastic porous material*. Materials & Design, 2017. **131**: p. 498-508.
77. Ahmadi, S., et al., *Effects of laser processing parameters on the mechanical properties, topology, and microstructure of additively manufactured porous metallic biomaterials: A vector-based approach*. Materials & Design, 2017. **134**: p. 234-243.
78. Parry, L., I.A. Ashcroft, and R.D. Wildman, *Understanding the effect of laser scan strategy on residual stress in selective laser melting through thermo-mechanical simulation*. Additive Manufacturing, 2016. **12**: p. 1-15.
79. Vandenbroucke, B. and J.P. Kruth, *Selective laser melting of biocompatible metals for rapid manufacturing of medical parts*. Rapid Prototyping Journal, 2007. **13**(4): p. 196-203.
80. Edwards, P. and M. Ramulu, *Fatigue performance evaluation of selective laser melted Ti-6Al-4V*. Materials Science and Engineering: A, 2014. **598**: p. 327-337.
81. Shalabi, M.M., et al., *Implant Surface Roughness and Bone Healing: a Systematic Review*. Journal of Dental Research, 2006. **85**(6): p. 496-500.
82. Pyka, G., et al., *Surface Roughness and Morphology Customization of Additive Manufactured Open Porous Ti6Al4V Structures*. Materials, 2013. **6**(10): p. 4737.
83. *Porosity in metal components made using Selective Laser Melting*. 2014: [www.insidemetaladditivemanufacturing.com/blog](http://www.insidemetaladditivemanufacturing.com/blog) accessed on 12/1/2019.
84. King, W.E., et al., *Observation of keyhole-mode laser melting in laser powder-bed fusion additive manufacturing*. Journal of Materials Processing Technology, 2014. **214**(12): p. 2915-2925.
85. International, A., *ASTM F136-13 Standard Specification for Wrought Titanium-6Aluminum-4Vanadium ELI (Extra Low Interstitial) Alloy for Surgical Implant Applications (UNS R56401)*. 2013: West Conshohocken, PA, USA.
-

## REFERENCES

---

86. Van Bael, S., et al., *Micro-CT-based improvement of geometrical and mechanical controllability of selective laser melted Ti6Al4V porous structures*. Materials Science and Engineering: A, 2011. **528**(24): p. 7423-7431.
87. Hollander, D.A., et al., *Structural, mechanical and in vitro characterization of individually structured Ti-6Al-4V produced by direct laser forming*. Biomaterials, 2006. **27**(7): p. 955-963.
88. Campbell, R.I., M. Martorelli, and H.S. Lee, *Surface roughness visualisation for rapid prototyping models*. Computer-Aided Design, 2002. **34**(10): p. 717-725.
89. Wysocki, B., et al., *Post Processing and Biological Evaluation of the Titanium Scaffolds for Bone Tissue Engineering*. Materials, 2016. **9**(3): p. 197.
90. Wu, M.-W. and P.-H. Lai, *The positive effect of hot isostatic pressing on improving the anisotropies of bending and impact properties in selective laser melted Ti-6Al-4V alloy*. Materials Science and Engineering: A, 2016. **658**: p. 429-438.
91. Qiu, C., et al., *On the role of melt flow into the surface structure and porosity development during selective laser melting*. Acta Materialia, 2015. **96**: p. 72-79.
92. Kasperovich, G. and J. Hausmann, *Improvement of fatigue resistance and ductility of TiAl6V4 processed by selective laser melting*. Journal of Materials Processing Technology, 2015. **220**: p. 202-214.
93. Qiu, C., et al., *Influence of processing conditions on strut structure and compressive properties of cellular lattice structures fabricated by selective laser melting*. Materials Science and Engineering: A, 2015. **628**: p. 188-197.
94. Murr, L.E., et al., *Microstructure and mechanical properties of open-cellular biomaterials prototypes for total knee replacement implants fabricated by electron beam melting*. Journal of the Mechanical Behavior of Biomedical Materials, 2011. **4**(7): p. 1396-1411.
95. Qiu, C., N.J.E. Adkins, and M.M. Attallah, *Microstructure and tensile properties of selectively laser-melted and of HIPed laser-melted Ti-6Al-4V*. Materials Science and Engineering: A, 2013. **578**: p. 230-239.
96. Polmear, I., et al., *Light Alloys, Metallurgy of the Light Metals*. 5th ed. 2017: Butterworth-Heinemann, Elsevier.

## REFERENCES

---

97. Facchini, L., et al., *Ductility of a Ti-6Al-4V alloy produced by selective laser melting of prealloyed powders*. Rapid Prototyping Journal, 2010. **16**(6): p. 450-459.
98. Xu, W., et al., *Additive manufacturing of strong and ductile Ti-6Al-4V by selective laser melting via in situ martensite decomposition*. Acta Materialia, 2015. **85**: p. 74-84.
99. Antonysamy, A.A., J. Meyer, and P.B. Prangnell, *Effect of build geometry on the  $\beta$ -grain structure and texture in additive manufacture of Ti6Al4V by selective electron beam melting*. Materials Characterization, 2013. **84**: p. 153-168.
100. Wu, X., et al., *Microstructures of laser-deposited Ti-6Al-4V*. Materials & Design, 2004. **25**(2): p. 137-144.
101. Simonelli, M., Y.Y. Tse, and C. Tuck, *On the Texture Formation of Selective Laser Melted Ti-6Al-4V*. Metallurgical and Materials Transactions A, 2014. **45**(6): p. 2863-2872.
102. Babu, B., *Physically based model for plasticity and creep of Ti-6Al-4V*, in *Department of Applied Physics and Mechanical Engineering, Division of Material Mechanics*. 2008, Luleå University of Technology.
103. Yan, M. and P. Yu, *An Overview of Densification, Microstructure and Mechanical Property of Additively Manufactured Ti-6Al-4V — Comparison among Selective Laser Melting, Electron Beam Melting, Laser Metal Deposition and Selective Laser Sintering, and with Conventional Powder*, in *Sintering Techniques of Materials*, A. Lakshmanan, Editor. 2015, IntechOpen.
104. Attanasio, A., et al., *Influence of Material Microstructures in Micromilling of Ti6Al4V Alloy*. Materials, 2013. **6**(9): p. 4268.
105. Vrancken, B., et al., *Microstructure and mechanical properties of a novel  $\beta$  titanium metallic composite by selective laser melting*. Acta Materialia, 2014. **68**: p. 150-158.
106. Vrancken, B., et al., *Heat treatment of Ti6Al4V produced by Selective Laser Melting: Microstructure and mechanical properties*. Journal of Alloys and Compounds, 2012. **541**: p. 177-185.
107. Vilari, T., C. Colin, and J.D. Bartout, *As-Fabricated and Heat-Treated Microstructures of the Ti-6Al-4V Alloy Processed by Selective Laser Melting*. Metallurgical and Materials Transactions A, 2011. **42**(10): p. 3190-3199.

## REFERENCES

---

108. Wauthle, R., et al., *Effects of build orientation and heat treatment on the microstructure and mechanical properties of selective laser melted Ti6Al4V lattice structures*. Additive Manufacturing, 2015. **5**: p. 77-84.
109. Ashby, M.F., *The properties of foams and lattices*. Philosophical Transactions of the Royal Society A: Mathematical, Physical and Engineering Sciences, 2006. **364**(1838): p. 15-30.
110. Gibson, L.J. and M.F. Ashby, *Cellular solids : structure and properties*. 2nd ed. 1999, Cambridge: Cambridge University Press.
111. Maxwell, J.C., L. *On the calculation of the equilibrium and stiffness of frames*. The London, Edinburgh, and Dublin Philosophical Magazine and Journal of Science, 1864. **27**(182): p. 294-299.
112. Scheffler, M. and P. Colombo, *Cellular Ceramics: Structure, Manufacturing, Properties and Applications*. 2005, Weinheim: WILEY-VCH.
113. Deshpande, V.S., M.F. Ashby, and N.A. Fleck, *Foam topology: bending versus stretching dominated architectures*. Acta Materialia, 2001. **49**(6): p. 1035-1040.
114. Tamburrino, F., S. Graziosi, and M. Bordegoni, *The Design Process of Additively Manufactured Mesoscale Lattice Structures: A Review*. Journal of Computing and Information Science in Engineering, 2018. **18**(4): p. 040801-040801-16.
115. Ahmadi, S., et al., *Additively Manufactured Open-Cell Porous Biomaterials Made from Six Different Space-Filling Unit Cells: The Mechanical and Morphological Properties*. Materials, 2015. **8**(4): p. 1871.
116. Onal, E., et al., *Mechanical Properties and In Vitro Behavior of Additively Manufactured and Functionally Graded Ti6Al4V Porous Scaffolds*. Metals, 2018. **8**(4): p. 200.
117. Harrysson, O.L.A., et al., *Direct metal fabrication of titanium implants with tailored materials and mechanical properties using electron beam melting technology*. Materials Science and Engineering: C, 2008. **28**(3): p. 366-373.
118. Challis, V.J., et al., *High specific strength and stiffness structures produced using selective laser melting*. Materials & Design, 2014. **63**: p. 783-788.



## REFERENCES

---

119. Yan, C., et al., *Microstructure and mechanical properties of aluminium alloy cellular lattice structures manufactured by direct metal laser sintering*. Materials Science and Engineering: A, 2015. **628**: p. 238-246.
120. Choy, S.Y., et al., *Compressive properties of Ti-6Al-4V lattice structures fabricated by selective laser melting: Design, orientation and density*. Additive Manufacturing, 2017. **16**: p. 213-224.
121. Yang, L., et al., *Non-stochastic Ti-6Al-4V foam structures with negative Poisson's ratio*. Materials Science and Engineering: A, 2012. **558**: p. 579-585.
122. Ahmadi, S., et al., *Fatigue performance of additively manufactured meta-biomaterials: The effects of topology and material type*. Acta Biomaterialia, 2018. **65**: p. 292-304.
123. Li, S.J., et al., *Compression fatigue behavior of Ti-6Al-4V mesh arrays fabricated by electron beam melting*. Acta Materialia, 2012. **60**(3): p. 793-802.
124. Neff, C., N. Hopkinson, and N.B. Crane, *Experimental and analytical investigation of mechanical behavior of laser-sintered diamond-lattice structures*. Additive Manufacturing, 2018. **22**: p. 807-816.
125. Zheng, X., et al., *Ultralight, ultrastiff mechanical metamaterials*. Science, 2014. **344**(6190): p. 1373-1377.
126. Fan, H., et al., *Modulus-density scaling behaviour and framework architecture of nanoporous self-assembled silicas*. Nature Materials, 2007. **6**: p. 418.
127. Schaedler, T.A., et al., *Ultralight Metallic Microlattices*. Science, 2011. **334**(6058): p. 962-965.
128. Torrents, A., et al., *Characterization of nickel-based microlattice materials with structural hierarchy from the nanometer to the millimeter scale*. Acta Materialia, 2012. **60**(8): p. 3511-3523.
129. Rayneau-Kirkhope, D., Y. Mao, and R. Farr, *Ultralight Fractal Structures from Hollow Tubes*. Physical Review Letters, 2012. **109**(20): p. 204301.
130. Meza, L.R., et al., *Resilient 3D hierarchical architected metamaterials*. Proceedings of the National Academy of Sciences, 2015. **112**(37): p. 11502-11507.
131. Ajdari, A., et al., *Hierarchical honeycombs with tailorable properties*. International Journal of Solids and Structures, 2012. **49**(11): p. 1413-1419.

## REFERENCES

---

132. Kadkhodapour, J., et al., *Failure mechanisms of additively manufactured porous biomaterials: Effects of porosity and type of unit cell*. Journal of the Mechanical Behavior of Biomedical Materials, 2015. **50**: p. 180-191.
133. Mazur, M., et al., *Deformation and failure behaviour of Ti-6Al-4V lattice structures manufactured by selective laser melting (SLM)*. The International Journal of Advanced Manufacturing Technology, 2016. **84**(5): p. 1391-1411.
134. Van Hooreweder, B., et al., *Improving the fatigue performance of porous metallic biomaterials produced by Selective Laser Melting*. Acta Biomaterialia, 2017. **47**: p. 193-202.
135. Ahmadi, S.M., et al., *Mechanical behavior of regular open-cell porous biomaterials made of diamond lattice unit cells*. Journal of the Mechanical Behavior of Biomedical Materials, 2014. **34**: p. 106-115.
136. Sallica-Leva, E., A.L. Jardini, and J.B. Fogagnolo, *Microstructure and mechanical behavior of porous Ti-6Al-4V parts obtained by selective laser melting*. Journal of the Mechanical Behavior of Biomedical Materials, 2013. **26**: p. 98-108.
137. Amin Yavari, S., et al., *Relationship between unit cell type and porosity and the fatigue behavior of selective laser melted meta-biomaterials*. Journal of the Mechanical Behavior of Biomedical Materials, 2015. **43**: p. 91-100.
138. Yan, C., et al., *Advanced lightweight 316L stainless steel cellular lattice structures fabricated via selective laser melting*. Materials & Design, 2014. **55**: p. 533-541.
139. Yan, X., et al., *Mechanical and in vitro study of an isotropic Ti6Al4V lattice structure fabricated using selective laser melting*. Journal of Alloys and Compounds, 2019. **782**: p. 209-223.
140. Brenne, F. and T. Niendorf, *Load distribution and damage evolution in bending and stretch dominated Ti-6Al-4V cellular structures processed by selective laser melting*. International Journal of Fatigue, 2019. **121**: p. 219-228.
141. Afshar, M., et al., *Additive manufacturing and mechanical characterization of graded porosity scaffolds designed based on triply periodic minimal surface architectures*. Journal of the Mechanical Behavior of Biomedical Materials, 2016. **62**: p. 481-494.

## REFERENCES

---

142. Al-Saedi, D.S.J., et al., *Mechanical properties and energy absorption capability of functionally graded F2BCC lattice fabricated by SLM*. Materials & Design, 2018. **144**: p. 32-44.
143. Choy, S.Y., et al., *Compressive properties of functionally graded lattice structures manufactured by selective laser melting*. Materials & Design, 2017. **131**: p. 112-120.
144. Han, C., et al., *Continuous functionally graded porous titanium scaffolds manufactured by selective laser melting for bone implants*. Journal of the Mechanical Behavior of Biomedical Materials, 2018. **80**: p. 119-127.
145. Maskery, I., et al., *A mechanical property evaluation of graded density Al-Si10-Mg lattice structures manufactured by selective laser melting*. Materials Science and Engineering: A, 2016. **670**: p. 264-274.
146. Li, S., et al., *Functionally Graded Ti-6Al-4V Meshes with High Strength and Energy Absorption*. Advanced Engineering Materials, 2016. **18**(1): p. 34-38.
147. Limmahakhun, S., et al., *Stiffness and strength tailoring of cobalt chromium graded cellular structures for stress-shielding reduction*. Materials & Design, 2017. **114**: p. 633-641.
148. van Grunsven, W., et al., *Fabrication and Mechanical Characterisation of Titanium Lattices with Graded Porosity*. Metals, 2014. **4**(3): p. 401.
149. Wang, Y., et al., *Design of graded lattice structure with optimized mesostructures for additive manufacturing*. Materials & Design, 2018. **142**: p. 114-123.
150. Kolken, H.M., et al., *Rationally designed meta-implants: a combination of auxetic and conventional meta-biomaterials*. Materials Horizons, 2018. **5**(1): p. 28-35.
151. Evans, K.E. and A. Alderson, *Auxetic Materials: Functional Materials and Structures from Lateral Thinking!* Advanced Materials, 2000. **12**(9): p. 617-628.
152. Zadpoor, A.A., *Mechanical performance of additively manufactured meta-biomaterials*. Acta Biomaterialia, 2019. **85**: p. 41-59.
153. Sanami, M., et al., *Auxetic Materials for Sports Applications*. Procedia Engineering, 2014. **72**: p. 453-458.
154. Schwerdtfeger, J., et al., *Auxetic cellular structures through selective electron-beam melting*. physica status solidi (b), 2010. **247**(2): p. 269-272.

## REFERENCES

---

155. Prawoto, Y., *Seeing auxetic materials from the mechanics point of view: A structural review on the negative Poisson's ratio*. Computational Materials Science, 2012. **58**: p. 140-153.
156. Campoli, G., et al., *Mechanical properties of open-cell metallic biomaterials manufactured using additive manufacturing*. Materials & Design, 2013. **49**: p. 957-965.
157. Silva, M., et al., *Average patient walking activity approaches 2 million cycles per year: Pedometers under-record walking activity*. The Journal of Arthroplasty, 2002. **17**(6): p. 693-697.
158. Zhao, D., et al., *Effect of pore geometry on the fatigue properties and cell affinity of porous titanium scaffolds fabricated by selective laser melting*. Journal of the Mechanical Behavior of Biomedical Materials, 2018. **88**: p. 478-487.
159. Yavari, S.A., et al., *Fatigue behavior of porous biomaterials manufactured using selective laser melting*. Mater Sci Eng C Mater Biol Appl, 2013. **33**(8): p. 4849-58.
160. Hrabe, N.W., et al., *Compression-compression fatigue of selective electron beam melted cellular titanium (Ti-6Al-4V)*. Journal of Biomedical Materials Research Part B: Applied Biomaterials, 2011. **99B**(2): p. 313-320.
161. Speirs, M., et al., *Fatigue behaviour of NiTi shape memory alloy scaffolds produced by SLM, a unit cell design comparison*. Journal of the Mechanical Behavior of Biomedical Materials, 2017. **70**: p. 53-59.
162. Lietaert, K., et al., *Fatigue life of additively manufactured Ti6Al4V scaffolds under tension-tension, tension-compression and compression-compression fatigue load*. Scientific Reports, 2018. **8**(1): p. 4957.
163. Özbilen, S., et al., *Fatigue behavior of highly porous titanium produced by powder metallurgy with temporary space holders*. Materials Science and Engineering: C, 2016. **60**: p. 446-457.
164. Liu, Y.J., et al., *Compressive and fatigue behavior of beta-type titanium porous structures fabricated by electron beam melting*. Acta Materialia, 2017. **126**: p. 58-66.
165. Ren, D., et al., *Fatigue behavior of Ti-6Al-4V cellular structures fabricated by additive manufacturing technique*. Journal of Materials Science & Technology, 2019. **35**(2): p. 285-294.

## REFERENCES

---

166. Hedayati, R., et al., *Computational prediction of the fatigue behavior of additively manufactured porous metallic biomaterials*. International Journal of Fatigue, 2016. **84**: p. 67-79.
167. Ahmadi, S.M., et al., *From microstructural design to surface engineering: A tailored approach for improving fatigue life of additively manufactured meta-biomaterials*. Acta Biomaterialia, 2019. **83**: p. 153-166.
168. Zhang, X.Z., et al., *Selective electron beam manufactured Ti-6Al-4V lattice structures for orthopedic implant applications: Current status and outstanding challenges*. Current Opinion in Solid State and Materials Science, 2018. **22**(3): p. 75-99.
169. Li, Y., et al., *New Developments of Ti-Based Alloys for Biomedical Applications*. Materials, 2014. **7**(3): p. 1709.
170. Lindahl, O., *Mechanical Properties of Dried Defatted Spongy Bone*. Acta Orthopaedica Scandinavica, 1976. **47**(1): p. 11-19.
171. Ding, M., et al., *Age variations in the properties of human tibial trabecular bone*. The Journal of Bone and Joint Surgery British volume, 1997. **79**(6): p. 995-1002.
172. Linde, F., I. Hvid, and B. Pongsoipetch, *Energy absorptive properties of human trabecular bone specimens during axial compression*. Journal of Orthopaedic Research, 1989. **7**(3): p. 432-439.
173. Zilch, H., et al., *Material properties of femoral cancellous bone in axial loading*. Archives of orthopaedic and traumatic surgery, 1980. **97**(4): p. 257-262.
174. Mosekilde, L., L. Mosekilde, and C.C. Danielsen, *Biomechanical competence of vertebral trabecular bone in relation to ash density and age in normal individuals*. Bone, 1987. **8**(2): p. 79-85.
175. Chang, H.-I. and Y. Wang, *Cell Responses to Surface and Architecture of Tissue Engineering Scaffolds*, in *Regenerative Medicine and Tissue Engineering - Cells and Biomaterials*. 2011.
176. Murr, L.E., *Strategies for creating living, additively manufactured, open-cellular metal and alloy implants by promoting osseointegration, osteoinduction and vascularization: An overview*. Journal of Materials Science & Technology, 2019. **35**(2): p. 231-241.
177. Laschke, M.W., et al., *Angiogenesis in Tissue Engineering: Breathing Life into Constructed Tissue Substitutes*. Tissue Engineering, 2006. **12**(8): p. 2093-2104.

## REFERENCES

---

178. Alexander, L.E., et al., *Biological Strategies for Improved Osseointegration and Osteoinduction of Porous Metal Orthopedic Implants*. Tissue Engineering Part B: Reviews, 2015. **21**(2): p. 218-230.
179. Parithimarkalaignan, S. and T.V. Padmanabhan, *Osseointegration: an update*. Journal of Indian Prosthodontic Society, 2013. **13**(1): p. 2-6.
180. Alla, R.K., et al., *Surface roughness of implants: a review*. Trends in Biomaterials and Artificial Organs, 2011. **25**: p. 112+.
181. Li, S., T. Chow, and J. Chu, *Engineering microdent structures of bone implant surfaces to enhance osteogenic activity in MSCs*. Biochemistry and Biophysics Reports, 2017. **9**: p. 100-105.
182. Karazisis, D., et al., *The role of well-defined nanotopography of titanium implants on osseointegration: cellular and molecular events in vivo*. International Journal of Nanomedicine, 2016. **11**: p. 1367-1382.
183. Spriano, S., et al., *A critical review of multifunctional titanium surfaces: New frontiers for improving osseointegration and host response, avoiding bacteria contamination*. Acta Biomaterialia, 2018. **79**: p. 1-22.
184. Junqueira, L.C.U.a., *Basic histology : text & atlas*. 10th ed. ed, ed. J. Carneiro. 2003, New York: New York : McGraw-Hill.
185. Yu-Liang, C., et al., *Biomechanical and morphometric analysis of hydroxyapatite-coated implants with varying crystallinity*. Journal of Oral and Maxillofacial Surgery, 1999. **57**(9): p. 1096-1108.
186. Stevenson, G., et al., *Combining 3D human in vitro methods for a 3Rs evaluation of novel titanium surfaces in orthopaedic applications*. Biotechnology and Bioengineering, 2016. **113**(7): p. 1586-1599.
187. Van Bael, S., et al., *The effect of pore geometry on the in vitro biological behavior of human periosteum-derived cells seeded on selective laser-melted Ti6Al4V bone scaffolds*. Acta Biomaterialia, 2012. **8**(7): p. 2824-2834.
188. Rumpler, M., et al., *The effect of geometry on three-dimensional tissue growth*. Journal of the Royal Society, Interface, 2008. **5**(27): p. 1173-1180.



## REFERENCES

---

189. Nune, K.C., et al., *Biological Response of Next-Generation of 3D Ti-6Al-4V Biomedical Devices Using Additive Manufacturing of Cellular and Functional Mesh Structures*. Journal of Biomaterials and Tissue Engineering, 2014. **4**(10): p. 755-771.
190. Di Luca, A., et al., *Tuning Cell Differentiation into a 3D Scaffold Presenting a Pore Shape Gradient for Osteochondral Regeneration*. Advanced Healthcare Materials, 2016. **5**(14): p. 1753-1763.
191. Nune, K., et al., *Osteoblast functions in functionally graded Ti-6Al-4 V mesh structures*. Journal of Biomaterials Applications, 2016. **30**(8): p. 1182-1204.
192. Cheng, A., et al., *Additively manufactured 3D porous Ti-6Al-4V constructs mimic trabecular bone structure and regulate osteoblast proliferation, differentiation and local factor production in a porosity and surface roughness dependent manner*. Biofabrication, 2014. **6**(4): p. 045007.
193. Fukuda, A., et al., *Osteoinduction of porous Ti implants with a channel structure fabricated by selective laser melting*. Acta Biomaterialia, 2011. **7**(5): p. 2327-2336.
194. Taniguchi, N., et al., *Effect of pore size on bone ingrowth into porous titanium implants fabricated by additive manufacturing: An in vivo experiment*. Materials Science and Engineering: C, 2016. **59**: p. 690-701.
195. Wang, H., et al., *The effect of 3D-printed Ti6Al4V scaffolds with various macropore structures on osteointegration and osteogenesis: A biomechanical evaluation*. Journal of the Mechanical Behavior of Biomedical Materials, 2018. **88**: p. 488-496.
196. Zhang, B., et al., *The biomimetic design and 3D printing of customized mechanical properties porous Ti6Al4V scaffold for load-bearing bone reconstruction*. Materials & Design, 2018. **152**: p. 30-39.
197. Li, Z., et al., *What we have achieved in the design of 3D printed metal implants for application in orthopedics? Personal experience and review*. Rapid Prototyping Journal, 2018. **24**(8): p. 1365-1379.
198. Stoffelen, D.V.C., K. Eraly, and P. Debeer, *The use of 3D printing technology in reconstruction of a severe glenoid defect: a case report with 2.5 years of follow-up*. Journal of Shoulder and Elbow Surgery, 2015. **24**(8): p. e218-e222.

## REFERENCES

---

199. Fan, H., et al., *Implantation of customized 3-D printed titanium prosthesis in limb salvage surgery: a case series and review of the literature*. World Journal of Surgical Oncology, 2015. **13**(1): p. 308.
200. Han, Q., et al., *Novel exploration of 3D printed wrist arthroplasty to solve the severe and complicated bone defect of wrist*. Rapid Prototyping Journal, 2017. **23**(3): p. 465-473.
201. Li, H., et al., *Custom Acetabular Cages Offer Stable Fixation and Improved Hip Scores for Revision THA With Severe Bone Defects*. Clinical Orthopaedics and Related Research®, 2016. **474**(3): p. 731-740.
202. Luo, W., et al., *Customized Knee Prosthesis in Treatment of Giant Cell Tumors of the Proximal Tibia: Application of 3-Dimensional Printing Technology in Surgical Design*. Medical Science Monitor : International Medical Journal of Experimental and Clinical Research, 2017. **23**: p. 1691-1700.
203. Xu, N., et al., *Reconstruction of the Upper Cervical Spine Using a Personalized 3D-Printed Vertebral Body in an Adolescent With Ewing Sarcoma*. Spine, 2016. **41**(1): p. E50-E54.
204. Fratzl, P. and R. Weinkamer, *Nature's hierarchical materials*. Progress in Materials Science, 2007. **52**(8): p. 1263-1334.
205. Barthlott, W., et al., *Plant Surfaces: Structures and Functions for Biomimetic Innovations*. Nano-Micro Letters, 2017. **9**(2): p. 23.
206. Yan, C., et al., *Evaluations of cellular lattice structures manufactured using selective laser melting*. International Journal of Machine Tools and Manufacture, 2012. **62**: p. 32-38.
207. Torres, P., *This UNBELIEVABLE Moth Cocoon*. 2013: <http://blog.perunature.com/this-unbelievable-moth-cocoon.html> accessed on 1/5/2019.
208. Jopp-van Well, E., et al., *The assessment of adipocere to estimate the post-mortem interval - a skeleton from the tidelands*. Anthropol Anz, 2016. **73**(3): p. 235-47.
209. Melchels, F.P.W., et al., *Effects of the architecture of tissue engineering scaffolds on cell seeding and culturing*. Acta Biomaterialia, 2010. **6**(11): p. 4208-4217.
210. Czekanska, E.M., et al., *In search of an osteoblast cell model for in vitro research*. Eur Cell Mater, 2012. **24**: p. 1-17.

## REFERENCES

---

- 211. Zhang, X.-Y., et al., *Effect of porosity variation strategy on the performance of functionally graded Ti-6Al-4V scaffolds for bone tissue engineering*. Materials & Design, 2018. **157**: p. 523-538.
- 212. Zhang, X.-Y., et al., *Topological design, permeability and mechanical behavior of additively manufactured functionally graded porous metallic biomaterials*. Acta Biomaterialia, 2019. **84**: p. 437-452.
- 213. Mahmoud, D. and M.A. Elbestawi, *Selective laser melting of porosity graded lattice structures for bone implants*. The International Journal of Advanced Manufacturing Technology, 2019. **100**(9): p. 2915-2927.
- 214. Liu, F., et al., *Functionally graded porous scaffolds in multiple patterns: New design method, physical and mechanical properties*. Materials & Design, 2018. **160**: p. 849-860.
- 215. Beyer, C. and D. Figueroa, *Design and Analysis of Lattice Structures for Additive Manufacturing*. Journal of Manufacturing Science and Engineering, 2016. **138**(12): p. 121014-121014-15.
- 216. Sing, S.L., et al., *Characterization of Titanium Lattice Structures Fabricated by Selective Laser Melting Using an Adapted Compressive Test Method*. Experimental Mechanics, 2016. **56**(5): p. 735-748.
- 217. Tancogne-Dejean, T., A.B. Spierings, and D. Mohr, *Additively-manufactured metallic micro-lattice materials for high specific energy absorption under static and dynamic loading*. Acta Materialia, 2016. **116**: p. 14-28.
- 218. Stamp, R., et al., *The development of a scanning strategy for the manufacture of porous biomaterials by selective laser melting*. Journal of Materials Science : Materials in Medicine, 2009. **20**(9): p. 1839-48.
- 219. Carter, L.N., et al., *The influence of the laser scan strategy on grain structure and cracking behaviour in SLM powder-bed fabricated nickel superalloy*. Journal of Alloys and Compounds, 2014. **615**: p. 338-347.
- 220. Onal, E., et al., *Novel microstructural features of selective laser melted lattice struts fabricated with single point exposure scanning*. Additive Manufacturing, 2019. **29**: p. 100785.

## REFERENCES

---

- 221. Tiferet, E., et al., *Mapping the Tray of Electron Beam Melting of Ti-6Al-4V: Properties and Microstructure*. Materials (Basel, Switzerland), 2019. **12**(9): p. 1470.
- 222. *Stainless Steel as an Architectural Material* 2019 [cited 2019].
- 223. Leijten, J., et al., *Advancing Tissue Engineering: A Tale of Nano-, Micro-, and Macroscale Integration*. Small (Weinheim an der Bergstrasse, Germany), 2016. **12**(16): p. 2130-2145.
- 224. Garikiparithi, M. *How to Improve the Health of Your Blood Vessels*. 2018 [cited 2019].
- 225. Meza, L.R., S. Das, and J.R. Greer, *Strong, lightweight, and recoverable three-dimensional ceramic nanolattices*. Science, 2014. **345**(6202): p. 1322-1326.
- 226. Valdevit, L., et al., *Compressive strength of hollow microlattices: Experimental characterization, modeling, and optimal design*. Journal of Materials Research, 2013. **28**(17): p. 2461-2473.
- 227. Ro, C.J. and C.S. Roper, *Analytical models of the geometric properties of solid and hollow architected lattice cellular materials*. Journal of Materials Research, 2017. **33**(3): p. 264-273.
- 228. Meza, L.R., et al., *Reexamining the mechanical property space of three-dimensional lattice architectures*. Acta Materialia, 2017. **140**: p. 424-432.
- 229. Wang, Y., et al., *Generative design method for lattice structure with hollow struts of variable wall thickness*. Advances in Mechanical Engineering, 2018. **10**(3): p. 1687814017752482.
- 230. Bonatti, C. and D. Mohr, *Large deformation response of additively-manufactured FCC metamaterials: From octet truss lattices towards continuous shell mesostructures*. International Journal of Plasticity, 2017. **92**: p. 122-147.
- 231. Bonatti, C. and D. Mohr, *Mechanical performance of additively-manufactured anisotropic and isotropic smooth shell-lattice materials: Simulations & experiments*. Journal of the Mechanics and Physics of Solids, 2019. **122**: p. 1-26.
- 232. Al-Ketan, O., R.K. Abu Al-Rub, and R. Rowshan, *The effect of architecture on the mechanical properties of cellular structures based on the IWP minimal surface*. Journal of Materials Research, 2018. **33**(3): p. 343-359.

## REFERENCES

---

- 233. Al-Ketan, O., et al., *On Mechanical Properties of Cellular Steel Solids With Shell-Like Periodic Architectures Fabricated by Selective Laser Sintering*. Journal of Engineering Materials and Technology, 2019. **141**(2): p. 021009-021009-12.
- 234. Köhnen, P., et al., *Mechanical properties and deformation behavior of additively manufactured lattice structures of stainless steel*. Materials & Design, 2018. **145**: p. 205-217.
- 235. Bonatti, C. and D. Mohr, *Smooth-shell metamaterials of cubic symmetry: Anisotropic elasticity, yield strength and specific energy absorption*. Acta Materialia, 2019. **164**: p. 301-321.
- 236. Han, S.C., J.W. Lee, and K. Kang, *A New Type of Low Density Material: Shellular*. Advanced Materials, 2015. **27**(37): p. 5506-5511.
- 237. Yan, C., et al., *Ti-6Al-4V triply periodic minimal surface structures for bone implants fabricated via selective laser melting*. Journal of the Mechanical Behavior of Biomedical Materials, 2015. **51**: p. 61-73.
- 238. Bauer, J., et al., *High-strength cellular ceramic composites with 3D microarchitecture*. Proceedings of the National Academy of Sciences, 2014. **111**(7): p. 2453-2458.
- 239. Jang, D., et al., *Fabrication and deformation of three-dimensional hollow ceramic nanostructures*. Nature Materials, 2013. **12**: p. 893.
- 240. Montemayor, L.C., L.R. Meza, and J.R. Greer, *Design and Fabrication of Hollow Rigid Nanolattices via Two-Photon Lithography*. Advanced Engineering Materials, 2014. **16**(2): p. 184-189.
- 241. *Innovative Developments in Virtual and Physical Prototyping - Proceedings of the 5th International Conference on Advanced Research and Rapid Prototyping*. 2012.
- 242. Bezuidenhout, M.B., et al., *Titanium-Based Hip Stems with Drug Delivery Functionality through Additive Manufacturing*. BioMed Research International, 2015. **2015**: p. 134093.
- 243. Burton, H.E., et al., *The design of additively manufactured lattices to increase the functionality of medical implants*. Materials Science and Engineering: C, 2019. **94**: p. 901-908.

## REFERENCES

---

- 244. Amani, Y., et al., *Compression behavior of lattice structures produced by selective laser melting: X-ray tomography based experimental and finite element approaches*. Acta Materialia, 2018. **159**: p. 395-407.
- 245. Zhao, M., et al., *Improved Mechanical Properties and Energy Absorption of BCC Lattice Structures with Triply Periodic Minimal Surfaces Fabricated by SLM*. Materials (Basel, Switzerland), 2018. **11**(12): p. 2411.
- 246. Koempel, J.A., et al., *The effect of recombinant human bone morphogenetic protein-2 on the integration of porous hydroxyapatite implants with bone*. Journal of Biomedical Materials Research, 1998. **41**(3): p. 359-363.
- 247. Zhao, C., et al., *Osteoinduction of porous titanium: A comparative study between acid-alkali and chemical-thermal treatments*. Journal of Biomedical Materials Research Part B: Applied Biomaterials, 2010. **95B**(2): p. 387-396.
- 248. Ponader, S., et al., *In vivo performance of selective electron beam-melted Ti-6Al-4V structures*. Journal of Biomedical Materials Research Part A, 2010. **92A**(1): p. 56-62.
- 249. Hao, Y., S.J. Li, and R. Yang, *Biomedical titanium alloys and their additive manufacturing*. Rare Metals, 2016. **35**(9): p. 661-671.
- 250. Sing, S.L., W.Y. Yeong, and F.E. Wiria, *Selective laser melting of titanium alloy with 50 wt% tantalum: Microstructure and mechanical properties*. Journal of Alloys and Compounds, 2016. **660**: p. 461-470.
- 251. Zhou, L., et al., *Microstructure and mechanical performance tailoring of Ti-13Nb-13Zr alloy fabricated by selective laser melting after post heat treatment*. Journal of Alloys and Compounds, 2019. **775**: p. 1164-1176.
- 252. Zhang, L.C., et al., *Manufacture by selective laser melting and mechanical behavior of a biomedical Ti-24Nb-4Zr-8Sn alloy*. Scripta Materialia, 2011. **65**(1): p. 21-24.
- 253. Cui, Q., et al., *Antibiotic-impregnated cement spacers for the treatment of infection associated with total hip or knee arthroplasty*. J. Bone Joint Surg.-Am. Vol., 2007. **89**(4): p. 871-882.